The Dissertation Committee for Douglas Edward Yeager Certifies that this is the approved version of the following dissertation:

Intravascular Photoacoustics as a Theranostic Platform for Atherosclerosis

Committee:

Stanislav Emelianov, Supervisor

Aaron Baker

Jonathan Sessler

Richard Smalling

Konstantin Sokolov

Intravascular Photoacoustics as a Theranostic Platform for Atherosclerosis

by

Douglas Edward Yeager, B.S.

Dissertation

Presented to the Faculty of the Graduate School of

The University of Texas at Austin

in Partial Fulfillment

of the Requirements

for the Degree of

Doctor of Philosophy

The University of Texas at Austin

August 2014

Dedication

To my family,

for their unwavering support and inspiration.

Acknowledgements

I have been extremely blessed to pursue this degree in great company, including that of both my peers and collaborators at UT-Austin and of my family and friends in Austin. And as a direct reflection of the support I have felt during this journey, there are a vast number of people to acknowledge. I would like to first thank my advisor, Dr. Stanislav Emelianov for his mentorship over the past five years. Stas, your mentorship, encouragement, and support have guided me back on track countless times throughout this journey. I would also like to thank my other committee members, Dr. Sokolov, Dr. Smalling, Dr. Baker, and Dr. Sessler for their collaboration over the last several years; I am honored to have each of you be a part of this dissertation and grateful for your time and feedback in agreeing to do so.

I truly believe that I would not be in this position today without the knowledge and encouragement passed on from an amazing array of prior and current lab members from the Ultrasound Imaging and Therapeutics Research Laboratory and beyond. Bo Wang and Andrei Karpiouk- for introducing IVPA imaging, from the theory to instrumentation. The original office members- Dr. Jimmy Su, Dr. Jason Cook, Dr. Seungsoo Kim, Dr. Yun-Sheng Chen, Dr. Pieter Kruizinga, Dr. Mohammad Mehrmohammadi, and Soon Joon Yoon- who helped get me up to speed on plasmonic nanoparticles and photoacoustic imaging principles on the dry erase board that doubled as a screen for the PS3 and World Cup games. Jim Amirian- for endless help with animal studies and protocol amendments has enabled much of the work in IVPA imaging studies. Drs. Yun-Sheng Chen, Tim Larson, Justina Tam, Pratixa Joshi, Frank Wu, Kimberly Homan, Justin Harris, and Carolyn Bayer - your knowledge and guidance with

nanoparticle synthesis and characterization have been instrumental. I would also like to thank Drs. Wolfgang Frey, Geoff Luke, Salavat Aglyamov, Richard Bouchard, Seung-Yun Nam, Srivalleesha Mallidi, Katie Wilson, Iulia Graf, Min Qu and Sangpil Yoon, as well as Alex Hannah, Nich Dana, Luara Ricles, Don Vanderlaan, Daniela Santiesteban, Kristen Meiburger, Angel Zubieta and Collin Johnson for their collaboration and support. I am also grateful to Dr. Christian Preihs and Dr. Gregory Thiabaud for agreeing to collaborate with me and provide guidance with the LuTex photosensitizers and PDT in general. I also owe a huge debt of gratitude to Tera Sherrard and Juili Kelvekar, without whom I would have forgotten to order products, or submit travel reimbursement forms, or even register, entirely too often.

Finally, I am absolutely grateful for the support of my family and friends. I have been simultaneously in awe of my colleagues who have traveled from all over the country and the world for their research and immensely grateful that I have had the opportunity to remain close to home, surrounded by immediate and extended family and lifelong friends. To my friends (and Miles), thank you for keeping me sane and grounded. To my parents and brother, from whom I have learned the value of hard work, I cannot thank you enough for the endless support and encouragement in all aspects of my life. Sarah, thank you for your love and for your patience, which we both know is tested far beyond the chaotic work hours of late. I am excited for our next chapters together.

Intravascular Photoacoustics as a Theranostic Platform for Atherosclerosis

Douglas Edward Yeager, Ph.D.

The University of Texas at Austin, 2014

Supervisor: Stanislav Emelianov

The persistence of high global mortality rates directly attributable to cardiovascular disease drives ongoing research into novel approaches for improved diagnosis and treatment of its primary underlying cause, atherosclerosis. Combined intravascular ultrasound and photoacoustic (IVUS/IVPA) imaging is one such modality, actively being developed as a tool for improved characterization of high-risk atherosclerotic plaques. The pathophysiology associated with progression and destabilization of atherosclerotic plaques leads to characteristic changes in arterial morphology and composition. IVUS/IVPA imaging seeks to expand upon the ability of clinically utilized intravascular ultrasound (IVUS) imaging to assess vessel anatomy by adding improved sensitivity to image the underlying cellular and molecular composition through intravascular photoacoustic (IVPA) imaging of either endogenous chromophores (e.g. lipid) or exogenously delivered contrast agents.

This dissertation focuses on the expansion of IVUS/IVPA imaging using exogenous contrast agents to enable the detection and subsequent optically-triggered therapy of atherosclerotic plaques. The passive extravasation and aggregation of systemically injected plasmonic gold nanorods absorbing within the near infrared tissue optical window within plaques of atherosclerotic rabbit models is first demonstrated,

along with the ability to localize the contrast agents using *ex vivo* IVUS/IVPA imaging. The motivation for nanoparticle labeling of atherosclerosis is then expanded from that of purely image contrast agents to vehicles for image-guided, dual-modality phototherapy. The integrated IVUS/IVPA imaging catheter is utilized for photothermal delivery with simultaneous IVPA temperature monitoring using the high optical absorption of gold nanorod contrast agents to enable localized heating. Subsequently, the potential role for IVUS/IVPA-guided phototherapy is further expanded through the characterization and *in vitro* assessment of novel multifunctional theranostic nanoparticles comprised of a gold nanorod core with a degradable, photosensitizer-doped silica shell. Together, the results presented within this dissertation provide a framework for ongoing research into the expansion of IVUS/IVPA imaging as a platform for complimentary diagnosis and local treatment of atherosclerotic plaques using multifunctional theranostic nanoparticle contrast agents.

Table of Contents

List of Tables

List of Figures

Chapter 1: Introduction- The Motivation for Atherosclerotic Plaque Characterization and Novel Therapy Guidance Using Intravascular Photoacoustics

The persistence of high global mortality rates which can be directly attributed to cardiovascular disease continues to motivate ongoing research into a more complete understanding of biological mechanisms for disease progression as well as novel approaches for improved diagnosis and treatment of its primary underlying cause, atherosclerosis. Coronary heart disease alone is responsible for an estimated 7.3 million annual deaths throughout the world and greater than one in six deaths within the United States, with estimated related domestic costs well in excess of one hundred billion dollars [1,2]. Together, these statistics clearly demonstrate the ongoing need for improved preventative, diagnostic, and therapeutic interventions. While several notable risk factors are well known, such as high blood pressure or cholesterol levels, smoking, obesity, and physical inactivity, their monitoring alone remains insufficient for reliable diagnosis of high risk patients. Therefore, improved clinical strategies are needed to aid in the diagnosis of atherosclerosis at the level of both the patient and their individual high-risk lesion(s).

Diagnostic imaging, particularly intravascular imaging modalities, represents an area of active research with potential to help meet the clinical demand for improved localization and characterization of coronary atherosclerosis. However, conventional imaging techniques within interventional cardiology provide an incomplete assessment of coronary artery plaque, particularly with regard to their ability to differentiate specific cellular and molecular biomarkers of atherosclerotic lesion vulnerability. To this end, a number of emerging intravascular imaging modalities are currently in development, utilizing differing technologies to supplement anatomical images of existing imaging

modalities with improved compositional information. Such techniques seek to take advantage of the increased understanding of the pathophysiology of atherosclerotic plaques, particularly those most prone to induce acute cardiac events.

1.1. Pathophysiology and Destabilization of Coronary Atherosclerosis

Continued molecular biology research over the past several decades has provided increased understanding of the fundamental pathophysiological pathways involved in the development and destabilization of coronary atherosclerosis. Plaque progression is a process involving disordered cholesterol metabolism, compromised endothelial function, and loss of vessel patency, with systemic and local inflammatory events occurring throughout its growth (Fig. 1.1A). Atherosclerosis develops from endothelial dysfunction, causing monocyte recruitment and eventual progression towards an advanced, thrombotic plaque [3]. High levels of low density lipoprotein (LDL), or infectious agents and toxins can cause endothelial dysfunction and expression of adhesion molecules and selectins. High levels of these molecules, in turn, promote the accumulation of monocytes, which subsequently form macrophage foam cells and an associated amplified inflammatory response with secretion of extracellular matrix proteins [4-6]. Ultimately, production of matrix metalloproteinases can weaken a plaque's fibrous cap, leaving the prothrombotic core prone to erosion, fissure, or rupture with subsequent thrombus formation which can result in acute complications.

Together, atherosclerotic lesions which have advanced to the point of being at high risk of acute thrombus formation are referred to as 'vulnerable plaques'. As high as 60% or more of acute coronary syndromes - a term which encompasses unstable angina, acute myocardial infarction, and sudden cardiac death – are the result of thrombi formation following atherosclerotic plaque rupture [7]. Several studies investigating the

underlying mechanisms and plaque compositions which lead to plaque rupture have led to modified classification schemes for staging atherosclerotic lesions, with thin-cap fibroatheroma (TCFA) being identified as the most common culprit lesions for plaque ruptures [7,8]. TCFA are defined as exhibiting a thin fibrous cap, with thickness <65 μm, overlaying a large, lipid-rich necrotic core and an increased infiltration of macrophages relative to healthy arterial tissue and more stable atherosclerotic plaque categories (Fig. 1.1B) [9-16]. Longitudinal sectioning of cadaver coronary arteries has also enabled an estimation of the occurrence and distribution of these high-risk plaques, finding that the majority of TCFA occur within the proximal third of the major coronary arteries and at focal sites within the arteries rather than diffusely spread of over long distances [17]. Together, this understanding of the local anatomy and composition lends itself to the implementation of targeted diagnostic imaging and localized therapeutic strategies.

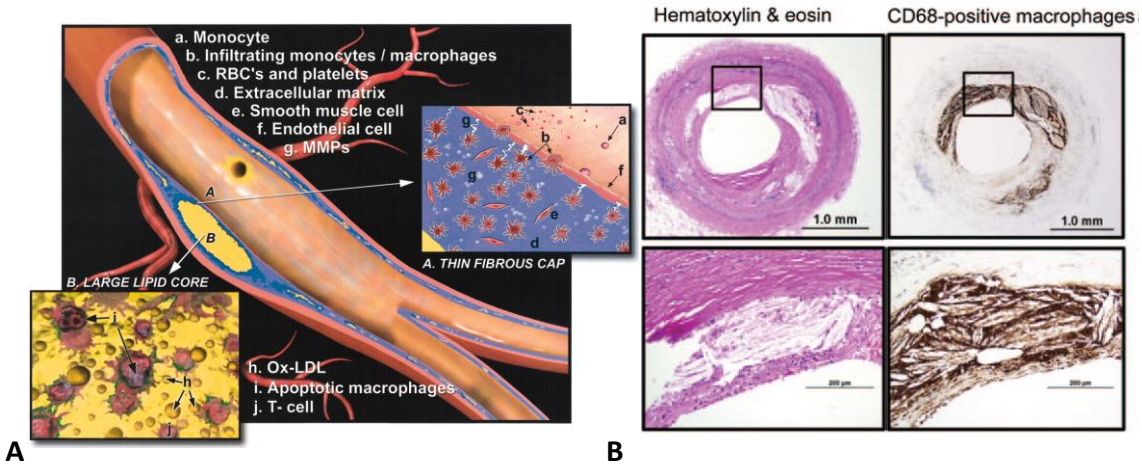

Figure 1.1: Anatomy and composition of vulnerable atherosclerotic plaques. (A) Schematic representation of vulnerable plaque cellular and molecular composition. Reprinted with permission from [8]. (B) Histology of a vulnerable plaque revealing a thin fibrous cap and high macrophage cell density. Reprinted with permission from [18].

The primary biological hallmarks of TCFA plaques include the presence of a necrotic core with acellular regions surrounded by elevated macrophage density. Both of these characteristics are indicative of an imbalance between intra-plaque apoptosis and the clearance of apoptotic cells or necrotic cell debris. In fact, while it is believed that the fate of most cells within atheroma is apoptosis, a form of programmed cell death in which caspases gradually dismantle the cells in a cascade which signals for their engulfment by phagocytes, the level number density of apoptotic cells within a plaque has been shown to closely related to its lesion stage and likelihood of plaque rupture [19]. The consequences of apoptosis within atheroma are highly dependent on both cell type and the plaque stage. In the case of macrophages, experimental models of atherosclerosis have shown that increasing apoptosis can lead to a stabilizing effect, with reduced plaque size, for early lesions, but result in increased plaque size in older lesions [20]. The driving mechanisms for this divergence in effect of macrophage apoptosis has been linked to the extent of efferocytosis, engulfment of apoptotic cells by phagocytes and other surrounding cells, within the plaques. In advanced lesions, delayed or compromised efferocytosis pathways allow apoptotic macrophages to become secondarily necrotic cells which, in turn, contribute to the expansion of the necrotic core of vulnerable plaques [21]. It has additionally been hypothesized that the predominant cause of compromised efferocytosis within advanced plaques is the transition of macrophages into foam cells, which yields them inefficient in engulfing nearby apoptotic cells [21]. As a result, the presence and biochemical state of macrophages within advanced atherosclerotic plaques play an important role in determining and, in many respects, driving the vulnerability of the lesion to rupture and induce acute coronary syndromes. Therefore, the ability to detect and differentiate macrophages in addition to other anatomical and compositional

biomarkers of TCFA plaques is of great interest for both the improved experimental understanding and the clinical diagnosis of vulnerable plaques.

1.2. Intravascular Imaging Techniques for Diagnosis and Characterization of Coronary Atherosclerosis

Despite the growing fundamental understanding of the pathophysiology involved in atheroma progression and destabilization, its translation into reliable clinical diagnoses remains limited by the capabilities of current imaging modalities. For example, the traditional gold standard for coronary imaging during percutaneous coronary interventions (PCI), contrast coronary angiography, provides only a two dimensional projection of vessel patency. While heavily used during intervention to guide catheter placement, the resulting images provide a primarily morphological characterization of the coronary tree, with little information gained beyond the verification of a local stenosis within a coronary artery region. Similarly, coronary computed tomography either utilizes contrast injections to obtain projections of the coronary artery patency or detects the presence of higher-density calcifications within the coronary arteries. While the amount of calcium within the coronary tree has been shown to be correlated with total plaque burden, the most vulnerable plaques frequently do not contain significant calcium and, therefore, the absence of coronary calcification detected by computed tomography does not exclude the potential for vulnerable plaques [22]. Additionally, both angiography and computed tomography techniques are fundamentally limited by using contrast to image the coronary lumen diameter. Positive remodeling enable preservation of the lumen diameter with plaque areas up to 40%, as was first shown by Glagov, through compensatory expansion of the arterial wall [23]. This phenomenon has clearly limiting implications for imaging techniques which detect only the luminal diameter. Furthermore, each of these techniques suffers from inadequate resolution and contrast to

detect critical characteristics of plaque stability, such as the thickness of a fibrous cap and underlying lipid and macrophage distribution.

Therefore, there remains a need for improved diagnostic imaging which provide interventional cardiologists with greater information regarding the morphology as well as the cellular and molecular composition of atheroma to help guide accurate lesion characterization and to monitor therapy delivery. Numerous intravascular imaging techniques, including those which have already been translated into clinical practice as well as those in preclinical development, are poised to help bridge this gap between diagnostic imaging capabilities and the fundamental understanding of disease pathology [24]. These techniques are briefly introduced below, with an emphasis on the benefits of each as an imaging tool for detecting and staging atherosclerotic plaques.

1.2.1. Intravascular Ultrasound

Intravascular ultrasound (IVUS) imaging has provided a tool for arterial assessment within the catheterization laboratory for several decades, particularly within Japan, Europe and the United States. At the time of intervention, an IVUS catheter is advanced into the coronary arteries and scanned using a high center frequency ultrasound transducer (20-60 MHz) which is rotated to provide real-time, cross-sectional images of arterial morphology to aid in diagnosis and therapy guidance during percutaneous coronary intervention. Volumetric renderings of coronary artery segments can also be obtained if the catheter is mechanically pulled back during rotation. IVUS is commonly used for the characterization of atherosclerotic lesions of unclear severity based on angiographic assessment to guide selection of the appropriate transcatheter therapy option through its ability to delineate the full vessel wall thickness and echogenicity to provide metrics associated with lesion severity (Fig. 1.2A) [25]. Despite its ongoing clinical

applications, however, IVUS provides limited histopathological information about the imaged artery, and histological studies have reported a generally low sensitivity of the technique's ability to differentiate thrombotic and lipid-rich lesions [26,27]. Efforts to overcome these fundamental limitations of IVUS have led to the investigation of numerous imaging techniques intended to supplement the morphological view provided by IVUS imaging with greater information regarding the compositional or mechanical characteristics of the interrogated arteries. Among these techniques are virtual histology IVUS (VH-IVUS) and integrated backscatter IVUS (IB-IVUS), both of which involve analysis of the spectral content of backscattered US signals as a means of predicting tissue composition. Although VH-IVUS and IB-IVUS are clinically available methods intended to improve the ability of IVUS to detect plaque composition, the reliability of these approaches has recently been questioned [28,29]. Additionally, IVUS palpography, a technique which involves the assessment of vessel wall deformation at variable intravascular pressures (e.g. systole and diastole) to detect soft versus hard lesions, has also been investigated [30].

1.2.2. Optical Coherence Tomography

Intravascular optical coherence tomography (OCT) has also been introduced as an alternative to IVUS imaging. OCT is conceptually analogous to IVUS imaging in that images from both modalities are generated based on signals reflected from tissue structures. However, whereas IVUS signals are received by the direct detection of time of flight of the propagating ultrasound pressure transients, in the case of OCT, interferometry techniques are used to detect either time delays or frequency shifts in received optical echoes, which travel five orders of magnitude faster than ultrasound waves. As a result, OCT is able to achieve a higher axial resolution than IVUS imaging

and can therefore provide greater ability to differentiate vessel wall and atherosclerotic plaque microstructures, with adequate axial resolution to detect the thin cap of TCFA plaques (Fig. 1.2B) [31]. In addition to general detection of vessel morphology and identification of atherosclerotic plaques, fibrous cap thickness, microcalcifications, neovascularization, thrombus, and macrophage infiltration have all been interrogated by OCT [32]. The modality is not without its own limitations, however, as it requires saline flushing to eliminate blood during signal acquisition, and is capable of providing a limited tissue penetration depth of less than approximately 1.25 mm, or even less in lipid-rich regions [33].

1.2.3. Near Infrared Spectroscopy

While both IVUS and OCT imaging provide clinicians with information primarily related to coronary artery morphology, each modality is limited in its ability to definitively diagnose arterial composition due to potential ambiguities and artifacts in their respective backscattered signals. Intracoronary diffuse reflectance near-infrared spectroscopy (NIRS) represents an additional, clinically approved, imaging technique which is capable of detecting lipid-rich plaques. NIRS relies on variations in the molecular overtone and combination vibrations of endogenous molecules, which result in molecular composition-specific optical absorption and scattering within the near-infrared region of the electromagnetic spectrum (approximately 1000 nm to 2400 nm). During intravascular NIRS imaging, a broadband NIR source is emitted into the arterial wall and the returned light is received to extract chemical compositional information of the illuminated region. First demonstrated as a tool for assessing atherosclerotic plaques in an animal model of atherosclerosis in the early 1990s [34], the capability of NIRS to detect several plaque risk indicators, including lipid pools, fibrous cap and inflammatory cells

was demonstrated nearly a decade later [35], and the modality was first utilized for *in vivo* human imaging for lipid detection soon thereafter [36]. Commercialized by Infraredx, Inc. (Burlington, Massachusetts), and approved by the Food and Drug Administration (FDA) in 2008, clinical intravascular NIRS provides a chemogram representing the likelihood of a lipid-rich plaque within an angular region of an arterial cross-section. A notable advantage of the technique is that this chemogram can be obtained through blood, thus avoiding the need for luminal flushing which is required for most other optical imaging modalities. However, because NIRS detects remitted light from within highly optically scattering blood and tissue, the received signal is not depth-resolved [37]. Therefore, while the absence or presence of a lipid-rich plaque can be detected using NIRS, it alone cannot provide corresponding morphological context without being coupled with IVUS or OCT.

The current clinical NIRS system couples the technique with IVUS imaging, providing a dual modality approach to coronary assessment (Fig. 1.2C). Both NIRS and IVUS image acquisition are performed simultaneously with a conventional IVUS image display encompassed within a chemogram revealing the likelihood of lipid-rich plaque within an angular region. In addition to a demonstrated general improvement in the ability to characterize high-risk, lipid-rich plaques [36,38], the hybrid NIRS/IVUS imaging technique is also being used to generate a database through the Chemometric Observations of Lipid Core Plaque of Interest in Native Coronary Arteries (COLOR) registry to be used for assessment of the varieties of lipid-rich plaques and their long-term clinical significance and responses to available therapies [39]. Additionally, a recently launched 9,000 patient Lipid-Rich Plaque Study trial is intended to assess whether this hybrid imaging technique can be utilized as a predictor of future coronary events.

Early clinical adoption of NIRS/IVUS has been found through its inclusion as an end point for lipid-lowering clinical trials [40] and is actively being investigated as a tool to help reduce risk of periprocedural complications during PCI through the Coronary Assessment by Near-infrared of Atherosclerotic Rupture-prone Yellow (CANARY) trial [41,42]. As results of the ongoing clinical trials come out, the true clinical impact of NIRS/IVUS imaging will be further clarified.

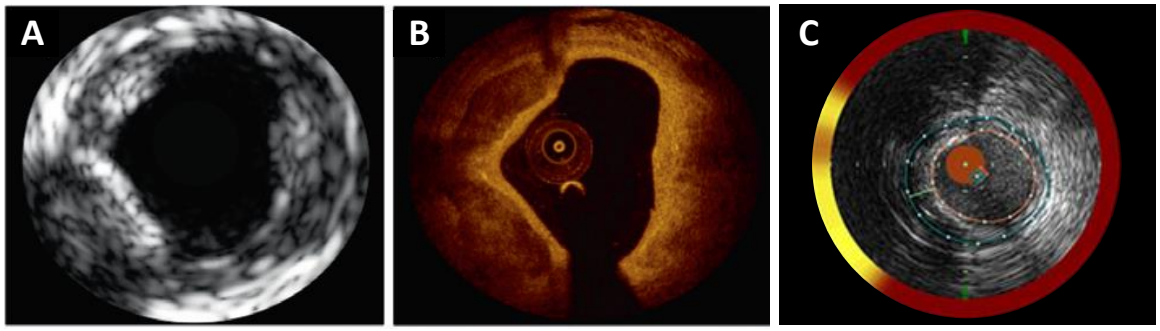

Figure 1.2: Representative images from clinical intravascular imaging systems: (A) IVUS and (B) OCT. Reprinted with permission from [43]. (C) NIRS with accompanying IVUS; source: infraredx.com.

1.2.4. Angioscopy

Coronary angioscopy (CAS) represents an alternative approach for intravascular imaging, enabling clear visualization of the luminal arterial wall. Originally introduced as early as the mid-1980s [44,45], CAS is a clinically approved, endoscopic technique which utilizes a fiber bundle to deliver a white light illumination source as well as to collect and return reflected light to a charge-coupled-device, color camera [39]. The generated CAS images have been demonstrated to enable the differentiation of atheroma composition based, in part, on the color of identified lesions. Fibrous lesions tend to appear as white lesions, whereas lipid-rich plaques tend to exhibit a yellow color upon CAS visualization, likely due to the carotenoid content of intimal cholesterol [46]. Furthermore, the intensity of the detected yellow color has also been associated with the

prevalence of thrombosis on the atheroma, suggesting a potential indicator of lesion vulnerability [47].

Despite its regulatory approval and ability to distinguish different arterial surface compositions, however, the utilization of CAS remains limited to research applications, and there are currently no clinical indications for the use of CAS over other imaging modalities during coronary intervention. Limitations of the technique include the inability to image beyond the surface of the arterial wall, the requirement of flushing luminal blood during imaging, and catheter diameters which are too large to enable imaging beyond the proximal regions of main coronary arteries. As a research tool, however, CAS continues to be refined and is commonly utilized to help evaluate the efficacy of both pharmacological treatment regimes, such as statin therapies [48,49], and evaluation of arterial wall response following stent placement [50,51]. Additionally, due to its limitation to imaging the arterial surface, CAS has been utilized in combination with IVUS [52,53] and OCT [54], as well as the combination of all three modalities [31] to provide a more comprehensive evaluation of atherosclerotic lesions. Despite these pairings, however, integrated intravascular probes combining CAS with other intravascular modalities have not yet been developed, and co-registration of CAS images with those obtained from the same arterial cross-section with different techniques remains a challenge for these dual- and tri-modality applications.

1.2.5. Investigational Intravascular Imaging Techniques

In addition to the aforementioned clinical approved imaging modalities for diagnosis atherosclerotic plaques and guiding their subsequent treatment, several novel approaches are currently being investigated within preclinical settings. These investigational intravascular techniques include fluorescence techniques, Raman

spectroscopy, magnetic resonance, and nuclear imaging. Each of the modalities offers the potential for improvement(s) over existing clinical intravascular imaging modalities, particularly enhanced capabilities for assessment of plaque composition or biomarkers.

1.2.5.1. Fluorescence Imaging Techniques

Fluorescence imaging techniques have also been introduced as a means of enhancing the ability to detect atherosclerotic plaque composition. Several distinct fluorescence imaging techniques are underway, including time resolved fluorescence spectroscopy (TRFS) and near-infrared fluorescence spectroscopy (NIRF). Initial studies were able to differentiate normal arterial tissue from atherosclerotic lesions by assessing the tissue molecular components, including lipid, elastin, and collagen based on their respective autofluorescence characteristics [55-57]. Increased molecular specificity, however, has been achieved through the introduction of TRFS, a technique which relies on the temporal profile of remitted photons following excitation with a pulsed optical source. TRFS has been demonstrated for the *ex vivo* classification of atherosclerotic plaques into three subtypes; intimal thickening, fibrotic and fibrocalcific, and inflamed and necrotic lesions [58]. The ability to detect the presence of macrophage foam cells was also demonstrated [59]. Further improvements were subsequently made through the introduction of fluorescence lifetime imaging microscopy (FLIM), a TRFS technique which enables the recording of two-dimensional lifetime information in an image format, compatible within an endoscopic design which permitted an improved imaging depth of approximately 4 mm [60,61]. The FLIM catheter was utilized for *ex vivo* characterization of 11 human aorta sections at a total of 48 locations, demonstrating that the technique can be used to distinguish clinically relevant plaque features with sensitivities as high as 86% and an all case specificity of 87% [62]. Notably, a hybrid imaging probe combining

fluorescence spectroscopy with reflectance spectroscopy and Raman spectroscopy has also been described [63] and utilized to characterize plaque composition [64].

As FLIM and, more generally, TRFS continue development towards clinical translation, they suffer from two primary drawbacks, a limited penetration depth of approximately 250 μm due to the high absorption and scattering of the excitation light and the inability to provide arterial morphology to compliment the compositional assessment [61].

1.2.5.2. Raman Spectroscopy

Raman spectroscopy, an alternative method for detecting the molecular signatures of biological tissues, has also been investigated as a potential intravascular imaging modality. Rather than molecular absorption spectra, as is the basis for NIRS assessment, Raman spectroscopy relies on frequency shifts of emitted light which are generated by an energy exchange between photons and molecular components of tissues. The magnitude of this energy exchange, and thus the extent of the frequency shift of received photons, is a function of a given molecule's vibrational and rotational energies. Raman spectroscopy, therefore, offers the potential for very high molecular specificity. Whereas NIRS is used to differentiate lipid-rich plaques, Raman spectroscopy offers the potential to differentiate specific chemical components such as triglycerides, cholesterol, cholesterol esters, elastin, and collagen [65-69]. Several intravascular Raman imaging catheter prototypes have been developed and utilized for arterial characterization, including in the presence of luminal blood [69-72].

Irrespective of the potential for high intravascular molecular sensitivity, Raman spectroscopy as a stand-alone modality suffers from similar limitations as NIRS, namely its inability to detect arterial morphology. To this end, offline approaches coupling the

modality with either IVUS or OCT have been investigated [73-77]. While these proof-of-concept demonstrations of hybrid Raman techniques are still in early stages, they offer the potential for development into an intravascular system analogous to that of NIRS/IVUS.

Despite early demonstrations of hybrid modalities combining Raman spectroscopy with IVUS or OCT, Raman spectroscopy has failed to be translated into the clinic. In comparison to NIRS, Raman spectroscopy typically yields low intensity signals, and the resulting low signal-to-noise ratio (SNR) is exacerbated by noise introduced within the optical fibers of Raman catheters. While high-wavenumber Raman spectroscopy techniques and new catheter designs have provided hope that the technical challenges preventing commercialization of a hybrid Raman-based approach to plaque assessment will be attained, significant validation is still required [71,75].

1.2.5.3. Magnetic Resonance Imaging

Noninvasive magnetic resonance imaging (MRI) has been utilized to image lipid within arterial walls, as well as other biomarkers of atherosclerotic plaque vulnerability or rupture through the use of contrast agents, based on the biochemical response of protons following the application of an electromagnetic radiofrequency pulse within the presence of a static magnetic field [78]. Noninvasive MRI, however, is ill-suited for such imaging of the coronary arteries due to a lack of adequate signal to noise ratio (SNR) and motion artifacts. To this end, various designs of intravascular MRI approaches have been developed for imaging coronary arteries, including the use of receiver coils and self-contained probes [79-82]. Utilizing a self-contained probe consisting of a magnet as well as transmitting and receiving coils, intravascular MRI was able to differentiate TCFA plaques from *in situ* coronary arteries with high sensitivity and specificity and no

complications arising in a first-in-man study of 29 patients [83,84]. However, intravascular MRI enables a limited penetration depth of only 250 μm, a circumferential view of only 120° with poor angular resolution, and an inability to produce a true image [85]. Instead, a map of chemical composition analogous to that utilized for NIRS imaging is created, with no corresponding anatomical context about the imaged arterial cross-section. Together, these drawbacks have largely limited the continued development of intravascular MRI as a viable solution to improve upon existing techniques, despite the high sensitivity of MRI for lipid detection.

1.2.5.4. Positron Emission Tomography

Conventional scintigraphic techniques, including positron emission tomography (PET) and single photon emission computed tomography (SPECT), have a wide array of applications within cardiovascular imaging. These techniques utilize radionuclide contrast agents to detect and monitor physiological processes, thus enabling functional imaging. However, in the case of coronary atherosclerosis, these noninvasive modalities suffer as a result of substantial physiological motion and provide insufficient resolution and sensitivity to effectively characterize functional activity within atherosclerotic lesions. Efforts to circumvent those limitations, however, have resulted in the development and *ex vivo* characterization of several prototype intravascular radiation detection catheters [86-90]. For such catheters, it is desirable to detect beta radiation, due to its short path length of only a few millimeters, rather than gamma and x-radiation, which have much longer path lengths and could increase undesirable background signal from tissue beyond the coronary adventitia. The distal ends of these intravascular catheters have typically utilized plastic scintillating fibers for beta detection, resulting in improved sensitivity radionuclide detection over noninvasive nuclear imaging techniques.

Intravascular positron detection alone, however suffers from a lack of anatomical information. Therefore, to compliment the functional information obtained from arterial lesions, a dual positron detection and OCT probe has been developed [91]. The hybrid probe was demonstrated on *ex vivo* arteries from animal models of atherosclerosis, demonstrating the complimentary functional and microstructure information offered by the two modalities. Despite this initial demonstration of the feasibility to combine these two modalities, intravascular positron detection has not continued to make advances towards a clinical catheter, likely a result of its limited resolution. Additional challenges include the need for improved catheter design and the optimization of radionuclide delivery and detection protocols, owing to their limited half-life and inherent circulation times.

1.2.6. Summary of Intravascular Imaging Modalities

Each of these clinical and investigational intravascular imaging modalities offers both distinct advantages and disadvantages for the assessment of coronary atherosclerosis, ranging from the high superior anatomical context provided by IVUS and OCT to the chemical compositional assessment enabled through many of the investigational techniques (Table 1.1). As a result, efforts to commercialize multimodal, hybrid imaging systems which strategically combine such benefits for improved plaque characterization are under way. However, none of these systems are capable of providing co-registered views of the arterial anatomy and its underlying composition, two key determinants of atherosclerotic plaque vulnerability. To this end, an additional hybrid intravascular imaging modality, combined intravascular ultrasound and photoacoustic (IVUS/IVPA) imaging, has recently been developed to provide inherently co-registered anatomical and cellular/molecular compositional information regarding the imaged

arterial tissue through the combination of conventional IVUS and photoacoustic imaging, a form of optically-induced ultrasound generation.

1.3. PHOTOACOUSTIC IMAGING PRINCIPLES

Photoacoustic (PA) imaging, also referred to as optoacoustic imaging or, more generally, thermoacoustic imaging, relies on the detection of acoustic pressure transients generated as a result of rapid thermal expansion following absorption of optical pulses. Although reported by Alexander Graham Bell in 1880 [92], widespread research into potential applications of PA imaging did not commence until after the development of laser-based technologies in the 1960s and 1970s. Even then, early PA applications predominantly focused on spectral characterization of gases or thin film solids and liquids [93,94]. It was more than a decade later before the PA effect was first applied for soft-tissue imaging [95] and began to be introduced as a biomedical imaging modality [96,97].

For PA imaging, the optically induced pressure amplitude is proportional to the delivered optical fluence, the absorption coefficient of the absorber(s) and the Grüneisen parameter, which accounts for the efficiency of conversion from optical to acoustic energy. Due to the dependence of the PA signal amplitude on the optical absorption properties of the illuminated medium, it is possible to differentiate particular absorbers of interest based on their unique spectral signatures. In this respect, PA imaging is similar to optical spectroscopy techniques such as NIRS. However, PA imaging offers a distinct advantage in comparison to purely optical-based techniques. Because the signal detection is achieved ultrasonically, locating the origin of the signal (i.e., optical absorber) can be achieved based on the ultrasound time-of-flight. As a result, PA signals can be readily depth-resolved to reveal the spatial distribution of absorbers. Furthermore, when coupled

with pulse-echo ultrasound imaging, combined ultrasound and PA imaging is well-suited to provide complimentary morphology as well as cellular and molecular compositional information using shared instrumentation and signal processing algorithms.

The combination of IVUS with intravascular photoacoustic (IVPA) imaging was recently introduced as a potential hybrid imaging modality for improved characterization of coronary arteries. Combined IVUS/IVPA imaging provides a means of supplementing the morphological information provided by IVUS with additional capability for assessing the composition of atherosclerotic lesions based on unique optical absorption properties of specific plaque components or delivered imaging contrast agents [98]. The mechanisms for this synergistic nature of the combined imaging modality are rooted in the fundamental principles of photoacoustic imaging.

1.3.1. Photoacoustic Pressure Generation

Photoacoustic imaging relies on absorption of optical energy, subsequent thermal expansion of the absorber, and the generation of a resultant pressure wave which can be detected and localized using acoustic imaging techniques. The application of modulated electromagnetic radiation, such as in the form of pulsed laser illumination, can lead to the generation of acoustic waves via five distinct processes, including dielectric breakdown, vaporization, thermal expansion, electrostriction, and radiation pressure [99,100]. The vast majority of biomedical applications of PA imaging utilize the mechanism of thermal expansion, a process by which optical absorption from a pulsed laser source induces a mechanical expansion and relaxation of the absorbing chromophore [95,101].

In order for highly efficient PA signal generation, both the thermal and stress confinement conditions should be satisfied. Thermal and stress confinement conditions are defined by Equations 1.1 and 1.2, respectively, where τ_0 is the optical pulse duration,

τ_{th} is the thermal diffusion time, τ_s is the stress relaxation time, d_c is a characteristic dimension of the excited region (determined by the size of an absorber or the penetration depth of light within an absorber), α_{th} is the thermal diffusivity, and v_s is the speed of sound [102].

$$\tau_0 \ll \tau_{th} = \frac{d_c^2}{\alpha_{th}} \quad \text{Eq. 1.1}$$

$$\tau_0 \ll \tau_s = \frac{d_c}{v_s} \quad \text{Eq. 1.2}$$

In effect, under thermal confinement, the laser pulse duration should be significantly shorter than the thermal diffusion time, thus meaning that thermal dissipation from the absorbing region is negligible during the excitation pulse and PA transient generation process. Similarly, under stress confinement, propagation of the acoustic wave which is generated as a result of the thermoelastic expansion and mechanical relaxation can be considered to be negligible over the duration of the optical pulse. While α_{th} and v_s are tissue-dependent and temperature-dependent parameters, typical values for soft tissues are on the order of approximately 1.3×10^{-3} cm^2/s and 1.5 mm/μs, respectively [103]. As an example, to resolve an absorber with a characteristic dimension of 100 μm, τ_{th} and τ_s would be approximately 77 ms and 67 ns, respectively, meaning that efficient PA signal generation is achieved if the pulse duration is less than 67 ns. Overall, the confinement conditions are satisfied for micrometer-sized absorbers through the use of nanosecond pulsed laser sources (< 10 ns/pulse) for PA imaging of endogenous biological tissues. Examples and descriptions of such sources are provided below in section 1.3.

Under thermal confinement, τ_{th}, the PA pressure, p, generated within a non-viscous and acoustically homogenous medium is described by Equation 1.3 [104,105]. The heating function, $H(r,t)$, represents a spatial position, r, and time, t, dependent conversion of the applied electromagnetic radiation to thermal energy, β represents the

isobaric volume expansion coefficient, and C_p represents the isobaric specific heat capacity.

$$\nabla^2 p - \frac{1}{v_s^2}\frac{\partial^2}{\partial t^2} p = -\frac{\beta}{C_p}\frac{\partial}{\partial t} H(r,t) \quad \text{Eq. 1.3}$$

Considering a pulsed optical illumination heating source, the heating function, *H(r,t)*, can be expressed in terms of the local optical absorption coefficient of the medium, μ_a, and the local laser fluence, Φ (Equation 1.4).

$$H(r,t) = \mu_a(r)\Phi(r,t) \quad \text{Eq. 1.4}$$

Further assuming that the stress confinement condition is satisfied, τ_s, the temporal component of the heating function can be approximated as a delta function, δ, effectively isolating the spatial dependency of the heating profile (Equation 1.5).

$$H(r,t) = H(r)\delta(t) \quad \text{Eq. 1.5}$$

Therefore, given a sufficiently short laser pulses and a large enough spot size to achieve both thermal and stress confinement conditions, the peak PA pressure, p_o, generated is defined by Equation 1.6, from which it can be seen that the generated pressure is defined by only the local optical fluence, Φ, the optical absorption coefficient, μ_a, and the Grüneisen parameter, Γ, which is itself dependent on the thermal coefficient of volume expansion, β, the speed of sound, and the isobaric specific heat capacity.

$$p_0 = \frac{\beta v_s^2}{C_p} H(r) = \frac{\beta v_s^2}{C_p}\mu_a(r)\Phi(r) = \Gamma\mu_a(r)\Phi(r) \quad \text{Eq. 1.6}$$

In the case of imaging biological tissues with nanosecond pulsed lasers, Equation 3 is widely utilized as the fundamental, albeit simplified, PA equation, whereby the generated PA signal magnitude is dependent on only three local parameters: light delivery, optical absorption, and efficiency of converting the absorbed energy into a pressure wave. Figure 1.3A schematically illustrates the generation of PA signal from within an artery using a catheter design to illuminate the tissue and receive an induced

acoustic response. The light delivery can be controlled, in part, by adjusting the delivered light energy. Typically, PA differentiation of specific absorbers of interest is achieved through the careful selection of imaging wavelength(s) which correspond to optical absorption peaks of the desired imaging target while reducing background signal and light attenuation. Such optical wavelength selection is highly tissue and target specific, as discussed below.

While PA imaging of endogenous tissues has several key applications within cardiovascular medicine, preclinical research also relies heavily on the utilization of exogenous absorbers for improved molecular imaging capabilities and enhanced contrast. PA contrast agents under investigation include dyes, carbon nanotubes and metallic nanoparticles. In the case of utilizing these nanometer-sized agents for PA imaging, however, it is important to note that the above equations describing generated PA pressure must be reconsidered because the thermal and stress confinement conditions are often not maintained using optical sources most commonly used for PA imaging. This ultimately means that, despite the high absorption, both the thermal confinement and stress confinement conditions may not be valid when using a nanosecond pulsed laser for nanoparticle-enhanced PA imaging applications. Under these conditions, it has been shown that the applied laser pulse-induced stress is quickly converted to heat, and that the heat rapidly diffuses throughout the nanoparticle and to the interface with the surrounding environment where the acoustic pressure wave is induced, shown schematically in Figure 1.3B [106]. This indicates that both the optical properties of the contrast agent and the efficiency of the heat transfer into the surrounding environment will significantly affect the generated acoustic pressure. To account for the lack of stress and thermal confinement in the case of imaging nanoparticle contrast agents, the simplified PA pressure equation can be modified as indicated in Equation 1.7, where η is the heat

transfer efficiency from the particle to its surroundings, Γ_{eff} is an effective Grüneisen parameter of the nanoparticle-environment mixture, and σ is the absorption cross-section of the nanoparticle [107].

$$p_0 \propto \eta \Gamma_{eff} \sigma \Phi \quad \text{Eq. 1.7}$$

Additionally, whereas variations in optical absorption spectra of either endogenous absorbers or exogenous contrast agents provide the most common means of PA imaging tissue characterization, it is important to note that the Grüneisen parameter offers a separate means for PA imaging and sensing. The terms comprising the Grüneisen parameter are tissue and temperature specific. Therefore, PA imaging performed at a single optical wavelength, and at a constant optical fluence, can also be utilized as a means to remotely monitor temperature change, thus providing a potential means of therapy guidance. As an example, in water based tissue, the Grüneisen parameter, and therefore the PA conversion efficiency, scales linearly with temperature, a characteristic which has been utilized for monitoring temperature rise during cancer photothermal therapy in preclinical studies [108,109]. The relationship between the Grüneisen parameter and temperature is also tissue-dependent. In an extreme case, it has been shown that the parameters comprising the Grüneisen parameter- the speed of sound, the thermal coefficient of volume expansion and the isobaric specific heat capacity- all exhibit opposite temperature-dependent trends for lipid than they do for water-based tissues [110]. As a result, lipid deposits may be differentiated from water-based tissue by monitoring the direction of PA signal intensity change with changing temperature [111].

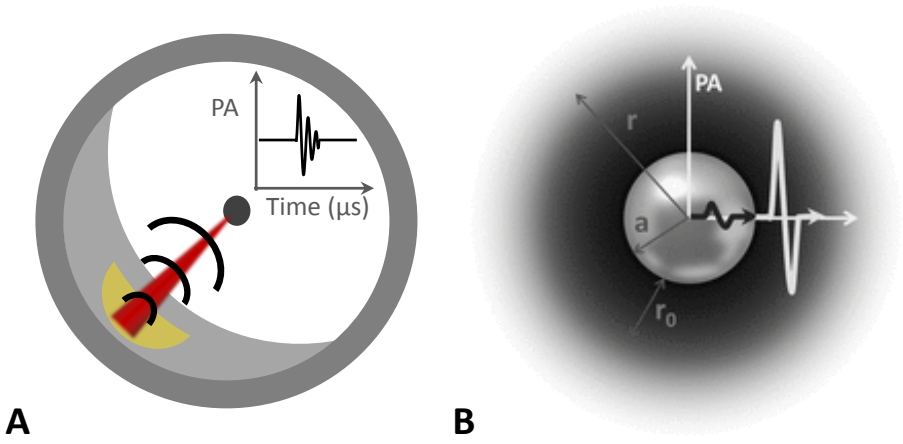

Figure 1.3: Photoacoustic signal generation from (A) endogenous lipid (yellow) within an atherosclerotic plaque using an intravascular imaging catheter, and (B) an exogenous plasmonic nanoparticle. Reprinted with presmission from [106].

1.3.2. Fundamental Photoacoustic Imaging Techniques

PA imaging is increasingly investigated as a modality capable of augmenting both preclinical and clinical imaging modalities. A multitude of different imaging techniques are possible using PA imaging, whereby adjustments in the instrumentation set-up, imaging procedure, and targeted signal sources can all be tailored to specific imaging needs. In particular, PA imaging can be categorized according to the physical parameter which is modified in order to induce photoacoustic signal changes- adjustment of optical wavelength(s) or induced local temperature changes during PA imaging.

1.3.2.1. Spectroscopic Photoacoustic Imaging

The amplitude of a generated photoacoustic signal is proportional to the optical absorption, the local laser fluence, and the efficiency of thermo-acoustic transfer within the local environment (the Grüneisen parameter), evident by Equations 1.6 and 1.7. Therefore, provided that the Grüneisen parameter does not vary during PA imaging, one major advantage of PA imaging is that it enables the detection of specific chromophores

of interest based on analysis of PA signal intensity when the optical excitation wavelength is varied and the local laser fluence is held constant. Using this approach, wavelength-dependent optical absorption spectral characteristics are exploited as an independent variable to enable PA detection of specific absorbers of interest, including both endogenous tissues and exogenous contrast agents.

This technique, termed spectroscopic photoacoustic (sPA) imaging or multispectral optoacoustic tomography, is widely utilized for both identifying the location of one or more absorber(s) as well as estimating their relative concentrations. Using sPA, differentiation of absorbers of interest, such as lipid or nanoparticle contrast agents can be achieved using a variety of spectral unmixing algorithms, ranging from a simple analysis of the spectral slope [112-114] or a ratiometric analysis [115] of the obtained PA signal to more computationally intensive methods which enable calculation of the relative contribution of multiple absorbers such as interclass correlation [116] or linear least squares algorithms [117]. Regardless of the approach, however, sPA provides a means of capitalizing on the compositional specificity which makes PA imaging an attractive modality to combine with the more limited molecular contrast, but improved anatomical contrast, of US imaging. In the case of imaging atherosclerosis, lipid is particularly well-suited for sPA differentiation from other plaque components based on unique optical peaks within the wavelength regions of approximately 1210 nm and 1720 nm, as are cellular- or molecular-targeted contrast agents. Each of these applications is discussed in greater detail below.

1.3.2.2. Photoacoustic Temperature Monitoring

In addition to sPA, the Grüneisen parameter provides for an alternative means of contrast during PA imaging. All components of the Grüneisen parameter, the thermal

coefficient of volume expansion, the speed of sound, and the isobaric specific heat capacity, are temperature sensitive and tissue-specific. Therefore, whereas sPA imaging techniques assume that the Grüneisen parameter remains constant during imaging, the deliberate modification of temperature within the imaged tissue provides an additional PA imaging technique, termed thermal photoacoustic (tPA) imaging. Using the tPA technique, the PA signal acquisition performed with the optical fluence and wavelength held constant and the obtained signal intensity is monitored over time as the temperature of the target tissue is modified. As a result, the magnitude of the tPA signal at each location within the tissue is linearly proportional to the local temperature within the tissue, thus allowing for temperature distribution mapping throughout the imaging field. Therefore, tPA has been investigated for applications in the non-invasive monitoring of the delivered thermal dosage during targeted hyperthermia or cryogenic treatments, with reported temperature resolutions as high as 0.15 °C have been reported in *ex vivo* studies [118]. Relative to other temperature monitoring techniques, tPA offers an advantage in that the signal is depth-resolved, meaning that the temperature at each location within the arterial wall can be monitored rather than merely the intimal surface. It is also noteworthy that ultrasound is capable of temperature monitoring as well, using temperature-dependent changes in the speed of sound to map changes in the time-of-flight to temperature changes. However, this technique relies on the detection of a shift in ultrasound signal temporal shift, which can be challenging to monitor *in vivo* due to motion artifacts. In contrast, tPA imaging utilizes a linear dependence of the PA signal intensity with temperature, meaning that the magnitude of the PA signal is monitored rather than its arrival time. This technique offers unique implications for potential image guidance during hypo- or hyper-thermic interventions during coronary interventions, both of which have been previously investigated [119,120].

1.4. COMBINED INTRAVASCULAR ULTRASOUND AND PHOTOACOUSTIC IMAGING

Recently, combined intravascular ultrasound and photoacoustic (IVUS/IVPA) imaging was introduced as a potentially clinically-translatable hybrid technique to help improve diagnostic accuracy of vulnerable atherosclerotic lesions by providing a means of supplementing the morphological information provided by IVUS with additional ability to assess atherosclerotic lesion cellular and biochemical composition based on unique optical absorption properties of specific plaque components or delivered contrast agents [98]. Custom fabricated integrated IVUS/IVPA catheters and imaging systems enable the acquisition of spatially co-registered and temporally consecutive IVUS and IVPA images, therefore allowing for complimentary IVUS/IVPA imaging of arterial cross-sections with shared signal detection hardware.

Table 1.1: Comparison of IVUS/IVPA with Clinical Intravascular Imaging Systems. Modified with permission from [121].

Image	Grayscale IVUS	VH-IVUS/iMap	NIRS	IVOCT	IVUS/IVPA*
Image Type/ Content	Cross-section structure	Cross-section tissue type	Lipid-core plaque map (chemogram)	Cross-section structure	Cross-section tissue type
Type of radiation	Ultrasound	Ultrasound	Near-IR light	Near-IR light	(Near-IR) light + ultrasound
Axial resolution (μm)	100-200	>250	N/A	10-15	100
Lateral resolution (μm)	300-500	300-500	1000	30-40	400-500
Penetration (mm)	10	5	unknown	1	5
Contrast mechanism	Acoustic Backscattering	Acoustic Backscatter Frequency Content	Optical absorption	Optical scattering	Optical absorption
Pullback rate	0.5 mm/s	0.5 mm/s	0.5 mm/s	20-40 mm/s	TBD 0.5 mm/s ?
Flushing	No	No	No	Yes	No
Current status	CS/CA	CS/CA	CS/CA	CS/CA	PCS
Lumen area	++	++	-	++	++
Plaque burden	++	++	-	-	++
Positive remodeling	++	++	-	-	++
Necrotic core	±	++	++	-	++
Fibrous-cap thickness	-	-	-	+	TBD
TCFA	-	±	-	+	TBD
Plaque rupture	+	+	-	++	-
Erosion	-	-	-	+	-
Thrombus	±	±	-	+	±
Inflammation	-	-	-	±	±
Calcium	++	++	-	+	++

IVUS = intravascular ultrasound; VH = virtual histology; NIRS = near-infrared spectroscopy; IVOCT = intravascular optical coherence tomography; IVUS/IVPA = combined intravascular ultrasound and photoacoustics;
CA = clinically, commercially available; CS = clinical studies; PCS = pre-clinical studies; N/A = not applicable; TBD = to be determined; TCFA = thin-cap fibroatheroma.

++excellent. +good. ±possible. −impossible.

1.4.1. Integrated Intravascular Ultrasound and Photoacoustic Imaging Catheter and System

In addition to the complimentary nature of the received information from the two modalities, there is an added benefit of shared hardware between IVUS and IVPA. Because the received signals for both modalities are acoustic pressures, a hybrid

IVUS/IVPA system can use a single ultrasound transducer, analog-to-digital converter (ADC), and many of the same signal processing algorithms. A schematic block diagram of an IVUS/IVPA imaging set-up designed for interrogation of vessel mimicking phantoms and freshly excised artery sections, is provided in Figure 1.4 [122]. Briefly, the distal end of an integrated IVUS/IVPA imaging catheter is inserted into the lumen of the imaging target. Output from a nanosecond pulsed laser is focused into a multimode optical fiber at the proximal end of an integrated IVUS/IVPA imaging catheter which also housed a single element IVUS transducer. The laser source is a Q-switched neodymium-doped yttrium aluminum garnet (Nd:YAG) which provides a pulse duration of approximately 5 -7 ns at a fundamental wavelength of 1064 nm. The output can be easily frequency doubled, tripled and quadrupled to obtain 532, 355 and 266 nm, respectively, and used to pump optical parametrical oscillators (OPOs) which are capable of generating output wavelengths across a wide spectral range (e.g. 680 nm to >2000 nm), thus providing versatility for IVPA imaging applications in which wavelength tunability remains critical for differentiation of target chromophores. During imaging, each pulse of the laser provides a trigger for collecting radio frequency (RF) signals from a pulser/receiver connected to the IVUS transducer within the integrated catheter. The received RF signals are digitized, resulting in a single IVPA A-line signal, a depth-resolved IVPA signal at from a single azimuthal angular position within an arterial cross-section. Following a user-defined delay, approximately 9 μs, the pulser/receiver is then triggered in order to acquire a conventional pulse-echo IVUS A-line. Therefore, the resulting acquired RF data is composed of spatially co-registered and temporally consecutive IVPA and IVUS signals. For generation of two-dimensional images of a vessel cross section, the integrated IVUS/IVPA catheter is rotated using a stepper motor.

Additionally, for three-dimensional imaging, a second motor was utilized to translate the image target.

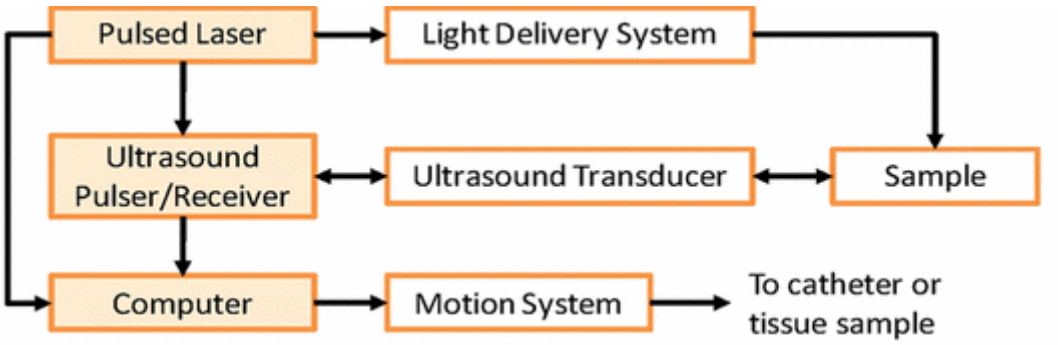

Figure 1.4: High level block diagram of experimental IVUS/IVPA imaging system Reprinted with permission from [122].

There are several unique challenges associated with the design of an integrated IVUS/IVPA imaging catheter, particularly the need to maintain a small profile for the catheter while ensuring that the optical and ultrasound beams overlap and are projected sideways onto the arterial wall from within the lumen. This has been achieved using a thin optical fiber as a waveguide to transfer optical energy, coupled from the external laser source at the proximal end of the integrated IVUS/IVPA catheter, to the distal end of the catheter where it is reflected towards the artery wall. Also located at the distal wall is an IVUS transducer. Commercial IVUS catheter designs utilize either a cylindrical array based transducer operating at a center frequency of approximately 20 MHz or a single element transducer which is mechanically rotated and typically have a center frequencies ranging from 30-60 MHz. To date, all integrated IVUS/IVPA catheters have utilized single element transducers, using either commercial IVUS transducers or custom fabricated elements.

Integrated IVUS/IVPA catheter prototypes utilize multimode optical fibers with core diameters ranging from 200 to 600 micrometers [123-125]. The redirection and alignment of light with the ultrasound beam has been realized using both micro-optics such as mirrors [124,126,127] or prisms [128] and side-fire fibers utilizing total internal reflection [123,125]. The mirror-based optical reflection approach is suitable to redirect light with lower energy lose and offers greater variability in the reflected angle compared to the side fire fiber approach. However, the small core diameter of the optical fibers results in high light intensity which can damage the mirror. This problem can be partially overcome by increasing the distance between the fiber and the mirror and using the same mirror to redirect both the ultrasound and light beams [124], but the rigid part of the catheter becomes elongated using this approach, potentially sacrificing the achievable catheter flexibility. To-date, most experimental achievements using integrated IVUS/IVPA catheters have been demonstrated using side-fire fiber-based light delivery systems and single-element transducers, a schematic and photograph of which is provided in Figure 1.5 [129]. The smallest integrated imaging catheter has the outer diameter of 1.25 mm with approximately 3.5-mm-long rigid part [125]. However, further miniaturization of integrated IVUS/IVPA catheters is likely to be achieved with future design modifications, to less than 1 mm outer diameter, resulting in more clinically acceptable catheter size and flexibility.

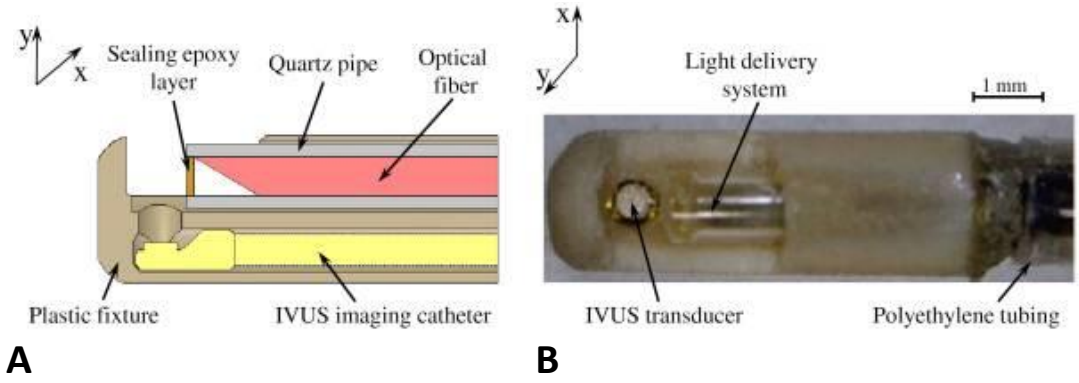

Figure 1.5: Integrated intravascular ultrasound and photoacoustic (IVUS/IVPA) imaging catheter. (A) Schematic design and (B) prototype photograph. Reprinted with permission from [129].

A 10 μm carbon fiber was used to simulate an impulse response received using such an IVUS/IVPA imaging system in order to characterize its resolution. The axial resolution was calculated based on the full width half maximum (FWHM) of the frequency response, whereas the lateral resolution was calculated based on the -6 dB lateral beam profile from the carbon fiber. The axial resolution for IVUS and IVPA imaging were measured to be 54 μm and 38 μm, respectively, whereas the lateral resolutions were measured to be 3.2° and 5.5°. In a separate experiment, demonstrating the complimentary nature of combined IVUS/IVPA imaging, a vessel mimicking phantom composed of a polyvinyl alcohol (PVA) cylindrical mold with a highly optically absorbing graphite inclusion was imaged [98]. Figure 1.6 shows obtained IVUS, IVPA and combined IVUS/IVPA images of the phantom, clearly demonstrating how IVPA imaging provides compositional information based on optical absorption properties within the context of the overall morphology demarcated by the corresponding IVUS image. These examples highlight the feasibility and characteristics of combined IVUS/IVPA imaging.

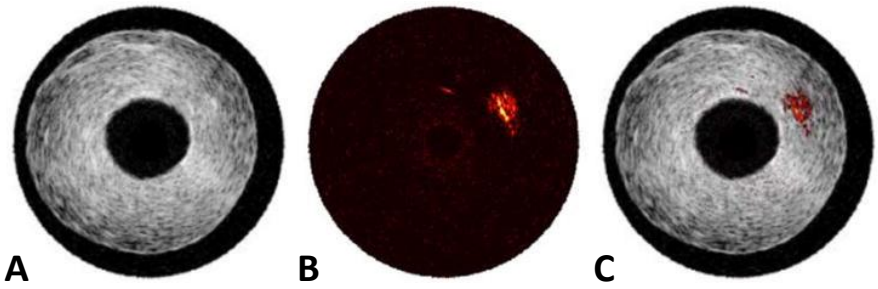

Figure 1.6: Vessel mimicking phantom images demonstrating complimentary nature of IVUS/IVPA imaging. (A) IVUS, (B) IVPA, (C) IVUS/IVPA. Reprinted with permission from [122].

1.4.2. Applications of Intravascular Photoacoustic Imaging

IVUS/IVPA imaging has been most heavily investigated for two distinct applications, the localization of lipid-rich atherosclerotic plaques and the detection of exogenous contrast agents. Both lipid and contrast agent localization using IVUS/IVPA offer the potential for improved atherosclerotic lesion characterization and therapy guidance over clinically available intravascular imaging modalities.

1.4.2.1. Intravascular Lipid Imaging

Due in large part to its correlation with atherosclerotic lesion instability, lipid has been a major focus of IVPA imaging. Endogenous lipid contains unique optical absorption peaks, relative to other endogenous absorbers within the arterial environment, at approximately 1210 nm and 1720 nm. Thus, spectroscopic IVPA (sIVPA) imaging has been utilized to identify the distribution of lipid within atherosclerotic plaques of excised arteries using combined IVUS/IVPA systems (Figure 1.7A,B) [114,130,131]. A direct comparison between results obtained from performing sIVPA imaging over the two spectral bands found similar results, with a lower pulse energy required for detection of

lipid at the 1720 nm spectral band but with a reduced achievable imaging depth [114]. IVUS/sIVPA has also been expanded to go beyond localizing lipid within plaques to the differentiation of specific cholesterol compositions as a way of further characterizing lesions and potentially differentiating lipid within plaques from adventitial fat [114]. For the absorption peak located at 1720 nm, the IVPA signal obtained using only a single wavelength was shown to correlate well with regions identified as lipid by both the sIVPA approach and subsequent histological staining [130]. In fact, this single wavelength lipid-detection technique was the approach utilized for the first *in vivo* IVUS/IVPA demonstration, which was performed on a rabbit model of atherosclerosis (Fig. 1.7C) [131].

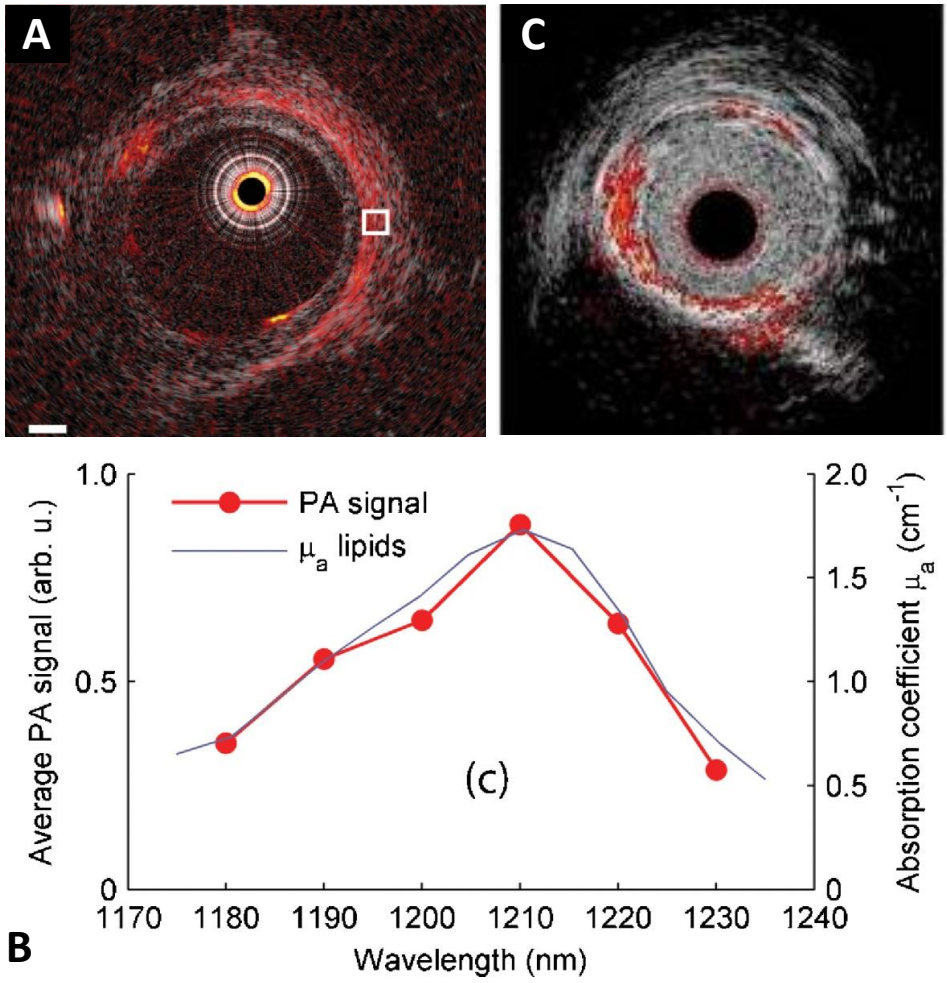

Figure 1.7: IVUS/IVPA imaging of lipid-rich atherosclerosis. (A) *Ex vivo* IVUS/IVPA image of human coronary atherosclerosis, with (B) corresponding spectroscopic validation of lipid signals. Reprinted with permission from [132]. (C) In vivo IVUS/IVPA detection of lipid in a rabbit model of atherosclerosis at 1720nm. Reprinted with permission from [133].

Continued development of IVUS/IVPA imaging as a system for localizing lipid within atherosclerotic plaques is a likely first application for the hybrid intravascular imaging technique. While the correlation between lipid-rich plaques and adverse coronary events is well established, continued investigation as to how the knowledge of lipid content and location within a plaque can improve patient diagnosis and

interventional outcomes are critical to the ultimate motivation for clinical adoption of the technique. An improved understanding of the relationships between clinical outcome and lipid-rich plaques, such as the aforementioned COLOR registry, CANARY trial, and the Lipid-Rich Plaque study, as well as future trials specific to IVUS/IVPA imaging the results are, therefore, critical in driving clinical adoption of IVUS/IVPA imaging.

1.4.2.2. Exogenous Contrast Agents for Intravascular Photoacoustic Imaging

While limited number of relevant tissues, particularly lipids, are well-suited for localization within arterial plaques using IVPA imaging, many critical cellular and molecular biomarkers of atherosclerotic plaque vulnerability cannot be differentiated using IVUS/IVPA imaging based on endogenous contrast alone. Therefore, the introduction of exogenous contrast agents with strong and unique optical absorption spectral characteristics provides a means of significantly increasing the potential imaging targets. It is important that the contrast agents provide IVPA signal within an optical region where background signal from endogenous chromophores, such as hemoglobin, is minimized. The near-infrared (NIR) tissue optical window, spanning from approximately 700 – 1100 nm, provides an optimal spectral region in which endogenous tissue optical absorption and scattering is sufficiently reduced to contrast-enhanced IVPA imaging.

A wide array of contrast agents have been developed and evaluated using photoacoustic imaging, many of which exhibit characteristics which make them of particular interest for IVPA imaging applications (Table 1.2) [134]. In general, PA contrast agents which have been widely investigated to date fall into three main categories- dyes, single-walled carbon nanotubes (SWNTs), and noble metal nanoparticles. Examples of dyes which have been utilized for PA imaging include indocyanine green (ICG) [135] and methylene blue [136], each of which are already

clinical approved for limited applications, as well as IRDye800CW [137], AlexaFluor750 [138], and the enzymatically-activated MMPSense680 [115]. Beyond molecular dyes, SWNTs and noble metal nanoparticles have also been utilized as PA contrast agents. SWNTs exhibit a high optical absorption over a broad wavelength range, supporting their ability to efficiently generate PA signals [139]. Additionally, both dyes and SWNTs can be modified to enabled conjugation of molecular targeting moieties [137-140]. However, both dyes and SWNTs have limitations as PA contrast agents. Dyes are prone to instability in biological and PA imaging conditions, which can cause photobleaching, quenching, or shifts in their optical absorption spectra. SWNT exhibit a broad absorbance spectrum without distinct peaks to detect using spectroscopic PA imaging techniques.

Table 1.2: Exogenous photoacoustic contrast agents of particular relevance to intravascular imaging applications. Modified, with permission, from [134].

Contrast agent	Description	Size (nm)	Peak absorption wavelength (nm)	Notable Prior Applications
MMPSense 680	Activatable fluorescent dye	< 2	620, 680	Imaging MMP activity within atherosclerotic plaque
Gold nanospheres	Solid gold spheres	2-60	520-540	Molecular PA imaging for identifying macrophages
Gold nanorods	Solid rice-shaped gold particles	10 by 40-60	650-1100	Cancer imaging, photothermal therapy
Gold nanoshells	Silica core and gold shell spheres	50-500	700-1100	Brain vascular imaging, photothermal therapy
Silver nanoplates	Thin triangular silver discs	6-20 by 100-200	600-1200	PA imaging at 1064 nm
Single-walled carbon nanotubes	1-atom thick cylinders of graphene	1 by 50-300	690	Cancer imaging with $\alpha_v\beta_3$ targeting
Nanobeacons	Liposomes containing plasmonic nanoparticles	100-200	520-1100	Cancer imaging with $\alpha_v\beta_3$ targeting
Photoacoustic nanoDroplets	Liquid perfluorocarbon droplets loaded with plasmonic nanoparticles	200	520-1200	Optically triggered, combined contrast in US and PA
Radiolabeled gold nanorods	Gold nanorods labeled with the radioisotope iodine-125	10 by 40-60	650-1100	Sensitive whole-body detection using SPECT
Gold nanoclusters	4-nm nanospheres connected with a biodegradable polymer	50-100	700-900	PA imaging with subsequent high clearance

Noble metal nanoparticles represent a widely investigated category of PA contrast agents. Metallic nanoparticles are of particular interest to researchers because they exhibit localized surface plasmon resonance (LSPR) coupling, a process in which free electrons at the nanoparticle surface oscillate with the applied electromagnetic field, which enables very high, tunable optical absorption properties based on modifications to the nanoparticles size and shape [141,142]. As a result of the LSPR effect, an individual nanoparticle exhibits optical absorption up to five orders of magnitude greater than that of a dye molecule, resulting in efficient PA signal generation [143]. Similar to the other

classes of PA contrast agents, the surface of plasmonic nanoparticles can be readily conjugated with targeting moieties for molecular imaging applications [144] or otherwise modified to improve their stability in biological environments [145] and PA signal generation efficiency [146]. Additionally, the size and shape of these plasmonic nanoparticles can be tailored, resulting in changes to their optical absorption spectrum and the ability to use sPA imaging for their detection over background endogenous tissues. In fact, a significant number of gold nanoparticle PA contrast agents have been developed, including spherical gold nanoparticles [116,147], gold nanoshells [148,149], gold nanorods [146,150-152], gold nanoplates [153], gold nanocages [154] and aggregated gold nanoclusters [155], each with their own unique physical and optical absorption properties. As a result, plasmonic nanoparticle delivery followed by sPA imaging can be employed to greatly expand cellular and molecular imaging capabilities from that which can be achieved based solely on endogenous absorbers. Gold nanorods (AuNR) are particularly applicable as PA imaging contrast agents because the location of their longitudinal peak absorbance can be readily adjusted within the NIR optical window by tuning the particles' aspect ratios [156,157]. Using a seed mediated growth method, tuning the concentration of silver ions during gold nanorod growth can be utilized adjust the nanoparticles' aspect ratio, thereby selectively tuning the location of the longitudinal optical absorption peak over a range from 600 nm to over 1000 nm, as demonstrated in Figure 1.8 [157].

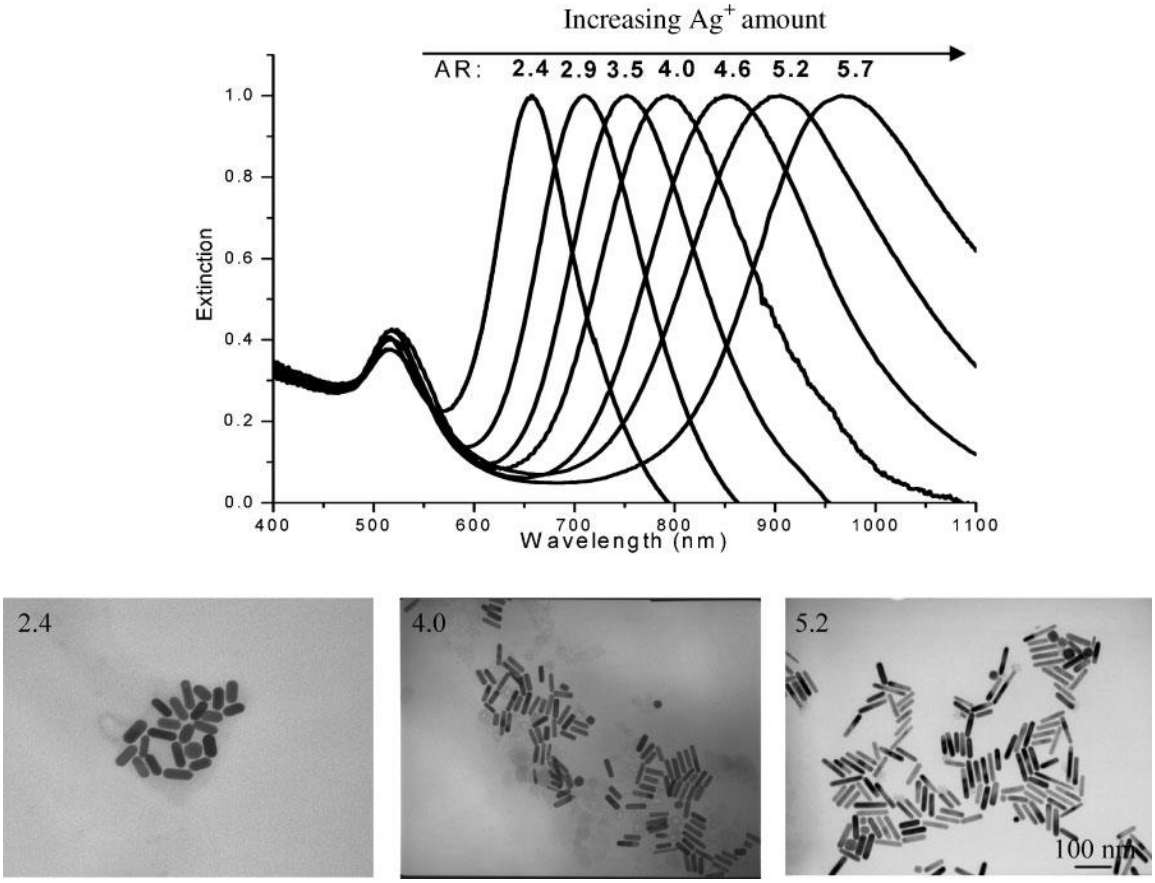

Figure 1.8: Demonstration of the tunability of the optical extinction properties of gold nanorods by adjusting the relative number of amount of silver ions present during their synthesis as a way of changing the resulting aspect ratio. Reprinted with permission from [157].

In the case of IVPA imaging, macrophages provide a clear target for contrast-enhanced, cellular-specific imaging. An indicator of the local inflammatory status of an atherosclerotic plaque, macrophage are scavenger cells which phagocytose foreign bodies. To this end, both *in vitro* phantom studies and *ex vivo* IVUS/sIVPA imaging performed on animal models of atherosclerosis following systemic injection of non-targeted, polymer-stabilized spherical gold nanoparticles was shown to enable localization of aggregated particles based on a broadening and red shift which occurs

upon aggregation of spherical gold nanoparticles. Figure 1.9 demonstrates, in an *in vitro* vessel mimicking phantom model, the ability to use sIVPA imaging to differentiate gold nanospheres aggregated within macrophage endosomes from background signal as well as from colloidal particles. Histological staining of atherosclerotic animal models following systemic injection of gold nanospheres confirmed the co-localization of sIVPA signal with regions of high macrophage density (RAM 11 stain) and the presence of the gold nanoparticles (silver stain), supporting the hypothesis that the particles are phagocytosed and concentrated within intraplaque macrophages [147]. One limitation of this approach, however, is that spherical gold nanoparticles yield a peak absorbance of approximately 520 nm, which overlaps with a strong absorption peak of oxygenated hemoglobin, the most abundant endogenous chromophore during IVPA imaging. While broadening and red shifting of the peak occurs upon aggregation of the particles, due to plasmon resonance coupling, IVUS/IVPA imaging of the gold nanoparticle-labeled macrophages was still not achieved in the presence of luminal blood. In order for contrast-enhanced IVUS/IVPA imaging using gold nanospheres to be demonstrated *in vivo*, the inability to image through luminal blood would necessitate saline flushing of the imaged artery, a technique which reduces image acquisition time and has been associated with increased risk of intra-procedural ischemia or pulmonary edema [158].

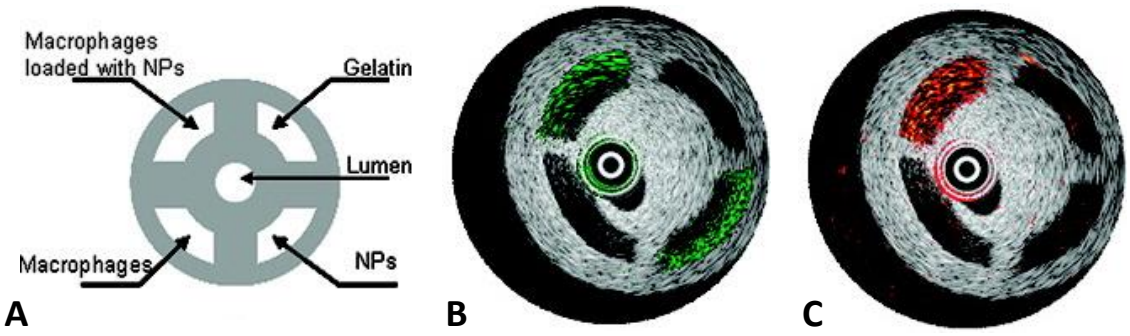

Figure 1.9: Vessel mimicking phantom demonstrating sIVPA detection of gold nanoparticles. (A) Phantom design schematic, (B) IVUS/IVPA image obtained at 532 nm, revealing the presence of gold nanospheres, (C) IVUS/IVPA image obtained at 680 nm revealing only the gold nanospheres aggregated within macrophage endosomes. Reprinted with permission from [147].

The introduction of metallic nanoparticle contrast agents, in combination with the optical delivery system of an integrated IVUS/IVPA catheter, for localizing cellular or molecular targets of interest within atherosclerotic plaques also opens the door for novel therapeutic strategies. As a result, one can conceive a theranostic strategy in which plasmonic nanoparticles are first localized within the context of atherosclerotic lesions using IVUS/IVPA imaging and then utilized to deliver a therapeutic effect which might include the release of a therapeutic compound or delivering thermal therapy through the direct heating of the nanoparticles and their surrounding tissue. Such a strategy is analogous, in many respects, to phototherapy-based techniques which have been previously investigated for the treatment of atherosclerotic plaques, each of which are described below.

1.5. Intravascular Phototherapy Techniques for Local Treatment of Atheroma

In addition to the ongoing need for improved diagnosis of atherosclerotic lesion composition and vulnerability to induce an acute coronary event, an appropriate therapeutic strategy for such plaques, once identified, has not yet been clinically adopted [159]. The current strategies during percutaneous coronary intervention, including angioplasty, stenting and bypass grafting, are all primarily designed to restore distal blood flow rather than to mitigate future risk by stabilizing the underlying lesion composition [160]. To this end, beyond improved characterization of coronary atheroma and image-guidance during a clinical intervention, the IVUS/IVPA system may also offer the potential to be further utilized as a vehicle for delivering, and monitoring, optically-triggered intravascular therapy. Several such optical-based therapeutic strategies have been investigated, including laser atherectomy, photothermal therapy, photodynamic therapy, and multimodal approaches. Through both the optical delivery enabled by the integrated catheter and its ability to monitor optically-induced tissue responses, including local temperature measurements, the IVUS/IVPA imaging system is uniquely suited to be combined with these techniques to create a theranostic platform [161].

1.5.1. Laser Atherectomy

Laser atherectomy, alternatively referred to as excimer laser angioplasty, is a clinically approved technique which uses an intravascular catheter to deliver pulsed optical energy within the ultraviolet (UV) wavelength range (308 nm) in order to eliminate stenosis or total occlusions through photoablative effects (Spectranetics Corporation, Colorado Springs, Colorado). The current clinical catheter designs deliver optical pulses with a duration of approximately 125 ns and repetition rate of 40 Hz, inducing photothermal and vaporization effects within the optically-excited tissue

[162,163]. Because the technique uses UV illumination where all tissue components are both highly scattering and highly absorbing, it is unable to selectively treat specific lesions components, acting instead as more of a layer-by-layer etching approach to restore the vascular lumen. While laser atherectomy has been approved for several niche indications, including moderately calcified lesions, total occlusions which are traversable by a guidewire, and occluded vein grafts, it has not achieved widespread clinical adoption. This is largely attributable to clinical trials which have shown increased rates of perforations to the artery relative to balloon angioplasty [164] and inferior procedural success rates relative to the mechanical alternative, rotational atherectomy [165].

1.5.2. Plasmonic Photothermal Therapy

Photothermal therapy (PTT) is a therapeutic technique which relies on the conversion of optical energy into heat in order to induce cell death via hyperthermia or other thermal effects. PTT has been broadly investigated within the field of cancer treatment for several decades, including its use in coordination with strong optically absorbing contrast agents such as organic dyes [166]. The same properties that make plasmonic nanoparticles attractive as IVPA contrast agents, namely the enhanced optical absorption efficiency which results from the LSPR effect, have also led to the investigation of gold nanoparticles as the thermal transducers during PTT. This use of noble metal nanoparticles as the absorbers triggering thermal conversion within tissue has evolved into a subset of PTT, termed plasmonic photothermal therapy (PPTT).

While most applications of PPTT have centered on cancer therapy [167], the techniques has also recently come under investigation for the treatment of atherosclerotic plaques [168,169]. In these investigations, the combined delivery of near-infrared absorbing gold nanoparticles for PPTT via either injection or local placement using an on

artery patch design was shown to reduce atheroma burden in both a swine model and first-in-man trials (NANOM FIM). Given the previously discussed ability to utilize gold nanoparticles as IVPA contrast agents, as PPTT continues to be evaluated as a novel therapeutic strategy for stabilizing atheroma, IVUS/IVPA may provide a means for improving the therapy guidance on several levels, including the localization of the delivered gold nanoparticles and the monitoring of their induced temperature rise during PPTT.

1.5.3. Photoangioplasty

Photodynamic therapy (PDT) relies on the excitation of a delivered photosensitizer agent using low energy (relative to PTT) optical excitation, inducing a cascade which leads to the production of cytotoxic singlet oxygen, $^1O_2$. Heavily investigated and clinically used within the field of cancer treatment, intravascular photodynamic therapy, termed photoangioplasty, has also shown promise as a technique for treating atherosclerotic plaques. Two different photosensitizers have been most widely studied for photoangioplasty, MV0611 (Miravant Medical Technologies, Santa Barbara, California) and Lutetium Texaphyrin (Pharmacyclics Inc., Sunnyvale, California). Each of these photosensitizers, both of which are water soluble, have been shown to preferentially localize within atherosclerotic plaques in animal models of atherosclerosis over the course of 24 hours following systemic injection [170,171]. The same studies have also demonstrated a reduction in plaque area with corresponding increases in lumen area as well as a reduction in the number of macrophages present within the lesions based on histological staining of the lesions approximately one month following the treatment (Fig. 1.10). By comparison however, Lutetium Texaphyrin (LuTex) offers the advantage of being excited by illumination at 732 nm, versus the

excitation wavelength of 542 nm for MV0611 which overlaps with a strong absorption peak of oxygenated hemoglobin. Phase I clinical trials using LuTex-excited photoangioplasty identified safe photosensitizer and light dosages, reporting no coronary complications and low incidence of side effects associated with the procedure [172,173]. However, despite these encouraging initial human trial results, which are now over a decade old, photoangioplasty has not continued to progress towards clinical adoption. This is likely due, in large part, to the widespread adoption of drug-eluting stents for the prevention of restenosis, an initial clinical target for photoangioplasty.

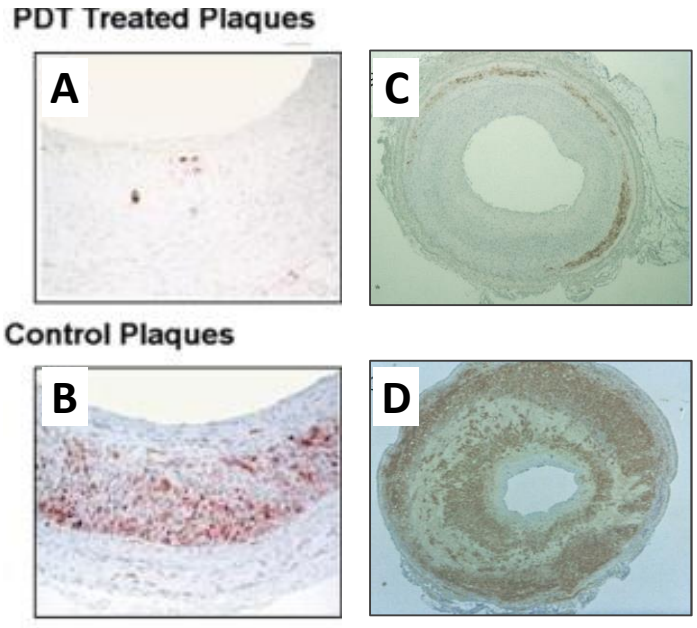

Figure 1.10: Reduced macrophage cell density following photoangioplasty. (A-B) Macrophage stain histology one month following photoangioplasty using MV0611 from a region which received PDT illumination (A) and one which did not (B). Reprinted with permission from [171]. (C-D) Macrophage stained histology cross sections following PDT using LuTex, from a region which received PDT illumination (C) and one which did not receive illumination (D). Reprinted with permission from [170].

While fluorescence imaging of histological sections from atherosclerotic animal models has shown a preferential uptake of photosensitizers within atherosclerotic plaques, it is noteworthy that, to date, none of the prior studies evaluating photoangioplasty efficacy have utilized an imaging modality capable of providing image guidance to verify delivery of the drug prior to applying illumination for its activation. In the future, however, combined IVUS/IVPA imaging may offer a means for providing such validation as well as for a more localized drug activation scheme. For example, the potential for image-guidance using IVUS/IVPA, revealing contrast agent location and arterial morphology, might enable activation of the drug at only the vulnerable shoulder regions of plaques rather than the prior practice of activating the photosensitizer throughout a long region (2 cm) using a diffuse optical fiber.

1.5.4. Dual Modality Photothermal and Photodynamic Therapy

Recently, the prospect of dual-modality nanoparticles capable of providing both plasmonic photothermal therapy (PPTT) and photodynamic therapy (PDT) have been investigated for cancer treatment applications [174-185]. Among these multifunctional nanoparticles, many have centered on the covalent attachment of photosensitizers to gold nanoparticles, while one has demonstrated the ability to embed the photosensitizer directly within a silica coating encapsulating a gold nanorod [180]. Interestingly, the combined PTT and PDT approach has been shown to provide enhanced therapeutic outcomes when compared to either modality independently for the treatment of various *in vitro* and *in vivo* cancer models [175,176,178,184].

The adoption of multifunctional PTT and PDT nanoparticles for the stabilization of atherosclerotic plaques is, therefore, a natural transition, particularly when considering the aforementioned preclinical demonstrations of both PPTT and photoangioplasty for the

treatment of atherosclerosis. With such an approach, the IVUS/IVPA imaging platform can provide a means of first detecting the particles and subsequently delivering the targeted irradiation necessary to induce a localized therapeutic effect, including both a photosensitizing and heating optical sources. The resulting thermal effects can then be monitored using IVPA imaging during the dual-modality therapy. Further investigation into this proposed strategy represents an overall theme of the research presented throughout this dissertation.

1.6. Overall Research Goals and Dissertation Organization

The overall goal of this research is to expand the applications of the recently introduced intravascular ultrasound and photoacoustic (IVUS/IVPA) imaging platform by demonstrating the ability for detection and optically-triggered treatment of atherosclerotic plaques through the delivery and excitation of multifunctional nanoparticle contrast agents. Specifically, rod-shaped gold nanoparticles are investigated as agents for both IVPA contrast and vehicles for selective optically-triggered therapy delivery.

In Chapter 2, the passive extravasation and aggregation of systemically injected gold nanorods (AuNR) absorbing within the near infrared tissue optical window within plaques of atherosclerotic rabbit models will be demonstrated. The AuNR-labeled atherosclerotic plaques are spectroscopically localized using *ex vivo* IVUS/IVPA imaging through both luminal saline and blood.

In Chapter 3 and Chapter 4, the motivation for nanoparticle labeling of atherosclerosis is expanded from that of purely image contrast agents to vehicles for image-guided, dual-modality phototherapy, opening the door for a potential strategy of complimentary diagnosis and local treatment of atherosclerotic plaques using an integrated IVUS/IVPA catheter. Chapter 3 focuses on the use of the integrated

IVUS/IVPA imaging catheter for photothermal delivery with simultaneous IVPA temperature monitoring using the high optical absorption of AuNR to enable localized heating. In Chapter 4, the potential role for IVUS/IVPA-guided phototherapy is further expanded through the characterization and *in vitro* assessment of novel multifunctional theranostic nanoparticles comprised of an AuNR core with a degradable, photosensitizer-doped silica shell.

Finally, in Chapter 5, conclusions from the overall research are presented along with limitations and next steps associated with each of the preceding chapters. An overall assessment of the future clinical outlook for IVUS/IVPA imaging as well as the utilization of exogenous contrast agents for imaging contrast and/or therapy delivery is also presented.

1.7. REFERENCES

1. V. r. L. Roger, A. S. Go, D. M. Lloyd-Jones, E. J. Benjamin, J. D. Berry, W. B. Borden, D. M. Bravata, S. Dai, E. S. Ford, C. S. Fox, H. J. Fullerton, C. Gillespie, S. M. Hailpern, J. A. Heit, V. J. Howard, B. M. Kissela, S. J. Kittner, D. T. Lackland, J. H. Lichtman, L. D. Lisabeth, D. M. Makuc, G. M. Marcus, A. Marelli, D. B. Matchar, C. S. Moy, D. Mozaffarian, M. E. Mussolino, G. Nichol, N. P. Paynter, E. Z. Soliman, P. D. Sorlie, N. Sotoodehnia, T. N. Turan, S. S. Virani, N. D. Wong, D. Woo and M. B. Turner, "Heart Disease and Stroke Statistics-2012 Update: A Report From the American Heart Association," *Circulation*, 125(1):e2-e220, (2012).

2. P. P. Mendis S, Norrving B, Global Atlas on Cardiovascular Disease Prevention and Control, W. H. O. W. h. F. W. S. Organization, (2011).

3. R. P. Choudhury, V. Fuster and Z. A. Fayad, "Molecular, cellular and functional imaging of atherothrombosis," *Nat Rev Drug Discov*, 3(11):913-925, (2004).

4. R. Ross, "Cell Biology of Atherosclerosis," *Annual Review of Physiology*, 57(1):791-804, (1995).

5. R. R. S. Packard and P. Libby, "Inflammation in Atherosclerosis: From Vascular Biology to Biomarker Discovery and Risk Prediction," *Clinical Chemistry*, 54(1):24-38, (2008).

6. P. S. Mullenix, C. A. Andersen and B. W. Starnes, "Atherosclerosis as Inflammation," *Annals of vascular surgery*, 19(1):130-138, (2005).

7. R. Virmani, A. P. Burke, A. Farb and F. D. Kolodgie, "Pathology of the Vulnerable Plaque," *Journal of the American College of Cardiology*, 47(8, Supplement):C13-C18, (2006).

8. M. Naghavi, P. Libby, E. Falk, S. W. Casscells, S. Litovsky, J. Rumberger, J. J. Badimon, C. Stefanadis, P. Moreno, G. Pasterkamp, Z. Fayad, P. H. Stone, S. Waxman, P. Raggi, M. Madjid, A. Zarrabi, A. Burke, C. Yuan, P. J. Fitzgerald, D. S. Siscovick, C. L. de Korte, M. Aikawa, K. E. Juhani Airaksinen, G. Assmann, C. R. Becker, J. H. Chesebro, A. Farb, Z. S. Galis, C. Jackson, I.-K. Jang, W. Koenig, R. A. Lodder, K. March, J. Demirovic, M. Navab, S. G. Priori, M. D. Rekhter, R. Bahr, S. M. Grundy, R. Mehran, A. Colombo, E. Boerwinkle, C. Ballantyne, W. Insull, R. S. Schwartz, R. Vogel, P. W. Serruys, G. K. Hansson, D. P. Faxon, S. Kaul, H. Drexler, P. Greenland, J. E. Muller, R. Virmani, P. M. Ridker, D. P. Zipes, P. K. Shah and J. T. Willerson, "From Vulnerable Plaque to Vulnerable Patient: A Call for New Definitions and Risk Assessment Strategies: Part I," *Circulation*, 108(14):1664-1672, (2003).

9. I. Chapman, "Relationships of recent coronary artery occlusion and acute myocardial infarction," *J Mt Sinai Hosp N Y*, 35(2):149-54, (1968).

10. P. Constantinides, "Pathogenesis of cerebral artery thrombosis in man," *Arch Pathol*, 83(5):422-8, (1967).

11. M. J. Davies and A. C. Thomas, "Plaque fissuring--the cause of acute myocardial infarction, sudden ischaemic death, and crescendo angina," *Br Heart J*, 53(4):363-73, (1985).

12. E. Falk, "Plaque rupture with severe pre-existing stenosis precipitating coronary thrombosis. Characteristics of coronary atherosclerotic plaques underlying fatal occlusive thrombi," *Br Heart J*, 50(2):127-34, (1983).

13. M. Friedman and G. J. Van den Bovenkamp, "Role of thrombus in plaque formation in the human diseased coronary artery," *Br J Exp Pathol*, 47(6):550-7, (1966).

14. J. E. Muller, G. S. Abela, R. W. Nesto and G. H. Tofler, "Triggers, acute risk factors and vulnerable plaques: The lexicon of a new frontier," *Journal of the American College of Cardiology*, 23(3):809-813, (1994).

15. J. E. Muller, G. H. Tofler and P. H. Stone, "Circadian variation and triggers of onset of acute cardiovascular disease," *Circulation*, 79(4):733-43, (1989).

16. J. T. Willerson, W. B. Campbell, M. D. Winniford, J. Schmitz, P. Apprill, B. G. Firth, J. Ashton, T. Smitherman, L. Bush and L. M. Buja, "Conversion from chronic to acute coronary artery disease: speculation regarding mechanisms," *Am J Cardiol*, 54(10):1349-54, (1984).

17. P. K. Cheruvu, A. V. Finn, C. Gardner, J. Caplan, J. Goldstein, G. W. Stone, R. Virmani and J. E. Muller, "Frequency and Distribution of Thin-Cap Fibroatheroma and Ruptured Plaques in Human Coronary Arteries: A Pathologic Study," *Journal of the American College of Cardiology*, 50(10):940-949, (2007).

18. A. V. Finn, M. Nakano, J. Narula, F. D. Kolodgie and R. Virmani, "Concept of Vulnerable/Unstable Plaque," *Arteriosclerosis, Thrombosis, and Vascular Biology*, 30(7):1282-1292, (2010).

19. E. A. Van Vré, H. Ait-Oufella, A. Tedgui and Z. Mallat, "Apoptotic Cell Death and Efferocytosis in Atherosclerosis," *Arteriosclerosis, Thrombosis, and Vascular Biology*, 32(4):887-893, (2012).

20. E. L. Gautier, T. Huby, J. L. Witztum, B. Ouzilleau, E. R. Miller, F. Saint-Charles, P. Aucouturier, M. J. Chapman and P. Lesnik, "Macrophage Apoptosis Exerts Divergent Effects on Atherogenesis as a Function of Lesion Stage," *Circulation*, 119(13):1795-1804, (2009).

21. E. Thorp and I. Tabas, "Mechanisms and consequences of efferocytosis in advanced atherosclerosis," *J Leukoc Biol*, 86(5):1089-95, (2009).

22. J. E. van Velzen, F. R. de Graaf, J. W. Jukema, G. J. de Grooth, G. Pundziute, L. J. Kroft, A. de Roos, J. H. C. Reiber, J. J. Bax, M. J. Schalij, J. D. Schuijf and E. E. van der Wall, "Comparison of the Relation Between the Calcium Score and Plaque Characteristics in Patients With Acute Coronary Syndrome Versus Patients With Stable Coronary Artery Disease, Assessed by Computed Tomography Angiography and Virtual Histology Intravascular Ultrasound," *The American Journal of Cardiology*, 108(5):658-664, (2011).

23. S. Glagov, E. Weisenberg, C. K. Zarins, R. Stankunavicius and G. J. Kolettis, "Compensatory Enlargement of Human Atherosclerotic Coronary Arteries," *New England Journal of Medicine*, 316(22):1371-1375, (1987).

24. S. Waxman, F. Ishibashi and J. E. Muller, "Detection and Treatment of Vulnerable Plaques and Vulnerable Patients: Novel Approaches to Prevention of Coronary Events," *Circulation*, 114(22):2390-2411, (2006).

25. P. J. Fitzgerald and P. G. Yock, "Mechanisms and outcomes of angioplasty and atherectomy assessed by intravascular ultrasound imaging," *J Clin Ultrasound*, 21(9):579-88, (1993).

26. S. E. Nissen and P. Yock, "Intravascular ultrasound: novel pathophysiological insights and current clinical applications," *Circulation*, 103(4):604-16, (2001).

27. D. Franzen, U. Sechtem and H. W. Hopp, "Comparison of angioscopic, intravascular ultrasonic, and angiographic detection of thrombus in coronary stenosis," *Am J Cardiol*, 82(10):1273-5, a9, (1998).

28. S. W. Kim, G. S. Mintz, Y. J. Hong, R. Pakala, K. S. Park, A. D. Pichard, L. F. Satler, K. M. Kent, W. O. Suddath, R. Waksman and N. J. Weissman, "The virtual histology intravascular ultrasound appearance of newly placed drug-eluting stents," *Am J Cardiol*, 102(9):1182-6, (2008).

29. T. Thim, M. K. Hagensen, D. Wallace-Bradley, J. F. Granada, G. L. Kaluza, L. Drouet, W. P. Paaske, H. E. Botker and E. Falk, "Unreliable assessment of necrotic core by virtual histology intravascular ultrasound in porcine coronary artery disease," *Circ Cardiovasc Imaging*, 3(4):384-91, (2010).

30. M. Gaglia, Jr., D. Steinberg and N. Weissman, "Intravascular ultrasound: Virtual histology IVUS, integrated backscatter IVUS, and palpography," *Current Cardiovascular Imaging Reports*, 2(4):268-274, (2009).

31. T. Kubo, T. Imanishi, S. Takarada, A. Kuroi, S. Ueno, T. Yamano, T. Tanimoto, Y. Matsuo, T. Masho, H. Kitabata, K. Tsuda, Y. Tomobuchi and T. Akasaka, "Assessment of culprit lesion morphology in acute myocardial infarction: ability of optical coherence tomography compared with intravascular ultrasound and coronary angioscopy," *J Am Coll Cardiol*, 50(10):933-9, (2007).

32. G. J. Tearney, E. Regar, T. Akasaka, T. Adriaenssens, P. Barlis, H. G. Bezerra, B. Bouma, N. Bruining, J.-m. Cho, S. Chowdhary, M. A. Costa, R. de Silva, J. Dijkstra, C. Di Mario, D. Dudeck, E. Falk, M. D. Feldman, P. Fitzgerald, H. Garcia, N. Gonzalo, J. F. Granada, G. Guagliumi, N. R. Holm, Y. Honda, F. Ikeno, M. Kawasaki, J. Kochman, L. Koltowski, T. Kubo, T. Kume, H. Kyono, C. C. S. Lam, G. Lamouche, D. P. Lee, M. B. Leon, A. Maehara, O. Manfrini, G. S. Mintz, K. Mizuno, M.-a. Morel, S. Nadkarni, H. Okura, H. Otake, A. Pietrasik, F. Prati, L. Räber, M. D. Radu, J. Rieber, M. Riga, A. Rollins, M. Rosenberg, V. Sirbu, P. W. J. C. Serruys, K. Shimada, T. Shinke, J. Shite, E. Siegel, S. Sonada, M. Suter, S. Takarada, A. Tanaka, M. Terashima, T. Troels, S. Uemura, G. J. Ughi, H. M. M. van Beusekom, A. F. W. van der Steen, G.-A. van Es, G. van Soest, R. Virmani, S. Waxman, N. J. Weissman and G. Weisz, "Consensus Standards for Acquisition, Measurement, and Reporting of Intravascular Optical

Coherence Tomography Studies: A Report From the International Working Group for Intravascular Optical Coherence Tomography Standardization and Validation," *Journal of the American College of Cardiology*, 59(12):1058-1072, (2012).

33. I.-K. Jang, B. E. Bouma, D.-H. Kang, S.-J. Park, S.-W. Park, K.-B. Seung, K.-B. Choi, M. Shishkov, K. Schlendorf, E. Pomerantsev, S. L. Houser, H. T. Aretz and G. J. Tearney, "Visualization of coronary atherosclerotic plaques in patients using optical coherence tomography: comparison with intravascular ultrasound," *Journal of the American College of Cardiology*, 39(4):604-609, (2002).

34. L. A. Cassis and R. A. Lodder, "Near-IR imaging of atheromas in living arterial tissue," *Anal Chem*, 65(9):1247-56, (1993).

35. P. R. Moreno, R. A. Lodder, K. R. Purushothaman, W. E. Charash, W. N. O'Connor and J. E. Muller, "Detection of lipid pool, thin fibrous cap, and inflammatory cells in human aortic atherosclerotic plaques by near-infrared spectroscopy," *Circulation*, 105(8):923-7, (2002).

36. J. D. Caplan, S. Waxman, R. W. Nesto and J. E. Muller, "Near-infrared spectroscopy for the detection of vulnerable coronary artery plaques," *J Am Coll Cardiol*, 47(8 Suppl):C92-6, (2006).

37. S. Brugaletta, H. M. Garcia-Garcia, P. W. Serruys, S. de Boer, J. Ligthart, J. Gomez-Lara, K. Witberg, R. Diletti, J. Wykrzykowska, R.-J. van Geuns, C. Schultz, E. Regar, H. J. Duckers, N. van Mieghem, P. de Jaegere, S. P. Madden, J. E. Muller, A. F. W. van der Steen, W. J. van der Giessen and E. Boersma, "NIRS and IVUS for Characterization of Atherosclerosis in Patients Undergoing Coronary Angiography," *JACC: Cardiovascular Imaging*, 4(6):647-655, (2011).

38. S. Waxman, S. R. Dixon, P. L'Allier, J. W. Moses, J. L. Petersen, D. Cutlip, J. C. Tardif, R. W. Nesto, J. E. Muller, M. J. Hendricks, S. T. Sum, C. M. Gardner, J. A. Goldstein, G. W. Stone and M. W. Krucoff, "In vivo validation of a catheter-based near-infrared spectroscopy system for detection of lipid core coronary plaques: initial results of the SPECTACL study," *JACC Cardiovasc Imaging*, 2(7):858-68, (2009).

39. M. J. Suter, S. K. Nadkarni, G. Weisz, A. Tanaka, F. A. Jaffer, B. E. Bouma and G. J. Tearney, "Intravascular optical imaging technology for investigating the coronary artery," *JACC Cardiovasc Imaging*, 4(9):1022-39, (2011).

40. C. Simsek, H. M. Garcia-Garcia, R. J. van Geuns, M. Magro, C. Girasis, N. van Mieghem, M. Lenzen, S. de Boer, E. Regar, W. van der Giessen, J. Raichlen, H. J. Duckers, F. Zijlstra, T. van der Steen, E. Boersma and P. W. Serruys, "The ability

of high dose rosuvastatin to improve plaque composition in non-intervened coronary arteries: rationale and design of the Integrated Biomarker and Imaging Study-3 (IBIS-3)," *EuroIntervention*, 8(2):235-41, (2012).

41. J. A. Goldstein, C. Grines, T. Fischell, R. Virmani, D. Rizik, J. Muller and S. R. Dixon, "Coronary embolization following balloon dilation of lipid-core plaques," *JACC Cardiovasc Imaging*, 2(12):1420-4, (2009).

42. J. A. Goldstein, B. Maini, S. R. Dixon, E. S. Brilakis, C. L. Grines, D. G. Rizik, E. R. Powers, D. H. Steinberg, K. A. Shunk, G. Weisz, P. R. Moreno, A. Kini, S. K. Sharma, M. J. Hendricks, S. T. Sum, S. P. Madden, J. E. Muller, G. W. Stone and M. J. Kern, "Detection of Lipid-Core Plaques by Intracoronary Near-Infrared Spectroscopy Identifies High Risk of Periprocedural Myocardial Infarction," *Circulation: Cardiovascular Interventions*, 4(5):429-437, (2011).

43. L. Raber, J. H. Heo, M. D. Radu, H. M. Garcia-Garcia, G. G. Stefanini, A. Moschovitis, J. Dijkstra, H. Kelbaek, S. Windecker and P. W. Serruys, "Offline fusion of co-registered intravascular ultrasound and frequency domain optical coherence tomography images for the analysis of human atherosclerotic plaques," *EuroIntervention*, 8(1):98-108, (2012).

44. J. R. Spears, A. M. Spokojny and H. J. Marais, "Coronary angioscopy during cardiac catheterization," *J Am Coll Cardiol*, 6(1):93-7, (1985).

45. C. T. Sherman, F. Litvack, W. Grundfest, M. Lee, A. Hickey, A. Chaux, R. Kass, C. Blanche, J. Matloff, L. Morgenstern and et al., "Coronary angioscopy in patients with unstable angina pectoris," *N Engl J Med*, 315(15):913-9, (1986).

46. F. Ishibashi, K. Aziz, G. S. Abela and S. Waxman, "Update on coronary angioscopy: review of a 20-year experience and potential application for detection of vulnerable plaque," *J Interv Cardiol*, 19(1):17-25, (2006).

47. Y. Ueda, T. Ohtani, M. Shimizu, A. Hirayama and K. Kodama, "Assessment of plaque vulnerability by angioscopic classification of plaque color," *Am Heart J*, 148(2):333-5, (2004).

48. M. Takano, K. Mizuno, S. Yokoyama, K. Seimiya, F. Ishibashi, K. Okamatsu and R. Uemura, "Changes in coronary plaque color and morphology by lipid-lowering therapy with atorvastatin: serial evaluation by coronary angioscopy," *J Am Coll Cardiol*, 42(4):680-6, (2003).

49. A. Tawakol and J. Muller, "Through the looking glass: an angioscopic view of the effect of statin therapy on coronary artery plaques," *J Am Coll Cardiol*, 42(4):687-9, (2003).

50. S. Yokoyama, M. Takano, M. Yamamoto, S. Inami, S. Sakai, K. Okamatsu, S. Okuni, K. Seimiya, D. Murakami, T. Ohba, R. Uemura, Y. Seino, N. Hata and K. Mizuno, "Extended follow-up by serial angioscopic observation for bare-metal stents in native coronary arteries: from healing response to atherosclerotic transformation of neointima," *Circ Cardiovasc Interv*, 2(3):205-12, (2009).

51. M. Yamamoto, K. Okamatsu, S. Inami, M. Takano, S. Yokoyama, T. Ohba, C. Ibuki, N. Hata, Y. Seino and K. Mizuno, "Relationship between neointimal coverage of sirolimus-eluting stents and lesion characteristics: a study with serial coronary angioscopy," *Am Heart J*, 158(1):99-104, (2009).

52. S. Koie, H. Matsuyama, M. Nomura and H. Hishida, "[Intravascular ultrasound and angioscopy]," *Nihon Rinsho*, 61(10):1744-50, (2003).

53. K. Tokuhiro, Y. Uchida, K. Kawamura, H. Sakuragawa, H. Masuhara, H. Oosawa and N. Koyama, "Evaluation of Annuloaortic Ectasia by Angioscopy and IVUS "Report of 2 cases"," *Diagn Ther Endosc*, 7(1):35-45, (2000).

54. T. Kubo, T. Imanishi, S. Takarada, A. Kuroi, S. Ueno, T. Yamano, T. Tanimoto, Y. Matsuo, T. Masho, H. Kitabata, A. Tanaka, N. Nakamura, M. Mizukoshi, Y. Tomobuchi and T. Akasaka, "Implication of plaque color classification for assessing plaque vulnerability: a coronary angioscopy and optical coherence tomography investigation," *JACC Cardiovasc Interv*, 1(1):74-80, (2008).

55. L. I. Deckelbaum, J. K. Lam, H. S. Cabin, K. S. Clubb and M. B. Long, "Discrimination of normal and atherosclerotic aorta by laser-induced fluorescence," *Lasers Surg Med*, 7(4):330-5, (1987).

56. R. Richards-Kortum, R. P. Rava, M. Fitzmaurice, L. L. Tong, N. B. Ratliff, J. R. Kramer and M. Feld, "A one-layer model of laser-induced fluorescence for diagnosis of disease in human tissue: applications to atherosclerosis," *Biomedical Engineering, IEEE Transactions on*, 36(12):1222-1232, (1989).

57. J. J. Baraga, R. P. Rava, P. Taroni, C. Kittrell, M. Fitzmaurice and M. S. Feld, "Laser induced fluorescence spectroscopy of normal and atherosclerotic human aorta using 306-310 nm excitation," *Lasers Surg Med*, 10(3):245-61, (1990).

58. L. Marcu, J. A. Jo, Q. Fang, T. Papaioannou, T. Reil, J. H. Qiao, J. D. Baker, J. A. Freischlag and M. C. Fishbein, "Detection of rupture-prone atherosclerotic plaques by time-resolved laser-induced fluorescence spectroscopy," *Atherosclerosis*, 204(1):156-64, (2009).

59. L. Marcu, Q. Fang, J. A. Jo, T. Papaioannou, A. Dorafshar, T. Reil, J. H. Qiao, J. D. Baker, J. A. Freischlag and M. C. Fishbein, "In vivo detection of macrophages

in a rabbit atherosclerotic model by time-resolved laser-induced fluorescence spectroscopy," *Atherosclerosis*, 181(2):295-303, (2005).

60. D. S. Elson, J. A. Jo and L. Marcu, "Miniaturized side-viewing imaging probe for fluorescence lifetime imaging (FLIM): validation with fluorescence dyes, tissue structural proteins and tissue specimens," *New J Phys*, 9:127, (2007).

61. J. Phipps, Y. Sun, R. Saroufeem, N. Hatami and L. Marcu, "Fluorescence lifetime imaging microscopy for the characterization of atherosclerotic plaques," *Proc Soc Photo Opt Instrum Eng*, 7161:71612g, (2009).

62. J. Phipps, Y. Sun, R. Saroufeem, N. Hatami, M. C. Fishbein and L. Marcu, "Fluorescence lifetime imaging for the characterization of the biochemical composition of atherosclerotic plaques," *J Biomed Opt*, 16(9):096018, (2011).

63. O. R. Šćepanović, Z. Volynskaya, C.-R. Kong, L. H. Galindo, R. R. Dasari and M. S. Feld, "A multimodal spectroscopy system for real-time disease diagnosis," *Review of Scientific Instruments*, 80(4):-, (2009).

64. O. R. Scepanovic, M. Fitzmaurice, A. Miller, C. R. Kong, Z. Volynskaya, R. R. Dasari, J. R. Kramer and M. S. Feld, "Multimodal spectroscopy detects features of vulnerable atherosclerotic plaque," *J Biomed Opt*, 16(1):011009, (2011).

65. J. J. Baraga, M. S. Feld and R. P. Rava, "In situ optical histochemistry of human artery using near infrared Fourier transform Raman spectroscopy," *Proc Natl Acad Sci U S A*, 89(8):3473-7, (1992).

66. R. Manoharan, J. J. Baraga, M. S. Feld and R. P. Rava, "Quantitative histochemical analysis of human artery using Raman spectroscopy," *J Photochem Photobiol B*, 16(2):211-33, (1992).

67. J. F. Brennan, T. J. Römer, R. S. Lees, A. M. Tercyak, J. R. Kramer and M. S. Feld, "Determination of Human Coronary Artery Composition by Raman Spectroscopy," *Circulation*, 96(1):99-105, (1997).

68. T. J. Romer, J. F. Brennan, 3rd, M. Fitzmaurice, M. L. Feldstein, G. Deinum, J. L. Myles, J. R. Kramer, R. S. Lees and M. S. Feld, "Histopathology of human coronary atherosclerosis by quantifying its chemical composition with Raman spectroscopy," *Circulation*, 97(9):878-85, (1998).

69. S. W. van de Poll, K. Kastelijn, T. C. Bakker Schut, C. Strijder, G. Pasterkamp, G. J. Puppels and A. van der Laarse, "On-line detection of cholesterol and calcification by catheter based Raman spectroscopy in human atherosclerotic plaque ex vivo," *Heart*, 89(9):1078-82, (2003).

70. H. P. Buschman, E. T. Marple, M. L. Wach, B. Bennett, T. C. Bakker Schut, H. A. Bruining, A. V. Bruschke, A. van der Laarse and G. J. Puppels, "In Vivo Determination of the Molecular Composition of Artery Wall by Intravascular Raman Spectroscopy," *Analytical Chemistry*, 72(16):3771-3775, (2000).

71. A. H. Chau, J. T. Motz, J. A. Gardecki, S. Waxman, B. E. Bouma and G. J. Tearney, "Fingerprint and high-wavenumber Raman spectroscopy in a human-swine coronary xenograft in vivo," *J Biomed Opt*, 13(4):040501, (2008).

72. J. T. Motz, M. Fitzmaurice, A. Miller, S. J. Gandhi, A. S. Haka, L. H. Galindo, R. R. Dasari, J. R. Kramer and M. S. Feld, "In vivo Raman spectral pathology of human atherosclerosis and vulnerable plaque," *J Biomed Opt*, 11(2):021003, (2006).

73. J. W. Evans, R. J. Zawadzki, R. Liu, J. W. Chan, S. M. Lane and J. S. Werner, "Optical coherence tomography and Raman spectroscopy of the ex-vivo retina," *J Biophotonics*, 2(6-7):398-406, (2009).

74. K. M. Khan, H. Krishna, S. K. Majumder, K. D. Rao and P. K. Gupta, "Depth-sensitive Raman spectroscopy combined with optical coherence tomography for layered tissue analysis," *Journal of Biophotonics*, 7(1-2):77-85, (2014).

75. J. F. Brennan Iii, J. Nazemi, J. Motz and S. Ramcharitar, "The vPredict™ Optical Catheter System: Intravascular Raman Spectroscopy," *EuroIntervention*, 3(5):635-638, (2008).

76. T. J. Romer, J. F. Brennan, 3rd, G. J. Puppels, A. H. Zwinderman, S. G. van Duinen, A. van der Laarse, A. F. van der Steen, N. A. Bom and A. V. Bruschke, "Intravascular ultrasound combined with Raman spectroscopy to localize and quantify cholesterol and calcium salts in atherosclerotic coronary arteries," *Arterioscler Thromb Vasc Biol*, 20(2):478-83, (2000).

77. S. W. E. van de Poll, C. L. De Korte, A. F. W. Van der Steen, G. J. Puppels and A. Van der Laarse, "Coronary atherosclerotic plaque characterization using IVUS elastography and Raman spectroscopy," *Ultrasonics Symposium, 2000 IEEE*, 2(1775-1778 vol.2), (2000).

78. X.-Q. Zhao, C. Yuan, T. S. Hatsukami, E. H. Frechette, X.-J. Kang, K. R. Maravilla and B. G. Brown, "Effects of Prolonged Intensive Lipid-Lowering Therapy on the Characteristics of Carotid Atherosclerotic Plaques In Vivo by MRI: A Case-Control Study," *Arteriosclerosis, Thrombosis, and Vascular Biology*, 21(10):1623-1629, (2001).

79. G. C. Hurst, J. Hua, J. L. Duerk and A. M. Cohen, "Intravascular (catheter) NMR receiver probe: preliminary design analysis and application to canine iliofemoral imaging," *Magn Reson Med*, 24(2):343-57, (1992).

80. A. J. Martin, D. B. Plewes and R. M. Henkelman, "MR imaging of blood vessels with an intravascular coil," *J Magn Reson Imaging*, 2(4):421-9, (1992).

81. C. M. Hillenbrand, D. R. Elgort, E. Y. Wong, A. Reykowski, F. K. Wacker, J. S. Lewin and J. L. Duerk, "Active device tracking and high-resolution intravascular MRI using a novel catheter-based, opposed-solenoid phased array coil," *Magn Reson Med*, 51(4):668-75, (2004).

82. A.-K. Homagk, R. Umathum, M. Korn, M.-A. Weber, P. Hallscheidt, W. Semmler and M. Bock, "An expandable catheter loop coil for intravascular MRI in larger blood vessels," *Magnetic Resonance in Medicine*, 63(2):517-523, (2010).

83. J. Schneiderman, R. L. Wilensky, A. Weiss, E. Samouha, L. Muchnik, M. Chen-Zion, M. Ilovitch, E. Golan, A. Blank, M. Flugelman, Y. Rozenman and R. Virmani, "Diagnosis of Thin-Cap Fibroatheromas by a Self-Contained Intravascular Magnetic Resonance Imaging Probe in Ex Vivo Human Aortas and In Situ Coronary Arteries," *Journal of the American College of Cardiology*, 45(12):1961-1969, (2005).

84. E. Regar, B. Hennen, E. Grube, D. Halon, R. L. Wilensky, R. Virmani, J. Schneiderman, S. Sax, H. Friedmann, P. W. Serruys and W. Wijns, "First-In-Man application of a miniature self-contained intracoronary magnetic resonance probe. A multi-centre safety and feasibility trial," *EuroIntervention*, 2(1):77-83, (2006).

85. W. M. Suh, A. H. Seto, R. J. P. Margey, I. Cruz-Gonzalez and I.-K. Jang, "Intravascular Detection of the Vulnerable Plaque," *Circulation: Cardiovascular Imaging*, 4(2):169-178, (2011).

86. R. J. Lederman, R. R. Raylman, S. J. Fisher, P. V. Kison, H. San, E. G. Nabel and R. L. Wahl, "Detection of atherosclerosis using a novel positron-sensitive probe and 18-fluorodeoxyglucose (FDG)," *Nucl Med Commun*, 22(7):747-53, (2001).

87. M. Janecek, B. E. Patt, J. S. Iwanczyk, L. MacDonald, Y. Yamaguchi, H. William Strauss, R. Tsugita, V. Ghazarossian and E. J. Hoffman, "Intravascular probe for detection of vulnerable plaque," *Mol Imaging Biol*, 6(3):131-8, (2004).

88. P. M. Shikhaliev, T. Xu, J. L. Ducote, B. Easwaramoorthy, J. Mukherjee and S. Molloi, "Positron autoradiography for intravascular imaging: feasibility evaluation," *Phys Med Biol*, 51(4):963-79, (2006).

89. R. Hosokawa, N. Kambara, M. Ohba, T. Mukai, M. Ogawa, H. Motomura, N. Kume, H. Saji, T. Kita and R. Nohara, "A Catheter-Based Intravascular Radiation Detector of Vulnerable Plaques," *Journal of Nuclear Medicine*, 47(5):863-867, (2006).

90. H. W. Strauss, C. Mari, B. E. Patt and V. Ghazarossian, "Intravascular Radiation Detectors for the Detection of Vulnerable Atheroma," *Journal of the American College of Cardiology*, 47(8, Supplement):C97-C100, (2006).

91. D. Piao, M. M. Sadeghi, J. Zhang, Y. Chen, A. J. Sinusas and Q. Zhu, "Hybrid positron detection and optical coherence tomography system: design, calibration, and experimental validation with rabbit atherosclerotic models," *J Biomed Opt*, 10(4):44010, (2005).

92. A. G. Bell, "Upon the production and reproduction of sound by light," *Telegraph Engineers, Journal of the Society of*, 9(34):404-426, (1880).

93. J. B. Kinney and R. H. Staley, "Applications of Photoacoustic Spectroscopy," *Annual Review of Materials Science*, 12(1):295-321, (1982).

94. A. Rosencwaig, "Photoacoustic Spectroscopy" in *Advances in Electronics and Electron Physics*, L. Marton, Editor. 1978, Academic Press. p. 207-311.

95. T. Bowen, "Radiation-Induced Thermoacoustic Soft Tissue Imaging," *1981 Ultrasonics Symposium*, (817-822), (1981).

96. R. A. Kruger, P. Liu, Y. R. Fang and C. R. Appledorn, "Photoacoustic ultrasound (PAUS)--reconstruction tomography," *Med Phys*, 22(10):1605-9, (1995).

97. J. S. L. Oraevsky A. A., Esenaliev R. O., and Tittel F. K., "Laser based optoacoustic imaging in biological tissues," *Proc. SPIE*, 0277-786X(2134A):122-128, (1994).

98. S. Sethuraman, S. R. Aglyamov, J. H. Amirian, R. W. Smalling and a. E. S. Y., "Intravascular photoacoustic imaging using an IVUS imaging catheter," *IEEE Trans. Ultrason. Ferroelectr. Freq. Control*, 54:978-986, (2007).

99. M. W. Sigrist, "Laser generation of acoustic waves in liquids and gases," *Journal of Applied Physics*, 60(7):R83-R122, (1986).

100. A. C. Tam, "Applications of photoacoustic sensing techniques," *Reviews of Modern Physics*, 58(2):381-431, (1986).

101. P. Beard, "Biomedical photoacoustic imaging," *Interface Focus*, 1(4):602-31, (2011).

102. V. E. Gusev and A. A. Karabutov, Laser optoacoustics, American Institute of Physics, (1993).

103. J. Walsh, "Basic Interactions of Light with Tissue" in *Optical-Thermal Response of Laser-Irradiated Tissue*, A.J. Welch and M.J.C. Gemert, Editors. 2011, Springer Netherlands. p. 13-26.

104. G. J. Diebold and T. Sun, "Properties of Photoacoustic Waves in One, Two, and Three Dimensions," *Acta Acustica united with Acustica*, 80(4):339-351, (1994).

105. C. Li and L. V. Wang, "Photoacoustic tomography and sensing in biomedicine," *Phys Med Biol*, 54(19):R59-97, (2009).

106. Y.-S. Chen, W. Frey, S. Aglyamov and S. Emelianov, "Environment-Dependent Generation of Photoacoustic Waves from Plasmonic Nanoparticles," *Small*, 8(1):47-52, (2012).

107. Y.-S. Chen, W. Frey, C. Walker, S. Aglyamov and S. Emelianov, "Sensitivity enhanced nanothermal sensors for photoacoustic temperature mapping," *Journal of Biophotonics*, 6(6-7):534-542, (2013).

108. J. Shah, S. Park, S. Aglyamov, T. Larson, L. Ma, K. Sokolov, K. Johnston, T. Milner and S. Y. Emelianov, "Photoacoustic imaging and temperature measurement for photothermal cancer therapy," *J Biomed Opt*, 13(3):034024, (2008).

109. K. Seungsoo, C. Yun-Sheng, G. P. Luke, M. Mehrmohammadi, J. R. Cook and S. Y. Emelianov, "Ultrasound and photoacoustic image-guided photothermal therapy using silica-coated gold nanorods: In-vivo study," *Ultrasonics Symposium (IUS), 2010 IEEE*, (233-236), (2010).

110. F.A. Duck, "Thermal Properties of Tissue" in *Physical Properties of Tissues*, F. A. Duck, Editor. 1990, Academic Press. p.9-42.

111. B. Wang and S. Emelianov, "Thermal intravascular photoacoustic imaging," *Biomed Opt Express*, 2(11):3072-8, (2011).

112. B. Wang, J. L. Su, J. Amirian, S. H. Litovsky, R. Smalling and S. Emelianov, "Detection of lipid in atherosclerotic vessels using ultrasound-guided spectroscopic intravascular photoacoustic imaging," *Opt. Express*, 18(5):4889-4897, (2010).

113. I. M. Graf, S. Kim, B. Wang, R. Smalling and S. Emelianov, "Noninvasive detection of intimal xanthoma using combined ultrasound, strain rate and photoacoustic imaging," *Ultrasonics*, 52(3):435-41, (2012).

114. K. Jansen, M. Wu, A. F. van der Steen and G. van Soest, "Lipid detection in atherosclerotic human coronaries by spectroscopic intravascular photoacoustic imaging," *Opt Express*, 21(18):21472-84, (2013).

115. D. Razansky, N. J. Harlaar, J. L. Hillebrands, A. Taruttis, E. Herzog, C. J. Zeebregts, G. M. van Dam and V. Ntziachristos, "Multispectral optoacoustic tomography of matrix metalloproteinase activity in vulnerable human carotid plaques," *Mol Imaging Biol*, 14(3):277-85, (2012).

116. S. Mallidi, T. Larson, J. Tam, P. P. Joshi, A. Karpiouk, K. Sokolov and S. Emelianov, "Multiwavelength photoacoustic imaging and plasmon resonance coupling of gold nanoparticles for selective detection of cancer," *Nano Lett*, 9(8):2825-31, (2009).

117. D. Yeager, A. Karpiouk, B. Wang, J. Amirian, K. Sokolov, R. Smalling and S. Emelianov, "Intravascular photoacoustic imaging of exogenously labeled atherosclerotic plaque through luminal blood," *Journal of Biomedical Optics*, 17(10):106016-106016, (2012).

118. M. Pramanik and L. V. Wang, "Thermoacoustic and photoacoustic sensing of temperature," *J Biomed Opt*, 14(5):054024, (2009).

119. J. Richard Spears, "Percutaneous laser treatment of atherosclerosis: An overview of emerging techniques," *CardioVascular and Interventional Radiology*, 9(5-6):303-312, (1986).

120. B. G. Schwartz, R. A. Kloner, J. L. Thomas, Q. Bui, G. S. Mayeda, S. Burstein, S. L. Hale, C. Economides and W. J. French, "Therapeutic hypothermia for acute myocardial infarction and cardiac arrest," *Am J Cardiol*, 110(3):461-6, (2012).

121. K. Jansen, G. van Soest and A. F. van der Steen, "Intravascular Photoacoustic Imaging: A New Tool for Vulnerable Plaque Identification," *Ultrasound Med Biol*, 40(6):1037-1048, (2014).

122. B. Wang, J. L. Su, A. B. Karpiouk, K. V. Sokolov, R. W. Smalling and S. Y. Emelianov, "Intravascular Photoacoustic Imaging," *IEEE J Quantum Electron*, 16(3):588-599, (2010).

123. A. B. Karpiouk, B. Wang and S. Y. Emelianov, "Development of a catheter for combined intravascular ultrasound and photoacoustic imaging," *Rev Sci Instrum*, 81(1):014901, (2010).

124. W. Wei, X. Li, Q. Zhou, K. K. Shung and Z. Chen, "Integrated ultrasound and photoacoustic probe for co-registered intravascular imaging," *J Biomed Opt*, 16(10):106001, (2011).

125. K. Jansen, A. F. van der Steen, H. M. van Beusekom, J. W. Oosterhuis and G. van Soest, "Intravascular photoacoustic imaging of human coronary atherosclerosis," *Opt Lett*, 36(5):597-9, (2011).

126. B. K. Andrei, W. Bo and Y. E. Stanislav, "Development of a catheter for combined intravascular ultrasound and photoacoustic imaging," *Review of Scientific Instruments*, 81(1):014901, (2010).

127. B. Y. Hsieh, S. L. Chen, T. Ling, L. J. Guo and P. C. Li, "All-optical scanhead for ultrasound and photoacoustic dual-modality imaging," *Opt Express*, 20(2):1588-96, (2012).

128. J. Yin, X. Li, J. Jing, J. Li, D. Mukai, S. Mahon, A. Edris, K. Hoang, K. K. Shung, M. Brenner, J. Narula, Q. Zhou and Z. Chen, "Novel combined miniature optical coherence tomography ultrasound probe for in vivo intravascular imaging," *J Biomed Opt*, 16(6):060505, (2011).

129. A. B. Karpiouk, B. Wang, J. Amirian, R. W. Smalling and S. Y. Emelianov, "Feasibility of in vivo intravascular photoacoustic imaging using integrated ultrasound and photoacoustic imaging catheter," *J Biomed Opt*, 17(9):96008-1, (2012).

130. B. Wang, A. Karpiouk, D. Yeager, J. Amirian, S. Litovsky, R. Smalling and S. Emelianov, "Intravascular photoacoustic imaging of lipid in atherosclerotic plaques in the presence of luminal blood," *Opt Lett*, 37(7):1244-6, (2012).

131. B. Wang, A. Karpiouk, D. Yeager, J. Amirian, S. Litovsky, R. Smalling and S. Emelianov, "In vivo intravascular ultrasound-guided photoacoustic imaging of lipid in plaques using an animal model of atherosclerosis," *Ultrasound Med Biol*, 38(12):2098-103, (2012).

132. K. Jansen, A. F. W. van der Steen, H. M. M. van Beusekom, J. W. Oosterhuis and G. van Soest, "Intravascular photoacoustic imaging of human coronary atherosclerosis," *Opt. Lett.*, 36(5):597-599, (2011).

133. B. Wang, A. Karpiouk, D. Yeager, J. Amirian, S. Litovsky, R. Smalling and S. Emelianov, "In vivo Intravascular Ultrasound-guided Photoacoustic Imaging of Lipid in Plaques Using an Animal Model of Atherosclerosis," *Ultrasound in medicine & biology*, 38(12):2098-2103, (2012).

134. G. Luke, D. Yeager and S. Emelianov, "Biomedical Applications of Photoacoustic Imaging with Exogenous Contrast Agents," *Annals of Biomedical Engineering*, 40(2):422-437, (2012).

135. G. Kim, S. W. Huang, K. C. Day, M. O'Donnell, R. R. Agayan, M. A. Day, R. Kopelman and S. Ashkenazi, "Indocyanine-green-embedded PEBBLEs as a contrast agent for photoacoustic imaging," *J Biomed Opt*, 12(4):044020, (2007).

136. K. H. Song, E. W. Stein, J. A. Margenthaler and L. V. Wang, "Noninvasive photoacoustic identification of sentinel lymph nodes containing methylene blue in vivo in a rat model," *J Biomed Opt*, 13(5):054033, (2008).

137. K. M. Stantz, M. Cao, B. Liu, K. D. Miller and L. Guo, "Molecular imaging of neutropilin-1 receptor using photoacoustic spectroscopy in breast tumors," 7564(75641O-75641O-7), (2010).

138. S. Bhattacharyya, S. Wang, D. Reinecke, W. Kiser, Jr., R. A. Kruger and T. R. DeGrado, "Synthesis and evaluation of near-infrared (NIR) dye-herceptin conjugates as photoacoustic computed tomography (PCT) probes for HER2 expression in breast cancer," *Bioconjug Chem*, 19(6):1186-93, (2008).

139. A. De la Zerda, C. Zavaleta, S. Keren, S. Vaithilingam, S. Bodapati, Z. Liu, J. Levi, B. R. Smith, T. J. Ma, O. Oralkan, Z. Cheng, X. Chen, H. Dai, B. T. Khuri-Yakub and S. S. Gambhir, "Carbon nanotubes as photoacoustic molecular imaging agents in living mice," *Nat Nanotechnol*, 3(9):557-62, (2008).

140. A. de la Zerda, Z. Liu, S. Bodapati, R. Teed, S. Vaithilingam, B. T. Khuri-Yakub, X. Chen, H. Dai and S. S. Gambhir, "Ultrahigh sensitivity carbon nanotube agents for photoacoustic molecular imaging in living mice," *Nano Lett*, 10(6):2168-72, (2010).

141. M. Grzelczak, J. Perez-Juste, P. Mulvaney and L. M. Liz-Marzan, "Shape control in gold nanoparticle synthesis," *Chemical Society Reviews*, 37(9):1783-1791, (2008).

142. Y. Xia, Y. Xiong, B. Lim and S. E. Skrabalak, "Shape-Controlled Synthesis of Metal Nanocrystals: Simple Chemistry Meets Complex Physics?," *Angewandte Chemie International Edition*, 48(1):60-103, (2009).

143. P. K. Jain, K. S. Lee, I. H. El-Sayed and M. A. El-Sayed, "Calculated absorption and scattering properties of gold nanoparticles of different size, shape, and composition: applications in biological imaging and biomedicine," *J Phys Chem B*, 110(14):7238-48, (2006).

144. S. Kumar, J. Aaron and K. Sokolov, "Directional conjugation of antibodies to nanoparticles for synthesis of multiplexed optical contrast agents with both delivery and targeting moieties," *Nat. Protocols*, 3(2):314-320, (2008).

145. Y.-S. Chen, W. Frey, S. Kim, K. Homan, P. Kruizinga, K. Sokolov and S. Emelianov, "Enhanced thermal stability of silica-coated gold nanorods for photoacoustic imaging and image-guided therapy," *Opt. Express*, 18(9):8867-8878, (2010).

146. Y.-S. Chen, W. Frey, S. Kim, P. Kruizinga, K. Homan and S. Emelianov, "Silica-Coated Gold Nanorods as Photoacoustic Signal Nanoamplifiers," *Nano Letters*, 11(2):348-354, (2011).

147. B. Wang, E. Yantsen, T. Larson, A. B. Karpiouk, S. Sethuraman, J. L. Su, K. Sokolov and S. Y. Emelianov, "Plasmonic intravascular photoacoustic imaging for detection of macrophages in atherosclerotic plaques," *Nano Lett*, 9(6):2212-7, (2009).

148. X. Liangzhong, X. Da, G. Huaimin, Y. Diwu, Z. Lvming and Y. Sihua, "Gold nanoshell-based photoacoustic imaging application in biomedicine," *Biophotonics, Nanophotonics and Metamaterials, 2006. Metamaterials 2006. International Symposium on*, (76-79), (2006).

149. X. Yang, S. E. Skrabalak, Z. Y. Li, Y. Xia and L. V. Wang, "Photoacoustic tomography of a rat cerebral cortex in vivo with au nanocages as an optical contrast agent," *Nano Lett*, 7(12):3798-802, (2007).

150. L. Meng-Lin, O. Jung-Taek, X. Xie, G. Ku, W. Wei, L. Chun, G. Lungu, G. Stoica and L. V. Wang, "Simultaneous Molecular and Hypoxia Imaging of Brain Tumors <emphasis emphasistype="italic">In Vivo</emphasis> Using Spectroscopic Photoacoustic Tomography," *Proceedings of the IEEE*, 96(3):481-489, (2008).

151. C. L. Bayer, Y. S. Chen, S. Kim, S. Mallidi, K. Sokolov and S. Emelianov, "Multiplex photoacoustic molecular imaging using targeted silica-coated gold nanorods," *Biomed Opt Express*, 2(7):1828-35, (2011).

152. K. H. Song, C. Kim, K. Maslov and L. V. Wang, "Noninvasive in vivo spectroscopic nanorod-contrast photoacoustic mapping of sentinel lymph nodes," *Eur J Radiol*, 70(2):227-31, (2009).

153. J. E. Millstone, S. J. Hurst, G. S. Metraux, J. I. Cutler and C. A. Mirkin, "Colloidal gold and silver triangular nanoprisms," *Small*, 5(6):646-64, (2009).

154. S. E. Skrabalak, J. Chen, Y. Sun, X. Lu, L. Au, C. M. Cobley and Y. Xia, "Gold nanocages: synthesis, properties, and applications," *Acc Chem Res*, 41(12):1587-95, (2008).

155. S. J. Yoon, S. Mallidi, J. M. Tam, J. O. Tam, A. Murthy, K. P. Johnston, K. V. Sokolov and S. Y. Emelianov, "Utility of biodegradable plasmonic nanoclusters in photoacoustic imaging," *Opt Lett*, 35(22):3751-3, (2010).

156. B. Nikoobakht and M. A. El-Sayed, "Preparation and Growth Mechanism of Gold Nanorods (NRs) Using Seed-Mediated Growth Method," *Chemistry of Materials*, 15(10):1957-1962, (2003).

157. X. Huang, S. Neretina and M. A. El-Sayed, "Gold Nanorods: From Synthesis and Properties to Biological and Biomedical Applications," *Advanced Materials*, 21(48):4880-4910, (2009).

158. K. C. Hoang, A. Edris, J. Su, D. S. Mukai, S. Mahon, A. D. Petrov, M. Kern, C. Ashan, Z. Chen, B. J. Tromberg, J. Narula and M. Brenner, "Use of an oxygen-carrying blood substitute to improve intravascular optical coherence tomography imaging," *J Biomed Opt*, 14(3):034028, (2009).

159. M. Naghavi, E. Falk, H. S. Hecht, M. J. Jamieson, S. Kaul, D. Berman, Z. Fayad, M. J. Budoff, J. Rumberger, T. Z. Naqvi, L. J. Shaw, O. Faergeman, J. Cohn, R. Bahr, W. Koenig, J. Demirovic, D. Arking, V. L. M. Herrera, J. Badimon, J. A. Goldstein, Y. Rudy, J. Airaksinen, R. S. Schwartz, W. A. Riley, R. A. Mendes, P. Douglas and P. K. Shah, "From Vulnerable Plaque to Vulnerable Patientâ€"Part III: Executive Summary of the Screening for Heart Attack Prevention and Education (SHAPE) Task Force Report," *The American Journal of Cardiology*, 98(2, Supplement 1):2-15, (2006).

160. S. C. Smith, J. T. Dove, A. K. Jacobs, J. W. Kennedy, D. Kereiakes, M. J. Kern, R. E. Kuntz, J. J. Popma, H. V. Schaff, D. O. Williams, R. J. Gibbons, J. P. Alpert, K. A. Eagle, D. P. Faxon, V. Fuster, T. J. Gardner, G. Gregoratos, R. O. Russell and S. C. Smith, "ACC/AHA Guidelines for Percutaneous Coronary Intervention (Revision of the 1993 PTCA Guidelines)â€"Executive Summary: A Report of the American College of Cardiology/American Heart Association Task Force on Practice Guidelines (Committee to Revise the 1993 Guidelines for Percutaneous Transluminal Coronary Angioplasty) Endorsed by the Society for Cardiac Angiography and Interventions," *Circulation*, 103(24):3019-3041, (2001).

161. D. Yeager, Y. S. Chen, S. Litovsky and S. Emelianov, "Intravascular photoacoustics for image-guidance and temperature monitoring during plasmonic

photothermal therapy of atherosclerotic plaques: a feasibility study," *Theranostics*, 4(1):36-46, (2013).

162. R. H. Clarke, J. M. Isner, R. F. Donaldson and G. Jones, 2nd, "Gas chromatographic-light microscopic correlative analysis of excimer laser photoablation of cardiovascular tissues: evidence for a thermal mechanism," *Circ Res*, 60(3):429-37, (1987).

163. T. G. van Leeuwen, L. van Erven, J. H. Meertens, M. Motamedi, M. J. Post and C. Borst, "Origin of arterial wall dissections induced by pulsed excimer and mid-infrared laser ablation in the pig," *J Am Coll Cardiol*, 19(7):1610-8, (1992).

164. D. R. Holmes, Jr., G. S. Reeder, Z. M. Ghazzal, J. F. Bresnahan, S. B. King, 3rd, M. B. Leon and F. Litvack, "Coronary perforation after excimer laser coronary angioplasty: the Excimer Laser Coronary Angioplasty Registry experience," *J Am Coll Cardiol*, 23(2):330-5, (1994).

165. N. Reifart, M. Vandormael, M. Krajcar, S. Gohring, W. Preusler, F. Schwarz, H. Storger, M. Hofmann, J. Klopper, S. Muller and J. Haase, "Randomized comparison of angioplasty of complex coronary lesions at a single center. Excimer Laser, Rotational Atherectomy, and Balloon Angioplasty Comparison (ERBAC) Study," *Circulation*, 96(1):91-8, (1997).

166. J. M. Brunetaud, S. Mordon, V. Maunoury and C. Beacco, "Non-PDT Uses of lasers in oncology," *Lasers in Medical Science*, 10(1):3-8, (1995).

167. X. Huang and M. A. El-Sayed, "Plasmonic photo-thermal therapy (PPTT)," *Alexandria Journal of Medicine*, 47(1):1-9, (2011).

168. A. N. Kharlamov and J. L. Gabinsky, "Plasmonic photothermic and stem cell therapy of atherosclerotic plaque as a novel nanotool for angioplasty and artery remodeling," *Rejuvenation Res*, 15(2):222-230, (2012).

169. A. N. Kharlamov, A. E. Tyurnina, V. S. Veselova, O. S. Novoselova, A. S. Filatova, O. P. Kovtun, V. Y. Shur and J. L. Gabinsky, "Plasmonics for Treatment of Atherosclerosis: Results of NANOM-FIM Trial," *Nanomedicine & Nanotechnology*, 4(160):doi: 10.4172/2157-7439.1000160, (2013).

170. M. Hayase, K. W. Woodburn, J. Perlroth, R. A. Miller, W. Baumgardner, P. G. Yock and A. Yeung, "Photoangioplasty with local motexafin lutetium delivery reduces macrophages in a rabbit post-balloon injury model," *Cardiovasc Res*, 49(2):449-55, (2001).

171. R. Waksman, P. E. McEwan, T. I. Moore, R. Pakala, F. D. Kolodgie, D. G. Hellinga, R. C. Seabron, S. J. Rychnovsky, J. Vasek, R. W. Scott and R. Virmani, "PhotoPoint photodynamic therapy promotes stabilization of atherosclerotic plaques and inhibits plaque progression," *J Am Coll Cardiol*, 52(12):1024-32, (2008).

172. S. G. Rockson, P. Kramer, M. Razavi, A. Szuba, S. Filardo, P. Fitzgerald, J. P. Cooke, S. Yousuf, A. R. DeVault, M. F. Renschler and D. C. Adelman, "Photoangioplasty for Human Peripheral Atherosclerosis: Results of a Phase I Trial of Photodynamic Therapy With Motexafin Lutetium (Antrin)," *Circulation*, 102(19):2322-2324, (2000).

173. D. J. Kereiakes, A. M. Szyniszewski, D. Wahr, H. C. Herrmann, D. I. Simon, C. Rogers, P. Kramer, W. Shear, A. C. Yeung, K. A. Shunk, T. M. Chou, J. Popma, P. Fitzgerald, T. E. Carroll, D. Forer and D. C. Adelman, "Phase I drug and light dose-escalation trial of motexafin lutetium and far red light activation (phototherapy) in subjects with coronary artery disease undergoing percutaneous coronary intervention and stent deployment: procedural and long-term results," *Circulation*, 108(11):1310-5, (2003).

174. J. Wang, G. Zhu, M. You, E. Song, M. I. Shukoor, K. Zhang, M. B. Altman, Y. Chen, Z. Zhu, C. Z. Huang and W. Tan, "Assembly of Aptamer Switch Probes and Photosensitizer on Gold Nanorods for Targeted Photothermal and Photodynamic Cancer Therapy," *ACS Nano*, 6(6):5070-5077, (2012).

175. D. Yoo, H. Jeong, C. Preihs, J.-s. Choi, T.-H. Shin, J. L. Sessler and J. Cheon, "Double-Effector Nanoparticles: A Synergistic Approach to Apoptotic Hyperthermia," *Angewandte Chemie International Edition*, 51(50):12482-12485, (2012).

176. W.-S. Kuo, C.-N. Chang, Y.-T. Chang, M.-H. Yang, Y.-H. Chien, S.-J. Chen and C.-S. Yeh, "Gold Nanorods in Photodynamic Therapy, as Hyperthermia Agents, and in Near-Infrared Optical Imaging," *Angewandte Chemie International Edition*, 49(15):2711-2715, (2010).

177. W.-S. Kuo, Y.-T. Chang, K.-C. Cho, K.-C. Chiu, C.-H. Lien, C.-S. Yeh and S.-J. Chen, "Gold nanomaterials conjugated with indocyanine green for dual-modality photodynamic and photothermal therapy," *Biomaterials*, 33(11):3270-3278, (2012).

178. B. Jang, J.-Y. Park, C.-H. Tung, I.-H. Kim and Y. Choi, "Gold Nanorod−Photosensitizer Complex for Near-Infrared Fluorescence Imaging and Photodynamic/Photothermal Therapy In Vivo," *ACS Nano*, 5(2):1086-1094, (2011).

179. M. K. Khaing Oo, Y. Yang, Y. Hu, M. Gomez, H. Du and H. Wang, "Gold Nanoparticle-Enhanced and Size-Dependent Generation of Reactive Oxygen Species from Protoporphyrin IX," *ACS Nano*, 6(3):1939-1947, (2012).

180. Y. Zhang, J. Qian, D. Wang, Y. Wang and S. He, "Multifunctional Gold Nanorods with Ultrahigh Stability and Tunability for In Vivo Fluorescence Imaging, SERS Detection, and Photodynamic Therapy," *Angewandte Chemie International Edition*, 52(4):1148-1151, (2013).

181. B. Jain, A. Uppal, P. K. Gupta and K. Das, "Photophysical properties of Chlorin-p6 bound to coated gold nanorods," *Journal of Molecular Structure*, 1032(0):23-28, (2013).

182. J. Wang, M. You, G. Zhu, M. I. Shukoor, Z. Chen, Z. Zhao, M. B. Altman, Q. Yuan, Z. Zhu, Y. Chen, C. Z. Huang and W. Tan, "Photosensitizer–Gold Nanorod Composite for Targeted Multimodal Therapy," *Small*:n/a-n/a, (2013).

183. J. Lin, S. Wang, P. Huang, Z. Wang, S. Chen, G. Niu, W. Li, J. He, D. Cui, G. Lu, X. Chen and Z. Nie, "Photosensitizer-Loaded Gold Vesicles with Strong Plasmonic Coupling Effect for Imaging-Guided Photothermal/Photodynamic Therapy," *ACS Nano*, 7(6):5320-5329, (2013).

184. J.-Y. Kim, W. I. Choi, M. Kim and G. Tae, "Tumor-targeting nanogel that can function independently for both photodynamic and photothermal therapy and its synergy from the procedure of PDT followed by PTT," *Journal of Controlled Release*, (0).

185. J. Oh, H. Yoon and J.-H. Park, "Nanoparticle platforms for combined photothermal and photodynamic therapy," *Biomedical Engineering Letters*, 3(2):67-73, (2013).

Chapter 2: Plasmonic Gold Nanorods as Intravascular Photoacoustic Imaging Contrast Agents[1]

2.1 Motivation for Gold Nanorods as Intravascular Photoacoustic Imaging Contrast Agents

Despite significant advances in preventative measures and interventional procedures, cardiovascular disease remains a leading cause of death within industrialized nations. The high mortality rate can be attributed, in part, to an inability to reliably differentiate atherosclerotic plaques which are prone to rupture [1]. These aptly named 'vulnerable plaques' initiate at sites with a dysfunctional endothelium and progress over the course of years or decades through a sequence of events involving low density lipoprotein (LDL) infiltration, macrophage accumulation, inflammation, and development of a necrotic lipid rich core [2]. The ability to locate atherosclerotic lesions and detect compositional and functional characteristics associated with plaque progression, such as the extent of endothelial dysfunction, can significantly improve the ability to determine lesion vulnerability and therefore provide a tool for clinicians when choosing an appropriate treatment and assessing overall patient risk of suffering a subsequent acute cardiac event.

Current clinical intravascular imaging techniques used for diagnosing atherosclerosis provide a primarily morphological assessment of the vessel. Intravascular imaging modalities such as intravascular ultrasound (IVUS) and optical coherence tomography (OCT) have each been demonstrated to allow differentiation of some

[1] Adapted with permission from D. Yeager, A. Karpiouk, B. Wang, J. Amirian, K. Sokolov, R. Smalling, S. Emelianov, "Intravascular photoacoustic imaging of exogenously labeled atherosclerotic plaque through luminal blood," *Journal of Biomedical Optics*, 17(10), 106016, (2012). Copyright 2012 Society of Photo Optical Instrumentation Engineers. Contribution of the coauthors- A. Karpiouk constructed the integrated imaging catheter, B. Wang developed the image acquisition software algorithms, J. Amirian and R. Smalling provided animal care expertise, K. Sokolov provided expertise related to gold nanoparticles and S. Emelianov provided overall supervision of the research.

relevant tissue types based on variations in their respective backscatter signal intensities [3]. However, each of these imaging techniques has inherent limitations. OCT offers high spatial resolution, on the order of 10 μm, but provides limited penetration depth and the attenuation of blood necessitates its removal via balloon occlusion or saline flushing during image acquisition [4]. IVUS, on the other hand, may be utilized in the presence of luminal blood and offers sufficient penetration depth to image the full vessel thickness, but with a lower spatial resolution and contrast.

Recently, combined intravascular ultrasound (IVUS) and intravascular photoacoustic (IVPA) imaging has been introduced and characterized [5]. Combined IVUS/IVPA imaging provides a means of supplementing morphological information obtained from conventional IVUS with a co-registered assessment of atherosclerotic plaque composition. In photoacoustic imaging, absorption of energy from nanosecond duration optical pulses by endogenous tissue chromophores or exogenous contrast agents result in a local thermal expansion of tissues which subsequently generates a pressure wave that is detected and localized using an ultrasound transducer, as explained in greater detail in Chapter 1, section 1.3. Because the pressure is generated following optical absorption and localized using an ultrasound receiver, photoacoustic imaging is less sensitive to effects of tissue scattering and the resulting loss of optical coherence. As a result, the achievable penetration depth of photoacoustic imaging is significantly greater than conventional optical techniques. Furthermore, in the case of IVPA imaging, the contrast between different tissue components is partially dictated by differences in their wavelength-dependent optical absorption. The optical contrast enables differentiation of composition based on unique spectral characteristics of tissues or exogenous contrast agents within plaques [6,7]. Therefore, combined IVUS/IVPA imaging preserves the

ability of conventional IVUS to image the full arterial wall thickness while improving the ability to differentiate plaque composition.

To date, IVUS/IVPA has been heavily investigated for the detection of lipid-rich regions within atherosclerotic plaques [8-14] and, to a lesser extent, for the guidance and monitoring of stent placement [15,16], and the detection of intra-plaque macrophages labeled with spherical gold nanoparticles [17,18]. In the case of detecting the nanoparticle contrast agents, spectroscopic IVPA (sIVPA) imaging was utilized as a means of better differentiating the unique optical absorption spectra of the contrast agents from background tissue. While the labeling of plaque biomarkers with spherical gold nanoparticles, followed by IVUS/IVPA imaging offers the potential for cellular and molecular imaging of atherosclerosis, detection of such contrast agents has not been demonstrated in the presence of luminal blood due to their peak optical absorption occurring within a wavelength region where endogenous tissues, particularly oxygenated hemoglobin, exhibit high optical attenuation and therefore reduce the achievable signal to noise ratio. Modification of the optical absorption properties of delivered exogenous contrast agents to enable imaging through blood is desirable because it avoids the need for blood removal through the use of an occluding balloon or saline flush during imaging, a procedure which limits image acquisition time and increases the risk of ischemia and pulmonary edema [4].

This chapter focuses on the extension of the use of exogenous contrast agents for IVUS/IVPA imaging to polyethylene glycol (PEG) stabilized gold nanorods (AuNR) with a longitudinal peak absorbance tuned to the near infrared (NIR) wavelength region where blood and endogenous tissues exhibit reduced optical absorption. The conjugation of PEG to the AuNR is commonly used as a means of increasing circulation time, reducing cytotoxicity, and preventing aggregation of the nanoparticles [19]. Several

groups have recently explored the potential of AuNR as exogenous contrast agents for photoacoustic imaging [20-22]. The current study aims to extend these uses of AuNR to include verification of their selective labeling of atherosclerotic plaque following systemic injection, enabling subsequent detection using combined IVUS/IVPA imaging.

The goal of this chapter is to introduce AuNR as IVPA contrast agents for labeling atherosclerotic plaque macrophages, including the demonstration that systemically-injected AuNR preferentially extravasate at sites of atherosclerotic plaque endothelial dysfunction and macrophage accumulation in rabbit models of atherosclerosis. Subsequently, the high optical absorption of AuNRs within the tissue optical window is utilized to evaluate the ability to detect AuNRs within atherosclerotic plaques in the presence of luminal saline and luminal blood using both single-wavelength and sIVPA imaging. The use of sIVPA, similar to prior work using spherical gold nanoparticle contrast agents, is implemented as a means of differentiating the AuNRs from background tissues. In addition, the use of single-wavelength IVPA imaging at the peak absorption of the AuNRs is also evaluated as a simplified imaging approach, capitalizing on the use of a contrast agent which strongly absorbs within the NIR region in which tissue produces a decreased background signal.

2.2. CHARACTERIZATION OF GOLD NANORODS AS IVPA IMAGING CONTRAST AGENTS

2.2.1. Gold Nanoparticle Synthesis and Characterization

Cetyltrimethylammonium bromide (CTAB) stabilized AuNRs with an aspect ratio of approximately 3.5 were prepared using a seed mediated growth method [23]. Briefly, a growth solution was prepared by adding 800 μL of $AgNO_3$ (10 mM) and 4 mL $HAuCl_4$ (10 mM) to 38 mL of CTAB (200 mM, Avocado Research Chemicals) at

30°C and stirring at 500 rpm. A solution of 440 μL of ascorbic acid was then added to the growth solution, resulting in a color change from yellow-orange to colorless solution. A seed solution was also prepared, consisting of 500 μL of CTAB (200 mM) and 500 μL of $HAuCl_4$ (0.5 mM) at 30°C. The seed solution was vigorously stirred and 60 μL of NaBH4 (10 mM) was added, inducing a colorless to brown color change. After 7 minutes of aging, 96 μL of the seed solution was added to the entire volume of the growth solution. The CTAB-AuNR were allowed to age over night at 30°C before being twice washed to remove excess CTAB via centrifugation at 18,000 rcf for 40 minutes. The washed CTAB-AuNR were re-suspended in deionized water at a final peak optical density (OD) of 15, as measured by UV-Vis spectroscopy (Synergy HT, BioTek).

The CTAB was replaced with polyethylene glycol (5kD mPEG-SH, Creative PEGWorks) by adding equal volumes of mPEG-thiol (0.2 mM) and the OD 15 CTAB-AUNR [24]. The mixture was sonicated for 10 minutes and allowed to react for four hours on a shaker under modest agitation. The resulting PEG-AuNR were twice washed via centrifuge filtration (Amicon ultra-15, Millipore, 100 kD) for 10 min at 3000 rcf and re-suspended in sterile phosphate buffered saline (PBS) at physiological pH. Figure 2.1A shows the normalized extinction of AuNR as prepared (blue), washed (red) and following the exchange of CTAB with PEG (green). A representative transmission electron microscopy (TEM, Tecnai) image of PEG-AuNR is also provided (Fig. 2.1B), revealing no signs of nanoparticle aggregation. Zeta potential measurements (DelsaNano C, Beckman Coulter) of the nanoparticles' surface charge were also used to further verify the exchange of CTAB with PEG on the AuNR surface. Typical measurements of CTAB-AuNR and PEG-AuNR were approximately +22.5 mV and -8.75 mV, respectively.

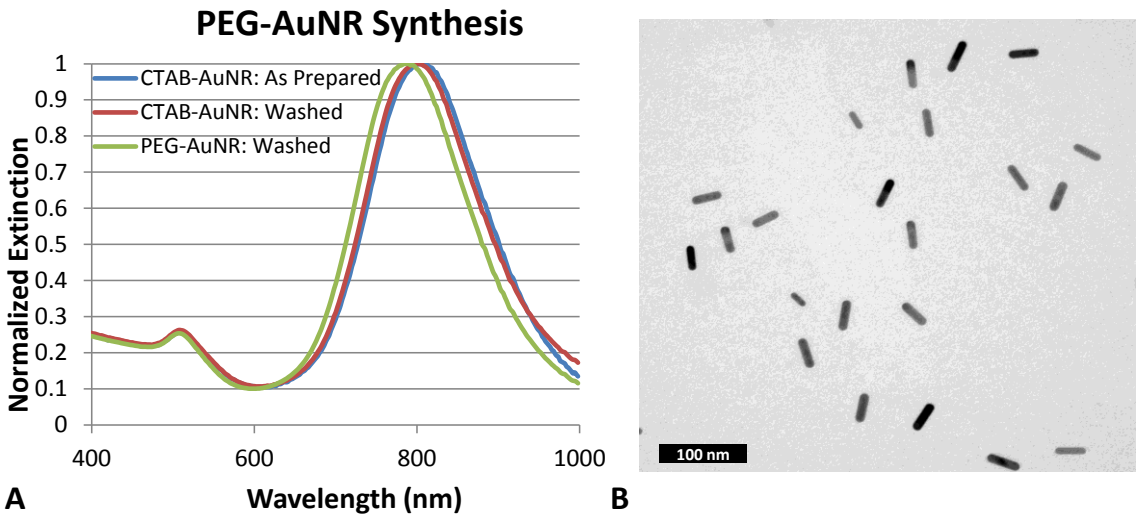

Figure 2.1: AuNR characterization. (A) Extinction coefficient of AuNR as prepared (blue), washed (red) and PEGylated (green). (B) Representative TEM image of PEG-AuNR. Scale bar = 100 nm.

2.2.2. *In Vitro* Nanoparticle Uptake and Toxicity

In vitro studies were performed to investigate the ability of macrophage cells to phagocytose PEG-AuNR and to evaluate subsequent toxicity, both with and without exposure of nanoparticle-labeled cells to the pulsed laser illumination required for IVPA imaging. First, J774A.1 murine macrophages were plated on a 96 well plate at a concentration of 1 x 10^4 cells per well in 100 µL of phenol-red free Dulbecco's Modified eagle's Medium (DMEM, ATCC) with 5% Fetal Bovine Serum and allowed to incubate for 24 hours at 37 °C and 5% CO_2. The culture medium was then changed and an additional 10 µL of variable concentrations of sterilized PEG-AuNR were added to the cells, ranging from control cells without nanoparticles to AuNR which yielded an optical density of ten when dispersed with the macrophages. In total, wells containing macrophages with PEG-AuNR optical densities of: 0, 0.1, 0.2, 0.3, 0.4, 0.5, 0.75, 1.0, 1.5, 2.0, 3.0, 5.0, and 10.0 were created in triplicate, representing a range of approximately 20

pM to 2 nM AuNR, or 10^4 to 10^6 AuNR per cell. The cells were incubated at 37 °C and 5% CO_2 for 24 hours, after which all cells were carefully washed with phosphate buffered saline (PBS) three times, followed addition of 100 µL of fresh culture media and further incubation of the cells for another 6 hours. The UV-Vis (Synergy HT, Biotek) optical extinction spectrum of the nanoparticle-labeled cells was then measured, and a single-step colorimetric cell viability assay was initiated by adding 20 µL of 3-(4,5-dimethylthiazol-2-yl)-5-(3-carboxymethoxyphenyl)-2-(4-sulfophenyl)-2H-tetrazolium (MTS). The assay was allowed to progress for three hours, over which time the dye was reduced by an active cellular process to yield a proportional increase in optical absorbance at 490 nm, which was subsequently measured using the UV-Vis. Figure 2.2 shows the relative viability of macrophages incubated with each of the different concentrations of PEG-AuNR (Fig. 2.2A) and representative extinction spectra of PEG-AuNR labeled macrophages (Fig. 2.2B). No statistically significant change in any of the groups of PEG-AuNR labeled macrophages was measured. Furthermore, macrophages incubated with optical densities of 1.0 and greater PEG-AuNR were detected by the UV-Vis spectrum.

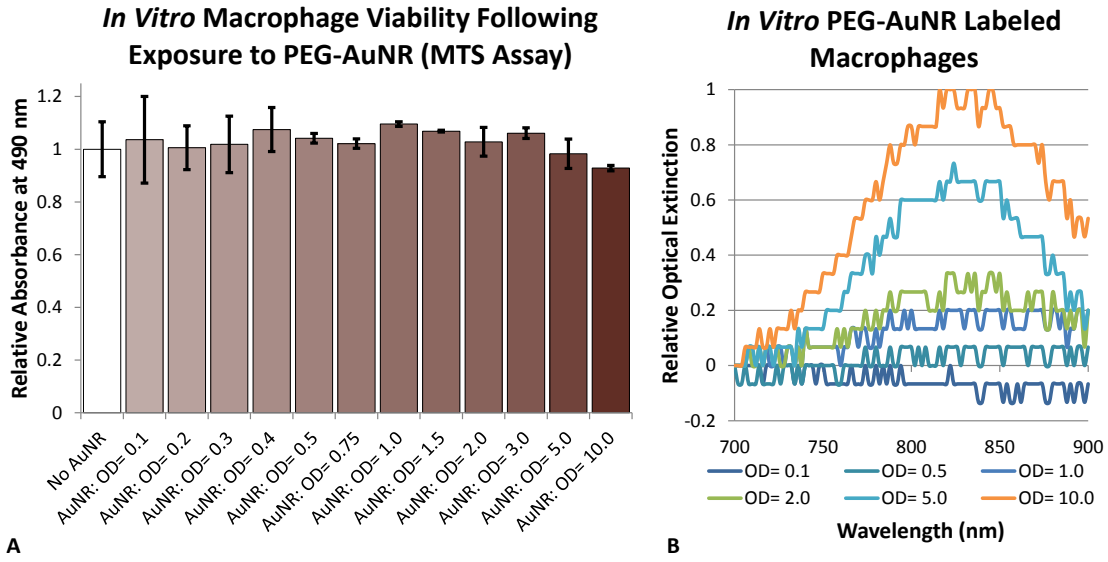

Figure 2.2: *In vitro* PEG-AuNR labeling and subsequent viability of macrophages. (A) MTS Assay viability of macrophages following incubation with variable concentrations of PEG-AuNR. (B) Representative optical extinction of macrophages incubated with variable concentration of PEG-AuNR after a 3x PBS wash.

A parallel study was also performed in which macrophages were incubated without nanoparticles (negative control) or with PEG-AuNR at an optical density of 5.0 for 24 hours before being harvested and fixed in 10% formalin. The diluted sampled of the fixed macrophages were then placed on a microscope slide and imaged using dark field microscopy (DM6000, Leica), revealing the presence of PEG-AuNR in the experimental group based on increased scattering of nanoparticle labeled cells (Figure 2.3).

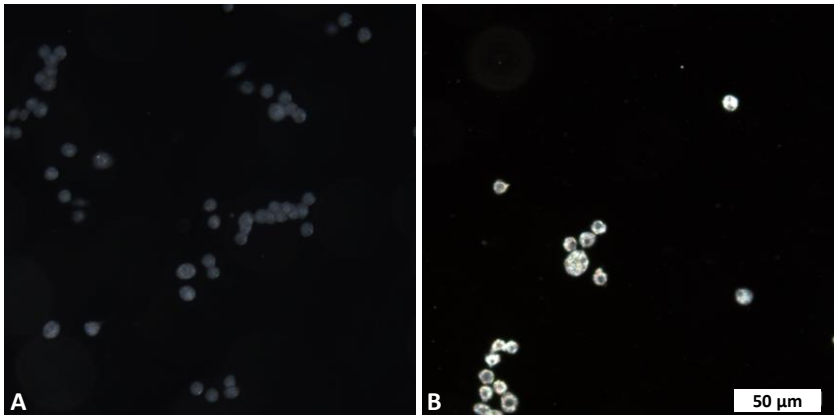

Figure 2.3: Darkfield microscopy of J774A.1 murine macrophages (A) without and (B) with PEG-AuNR. Scale bar = 50 µm.

Assessment of AuNR labeled macrophage viability was further expanded to the investigation of potential effects of the nanosecond pulsed illumination which is required for IVPA imaging. Using the same experimental procedure for the MTS viability assay, cells were incubated with PEG-AuNR at optical densities of 2.0 and 5.0. After washing excess nanoparticles, the cells were illuminated with variable intensity nanosecond pulsed laser illumination for 200 pulses (20 seconds) using the same laser source and optical fiber setup designed for IVPA imaging, described in detail in Section 2.3. The cells were then incubated for an additional 6 hours prior to initializing the MTS assay. Figure 2.4 shows the relative viability of the PEG-AuNR labeled macrophages following pulsed laser illumination, revealing no statistically significant decline in viability across any of the groups. Representative bright field microscopy images of control cells without nanoparticles, and following incubation with optical density 2.0 and 5.0 are also provided in Figure 2.4B-D, respectively.

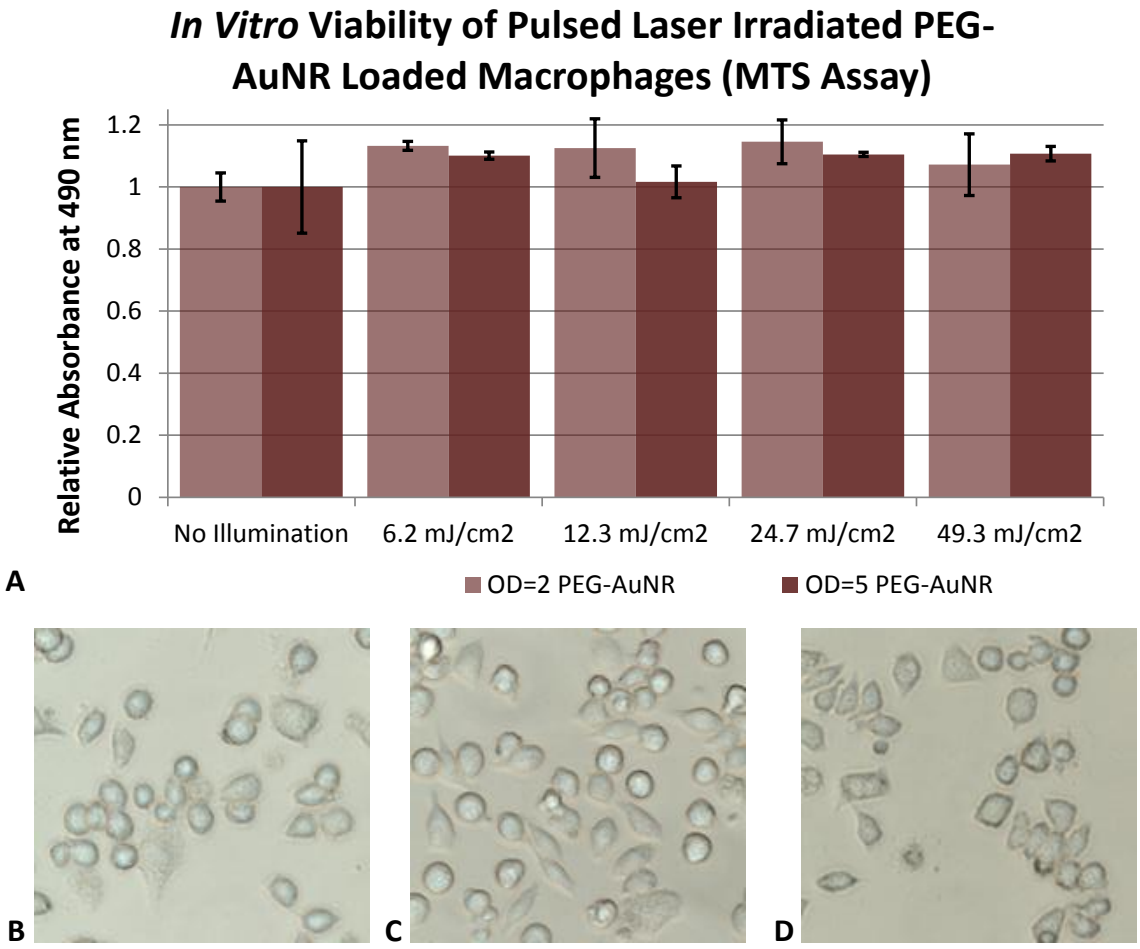

Figure 2.4: *In vitro* viability of PEG-AuNR labeled macrophages following exposure to IVPA laser irradiation at variable intensity. (A) MTS assay as a function of laser fluence. (B-D) Representative microscopy images of macrophages with increasing PEG-AuNR labeling (40x).

2.3. IVUS/IVPA IMAGING: EXPERIMENTAL SETUP AND IMAGE PROCESSING ALGORITHMS

2.3.1. IVUS/IVPA Imaging Setup

A schematic diagram of the imaging setup used for IVUS/IVPA imaging with a previously reported integrated catheter is provided in Figure 2.5. The output of a tunable OPO laser (SpectraPhysics Inc.) capable of producing 5 ns pulses at 10 Hz with a spectral bandwidth of 2-3 nm at NIR wavelengths was coupled to an optical fiber with a core diameter of 600 μm [25]. The distal tip of the optical fiber was polished at an angle (approximately 40°) and positioned within a gas-trapping cup to produce side-projecting illumination and this distal housing was coupled to a commercially available, single element 40 MHz IVUS imaging catheter (Boston Scientific Inc.), resulting in overlapping ultrasound and optical beams within the aorta lumen. With each laser pulse, the radio frequency IVPA signals were collected using the IVUS imaging catheter and digitized using a 14 bit data acquisition (DAQ) card with a sampling rate of 200 MHz (CompuScope 14200, GaGe Applied Technologies, Inc.). Following the triggering of each optical pulse, a user-defined delay of 9 μs was implemented (DPR-2515, Directed Energy, Inc.) after which an ultrasound pulser-receiver (5073PR, Panametrics-NDT, Inc.) was triggered to transmit an ultrasound pulse and subsequent receiving of an echo signal by the IVUS transducer. The resulting acquired data was composed of spatially co-registered and temporally consecutive IVPA and IVUS signals in R-theta coordinates. A temporal separation was therefore utilized to isolate the IVPA and IVUS components of the signal. Furthermore, because IVPA imaging involves only one way travel of ultrasound, whereas IVUS signal represent a round-trip travel, the IVPA signal must be stretched by a factor of two using an interpolation algorithm to obtain spatially matched

IVUS/IVPA images. The IVUS/IVPA data was then band-pass filtered, and envelope detected using a Hilbert transform to base-band the raw IVUS and IVPA signals.

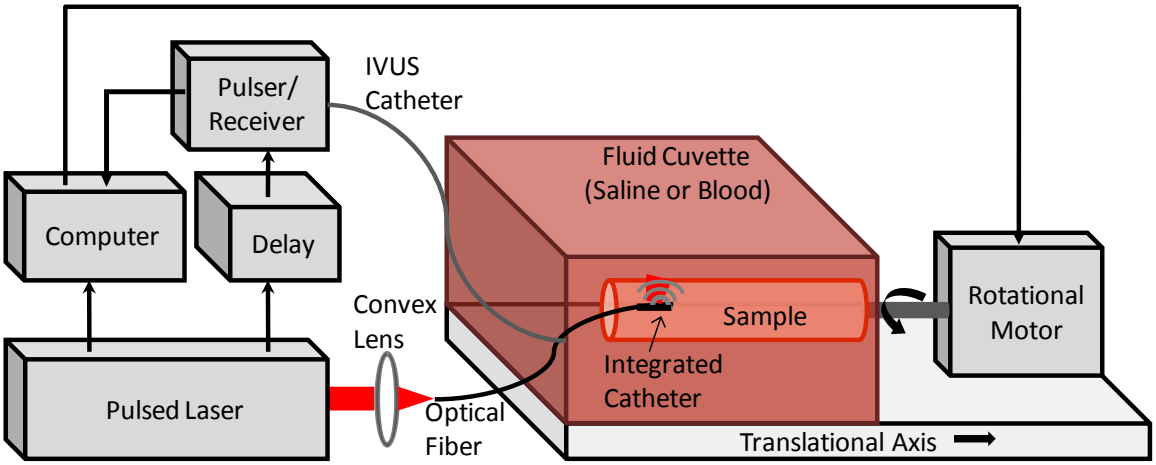

Figure 2.5: Schematic representation of experimental setup for spatially co-registered ultrasound and photoacoustic imaging of ex vivo arterial samples using an integrated IVUS/IVPA catheter.

The aorta or arterial phantom sample, placed in a cuvette filled with either saline or blood, was secured to rotational and translational stepper-motors (T-LSR150A, Zaber, Inc.), allowing for generation of cross-sectional 2D images and 3D pullback images, respectively. Each 2D image consisted of 256 spatially co-registered IVUS/IVPA A-lines per rotation of the aorta sample. Four A-lines were averaged at each position prior to rotation. In the case of 3D pullback data acquisition, a rotation was performed to generate a 2D cross sectional image, followed by translation of the aorta with a step size of 500 μm. The R-theta IVUS and IVPA data was scan converted from polar to Cartesian coordinates using an interpolation algorithm prior to image display in order to provide conventional cross-sectional views of the image target.

The *ex vivo* imaging setup allowed for imaging though saline as well as through blood. For imaging performed through blood, human hematocrit (The Blood Center of

Central Texas, Austin, TX) was diluted back to the physiological concentration based on a packed cell volume of approximately 40 percent using saline. Additionally, in the case of 3D IVUS/IVPA imaging through blood, a centrifugal fluid pump was incorporated with the outlet aligned to produce continuous luminal blood flow through the aorta section to reduce ultrasound speckle from blood stasis.

2.3.2. Image Processing Algorithms

Prior to each experiment, the output energy of the illumination fiber was calibrated by adjusting the Q-switch delay to maintain an equal energy at each wavelength to be used for imaging. A beam splitter was positioned proximal to the fiber coupler to deflect a portion of the beam to a power meter (Ophir Optronics Ltd). A look-up table was generated to relate the distal output energy to the measured energy at the position of the power meter. Due to the proportional relationship between local fluence and photoacoustic pressure, variations in the laser output energy can significantly impact the detected IVPA signal. During imaging, the energy of each pulse was recorded and subsequently used to normalize the IVPA signal to account for variation in illumination intensity.

Following normalization for pulse-to-pulse energy variations, IVPA signals over a fixed distance from the integrated catheter were masked-out (i.e. set to zero) to eliminate the effect of ringdown artifacts produced by direct excitation of the IVUS transducer by optical pulse reflected and scattered from tissues. Additionally, the intensity of each spatially co-registered IVUS image was used to generate a binary mask of the arterial wall where regions prior to and beyond the arterial wall were set to zero. This binary mask was then applied to the spatially co-registered IVPA signal to eliminate photoacoustic signal artifacts and signals from non-tissue (e.g., tissue holder) structures

associated with the experimental setup. In the case of imaging through blood, depth dependent fluence attenuation compensation was performed by assuming a Beer's law attenuation of the illumination intensity with the appropriate wavelength dependent extinction coefficient of the reconstituted human blood, which was measured with the UV-VIS spectrophotometer prior to IVUS/IVPA imaging. A user-defined noise floor was then established for all IVPA images, below which signals were ignored for subsequent signal processing steps. Finally, the IVUS and IVPA signals were scan converted from polar to Cartesian coordinates to obtain the cross sectional images of the aorta, and, in the case of 3D pullbacks, the serial cross sections were displayed as a volume rendered image stack.

In addition to single-wavelength imaging at the peak absorption of the AuNRs, imaging of sample arterial cross sections was also performed at multiple wavelengths to enable a sIVPA imaging in order to differentiate IVPA signal which originated from AuNRs from those originating from endogenous absorbers or ringdown artifacts. For a given cross section, sIVPA imaging was performed by obtaining IVPA signals from 730 - 830 nm wavelength in 20 nm increments. A constant optical energy was maintained across all wavelengths by adjusting the laser Q-switch delay. More specifically, prior to imaging, a look up table was created to establish the appropriate delay need to maintain constant optical output across the desired wavelengths. Furthermore, during imaging, the recorded energy of each pulse was also monitored to verify that the output energy remained constant during sIVPA imaging. The IVPA signals were processed as described above, with an identical noise floor selected across all wavelengths. Prior to scan conversion, the IVPA signals at each pixel of the cross sectional image were then normalized as a function of wavelength and compared to normalized reference spectra of known absorbers suspected within the intravascular environment. The reference spectra

considered included the extinction spectrum of the AuNRs isolated from blood at the time of animal sacrifice, the absorbance spectrum oxygenated hemoglobin, and an artificial uniform spectrum. Figure 2.6A and Figure 2.6B provide a graphical representation of the reference spectra and schematic representation of the IVPA data utilized for sIVPA analysis, respectively. The uniform spectrum was intended to account for IVPA signals which may have originated from artifacts such as ultrasound transducer ringdown or increased subsurface fluence at tissue boundaries or air bubbles within the fluid filled tank. These artifacts are expected to yield wavelength-independent IVPA signals over the wavelength range of interest.

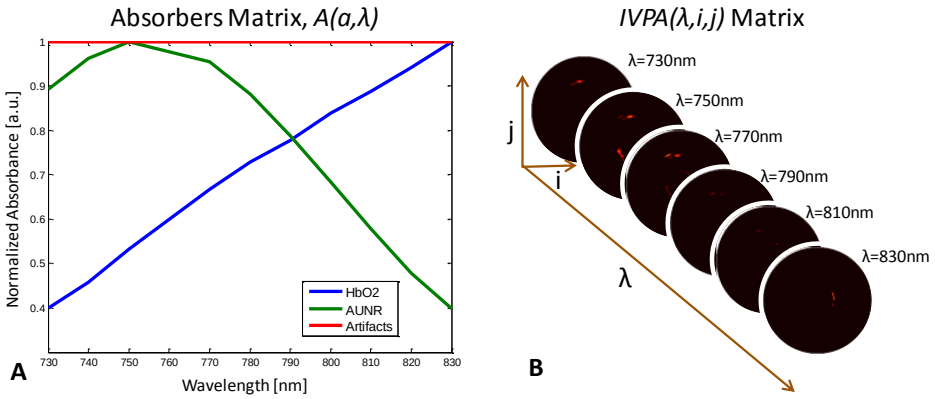

Figure 2.6: Overview of spectroscopic IVPA (sIVPA) image processing system of equations. The absorption spectra of the three reference absorbers were normalized with respect to wavelength, (A) and the acquired IVPA signal intensity as a function of position and wavelength (B) was utilized to determine the relative concentration of each reference absorber at each position using a linear least squares algorithm.

A linear least squares algorithm was then utilized to calculate the relative concentrations of the three reference absorbers (AuNRs, oxygenated hemoglobin and artifacts) at each position within the sIVPA image. More specifically, the least squares algorithm is intended to solve for Equation 2.1, where the matrix A is composed of the

wavelengths dependent, normalized absorption coefficients of each of the three reference absorbers, IVPA(λ,i,j) is a three dimensional matrix composed of the obtained IVPA signals as a function of wavelength (⌊) and position (i,j), and C(a,i,j) represents a matrix of unknown relative concentrations of the references absorbers (a) as a function of position, where 0≤C≤1. The unknown relative concentrations C(a,i,j) for the three reference absorbers is obtained by minimizing the squared residuals as expressed in Equation 2.2. After computing the matrix C, a relative correlation 0.6 or greater was selected as a threshold for identifying and displaying a pixel containing a particular absorber (e.g. AuNRs).

$$\boldsymbol{C(a,i,j) \times A(a,\lambda) = IVPA(\lambda,i,j)} \quad \text{Eq. 2.1}$$

$$\boldsymbol{\min \| C(a,i,j) \times A(a,\lambda) - IVPA(\lambda,i,j) \|_2^2} \quad \text{Eq. 2.2}$$

2.4 IVUS/IVPA IMAGING OF AUNR-LABELED ATHEROSCLEROTIC ARTERIES FOLLOWING SYSTEMIC INJECTION

2.4.1. Animal Models of Atherosclerosis

Two distinct rabbit models of atherosclerosis were utilized for this study. For the first model, a New Zealand white (NZW) rabbit was fed a high cholesterol (0.5%) chow diet for 25 days prior to being subjected to balloon injury within the thoracic aorta in order to induce endothelial denudation and inflammation. Following the balloon injury procedure, the rabbit was continued on the high cholesterol chow diet for an additional 8 months prior to nanoparticle injection and *ex vivo* imaging. The second atherosclerotic animal model utilized the Watanabe heritable hyperlipidemic (WHHL) rabbit. Due to a deficiency of low density lipoprotein receptors, WHHL rabbits develop

hypercholesterolemia and advanced atherosclerotic lesions on a normal chow diet over the course of one to two years [26].

2.4.2. Validation of *In Vivo* AuNR-Labeling of Atherosclerotic Plaques

PEG-AuNRs (100 mg, O.D. 200) were injected into the rabbit ear vein and allowed to circulate for 26 hours, after which the animal was sacrificed and the aorta was harvested for *ex vivo* imaging. At the time of sacrifice, a blood sample was also taken to determine the absorption spectra of the PEG-AuNRs in order to determine the wavelength of peak absorption for IVPA imaging. Specifically, 5 mL of blood were centrifuged at 1000g for 5 minutes and the extinction spectrum of the plasma was measured using a spectrophotometer (BioTek). Figure 2.7 shows the normalized extinction spectra of as prepared CTAB stabilized AuNRs (dotted line), following replacement of the CTAB with mPEG-SH and re-suspension in PBS (dash-dotted line), and AuNRs isolated from the blood of a systemically injected atherosclerotic rabbit at the time of animal sacrifice (solid line). AuNRs isolated at the time of animal sacrifice show a 20 nm blue shift of the longitudinal absorbance peak relative to the spectrum obtained prior to injection as well as an increased background signal, particularly affecting the transverse peak.

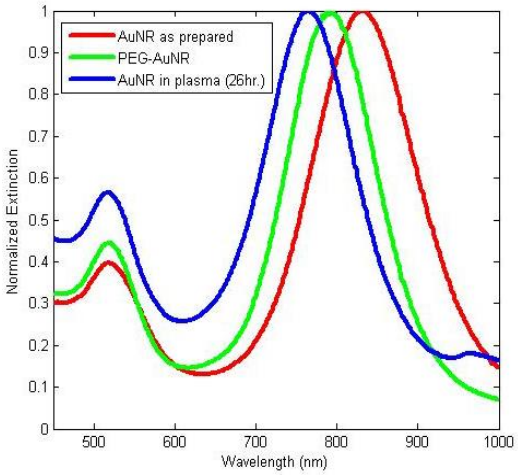

Figure 2.7: Extinction spectra of systemically-injected particles as prepared (red), after conjugation of PEG (green), and isolated from blood following rabbit sacrifice (blue).

The excised aorta was maintained at 4°C wrapped in saline-dampened gauze to allow imaging of fresh, unfrozen, tissue for up to 48 hours following euthanization of the animals. After imaging, the tissue was fixed in 10% formaldehyde to allow for histological analysis and additional imaging of fixed tissue.

Combined IVUS/IVPA imaging was performed on atherosclerotic rabbit aortas subjected to systemic injection of PEG-AuNR contrast agents approximately 26 hours prior to excision of the arteries for *ex vivo* imaging. Results from both a balloon injured NZW rabbit and WHHL rabbit are presented. A representative cross section of the aorta from the balloon injured NZW rabbit model is shown in Figure 2.8. Immunohistological staining and dark field microscopy images of unstained samples were utilized to evaluate the specificity of AuNR labeling to atherosclerotic plaques. H&E stain shows the presence of an atherosclerotic plaque in the region spanning from 2 o'clock to 10 o'clock (Fig. 2.8A). Anti-CD31 stains specific for platelet endothelial cell adhesion molecule

(PECAM-1), a ligand expressed by endothelial cells, macrophage, and platelets are provided in Figure 2.8B and 2.8C as an assessment of the arterial endothelial layer integrity. RAM11, a mouse monoclonal anti-rabbit macrophage antibody stain, reveals the presence of macrophages near the luminal surface of the plaque (Fig. 2.8D). Additionally, silver stain histology, used to identify the presence of heavy metals, further indicated the presence of AuNRs near the luminal boundary of the plaque region in agreement with the distribution of macrophages (Fig. 2.8E). Furthermore, dark field microscopy revealed the lack of a healthy endothelial layer at the luminal boundary in plaque regions where AuNRs were present (Fig. 2.8F).

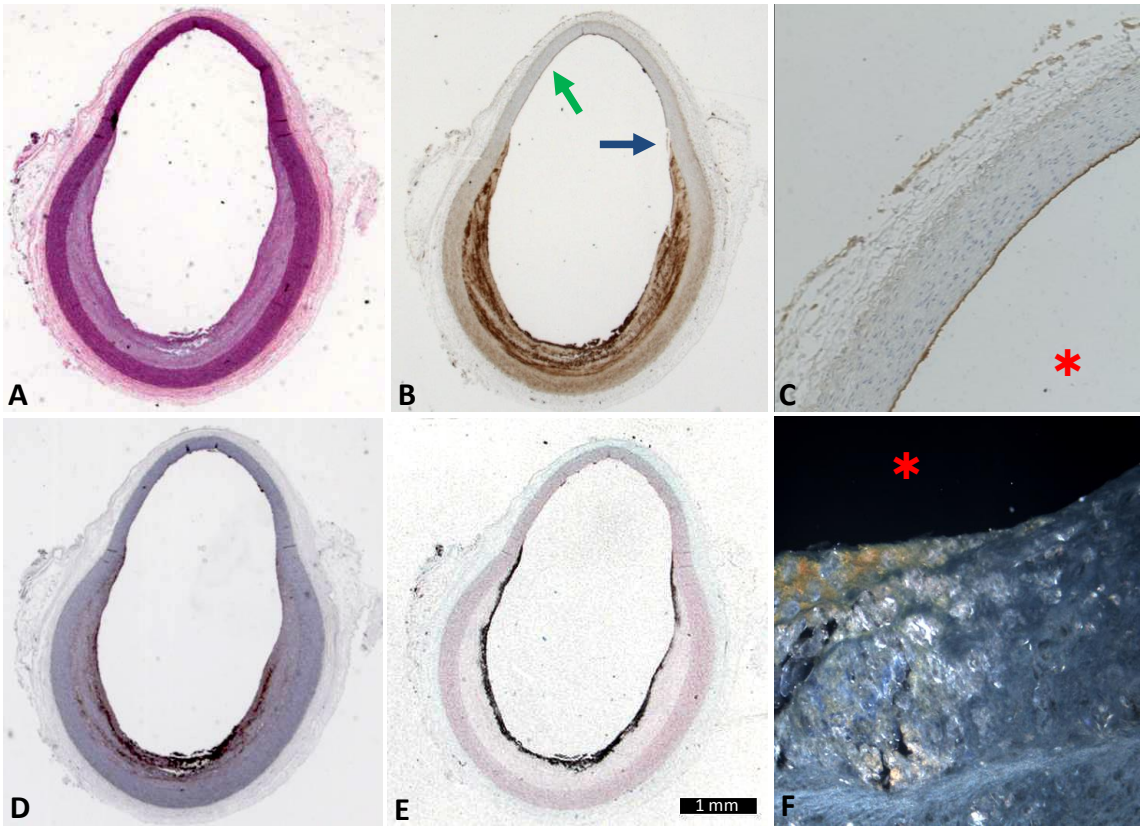

Figure 2.8: Evaluation of AuNR labeling of atherosclerotic plaque. Histological staining of adjacent cross sections using (A) H&E stain, (B) CD31 stain, (C) High resolution (10x) view of the CD31 stain of healthy region of arterial wall indicated by green arrow, (D) Macrophage-specific RAM11 stain, (E) Silver stain for labeling AuNR distribution. (F) High resolution (20x) dark field microscopy image of an unstained artery section revealing AuNRs (gold color) at the luminal boundary at the edge of a plaque which lacks a healthy endothelium, indicated by blue arrow. The asterisk (*) indicates arterial lumen.

2.4.3. *Ex Vivo* IVUS/IVPA Imaging of AuNR Labeled Atherosclerotic Plaque

Combined IVUS/IVPA imaging was performed on AuNRs-labeled atherosclerotic artery sections in the presence of both luminal saline and luminal blood using the *ex vivo* imaging setup schematically shown in Figure 2.5. IVPA and sIVPA images obtained from a sample cross-section of a freshly-excised WHHL aorta which was imaged in both

saline and blood at 750 nm with output energy of 0.5 mJ are shown in Figure 2.9. All IVUS/IVPA images displayed in Figure 2.9 represent a total diameter of 22.5 mm and the optical path length from the integrated IVUS/IVPA catheter to the luminal boundary was measured to range from approximately 2.5 mm to 5.5 mm. IVPA images are displayed using a 20 dB dynamic range scale (Fig. 2.9A,B). Silver stain histology from the corresponding cross-section is shown in Figure 2.9C. Combined IVUS/sIVPA images display the IVUS signal using a 40 dB dynamic range scale with the regions of spectroscopically detected AuNRs overlaid in green (Fig. 2.9D,E). Examples of spectroscopic IVPA plots for signals determined to arise from oxygenated hemoglobin (HbO_2) and AuNRs when imaging through saline and a region identified as containing AuNRs through blood are shown in Figure 2.9F with the corresponding reference spectra. Errors bars in Figure 2.9F represent the standard deviation of IVPA signal intensity calculated using a kernel size of approximately 4.5º azimuthal by 55 μm axial. The plotted spectroscopic response for the AuNR samples was taken from a point near the luminal border at approximately 9 o'clock where the images obtained through both saline and blood show a strong IVPA signal. Contrarily, the sample HbO_2 spectroscopic signal was taken from the region in the adventitia at approximately 12 o'clock which was identified as HbO_2 by the sIVPA analysis when imaging through saline. Comparison of the single wavelength IVPA and sIVPA signals are in agreement with one another for each imaging environment, saline and blood, as well as with the corresponding silver stain histology (Fig. 2.9C). Upon evaluation of the 2D cross-section, the IVPA signals obtained at the AuNRs' peak absorbance wavelength (750 nm) show similarly high photoacoustic signals at the three o'clock and nine o'clock positions near the position of the arterial wall, which correlate with AuNR accumulation as identified by the silver stain histology image. However, the twelve o'clock position of the IVPA image obtained

through blood does not reveal the high intensity signal seen in the case of imaging through luminal saline, and identified as a region with AuNR accumulation in the silver stain histology section. Additionally, the signal-to-noise ratio (SNR) of the image obtained through blood is noticeably reduced in the case of imaging through luminal blood at the same optical fluence. As an example, the SNR of the 9 o'clock region of the IVPA images acquired using at 750 nm through saline and blood were calculated to be approximately 28 dB and 24 dB, respectively.

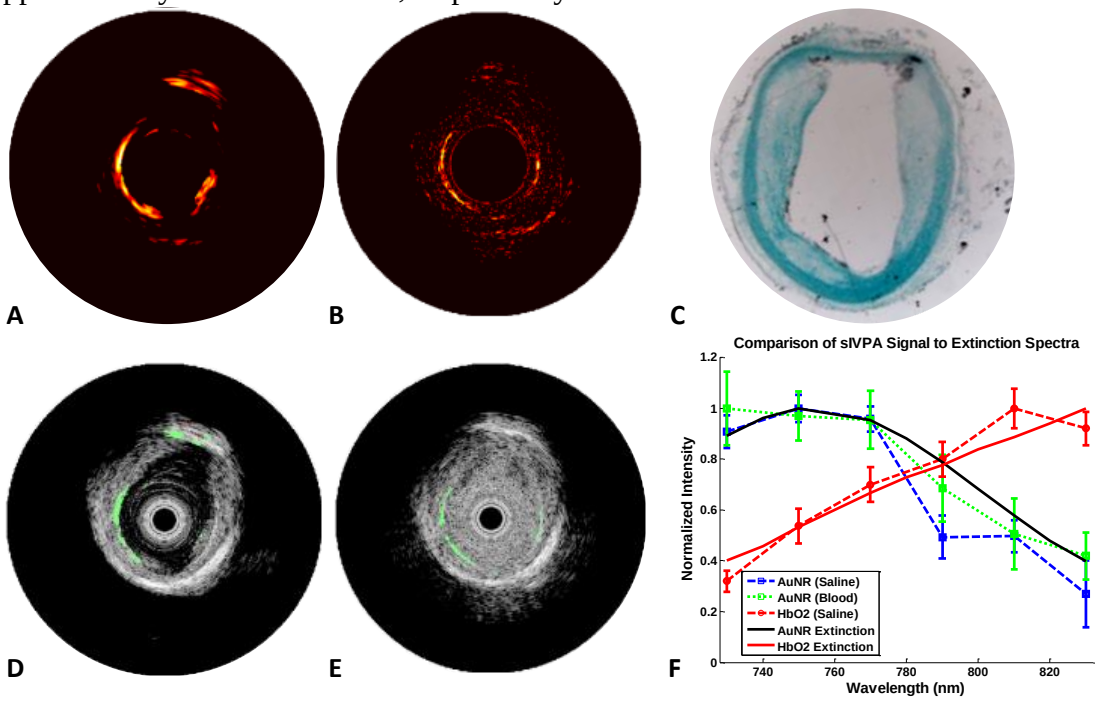

Figure 2.9: Intravascular photoacoustic imaging of AuNR labeled atherosclerotic plaque cross section (color online). A,B) IVPA signal obtained from imaging at the AuNRs peak absorbance wavelength through saline and blood, respectively. IVPA images displayed with -20 dB dynamic range. C) Corresponding silver stain histology revealing distribution of AuNRs within the plaque. D,E) Intravascular ultrasound images (40 dB display dynamic range) with overlay of spectroscopic detection of AuNRs through saline and blood, respectively. F) Comparison of representative spectroscopic IVPA signals, shown as dashed lines, to normalized extinction spectra of AuNRs and oxygenated hemoglobin (HbO_2), shown as solid lines.

Due to the high acoustic backscatter detected in the case of imaging through static luminal blood (Fig. 2.9E), a centrifugal blood pump was incorporated into the *ex vivo* imaging setup. The pump was aligned to produce a continuous luminal blood flow during 3 dimensional data acquisition. IVUS images of an arterial cross section obtained through static blood (Fig. 2.10A) and luminal blood flowing at a rate of 100 mL/min (Fig. 2.10B) clearly demonstrate a reduction in acoustic scattering produced by flowing blood.

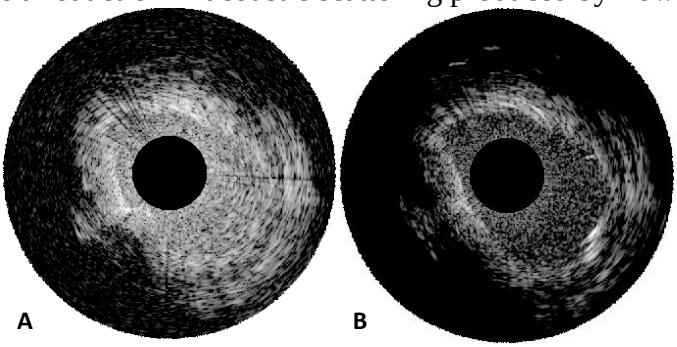

Figure 2.10: IVUS images of an atherosclerotic artery obtained through (A) static and (B) flowing luminal blood. Both images are shown using a 35 dB display dynamic range.

Fixed sections of a balloon injured New Zealand white rabbit aorta were subsequently imaged using the integrated IVUS/IVPA catheter. For all combined IVUS/IVPA 3D renderings shown in Figure 2.11, imaging was performed at the AuNRs' peak absorbance wavelength by obtaining full serial cross sections with a step size of 500 μm. In reconstructing a continuous rendered volume, the combined images were cropped to create a hemispherical view showing the morphology and AuNR distribution within a section of the arterial lumen. A hemispherical view of the IVUS/IVPA signal obtained from imaging an 8 mm arterial section with 0.7 mJ output energy in the presence of saline within the lumen is provided in Figure 2.11A. Following imaging, a digital photograph of the imaged cross section was obtained, revealing the presence and

distribution of regions with a high density of AuNRs at the lumen surface, evident by the red color (Fig. 2.11B). AuNRs visible in the digital photograph are in spatial agreement with regions which provided high signal intensity upon IVPA imaging at the AuNR peak absorbance wavelength. A separate arterial section was then imaged in both saline and blood to further evaluate the potential to detect the AuNRs in the presence of luminal blood using a single optical wavelength. A 6 mm section of the artery was first imaged using the integrated catheter in saline with 0.7 mJ output energy (Fig. 2.11C). The saline was then replaced with the reconstituted human blood, which was pumped through the aorta lumen, and the same cross section was again imaged at the peak wavelength, but with output energy of 1.4 mJ (Fig. 2.11D). The similarities of localized IVPA signals obtained through saline and through blood suggest that the AuNRs can be detected through blood.

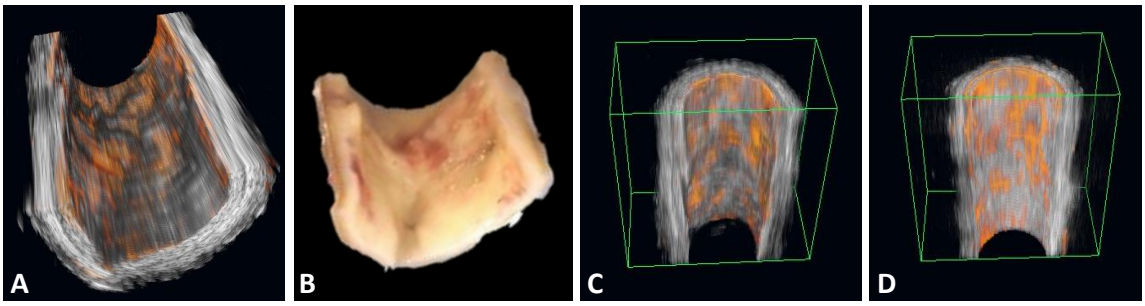

Figure 2.11: Three dimensional IVUS/IVPA renderings of AuNR labeled atherosclerotic plaque (color online). (A) Combined IVUS/IVPA rendering of an 8 mm long section of atherosclerotic rabbit artery obtained through saline. (B) Photograph of the corresponding artery section revealing AuNR distribution at the luminal surface (red). Combined IVUS/IVPA images obtained through saline (C), and through blood (D) of a separate 6 mm arterial section. Step size, 500 μm.

2.5 DISCUSSION AND CONCLUSIONS

Gold nanorods (AuNR) conjugated with polyethylene glycol were investigated as an exogenous contrast agents to expand the use of IVUS/IVPA imaging to detect and characterize atherosclerotic plaques. *In vitro* studies demonstrated the high tolerance of macrophages to PEG-AuNR at concentrations ranging from optical densities of 0.1 (22.2 pM) to 10 (2.2 nM), showing no change in cell proliferation from control cells without any nanoparticles (Fig. 2.2). It was also demonstrated that exposure of PEG-AuNR labeled macrophages to nanosecond-pulsed illumination of variable intensity from the optical setup used for IVPA imaging did not result in adverse effects on cell viability (Fig. 2.4).

In vivo systemic injection of PEG-AuNR was shown to result in the preferential labeling of sites of atherosclerosis, which were subsequently localized using *ex vivo* combined IVUS/IVPA imaging. Histological staining of sample arterial cross sections was performed to assess AuNR labeling (Fig. 2.8). AuNR accumulation was limited to the regions of the arterial cross section with atherosclerotic plaque formation (Fig. 2.8E). The nanoparticle labeling is also co-localized with the absence of a healthy, continuous endothelial layer and the lumen boundary (Fig. 2.8B-C) and the presence of macrophages (Fig. 2.8D). While the co-localization of AuNR with macrophages near the luminal boundary is observed, it is unclear whether this co-localization with macrophages is due to phagocytosis of AuNR or if the relationship is the result of a more passive process, such as common sites of extravasation into atherosclerotic plaques. The correlation between AuNR labeling and missing endothelial or protective fibrous cap layer suggests that the PEG-AuNRs are able to extravasate into the luminal margins of the plaque through discontinuous luminal boundaries. The nanoparticles may also extravasate from the vasa vasorum, as neovasculature associated with atherosclerosis has been shown to

exhibit a leaky endothelium [27]. This hypothesis is further supported by recent reports demonstrating that PEG-AuNRs are not endocytosed by endothelial cells following systemic injection [28] and that injection of other contrast agents including the organic fluorochrome indocyanine green and perfluorocarbon nanoparticles resulted in a similar pattern of preferential labeling of atherosclerotic plaques [29,30]. Therefore, the present results are in agreement with similar studies which have found that systemically injected contrast agents containing no specific biological targeting moiety still tend to preferentially aggregate at atherosclerotic regions.

Additionally, the feasibility of detecting AuNR-labeled atherosclerotic plaques was demonstrated through the use of IVPA imaging to detect the location of contrast agents through within the context of spatially co-registered IVUS images of arterial morphology. An integrated IVUS/IVPA catheter was utilized to enable imaging in the presence of luminal saline as well as luminal blood in simulated *in vivo* imaging conditions. IVPA imaging of AuNR in the presence of luminal blood is significant in that it simplifies an eventual clinical imaging procedure and avoids potential adverse effects to the patient by eliminating the need for upstream occlusion or saline flushing of the artery [4]. Notably, when the artery sample was imaged in static whole blood, the presence of blood stasis within the lumen of the aorta resulted in significant ultrasound speckle which reduced the ability to detect the arterial morphology (Figs. 2.9E, 2.10A). The enhanced IVUS speckle has previously been well documented [31]. To reduce this effect and better enable IVUS detection of the arterial wall morphology as is achieved in the case of *in vivo* imaging, a centrifugal pump was positioned to maintain luminal flow while conducting 3D pullback IVUS/IVPA imaging through blood (Figs. 2.10B, 2.11D).

In comparing IVPA images obtained from imaging through luminal saline to those obtained imaging through luminal blood, the similarity of the signals suggests that

the relatively low optical attenuation of luminal blood within the NIR wavelength region permits the detection of AuNRs (Figs. 2.9, 2.11). However, differences were noted for the cross sectional image between the 12 o'clock region of the IVPA signal obtained when imaging through saline (Fig. 2.9A) and that achieved through blood (Fig. 2.9B). Additionally, an overall reduction in the signal-to-noise ratio between the IVPA signals detected from arterial regions with AuNR labeling and using equal catheter output energy of 0.5 mJ was also observed. Both of these effects are likely due to the increased optical attenuation of blood and can be partially overcome by increasing the delivered pulse energy, as shown in Figure 2.11D.

Notably, when imaging through both saline and blood, the regions which were identified as consisting of AuNR using the sIVPA imaging algorithm are in close agreement with the IVPA signal obtained from imaging only at the AuNR peak absorbance wavelength (Fig. 2.9). This similarity suggests the potential for localizing accumulated AuNR using combined IVUS/IVPA imaging at a single NIR wavelength rather than across a broad spectral range. This simplification offers the potential to reduce both image acquisition time and IVPA imaging instrumentation costs. However, further studies should be conducted to quantify the reduction in sensitivity and specificity which result from a single wavelength IVPA AuNR detection approach, particularly as integrated IVUS/IVPA catheter continue to evolve and injected AuNR doses are further reduced to become more clinically appealing.

This chapter has demonstrated that PEG-AuNRs accumulate within macrophages *in vitro* and preferentially label atherosclerotic regions following *in vivo* systemic injection. The AuNR-labeled plaques can subsequently be detected using combined IVUS/IVPA imaging in the presence of luminal blood. Due to the tendency of the AuNRs to extravasate at sites with dysfunctional endothelium, this application of IVPA imaging

may be utilized to identify the location of acute inflammation within atherosclerotic plaques, which usually locate within the cap and shoulder regions [32]. Higher aspect ratio AuNRs, which exhibit a longer wavelength longitudinal peak absorbance, as well as the addition of a silica coating, are utilized for IVUS/IVPA imaging applications discussed in Chapters 3 and 4 as a means of increasing the signal-to-noise ratio and thermal stability of the particles. The use of AuNRs can also be further expanded to enable the investigation of molecular IVPA imaging through the conjugation of targeting moieties onto the surface of the AuNR. Integration of the presented results demonstrating the ability of combined IVUS/IVPA imaging to localize AuNRs through luminal blood with prior work related to the bioconjugation of targeting moieties to nanoparticle surfaces suggests an avenue for molecular specific IVPA imaging of atherosclerosis biomarkers.

Additionally, the demonstrated ability to localize preferential AuNR labeling of atherosclerotic lesions motivates the expansion of the technique to include the investigation of a localized thermal therapy, whereby the AuNR themselves can serves as thermal sources heated by a continuous wave laser source delivered through the IVUS/IVPA integrated catheter following their localization. This expansion of IVUS/IVPA imaging using AuNR as theranostic agents is examined in greater detail in the remaining chapters of this dissertation, with the results presented in this chapter serving as the foundation for AuNR-based theranostic applications for the monitored treatment of atherosclerotic plaques.

2.6 REFERENCES

1. V. R. L. Roger, A. S. Go, D. M. Lloyd-Jones, E. J. Benjamin, J. D. Berry, W. B. Borden, D. M. Bravata, S. Dai, E. S. Ford, C. S. Fox, H. J. Fullerton, C. Gillespie, S. M. Hailpern, J. A. Heit, V. J. Howard, B. M. Kissela, S. J. Kittner, D. T. Lackland, J. H. Lichtman, L. D. Lisabeth, D. M. Makuc, G. M. Marcus, A.

Marelli, D. B. Matchar, C. S. Moy, D. Mozaffarian, M. E. Mussolino, G. Nichol, N. P. Paynter, E. Z. Soliman, P. D. Sorlie, N. Sotoodehnia, T. N. Turan, S. S. Virani, N. D. Wong, D. Woo and M. B. Turner, "Heart Disease and Stroke Statistics-2012 Update: A Report From the American Heart Association," *Circulation*, 125(1):e2-e220, (2012).

2. J. Sanz and Z. A. Fayad, "Imaging of atherosclerotic cardiovascular disease," *Nature*, 451(7181):953-957, (2008).

3. B. D. MacNeill, H. C. Lowe, M. Takano, V. Fuster and I. K. Jang, "Intravascular modalities for detection of vulnerable plaque: current status," *Arterioscler Thromb Vasc Biol*, 23(8):1333-42, (2003).

4. K. C. Hoang, A. Edris, J. Su, D. S. Mukai, S. Mahon, A. D. Petrov, M. Kern, C. Ashan, Z. Chen, B. J. Tromberg, J. Narula and M. Brenner, "Use of an oxygen-carrying blood substitute to improve intravascular optical coherence tomography imaging," *J Biomed Opt*, 14(3):034028, (2009).

5. S. Sethuraman, S. R. Aglyamov, J. H. Amirian, R. W. Smalling and a. E. S. Y., "Intravascular photoacoustic imaging using an IVUS imaging catheter," *IEEE Trans. Ultrason. Ferroelectr. Freq. Control*, 54:978-986, (2007).

6. H.-W. Wang, N. Chai, P. Wang, S. Hu, W. Dou, D. Umulis, L. V. Wang, M. Sturek, R. Lucht and J.-X. Cheng, "Label-Free Bond-Selective Imaging by Listening to Vibrationally Excited Molecules," *Physical Review Letters*, 106(23):238106, (2011).

7. T. J. Allen, A. Hall, A. P. Dhillon, J. S. Owen and P. C. Beard, "Spectroscopic photoacoustic imaging of lipid-rich plaques in the human aorta in the 740 to 1400 nm wavelength range," *J Biomed Opt*, 17(6):061209, (2012).

8. S. Sethuraman, J. H. Amirian, S. H. Litovsky, R. W. Smalling and S. Y. Emelianov, "Ex vivo Characterization of Atherosclerosis using Intravascular Photoacoustic Imaging," *Opt. Express*, 15(25):16657-16666, (2007).

9. S. Sethuraman, J. H. Amirian, S. H. Litovsky, R. W. Smalling and S. Y. Emelianov, "Spectroscopic intravascular photoacoustic imaging to differentiate atherosclerotic plaques," *Optics Express*, 16(5):3362-3367, (2008).

10. B. Wang, J. L. Su, J. Amirian, S. H. Litovsky, R. Smalling and S. Emelianov, "Detection of lipid in atherosclerotic vessels using ultrasound-guided spectroscopic intravascular photoacoustic imaging," *Opt. Express*, 18(5):4889-4897, (2010).

11. K. Jansen, A. F. W. van der Steen, H. M. M. van Beusekom, J. W. Oosterhuis and G. van Soest, "Intravascular photoacoustic imaging of human coronary atherosclerosis," *Opt. Lett.*, 36(5):597-599, (2011).

12. B. Wang, A. Karpiouk, D. Yeager, J. Amirian, S. Litovsky, R. Smalling and S. Emelianov, "Intravascular photoacoustic imaging of lipid in atherosclerotic plaques in the presence of luminal blood," *Opt Lett*, 37(7):1244-6, (2012).

13. B. Wang, A. Karpiouk, D. Yeager, J. Amirian, S. Litovsky, R. Smalling and S. Emelianov, "In vivo Intravascular Ultrasound-guided Photoacoustic Imaging of Lipid in Plaques Using an Animal Model of Atherosclerosis," *Ultrasound in medicine & biology*, 38(12):2098-2103, (2012).

14. K. Jansen, M. Wu, A. F. van der Steen and G. van Soest, "Lipid detection in atherosclerotic human coronaries by spectroscopic intravascular photoacoustic imaging," *Opt Express*, 21(18):21472-84, (2013).

15. J. L.-S. Su, B. Wang and S. Y. Emelianov, "Photoacoustic imaging of coronary artery stents," *Optics Express*, 17(22):19894-19901, (2009).

16. A. B. Karpiouk, B. Wang, J. Amirian, R. W. Smalling and S. Y. Emelianov, "Feasibility of in vivo intravascular photoacoustic imaging using integrated ultrasound and photoacoustic imaging catheter," *J Biomed Opt*, 17(9):96008-1, (2012).

17. B. Wang, E. Yantsen, T. Larson, A. B. Karpiouk, S. Sethuraman, J. L. Su, K. Sokolov and S. Y. Emelianov, "Plasmonic intravascular photoacoustic imaging for detection of macrophages in atherosclerotic plaques," *Nano Lett*, 9(6):2212-7, (2009).

18. B. Wang, P. Joshi, V. Sapozhnikova, J. Amirian, S. H. Litovsky, R. Smalling, K. Sokolov and S. Emelianov, "Intravascular photoacoustic imaging of macrophages using molecularly targeted gold nanoparticles," 7564(75640A-75640A-7), (2010).

19. T. Niidome, M. Yamagata, Y. Okamoto, Y. Akiyama, H. Takahashi, T. Kawano, Y. Katayama and Y. Niidome, "PEG-modified gold nanorods with a stealth character for in vivo applications," *J Control Release*, 114(3):343-7, (2006).

20. M. Eghtedari, A. Oraevsky, J. A. Copland, N. A. Kotov, A. Conjusteau and M. Motamedi, "High Sensitivity of In Vivo Detection of Gold Nanorods Using a Laser Optoacoustic Imaging System," *Nano Letters*, 7(7):1914-1918, (2007).

21. P. C. Li, C. R. Wang, D. B. Shieh, C. W. Wei, C. K. Liao, C. Poe, S. Jhan, A. A. Ding and Y. N. Wu, "In vivo photoacoustic molecular imaging with simultaneous

multiple selective targeting using antibody-conjugated gold nanorods," *Opt Express*, 16(23):18605-15, (2008).

22. A. Taruttis, E. Herzog, D. Razansky and V. Ntziachristos, "Real-time imaging of cardiovascular dynamics and circulating gold nanorods with multispectral optoacoustic tomography," *Opt Express*, 18(19):19592-602, (2010).

23. N. R. Jana, L. Gearheart and C. J. Murphy, "Seed-Mediated Growth Approach for Shape-Controlled Synthesis of Spheroidal and Rod-like Gold Nanoparticles Using a Surfactant Template," *Advanced Materials*, 13(18):1389-1393, (2001).

24. C. Grabinski, N. Schaeublin, A. Wijaya, H. D'Couto, S. H. Baxamusa, K. Hamad-Schifferli and S. M. Hussain, "Effect of Gold Nanorod Surface Chemistry on Cellular Response," *ACS Nano*, 5(4):2870-2879, (2011).

25. A. B. Karpiouk, B. Wang and S. Y. Emelianov, "Development of a catheter for combined intravascular ultrasound and photoacoustic imaging," *Rev Sci Instrum*, 81(1):014901, (2010).

26. M. Shiomi and T. Ito, "The Watanabe heritable hyperlipidemic (WHHL) rabbit, its characteristics and history of development: a tribute to the late Dr. Yoshio Watanabe," *Atherosclerosis*, 207(1):1-7, (2009).

27. R. Virmani, F. D. Kolodgie, A. P. Burke, A. V. Finn, H. K. Gold, T. N. Tulenko, S. P. Wrenn and J. Narula, "Atherosclerotic plaque progression and vulnerability to rupture: angiogenesis as a source of intraplaque hemorrhage," *Arterioscler Thromb Vasc Biol*, 25(10):2054-61, (2005).

28. A. M. Alkilany, A. Shatanawi, T. Kurtz, R. B. Caldwell and R. W. Caldwell, "Toxicity and cellular uptake of gold nanorods in vascular endothelium and smooth muscles of isolated rat blood vessel: importance of surface modification," *Small*, 8(8):1270-8, (2012).

29. C. Vinegoni, I. Botnaru, E. Aikawa, M. A. Calfon, Y. Iwamoto, E. J. Folco, V. Ntziachristos, R. Weissleder, P. Libby and F. A. Jaffer, "Indocyanine green enables near-infrared fluorescence imaging of lipid-rich, inflamed atherosclerotic plaques," *Sci Transl Med*, 3(84):84ra45, (2011).

30. H. Zhang, L. Zhang, J. Myerson, K. Bibee, M. Scott, J. Allen, G. Sicard, G. Lanza and S. Wickline, "Quantifying the evolution of vascular barrier disruption in advanced atherosclerosis with semipermeant nanoparticle contrast agents," *PLoS One*, 6(10):e26385, (2011).

31. G. S. Mintz, Quantitative and Qualitative Analyses, Taylor & Francis, 23-25, (2005).

32. G. Pasterkamp, A. H. Schoneveld, A. C. van der Wal, D. J. Hijnen, W. J. van Wolveren, S. Plomp, H. L. Teepen and C. Borst, "Inflammation of the atherosclerotic cap and shoulder of the plaque is a common and locally observed feature in unruptured plaques of femoral and coronary arteries," *Arterioscler Thromb Vasc Biol*, 19(1):54-8, (1999).

Chapter 3: Intravascular Photoacoustics for Temperature Monitoring During Localized Heating of Gold Nanorods[2]

3. 1 Introduction to Photoacoustic Temperature Monitoring During Gold Nanorod Heating

Coronary heart disease remains a leading cause of death throughout industrialized nations, responsible for more than 7 million deaths annually throughout the world [1]. In the United States alone, coronary heart disease accounts for approximately one in every six deaths, with a coronary event occurring approximately every 25 seconds [2]. In the majority of cases, onset of an acute coronary event is triggered by the rupture of so-called "vulnerable plaques" which were undetected using conventional diagnostic procedures [3]. Therefore, there remains a clinical need for improved imaging modalities and therapeutic approaches to enable differentiation and selective, local treatment of these high-risk vulnerable atherosclerotic plaques.

As reviewed in Chapter 1, Section 1.2, current clinical imaging modalities utilized to detect the presence of atherosclerosis lack the ability to reliably differentiate plaques which are vulnerable to rupture from those which are stable. Noninvasive techniques, such as the gold standard x-ray angiography or coronary computed tomography, lack sufficient resolution to visualize critical vulnerable plaque characteristics- a thin fibrous cap with an underlying lipid-rich necrotic core and extensive macrophage accumulation. Intravascular imaging modalities, including intravascular ultrasound (IVUS) and optical coherence tomography (OCT), offer trade-offs in terms of morphological assessment capabilities based on their respective imaging depths and resolutions. However, each

[2] Adapted with permission from D. Yeager, Y.-S. Chen, S. Litovsky, and S. Emelianov, "Intravascular Photoacoustics for Image-Guidance and Temperature Monitoring During Plasmonic Photothermal Therapy of Atherosclerotic Plaques: A Feasibility Study," *Theranostics*, 4(1), 36-46, (2014). Copyright 2014 Ivyspring Internaional Publisher. Contribution of coauthors- Y.-S. Chen provided guidance for temperature monitoring of silica-coated gold nanorods, S. Litovsky provided experimental materials, and S. Emelianov provided overall supervision of the research.

modality is inherently limited in terms of compositional characterization due to similarities in the backscattered signal produced by different tissue types [4]. Virtual histology IVUS (VH-IVUS) seeks to expand the ability to differentiate plaque composition through analysis of the tissue-dependent changes in the frequency content of backscattered ultrasound, however the efficacy of the approach has recently been called into question [5,6]. Moreover, the emerging technique of diffuse reflectance near-infrared spectroscopy (NIRS) has been demonstrated to differentiate some plaque lipid, but the modality is limited by its inability to provide a depth resolved signal [7].

Beyond the challenge of diagnosing vulnerable plaques, an effective treatment strategy has not yet been clinically adopted [8]. While preventative measures and systemic treatments are desirable as an overall policy for atherosclerosis management, localized treatment strategies are likely to remain a necessary tool for effectively treating identified vulnerable plaques. Traditional percutaneous coronary interventions, such as angioplasty and stenting have focused on mechanically restoring lumen diameter in regions with severe stenosis rather than on stabilizing plaque composition [9]. The introduction of drug eluting stents has more recently introduced a dual treatment which adds a pharmacological agent to reduce the extent of inflammation or proliferation following deployment of a stent. However, even in the case of drug eluting stents, the treatment is not specific to atherosclerotic tissue alone, and particularly not to specific biomarkers of interest within vulnerable plaques.

Several light based therapeutic strategies have also been investigated, as introduced in Chapter 1, Section 1.5. While these phototherapy-based approaches have resulted in marginal clinical approval for limited applications, none have obtained widespread adoption for the treatment of coronary atherosclerosis. For example, the clinical adoption of excimer laser atherectomy has been limited by an increased risk of

adverse effects which are largely related to a lack of specificity and undesirable damage to the vessel wall [10]. Photodynamic therapy has more recently expanded the capability of laser-based treatments and shown promise as a technique for stabilizing atherosclerotic plaques, yet has not been translated to the clinic on a large scale [11,12].

Combined intravascular ultrasound and photoacoustic (IVUS/IVPA) imaging, introduced in Chapter 1, Section 1.4, has been developed as a means of supplementing the morphological information provided by IVUS with additional capability for assessing plaque composition based on unique optical absorption spectra of tissue components or contrast agents [13]. In Chapter 2, applications of IVUS/IVPA imaging were expanded to include the localization of plasmonic gold nanorods which passively label atherosclerotic lesions following systemic injection [14]. The strong and tunable absorption of gold nanorods within the near-infrared wavelength range, where endogenous tissue absorption is relatively low, makes gold nanorods attractive agents for photothermal therapy, particularly for cancer treatment applications [15-17]. This therapeutic approach, termed plasmonic photothermal therapy (PPTT), has more recently come under investigation as a tool for the localized treatment of atherosclerotic plaques, introduced in Chapter 1, Section 1.5.2 [18,19].

To date, PPTT for atherosclerotic plaque treatment has required a local delivery of gold nanoparticles and has been limited by an inability to monitor the delivery of therapy. IVUS/IVPA imaging offers a means to locate gold nanoparticles following systemic delivery [14,20], based on unique optical absorption spectral characteristics, and to subsequently monitor temperature during PPTT, based on the temperature dependence of the generated photoacoustic signal intensity. In the case of imaging gold nanoparticles, it has been shown that commonly utilized 3-5 ns pulsed illumination from an Nd:YAG laser does not satisfy stress confinement or thermal confinement (see Chapter 1, Section

1.3.1 for definitions) of the metallic structures. Therefore, the general equation for induced photoacoustic pressure within endogenous tissues, Equation 1.6, must be modified to reflect a dependency on the local environment of the nanoparticles, as shown in Equation 3.1 (also Equation 1.7) [21]:

$$p_0 \propto \eta \Gamma_{eff} \sigma \Phi \tag{3.1}$$

In addition to the IVPA signal dependence on the local optical absorption cross section of the highly absorbing nanoparticle (σ), the generated photoacoustic pressure also exhibits a dependence on local optical fluence (Φ), the heat transfer efficiency (η) from the nanoparticle to its surroundings, and the effective Grüneisen parameter (Γ_{eff}) of the environment immediately surrounding the nanoparticle. In the case of imaging nanoparticles distributed within water-based tissue, the effective Grüneisen parameter is approximated to exhibit similar temperature dependence to that of pure water. The Grüneisen parameter is a function of the speed of sound, the thermal coefficient of volume expansion, and the isobaric specific heat capacity, all of which are temperature dependent properties. Therefore, the photoacoustic signal intensity generated by gold nanoparticles in water-based tissues is expected to result in a linear relationship with temperature. Therefore, photoacoustic imaging can be implemented as a tool for monitoring temperature within the local environment of optical absorbers of interest. To that end, silica-coated gold nanorods (SiO_2AuNR) have been investigated as thermally stable nanosensors which, together with photoacoustic imaging, enable temperature mapping with improved sensitivity over polyethylene glycol (PEG) coated gold nanorods [21-23].

In this chapter, the ability to utilize a modified IVUS/IVPA imaging system as a platform for detecting and subsequently monitoring local temperature rise during selective laser heating of SiO_2AuNR is introduced. A single optical fiber is used to deliver illumination required for both IVPA signal generation, via the nanosecond pulsed laser, and simultaneous tissue heating, via continuous wave near-infrared illumination. As such, it is hypothesized that IVUS/IVPA imaging can be expanded from a purely diagnostic imaging-based modality to a potential theranostic platform for atherosclerotic plaque management.

3. 2 SILICA-COATED GOLD NANOROD SYNTHESIS AND CHARACTERIZATION

Cetyltrimethylammonium bromide (CTAB) stabilized gold nanorods were synthesized by a seed mediated growth method reported in literature and described in Chapter 2, Section 2.3.1 [24]. Briefly, a seed solution was prepared by adding 60 μL of NaBH4 (10 mM) to a vigorously stirring solution of 500 μL of CTAB (200 mM) and 500 μL of $HAuCl_4$ (0.5 mM) at 30°C. After 7 minutes of aging, 96 μL of the seed solution was added to a growth solution containing 800 μL of $AgNO_3$ (10 mM), 4 mL $HAuCl_4$ (10 mM), 38 mL of CTAB (200 mM), and 440 μL of ascorbic acid at 30°C and stirring at 500 rpm. The CTAB-AuNR were aged overnight at 30°C before being twice washed to remove excess CTAB via centrifugation at 18,000 rcf for 40 minutes. The washed CTAB-AuNR were re-suspended in deionized water at a final peak optical density (OD) of 15, as measured by UV-Vis spectroscopy (Synergy HT, BioTek). At this stage, it is possible to fine tune the longitudinal peak absorbance of the CTAB-AuNR by heating the solution to induce a blue shift of the peak. Figure 3.1 shows the optical absorption spectrum of a batch of AuNR which were heating to induce blue shifting over several hours prior to replacement of the CTAB with PEG. Temperature settings of the heating

plate for the indicated times was 120°C for all time points except for the overnight heating which progressed at 70°C. Note that silica coating of the AuNR results in a red shift of the peak absorbance wavelength of approximately 20 nm for a 20 nm silica shell thickness. Therefore, the CTAB-AuNR peak absorbance should be tuned such that it is blue shifted from the final desired absorbance peak, approximately 788 nm for a final absorbance peak at 808 nm. After tuning to the desired peak absorbance, the CTAB was replaced with polyethylene glycol (PEG, 2 kD) by adding equal volumes of mPEG-thiol (0.2 mM) and the OD 15 CTAB-AUNR. The mixture was sonicated for 10 minutes and allowed to react for four hours on a shaker under modest agitation. The resulting PEG-AuNR were washed via centrifuge filtration (Amicon ultra-15, Millipore) for 10 min at 3000 rcf and re-suspended in water at an OD of 10.

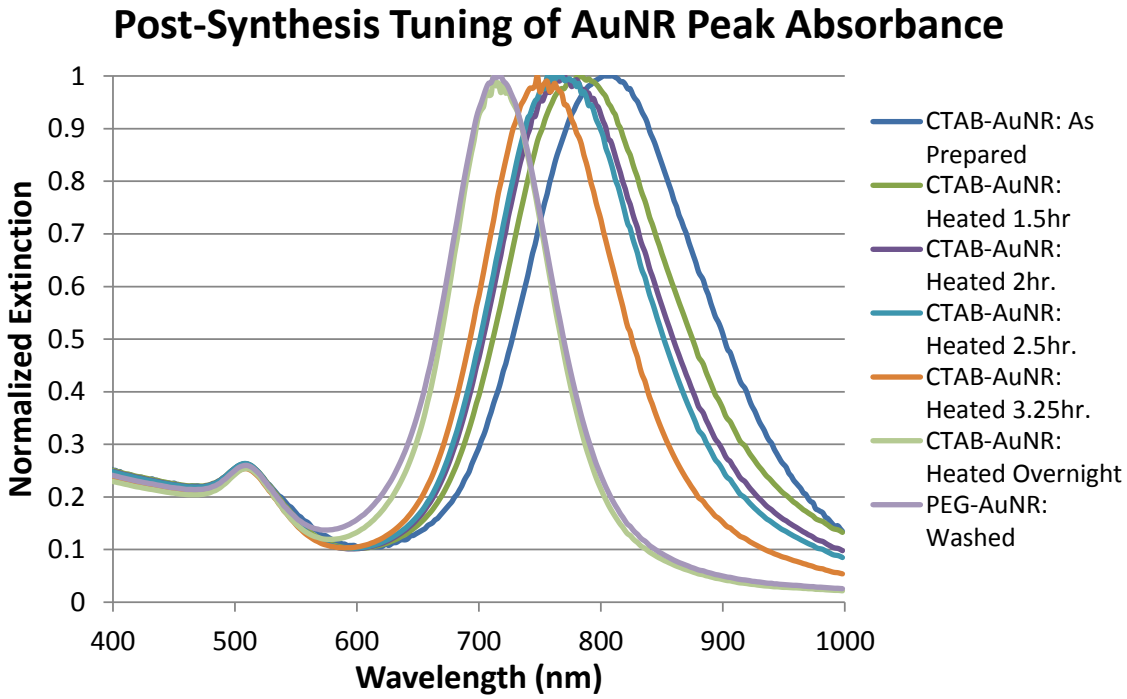

Figure 3.1: Heat induced tuning of the AuNR peak absorbance wavelength.

Silica coating of the PEG-AuNR was achieved by a previously reported modified Stöber method [22]. In short, under vigorous stirring, 1.2 mL of the PEG-AuNR were added to 1.8 mL of isopropanol, followed by the addition of 40 µL of tetraethyl orthosilicate (TEOS) in isopropanol (100 mM). A 3.8% ammonia solution in isopropanol was added to adjust the solution to a pH of 11, and the solution was reacted under moderate stirring for 4 hours. The resulting silica-coated gold nanorods (SiO_2AuNR) were twice washed via centrifuge filtration for 10 min at 1000 rcf and re-suspended in water at the desired final OD. Figure 3.2 provides optical spectra at various stages of synthesis of SiO_2AuNR and representative transmission electron microscopy (TEM) images revealing the presence of AuNR/silica core-shell nanoparticles with consistent intra- and inter-particle silica thickness.

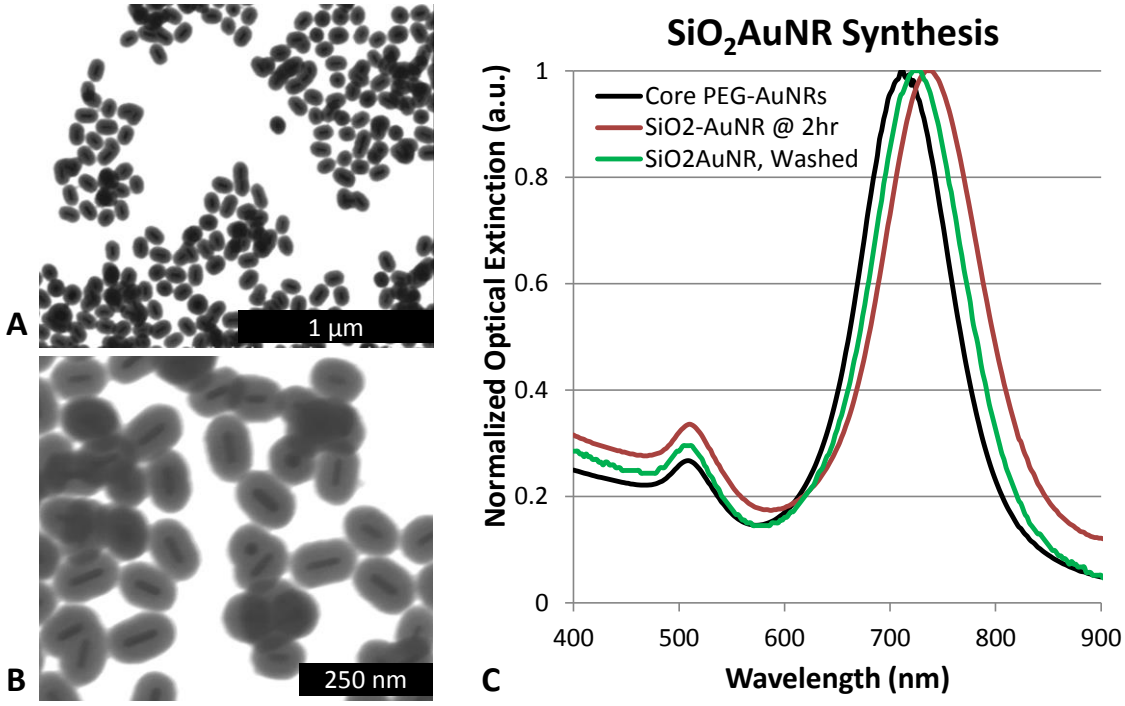

Figure 3.2: Characterization of SiO_2AuNR. TEM images of as prepared SiO_2AuNR at (A) low and (B) high magnification. (C) Optical absorption spectra of AuNR prior to, during, and after SiO_2 coating.

3. 3 *IN VITRO* VALIDATION OF MACROPHAGE-SPECIFIC SiO_2AUNR LABELING

In vitro nanoparticle incubation studies were conducted in order to validate macrophage-specific labeling of SiO_2AuNR. In particular, the endothelium at the boundary of the arterial lumen is a critical regulator of numerous vascular processes and its dysfunction or damage has been shown to correlate with atherosclerosis and increased rates of coronary events [25]. Given their proximity to nanoparticles in circulation following a systemic injection, endothelial cells are also a likely cell type for unintended SiO_2AuNR uptake. Therefore, *in vitro* incubation studies were performed to compare the tendency of endothelial cells and macrophages to phagocytose SiO_2AuNR. Mouse monocyte-derived macrophages (J774A.1) or human umbilical vein endothelial cells (HUVEC) were counted using a hemocytometer and plated in a 96 well plate at a concentration of 1 x 10^4 cells/well incubated at 37°C in 5% CO_2 in their respective culture mediums overnight. The media was then replaced and SiO_2AuNR were added, yielding a final nanoparticle OD of 0.5 (0.1 nM). The nanoparticles were incubated with the cells for 18 hours before being triple washed with phosphate buffered saline (PBS) and imaged to evaluate nanoparticle uptake. Figure 3.3 provides microscopy images of J774A.1 macrophages (left) and HUVEC (right) without exposure to nanoparticles (top) and following incubation with SiO_2AuNR and washing (bottom). Significantly greater SiO_2AuNR labeling is observed in the macrophages than the endothelial cells.

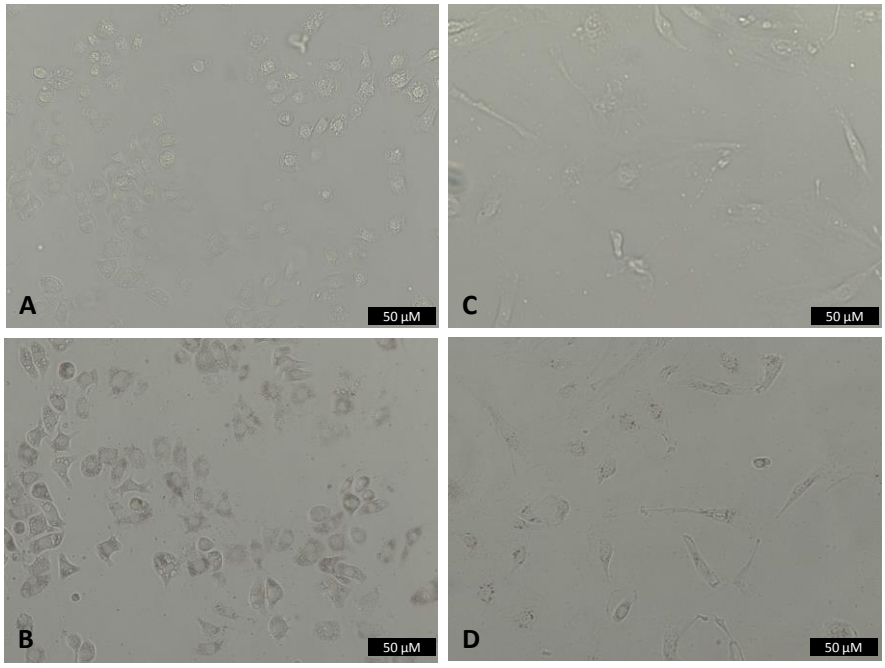

Figure 3.3: Comparison of SiO_2AuNR uptake by J774A.1 macrophages and HUVEC. J774A.1 macrophages (A) without and (B) following SiO_2AuNR exposure. HUVEC (C) without and (D) following SiO_2AuNR exposure. Scale bars = 50 µm.

To further evaluate the extent of preferential macrophage uptake, SiO_2AuNR were incubated with a co-culture containing both macrophages and HUVEC cells. HUVEC cells were plated in a 96 well plate at a density of 1 x 10^4 cells/well incubated overnight. Simultaneously, J774A.1 macrophages were incubated with 2 µM Rhodamine-B isothiocyanate. The macrophages were then added to the HUVEC cells at a density of 1 x 10^4 cells/well and allowed to incubate for 4 hours at 37°C in 5% CO_2 to permit adherence of the macrophages. SiO_2AuNR were then added to the co-cultured cells at a final OD of 0.5 (0.1 nM) and allowed to incubate overnight. Cells were then triple washed with PBS and imaged using bright field and fluorescence microscopy. The rhodamine-labeled J774 macrophages were differentiated from HUVEC cells using fluorescence imaging (excitation/emission: 530/590 nm). Figure 3.4 provides images of

co-cultured macrophages without (left) and with SiO_2AuNR (right). Preferential phagocytosis of SiO_2AuNR by macrophages is confirmed by the fluorescence of rhodamine-labeled J774 macrophages.

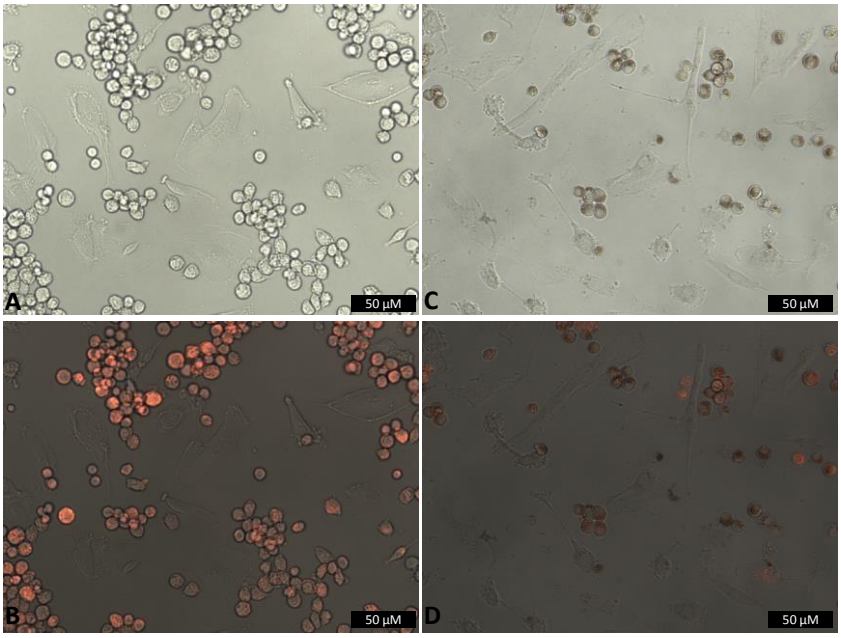

Figure 3.4: Co-culture of J774A.1 macrophages and HUVEC. (A) Brightfield and (B) Rhodamine fluorescence overlay revealing macrophage distribution within a co-culture without nanoparticle labeling. (C) Brightfield revealing SiO_2AuNR distribution and (D) Rhodamine fluorescence overlay revealing macrophage distribution within a co-culture following nanoparticle labeling. Scale bar = 50 µm.

For experiments used to validate IVPA temperature sensitivity of intracellular SiO_2AuNR, J774A.1 macrophages were grown to 70% confluence and incubated in phenol free DMEM F-12 media containing 5% fetal bovine serum and SiO_2AuNR with a final nanoparticle OD of 0.5 for 24 hours at 37°C in 5% CO_2. The cells were then scraped and twice washed with PBS via centrifugation at 300 rcf for 5 minutes to remove excess nanoparticles and finally fixed in a 10% buffered formalin solution. Two separate batches

of SiO_2AuNR were utilized for the polymethylmethacrylate (PMMA) tube imaging experiment and the gelatin phantom experiment described below, with peak longitudinal absorbance of 735 nm and 800 nm, respectively.

3. 4 VERIFICATION OF SiO_2AUNR-INDUCED INTRAVASCULAR PHOTOACOUSTIC SIGNAL LINEARITY VERSUS TEMPERATURE

The combined IVUS/IVPA imaging system and the associated integrated IVUS/IVPA imaging catheter are described in Chapters 1 and 2 [13,26]. Briefly, an optical parametric oscillator (OPO) and coupled laser (PermiScan, SpectraPhysics, Inc.) providing nanosecond pulse duration at variable optical wavelengths. For detection of AuNRs, the pulsed laser optical output at wavelengths between 700 nm and 850 nm was focused into the 600 μm core diameter multimode optical fiber of the integrated IVUS/IVPA imaging catheter which also housed a commercially available, single element 40 MHz IVUS transducer (Atlantis SR Pro2, Boston Scientific, Inc.). The output energy at the distal end of the integrated catheter was maintained at approximately 0.4 mJ per pulse for all IVPA imaging discussed within this chapter. The resulting RF signals were digitized using a 14 bit, 200 MHz data acquisition card (CompuScope 14200, GaGe Applied Technologies, Inc.) and temporally decoupled to obtain the co-registered IVUS and IVPA images in R-theta coordinates. The IVUS/IVPA data was then band-pass filtered, and envelope detected using a Hilbert transform to baseband the raw IVUS and IVPA signals. For generation of 2 dimensional images of a vessel cross section, the integrated IVUS/IVPA imaging catheter was rotated using a stepper motor (T-NM17A200, Zaber Technologies, Inc.) for a total of 256 co-registered IVUS and IVPA signal pairs per complete rotation. The R-theta data was scan converted from polar to Cartesian coordinates, using a bicubic interpolation algorithm, prior to image display in order to provide conventional cross-sectional views of the image target.

For initial demonstration of the temperature dependence of IVPA signal intensity, IVUS/IVPA imaging was performed using an experimental setup intended to model a SiO_2AuNR labeled artery. Either colloidal SiO_2AuNR (OD=20) or formalin fixed macrophages which had endocytosed PLL-SiO_2AuNR (OD=7) were sealed within optically clear PMMA tubing (inner/outer diameter = 375 μm/500 μm) and aligned within the water tank of the IVUS/IVPA imaging system. These SiO_2AuNR containing inclusions were oriented perpendicular to the axis of the integrated IVUS/IVPA imaging catheter and at a radial distance of approximately 4 mm from the transducer surface. The integrated catheter was fixed in a position facing the SiO_2AuNR containing inclusions. The water tank was positioned on a heating plate, allowing the temperature of the entire tank and, therefore, the SiO_2AuNR containing inclusions to be slowly heated and cooled, during which IVUS/IVPA signals were periodically recorded.

The linearity of IVPA signal intensity change with temperature was first verified through a set of experiments in which the environment surrounding the imaging target was incrementally heated or cooled. Imaging targets ranged from SiO_2AuNR at varying concentrations and macrophages which had phagocytosed SiO_2AuNR to vessel-mimicking phantoms and *ex vivo* tissue labeled with SiO_2AuNR. The experimental set-up was subsequently modified to incorporate the addition of a continuous wave laser emitting at a wavelength of 808 nm and coupled into the same optical fiber of the integrated IVUS/IVPA imaging catheter that was used to deliver the nanosecond pulsed laser illumination necessary for IVPA signal generation. The ability to induce selective heating of the SiO_2AuNR with the CW laser and to monitor the resulting targeted heating using IVUS/IVPA imaging was then investigated in a series of similar experiments.

Figure 3.5A demonstrates the change in IVPA signal intensity versus temperature. The presented data was recorded during cooling (blue) and subsequent reheating (red) of the water tank containing SiO_2AuNR within PMMA tubing at an OD of 20 over a temperature range from approximately 29°C to 43°C. The monotonic change in measured IVPA signal intensity demonstrates the linearity and reproducibility of IVPA temperature response. Similarly, Figure 3.5B presents the percent change in IVPA signal intensity as a function of change in temperature for both the OD 20 SiO_2AuNR (green) and a solution containing formalin fixed J774A.1 macrophages which had previously phagocytosed SiO_2AUNR with a final OD of 7. The linearity of IVPA temperature response is again confirmed for SiO_2AuNR, including both the colloidal particles and those within endosomes. Additionally, a change in IVPA signal of approximately 50% was measured for the OD 20 SiO_2AuNR over a 10°C temperature change versus a 90% change in IVPA signal from SiO_2AuNR within macrophages over the same range. This variation in temperature sensitivity is indicative of a variation in the effective Grüneisen parameter of solutions containing colloidal nanoparticles versus those aggregated within endosomes.

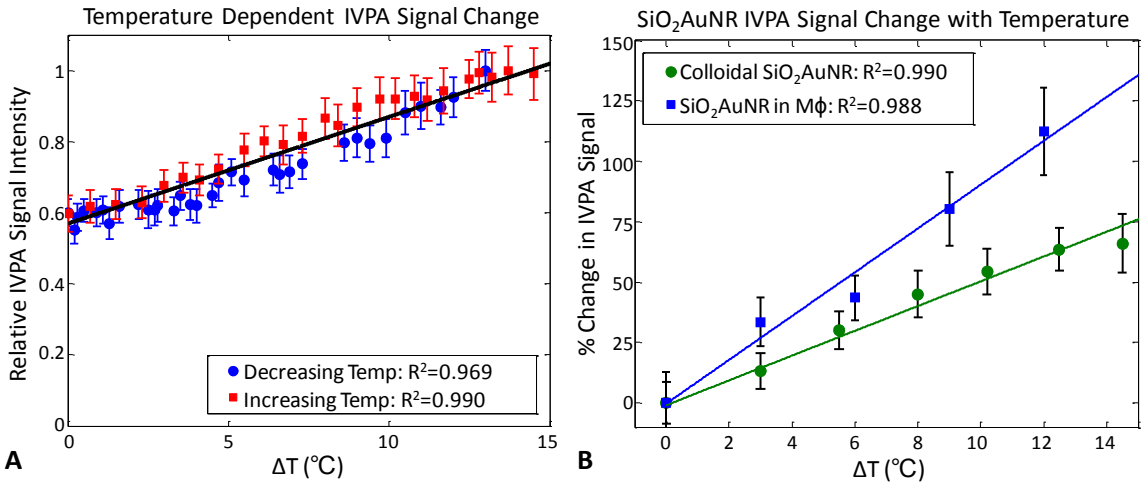

Figure 3.5: Temperature dependence of IVPA signal from SiO_2AuNR within PMMA tubing. (A) Peak IVPA signals during cooling (blue) and subsequent reheating (red) of a water tank containing an inclusion of OD=20 SiO_2AuNR. (B) Percent change in peak IVPA signal versus change in temperature for OD 20 SiO_2AUNR (green) and SiO_2AuNR phagocytosed by macrophages (blue) at a final concentration of OD=7. Data represents the mean and standard deviation from 100 IVPA measurements.

3. 5 Comparison of Intravascular Photoacoustic Imaging Temperature Sensitivity of Gold Nanorods to Endogenous Absorbers: a Plaque-Mimicking Phantom Study

A vessel-mimicking gelatin phantom was subsequently utilized to assess the temperature dependent IVPA signal response of more clinically-relevant tissue components. A solution containing 10% gelatin and 2% silica particles with an average diameter of 30 µm, to provide optical and acoustic scattering, was molded into a hollow cylindrical shape with lumen diameter and wall thickness of approximately 5 mm each. A piece of bovine lipid-rich tissue was implanted into the gelatin mold as the phantom solidified at 4°C. After solidifying, an inclusion containing additional gelatin/silica solution mixed with fixed macrophages loaded with SiO_2AuNR at a final OD of 2.5 was placed on the luminal surface of the phantom adjacent to the lipid-rich tissue inclusion

and the phantom was again cooled to 4°C. The Vevo LAZR (VisualSonics, Inc., Toronto, Canada) ultrasound and photoacoustic imaging system, coupled with a 40 MHz linear array transducer was utilized to noninvasively confirm the orientation of the vessel-mimicking phantom, revealing the position of both the SiO_2AuNR-labeled macrophages and bulk lipid tissue inclusions (Fig. 3.6).

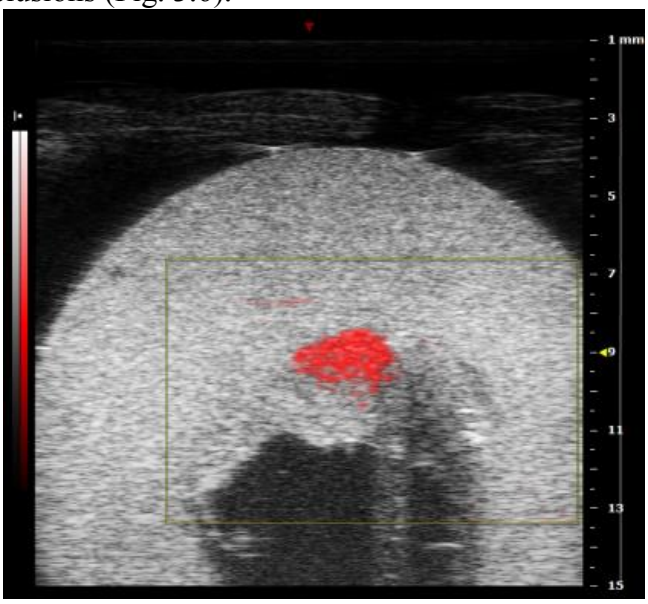

Figure 3.6: Vevo LAZR ultrasound and photoacoustic validation of inclusion position and orientation within vessel-mimicking phantom.

During IVUS/IVPA imaging, IVPA temperature monitoring was performed by slowly changing the temperature of the surrounding water tank and periodically imaging at the peak absorbance of the endocytosed nanoparticles (735 nm) and lipid (1720 nm) to differentiate the two inclusions. Figure 3.7 demonstrates the temperature dependence of the IVPA signal intensity detected within the two inclusions. Imaging performed at the SiO_2AuNR absorbance peak of 735 nm with the phantom at 11°C (Fig. 3.7A) results in a significantly lower signal than that detected at 26°C (Fig. 3.7B). Likewise, imaging of the lipid-rich tissue inclusion, performed at a lipid absorbance peak located at 1720 nm

which has been previously utilized for IVPA imaging of lipid-rich plaques, reveals a similar trend over the same temperature range (Fig. 3.7C,D). Note that the lipid-rich inclusion also causes a significant shadowing effect in the IVUS image within the 1-2 o'clock region. All IVPA images are displayed on the same linear scale, overlaying IVUS images displayed at a dynamic range of 40 dB.

Figure 3.7E provides a plot of the IVPA signal intensity with varying temperature for three regions, the SiO_2AuNR loaded macrophage inclusion (12 o'clock), the adjacent lipid-rich tissue inclusion (1 o'clock), and a control region from within the gelatin phantom (9 o'clock). Data for the SiO_2AuNR loaded macrophage inclusion and the control region were obtained from IVPA imaging at 735 nm, while the data obtained for the lipid-rich tissue region was obtained from IVPA imaging at 1720 nm. The plot reveals a linear increase in IVPA signal with temperature for all three regions, but a significantly greater slope for the SiO_2AuNR containing inclusion. An increase in temperature of 10°C resulted in corresponding percent increases in IVPA signal of 98.4%, 20.5%, and 4.4% for the SiO_2AuNR loaded macrophage inclusion, lipid-rich tissue inclusion, and control region, respectively. This large difference in temperature-dependent signal change further supports the use of SiO_2AuNR as sensitive thermal sensors for IVPA imaging.

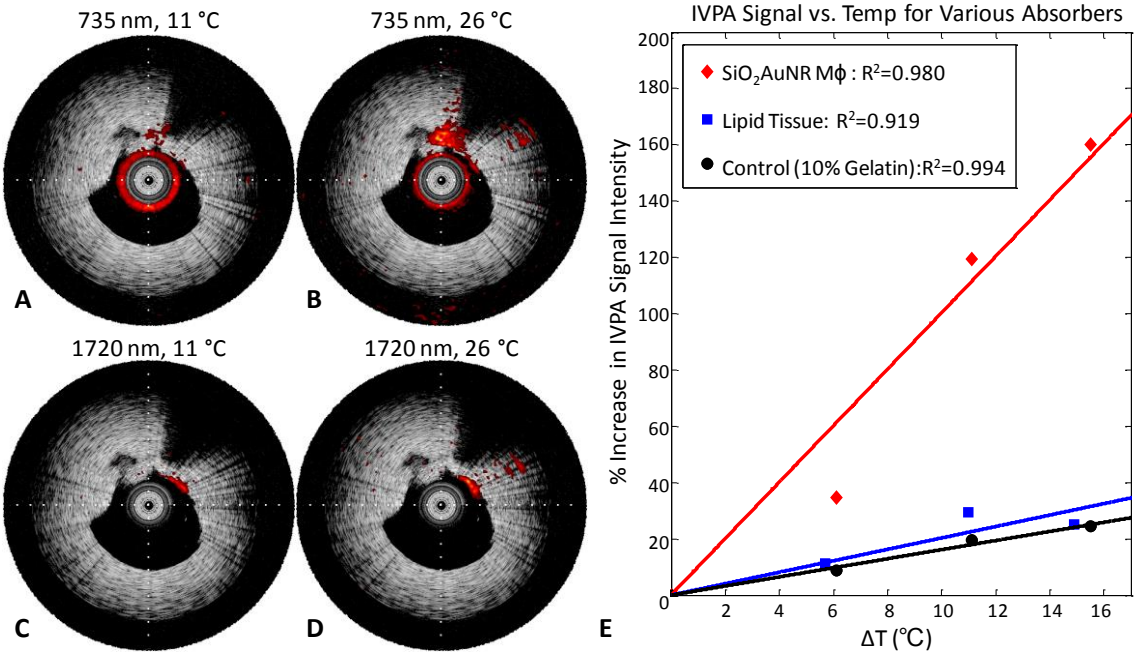

Figure 3.7: IVUS/IVPA imaging of a tissue-mimicking phantom with lipid and SiO_2AuNR inclusions. IVUS/IVPA image of an inclusion with macrophages (MΦ) labeled with SiO_2AuNR, acquired at an imaging wavelength of 735 nm, at temperatures of (A) 11°C and (B) 26°C. IVUS/IVPA image of an inclusion with lipid-rich tissue, acquired at an imaging wavelength of 1720 nm, at temperatures of (C) 11°C and (D) 26°C. Tick marks on IVUS/IVPA images are spaced at 1 mm. Plot of the temperature dependence of IVPA signal intensity for the PLL-SiO_2AuNR loaded macrophages, lipid-rich tissue, and a control region within the phantom (E).

3. 6 Modification of the Intravascular Ultrasound and Photoacoustic Imaging System to Enable Simultaneous Imaging and Laser Heating of Gold Nanorods

To enable photothermal heating specific to the imaged vessel region, a continuous wave (CW) diode laser (NIR DL 808-2000, Laser Lab Components Inc.) emitting at 808 nm was additionally focused into the optical fiber of the integrated catheter using a prism, aligned to serve as an optical beam combiner, positioned proximal to the focusing lens. CW laser output energies ranging from 60 mW to 200 mW at the distal end of the

integrated IVUS/IVPA catheter were used to assess photothermal heating and subsequent temperature dependent IVPA signal change. Reducing the output power below 200 mW was achieved through the addition of a neutral density filters proximal to the laser beam combiner. A schematic of the integrated IVUS/IVPA imaging and photothermal heating experimental system is presented in Figure 3.8.

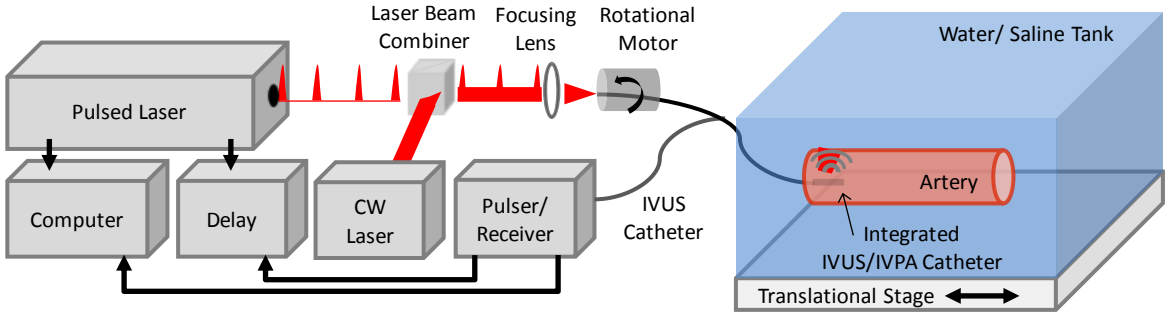

Figure 3.8: Schematic of IVUS/IVPA imaging system modified to incorporate continuous wave (CW) laser illumination within the integrated catheter to enable simultaneous CW laser heating and IVPA temperature monitoring.

The need for a second optical source, separate from the nanosecond pulsed laser utilized for IVPA imaging, in order to induce a photothermal effect is verified by Figure 3.9. Solutions containing 300 µL of SiO_2AuNR at an optical density of 2.0 were illuminated using the integrated IVUS/IVPA catheter for a period of 4 minutes with either the pulsed laser only or both the pulsed and CW lasers with outputs measured at 3.0 mJ and 110 mW, respectively. As expected, the externally measured temperature of the AuNR solutions during illumination reveals minimal heating effect using only the pulsed laser, while the solution also receiving CW illumination exhibited significantly greater bulk heating.

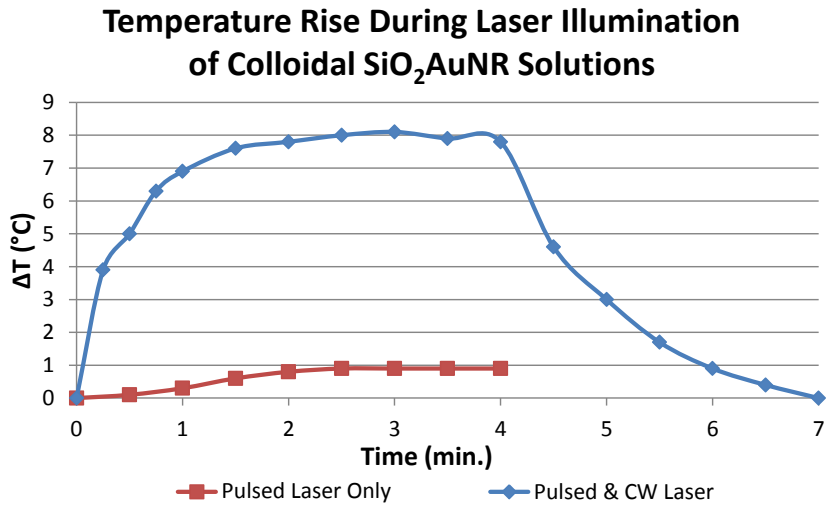

Figure 3.9: Induced temperature rise of SiO_2AuNR containing solutions illuminated with CW and nanosecond pulsed lasers (blue) or with the nanosecond pulsed laser only (red).

3. 7 *Ex Vivo* Intravascular Photoacoustic Imaging for Localizing and Monitoring of Continuous Wave Laser Heating of Gold Nanorod within Arterial Tissue

An atherosclerotic coronary artery section was directly injected with a concentrated colloidal solution of SiO_2AuNR on the outer surface of artery between adventitial fat and media. After 5 minutes, the artery was thoroughly washed with PBS and secured in a saline-filled tank for imaging and monitored CW photothermal heating. IVUS/IVPA imaging was performed at 808 nm to create a cross-sectional image revealing the artery morphology and location of the nanoparticle inclusion. The integrated catheter was then oriented to detect a region of high IVPA signal from the nanoparticles and temperature monitoring along a single A-line was performed by adjusting the temperature of the saline tank as well as by inducing CW photothermal heating. A separate location from the cross-section which did not contain the SiO_2AuNR inclusion was also imaged as a control.

The CW laser-integrated IVUS/IVPA system was utilized as a means of selectively heating SiO_2AuNR, capitalizing on the overlap of the emission wavelength of 808 nm with the nanoparticles' longitudinal peak absorbance and the relatively low blood and tissue absorption within the tissue optical window. SiO_2AuNR injected into the adventitial fat of a coronary artery were imaged *ex vivo* and utilized to demonstrate the ability to induce and monitor CW laser heating, Figure 3.10. The IVUS/IVPA image reveals the presence of the SiO_2AuNR region at approximately 2 o'clock (Fig. 3.10A). CW laser heating with IVPA monitoring was subsequently performed along the two lines indicated, without rotation of the integrated catheter. Figure 3.10B reveals the peak IVPA signal intensity along the indicated lines, with the SiO_2AuNR containing line (green) on the top, and the control line (blue) on the bottom. As expected from the IVUS/IVPA image in Figure 3.10A, the control line has a significantly lower peak IVPA signal intensity than that of the SiO_2AuNR containing line. Additionally, an increase in the peak IVPA singal for the line containing SiO_2AuNR can be seen while the CW laser is applied, indicative of heating. Conversely, no similar increase is seen from the region without SiO_2AuNR. Further evidence of SiO_2AuNR heating can be seen in Figure 3.10C, which provides a plot of the SiO_2AuNR containing line from representative times while the CW laser was off (blue) and on (red). The peak IVPA signal obtained from the SiO_2AuNR region reveals a reversible increase and proximal shift (decrease in the temporal occurance of the peak) while CW heating is applied.

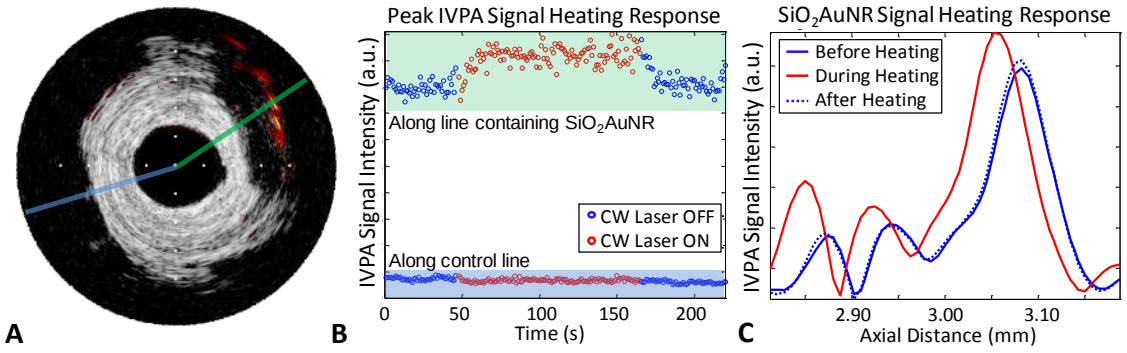

Figure 3.10: *Ex vivo* demonstration of IVPA monitored CW laser induced heating of SiO_2AUNR within a human coronary artery. (A) IVUS/IVPA image obtained at 808 nm revealing the location of SiO_2AuNR at 2 o'clock. Tick marks are spaced at 1 mm. (B) Maximum IVPA signal along the SiO_2AuNR containing and control lines, indicated in A, versus time. The CW laser initially off (blue), then turned on to induce heating (red) and back off (blue). (C) Section of the IVPA A-line shown in green in part A which containing the SiO_2AuNR inclusion, revealing the reversibly induced increase and shift in peak IVPA intensity during CW laser heating.

3. 8 Quantification of IVPA-Measured Continuous Wave Laser-Induced Heating

A forward looking infrared (FLIR) thermal camera was utilized to confirm the extent and specificity of CW heating of SiO_2AuNR relative to background tissue of the human coronary artery sample. The FLIR thermal camera is capable of providing only surface temperature measurements, so the experimental set-up was modified following IVPA monitored heating to enable confirmation of heating using the thermal camera. Specifically, the coronary artery remained fixed within the saline tank, but the saline level was reduced to the surface of the artery. The optical fiber from the integrated IVUS/IVPA catheter was then positioned outside of the artery and focused onto a region of interest of the coronary artery, including the SiO_2AuNR inclusion and a control region

without SiO_2AuNR. The FLIR thermal camera (FLIR A325sc, FLIR Systems, Inc.) was focused on the saline tank, and temperature profiles of regions of interest were recorded for 90 seconds (ExaminIR software, FLIR Systems, Inc.), beginning at approximately the same time as the start of the application of CW laser. CW laser heating was applied for approximately the first 45 seconds, after which the CW laser was turned off, allowing the artery to cool. The temporal temperature profiles were obtained from a region of interest within the CW laser spot on the arterial surface for three different data sets; the arterial region containing the SiO_2AuNR inclusion which was illuminated with 200 mW laser output power, the arterial region containing the SiO_2AuNR inclusion which was illuminated with 60 mW laser output power, and a control region on the arterial surface which did not contain SiO_2AuNR but which was illuminated with 200 mW laser output power. Additionally, for each case, thermal images were taken after a time of 45 seconds of CW laser heating, just prior to the CW laser being turned off, when the laser-induced heating is expected to have been at its maximum. The acquired raw thermal data was then converted to surface temperature (°C) using a black body temperature calibration curve.

The consistency of the IVPA signal change with respect to both changing saline environment temperature and CW laser induced heating of a single location containing SiO_2AuNR within the human coronary artery is demonstrated in Figure 3.11A. The percent change in IVPA signal with respect to change in the saline tank temperature in the absence of any CW laser heating is provided in black, with a 10°C temperature rise resulting in an 83.6% change in measured IVPA signal intensity. At varying saline tank temperatures, the CW laser was also briefly turned on to produce additional heating of the SiO_2AuNR using distinct output energies of either 60 mW (orange) or 200 mW (blue). Each of the plotted lines represents the total percent IVPA signal increase from the baseline saline tank temperature, including both the increased temperature of the

saline environment and the locally induced temperature rise caused by CW heating, if applied. By inspection of the percent change in IVPA signal induced by the CW laser, it is evident that the IVPA monitored heating of the SiO_2AuNR amounted to average local temperature rises of approximately 3.0°C (21.1 % increase in IVPA signal intensity) and 7.1°C (58.8 % increase in IVPA signal intensity) over the baseline saline and arterial temperature (black) for the 60 mW and 200 mW output energies, respectively.

The FLIR images and temperature profiles presented in Figure 3.11B further confirm the extent of CW laser induced heating and the specificity of heating to the region of the human coronary artery containing SiO_2AuNR. Each of the FLIR thermal images shown were generated following approximately 45 seconds of CW laser heating. The optical fiber, seen on the right of each image, was focused on a region of interest, either the SiO_2AuNR inclusion (top and middle) or a control region (bottom) of the human coronary artery. Illumination of the SiO_2AuNR inclusion with optical fiber output powers of 200 mW and 60 mW resulted in maximum temperature rises of 6.9°C (top) and 2.8°C (middle), respectively, as demonstrated by the temporal profile of the region of interest from the thermal image which corresponds to the surface of the SiO_2AuNR inclusion. These values are in good agreement with the measured temperature rise using the integrated IVPA imaging catheter (Fig. 3.11A). The slight differences observed between the IVPA monitored temperature rise and that measured using FLIR imaging are likely due to the required modifications in their respective experimental set-ups and the fact that FLIR thermal imaging yields only a superficial temperature measurement. The elapsed time which was required to reach steady-state temperature during and following CW laser heating which was observed in the case of 200 mW power output (top) is also in agreement with the temporal rise and fall profiles of the recorded IVPA signal intensity (Fig. 3.10B). Additional FLIR thermal imaging performed with an optical fiber output

power of 200 mW illuminating a region of the coronary artery which did not contain SiO_2AuNR reveals a temperature rise of less than 1.5°C (bottom), further confirming that background tissue heating is minimized by utilizing CW laser heating of SiO_2AuNR strongly absorbing within the near-infrared optical wavelength range.

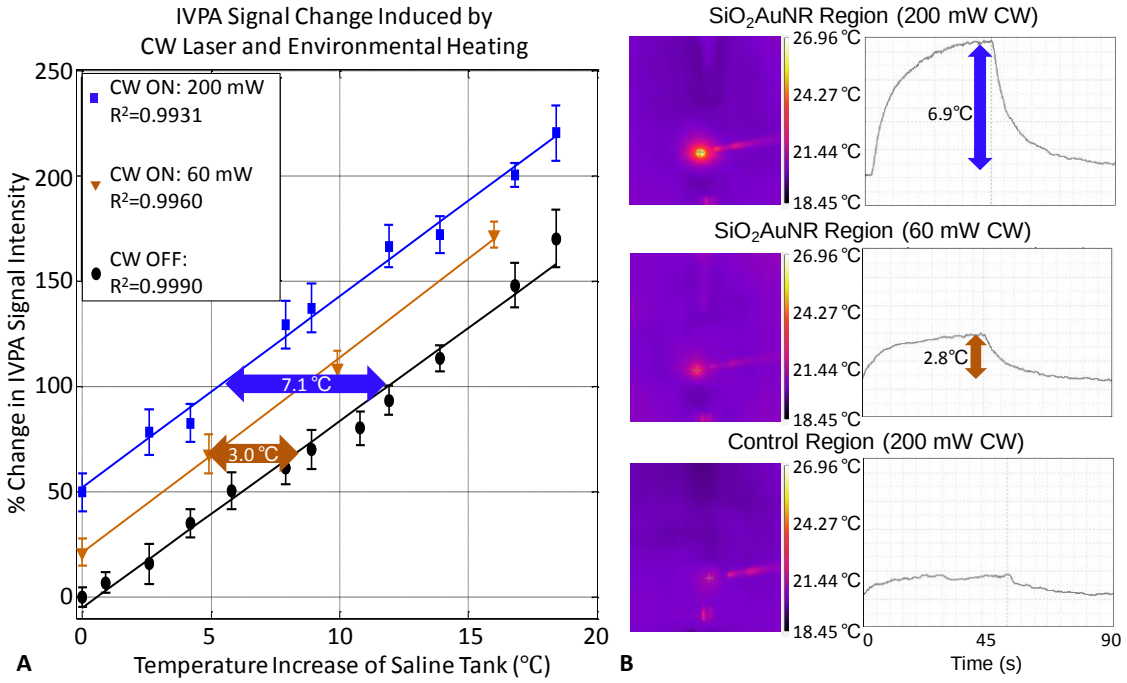

Figure 3.11: Confirmation of IVPA temperature monitoring during heating of SiO_2AuNR on a human right coronary artery ex-vivo. (A) The percent IVPA signal change versus relative baseline temperature are plotted in the absence of CW laser heating (black), and following CW laser heating of the SiO_2AuNR inclusion using output energies of 60 mW (orange) and 200 mW (blue) from the integrated IVUS/IVPA imaging catheter. (B) FLIR thermal images and temporal profiles of surface temperature rise of the SiO_2AuNR inclusion exposed to 200 mW (top) and 60 mW (middle) CW laser heating and a control region of the artery exposed to 200 mW CW laser heating (bottom).

3. 9 DISCUSSION AND CONCLUSIONS

The linearity of IVPA signal intensity dependence on temperature was demonstrated on both colloidal particles and those aggregated within macrophage endosomes. Such a relationship was anticipated based on the sensitivity of the Grüneisen parameter to variations in temperature. Therefore, provided that there is adequate absorption to produce a photoacoustic pressure wave, IVPA provides a mechanism for measuring temperature variations within the local environment surrounding the absorbers. AuNR were previously found to preferentially accumulate within plaques of atherosclerotic rabbit models following systemic injection, and the ability to localize the nanoparticles using spectroscopic IVUS/IVPA imaging, including imaging in the presence of luminal blood, was recently demonstrated [20]. Herein, the ability to further utilize such a delivery method and the resulting AuNR contrast over surrounding blood and endogenous tissue within the near-infrared wavelength range for selective CW laser heating and IVPA temperature monitoring was introduced. By measuring the percent change in IVPA signal intensity versus the change in temperature, it is possible to assess local temperature rise independent of the local pulsed laser fluence. This method, therefore, effectively self-normalizes based on the change in photoacoustic signal, accounting for possible depth-dependent variations in both the local laser fluence and integrated IVUS/IVPA catheter sensitivity.

In addition to the IVPA monitored local temperature rise, the IVUS signal can be used to monitor the cumulative heating along a given line due to the temperature dependence of the speed of sound, which affects not only the photoacoustic signal amplitude based on its inclusion as part of the Grüneisen parameter, but also the acoustic time of flight. This effect is demonstrated in Figures 3.10C and 3.10D in which proximal shifts (i.e., reduced acoustic time of flight) of both the IVPA and IVUS peaks are

noticeable as a result of the increased speed of sound during CW laser heating (red lines). Additionally, a qualitative comparison of the extent of IVUS peak signal shifts at the location of the SiO_2AuNR inclusion, approximately 6.1 mm, and at the luminal boundary of the coronary artery, approximately 3 mm, suggests that the use of a near-infrared wavelength laser causes minimal diffuse heating at the lumen border. For uniform heating, the ratio of the signal shift to the distance from the transducer would be expected to remain constant, however the ratio is greater at the location of the nanoparticle inclusion than it is at the tissue luminal surface. This further confirms the ability to selectively heat the SiO_2AuNR with minimal nonspecific vascular heating.

Interestingly, results presented in Figures 3.5, 3.7, and 3.11 provide evidence that the slope of the IVPA signal change with temperature is dependent on more than the net SiO_2AuNR density alone. This is particularly evident in Figure 3.7B, in which cells containing the nanoparticles within endosomes exhibit a significantly greater percent IVPA signal change with temperature change than do colloidal particles with a higher net OD. This apparent discrepancy, along with variability in the measured percent IVPA signal change per 10°C temperature rise between experiments, is presumably due to variations in the aggregation state and distribution of the SiO_2AuNR. In the case of endocyosed SiO_2AuNR, groups of particles are expected to be closely packed, resulting in an enhanced efficiency of photoacoustic signal generation for a given change in the local temperature based on a greater temperature sensitivity of the effective Grüneisen parameter. Given that variations in both SiO_2AuNR concentration and distribution can influence a perceived temperature rise based on a measured IVPA signal change, further studies are needed in order to establish an understanding of the variability of CW induced heating as a function of nanoparticle concentration within cells, followed by a longitudinal study to validate the therapeutic efficacy of IVUS/IVPA-monitored PPTT of

atherosclerotic plaques *in vivo*. Additionally, a recent theoretical and *in vitro* experimental study evaluating the most effective gold nanorod size for plasmonic photothermal therapy has proposed particles with dimensions of 28 nm by 8 nm as the optimal size, while particles utilized for the results presented in this chapter exhibit a size of approximately 50 nm by 12 nm [27]. Further studies should be conducted to evaluate if the proposed optimal size remains the same following the silica coating as well as what effect the modification of core gold nanorod size will have on the efficiency of photoacoustic signal generation. These future studies will seek to evaluate the minimum temperature sensitivity of the proposed approach based on the extent of SiO_2AuNR loading which can be achieved within atherosclerotic plaques following systemic injection, as well as to establish a desirable thermal dose for optimal PPTT therapeutic efficacy.

The results in this chapter have demonstrated that IVPA imaging can be used to monitor temperature change of the local environment surrounding SiO_2AuNR based on the linear relationship between photoacoustic pressure generation and the temperature dependent Grüneisen parameter, and that such temperature change can be effectively achieved by incorporating near-infrared wavelength emitting CW laser illumination into the integrated IVUS/IVPA catheter's optical fiber to induce preferential heating of SiO_2AuNR contrast agents. IVUS/IVPA can, therefore, be used as a theranostic platform to first detect the presence of systemically injected gold nanoparticles within atherosclerotic plaques, as was demonstrated in Chapter 2, followed by subsequent IVPA-monitored, selective plasmonic photothermal heating delivered through the integrated imaging catheter. This method offers a potential solution to limitations of other intravascular laser based therapies which suffer from both a lack of specificity in the induced thermal damage and an inability to monitor the delivered thermal dose. The

tendency of gold nanoparticles to be preferentially endocytosed by macrophages (Figs. 3.3, 3.4) further support the adoption of this contrast enhanced technique as a cellular-specific therapeutic strategy for atherosclerotic plaques, and the future conjugation of targeting moieties to the SiO_2AuNR surface may provide a means of cellular/molecular specificity beyond macrophages.

3. 10 REFERENCES

1. P. P. Mendis S, Norrving B, Global Atlas on Cardiovascular Disease Prevention and Control, W. H. O. W. h. F. W. S. Organization, (2011).

2. V. r. L. Roger, A. S. Go, D. M. Lloyd-Jones, E. J. Benjamin, J. D. Berry, W. B. Borden, D. M. Bravata, S. Dai, E. S. Ford, C. S. Fox, H. J. Fullerton, C. Gillespie, S. M. Hailpern, J. A. Heit, V. J. Howard, B. M. Kissela, S. J. Kittner, D. T. Lackland, J. H. Lichtman, L. D. Lisabeth, D. M. Makuc, G. M. Marcus, A. Marelli, D. B. Matchar, C. S. Moy, D. Mozaffarian, M. E. Mussolino, G. Nichol, N. P. Paynter, E. Z. Soliman, P. D. Sorlie, N. Sotoodehnia, T. N. Turan, S. S. Virani, N. D. Wong, D. Woo and M. B. Turner, "Heart Disease and Stroke Statistics-2012 Update: A Report From the American Heart Association," *Circulation*, 125(1):e2-e220, (2012).

3. F. D. Kolodgie, R. Virmani, A. P. Burke, A. Farb, D. K. Weber, R. Kutys, A. V. Finn and H. K. Gold, "Pathologic assessment of the vulnerable human coronary plaque," *Heart*, 90(12):1385-1391, (2004).

4. B. D. MacNeill, H. C. Lowe, M. Takano, V. Fuster and I.-K. Jang, "Intravascular Modalities for Detection of Vulnerable Plaque: Current Status," *Arteriosclerosis, Thrombosis, and Vascular Biology*, 23(8):1333-1342, (2003).

5. T. Thim, M. K. Hagensen, D. Wallace-Bradley, J. F. Granada, G. L. Kaluza, L. Drouet, W. P. Paaske, H. E. BÃ¸tker and E. Falk, "Unreliable Assessment of Necrotic Core by Virtual Histology Intravascular Ultrasound in Porcine Coronary Artery Disease," *Circulation: Cardiovascular Imaging*, 3(4):384-391, (2010).

6. D. R. Obaid, P. A. Calvert, D. McNab, N. E. J. West and M. R. Bennett, "Identification of Coronary Plaque Sub-Types Using Virtual Histology Intravascular Ultrasound Is Affected by Inter-Observer Variability and Differences in Plaque Definitions," *Circulation: Cardiovascular Imaging*, 5(1):86-93, (2011).

7. C. M. Gardner, H. Tan, E. L. Hull, J. B. Lisauskas, S. T. Sum, T. M. Meese, C. Jiang, S. P. Madden, J. D. Caplan, A. P. Burke, R. Virmani, J. Goldstein and J. E. Muller, "Detection of Lipid Core Coronary Plaques in Autopsy Specimens With a Novel Catheter-Based Near-Infrared Spectroscopy System," *JACC: Cardiovascular Imaging*, 1(5):638-648, (2008).

8. M. Naghavi, E. Falk, H. S. Hecht, M. J. Jamieson, S. Kaul, D. Berman, Z. Fayad, M. J. Budoff, J. Rumberger, T. Z. Naqvi, L. J. Shaw, O. Faergeman, J. Cohn, R. Bahr, W. Koenig, J. Demirovic, D. Arking, V. L. M. Herrera, J. Badimon, J. A. Goldstein, Y. Rudy, J. Airaksinen, R. S. Schwartz, W. A. Riley, R. A. Mendes, P. Douglas and P. K. Shah, "From Vulnerable Plaque to Vulnerable Patientâ€"Part III: Executive Summary of the Screening for Heart Attack Prevention and Education (SHAPE) Task Force Report," *The American Journal of Cardiology*, 98(2, Supplement 1):2-15, (2006).

9. S. C. Smith, J. T. Dove, A. K. Jacobs, J. W. Kennedy, D. Kereiakes, M. J. Kern, R. E. Kuntz, J. J. Popma, H. V. Schaff, D. O. Williams, R. J. Gibbons, J. P. Alpert, K. A. Eagle, D. P. Faxon, V. Fuster, T. J. Gardner, G. Gregoratos, R. O. Russell and S. C. Smith, "ACC/AHA Guidelines for Percutaneous Coronary Intervention (Revision of the 1993 PTCA Guidelines)â€"Executive Summary: A Report of the American College of Cardiology/American Heart Association Task Force on Practice Guidelines (Committee to Revise the 1993 Guidelines for Percutaneous Transluminal Coronary Angioplasty) Endorsed by the Society for Cardiac Angiography and Interventions," *Circulation*, 103(24):3019-3041, (2001).

10. A. Baumbach, J. A. Bittl, E. Fleck, H. J. Geschwind, T. A. Sanborn, J. E. Tcheng and K. R. K. Arsch, "Acute complications of excimer laser coronary angioplasty: A detailed analysis of multicenter results," *Journal of the American College of Cardiology*, 23(6):1305-1313, (1994).

11. R. Waksman, P. E. McEwan, T. I. Moore, R. Pakala, F. D. Kolodgie, D. G. Hellinga, R. C. Seabron, S. J. Rychnovsky, J. Vasek, R. W. Scott and R. Virmani, "PhotoPoint Photodynamic Therapy Promotes Stabilization of Atherosclerotic Plaques and Inhibits Plaque Progression," *Journal of the American College of Cardiology*, 52(12):1024-1032, (2008).

12. S. G. Rockson, P. Kramer, M. Razavi, A. Szuba, S. Filardo, P. Fitzgerald, J. P. Cooke, S. Yousuf, A. R. DeVault, M. F. Renschler and D. C. Adelman, "Photoangioplasty for Human Peripheral Atherosclerosis: Results of a Phase I Trial of Photodynamic Therapy With Motexafin Lutetium (Antrin)," *Circulation*, 102(19):2322-2324, (2000).

13. S. R. A. S. Sethuraman, J. H. Amirian, R. W. Smalling, and S. Y. Emelianov, "Intravascular photoacoustic imaging using an IVUS imaging catheter," *IEEE Trans. Ultrason. Ferroelectr. Freq. Control*, 54:978-986, (2007).

14. D. Yeager, A. Karpiouk, B. Wang, J. Amirian, K. Sokolov, R. Smalling and S. Emelianov, "Intravascular photoacoustic imaging of exogenously labeled atherosclerotic plaque through luminal blood," *Journal of Biomedical Optics*, 17(10):106016-106016, (2012).

15. A. M. Alkilany, L. B. Thompson, S. P. Boulos, P. N. Sisco and C. J. Murphy, "Gold nanorods: Their potential for photothermal therapeutics and drug delivery, tempered by the complexity of their biological interactions," *Advanced Drug Delivery Reviews*, 64(2):190-199, (2012).

16. W. J. Zhang Z, Chen C, "Gold Nanorods Based Platforms for Light-Mediated Theranostics," *Theranostics*, 3(3):223-238, (2013).

17. X. Huang and M. A. El-Sayed, "Plasmonic photo-thermal therapy (PPTT)," *Alexandria Journal of Medicine*, 47(1):1-9, (2011).

18. A. N. Kharlamov and J. L. Gabinsky, "Plasmonic photothermic and stem cell therapy of atherosclerotic plaque as a novel nanotool for angioplasty and artery remodeling," *Rejuvenation Res*, 15(2):222-230, (2012).

19. A. N. Kharlamov, A. E. Tyurnina, V. S. Veselova, O. S. Novoselova, A. S. Filatova, O. P. Kovtun, V. Y. Shur and J. L. Gabinsky, "Plasmonics for Treatment of Atherosclerosis: Results of NANOM-FIM Trial," *Nanomedicine & Nanotechnology*, 4(160):doi: 10.4172/2157-7439.1000160, (2013).

20. B. Wang, E. Yantsen, T. Larson, A. B. Karpiouk, S. Sethuraman, J. L. Su, K. Sokolov and S. Y. Emelianov, "Plasmonic Intravascular Photoacoustic Imaging for Detection of Macrophages in Atherosclerotic Plaques," *Nano Letters*, 9(6):2212-2217, (2008).

21. Y.-S. Chen, W. Frey, S. Kim, P. Kruizinga, K. Homan and S. Emelianov, "Silica-Coated Gold Nanorods as Photoacoustic Signal Nanoamplifiers," *Nano Letters*, 11(2):348-354, (2011).

22. Y.-S. Chen, W. Frey, S. Kim, K. Homan, P. Kruizinga, K. Sokolov and S. Emelianov, "Enhanced thermal stability of silica-coated gold nanorods for photoacoustic imaging and image-guided therapy," *Opt. Express*, 18(9):8867-8878, (2010).

23. Y.-S. Chen, W. Frey, C. Walker, S. Aglyamov and S. Emelianov, "Sensitivity enhanced nanothermal sensors for photoacoustic temperature mapping," *Journal of Biophotonics*, 6(6-7):534-542, (2013).

24. N. R. Jana, L. Gearheart and C. J. Murphy, "Seed-Mediated Growth Approach for Shape-Controlled Synthesis of Spheroidal and Rod-like Gold Nanoparticles Using a Surfactant Template," *Advanced Materials*, 13(18):1389-1393, (2001).

25. J. Davignon and P. Ganz, "Role of Endothelial Dysfunction in Atherosclerosis," *Circulation*, 109(23 suppl 1):III-27-III-32, (2004).

26. B. K. Andrei, W. Bo and Y. E. Stanislav, "Development of a catheter for combined intravascular ultrasound and photoacoustic imaging," *Review of Scientific Instruments*, 81(1):014901, (2010).

27. M. A. Mackey, M. R. K. Ali, L. A. Austin, R. D. Near and M. A. El-Sayed, "The Most Effective Gold Nanorod Size for Plasmonic Photothermal Therapy: Theory and In Vitro Experiments," *The Journal of Physical Chemistry B*, 118(5):1319-1326, (2014).

Chapter 4: Photosensitizer-Doped Gold Nanorods as Multifunctional Theranostic Agents

4. 1 INTRODUCTION

Coronary heart disease remains a leading global cause of mortality in the United States and throughout the industrialized world. In the United States alone, it is estimated that over 1 million people suffered a myocardial infarction in 2010, with nearly 380,000 associated fatalities [1]. This high mortality rate can be attributed, in part, to an inability to adequately diagnose and treat high-risk atherosclerotic lesions such as thin-capped fibroatheroma (TCFA). Over the past several decades, our understanding of the cellular and molecular mechanisms which promote coronary plaque progression and destabilization has improved significantly. Advances in molecular biology have led to the evolution from a view of coronary atherosclerosis as sites of passive lipid accumulation and storage to a much more dynamic biological process involving endothelial dysfunction with low density lipoprotein infiltration, monocyte recruitment and subsequent foam cell formation, and over expression of destabilizing extracellular matrix proteins, all of which lead to the formation of a prothrombotic core which can induce a myocardial infarction and sudden cardiac death if exposed to the artery lumen [2-5].

Despite increased appreciation for the dynamic cellular and molecular processes involved in the development of a vulnerable atherosclerotic plaque, clinical diagnostic and interventional practices have failed to fully keep pace. Rather, the most common diagnostic imaging modalities, including contrast angiography, cardiac computed tomography, intravascular ultrasound (IVUS), and intravascular optical coherence tomography (OCT), provide clinicians with a view of vessel morphology, as discussed in greater detail in Chapter 1 [6]. As a result, diagnosis and associated decisions regarding intervention for a particular arterial lesion is based primarily on the severity of lumen

narrowing and obstruction of blood flow, with limited characterization of its underlying composition. The limitations associated with basing diagnoses on the extent of arterial narrowing are made particularly evident by studies showing that arteries exhibit positive remodeling to maintain lumen area as plaques develop up to a total burden of 40% wall [7] and that extreme narrowing of arteries in the weeks or months before a myocardial infarction are found in only about 15% of cases [8]. In light of the limited plaque information provided by clinical imaging modalities, it is not surprising that procedures performed during percutaneous coronary interventions are also aimed at restoring luminal flow, largely irrespective of potential variations in the molecular composition of the atherosclerotic plaque being treated. While recent advances in the related technologies, such as the widespread adoption of drug eluting stents, has led to significant improvements in achieving their primary goal of revascularization [9], such techniques do not directly account for or stabilize the underlying composition of atherosclerotic lesions [10]. In this respect, coronary interventional practices are similar to the available, widely-utilized diagnostic techniques, both of which do little to account for underlying biological processes that drive atherosclerotic plaque destabilization.

Recent clinical approval of an intravascular imaging modality combining near infrared spectroscopy with intravascular ultrasound (Infraredx Inc., Burlington Massachusetts) offers an improvement for assessment of atherosclerotic lesion composition through its ability to detect the presence of lipid. The modality is being implemented in clinical settings and actively evaluated in clinical trials designed to investigate if and how interventional treatment strategies should be affected based on the composition of a plaque rather than its structural features alone. For example, the Coronary Assessment by Near-infrared of Atherosclerotic Rupture-prone Yellow (CANARY) trial is investigating the presence of lipid-rich plaque as a potential indicator

of increased periprocedural risk which could provide an indication for distal embolic protection [11,12]. Such studies represent a potential step towards the adoption of novel diagnostic imaging modalities to tailor treatment strategies based on known compositional risk factors within atherosclerotic plaques.

Combined intravascular ultrasound and photoacoustic (IVUS/IVPA) imaging has also been introduced and investigated within the preclinical setting as a dual-modality approach for complimentary assessment of arterial morphology and composition [13]. IVPA imaging relies on the delivery of nanosecond-pulsed optical illumination to elicit an acoustic response which can enable selective detection of specific endogenous chromophores or exogenous contrast agents (see Chapter 1 for a more thorough description of photoacoustic signal generation). The induced photoacoustic transients can then be detected and localized using an ultrasound transducer, while conventional pulse echo ultrasound enables the formation of an inherently co-registered assessment of arterial morphology. Combined IVUS/IVPA imaging has been particularly heavily investigated as a tool for imaging the distribution of lipid within atherosclerotic plaques [14-20].

In Chapter 2, the expansion of the modality as a platform to differentiate systemically injected gold nanorod (AuNR) contrast agents was introduced. AuNR were shown to be phagocytosed by macrophages and to preferentially extravasate into atherosclerotic lesions in rabbit models of atherosclerosis, thereby enabling their localization using IVPA imaging within the near infrared tissue optical window injection [19]. In Chapter 3, motivation for the potential use of AuNR in characterizing atherosclerotic plaque was further expanded through the demonstration that the IVUS/IVPA imaging platform can be utilized to deliver and monitor photothermal heating of the plasmonic nanoparticles. The integration of light emitted from a

continuous wave laser source into the optical fiber of the imaging catheter was shown to enable heating of the local environment surrounding AuNR, with simultaneous monitoring of the temperature-dependent change in IVPA signal intensity plaques [21]. Together, Chapters 2 and 3 introduced the potential for visualizing the location of macrophages within atherosclerotic plaques as well as the subsequent application of localized and controlled photothermal treatment using the IVUS/IVPA imaging platform, thus enabling an improved ability for treatment strategies more specific to lesion composition.

4.1.1. Motivation for Combined Plasmonic Photothermal Therapy and Photodynamic Therapy

Recently, multimodality therapy using hybrid nanoparticle constructs for complimentary plasmonic photothermal therapy (PPTT) and photodynamic therapy (PDT) have come under increasing investigation as a result of the demonstrated potential to achieve improved therapeutic efficacy using combination therapy [22]. As discussed in Chapter 3, Section 3.1 and Chapter 1, Section 1.5.2, PPTT utilizes the illumination of highly optically absorbing plasmonic nanoparticles to induce cytotoxic photothermal effects. Similarly, PDT relies on the delivery and subsequent low energy illumination of a photosensitizing agent which induces a cascade resulting in the intracellular formation of cytotoxic reactive oxygen species (see Chapter 1, Section 1.5.3). Many investigational studies have explored the use of hybrid nanoconstructs combining photosensitizers with highly absorbing nanoparticles for cancer treatment applications [23-33]. Among these multifunctional nanoparticles, many have centered on the covalent attachment of photosensitizers to gold nanoparticles, while one has demonstrated the ability to embed the photosensitizer directly within a silica layer surrounding a gold nanorod [29].

Both PDT and PPTT have been independently investigated for the treatment of atherosclerotic plaques. The use of gold nanoparticles for PPTT was recently reported as a tool for atherosclerotic plaque treatment, including the initiation of first-in-man clinical trials [34,35]. Furthermore, the application of PDT for the reduction or stabilization of atherosclerotic plaques, termed photoangioplasty, has also been heavily investigated using the photosensitizers Lutetium Texaphyrin (LuTex), marketed under the trade name Antrin (Pharmacyclics Inc., Sunnyvale, California), and MV0611 (Miravant Medical Technologies, Santa Barbara, California). Each of these photosensitizers has been shown to preferentially localize within atherosclerotic plaques in animal models of atherosclerosis over the course of 24 hours following systemic injection [36,37]. These same studies have also demonstrated a reduction in plaque area with corresponding increases in lumen area as well as a reduction in the number of macrophages present within the lesions based on histological staining of the lesions approximately one month following the treatment. Phase I clinical trials using LuTex-excited photoangioplasty identified safe photosensitizer and light dosages, reporting no coronary complications and low incidence of side effects associated with the procedure [38,39].

Despite the established potential for improved multimodal therapeutic efficacy and these separate investigations of PPTT and PDT for intravascular treatments, investigation into their combined use with a hybrid nanoparticle designed specifically for therapy of atherosclerotic plaques has not yet been reported. Given the prior and ongoing investigation of gold nanoparticles for PPTT and LuTex photosensitizers for PDT of atherosclerotic lesions, the combination of these exogenous agents represents a natural first choice for such an application. To that end, this chapter focuses on the synthesis and *in vitro* characterization of a novel multifunctional nanoparticle platform combining LuTex-loaded silica-coated gold nanorods (LuTex/SiO_2AuNR) designed to extend the

utility of the IVUS/IVPA imaging platform to enable image-guided, dual PPTT-PDT therapy of atherosclerotic plaques.

4. 2 SYNTHESIS AND CHARACTERIZATION OF LUTETIUM TEXAPHYRIN-LOADED SILICA-COATED GOLD NANORODS

Multifunctional nanoparticles containing AuNR as strong absorbers for PPTT and LuTex for PDT were synthesized by directly encapsulating photosensitizers within a silica shell surrounding the AuNR, yielding LuTex-doped silica-coated gold nanorods (LuTex/SiO_2AuNR) (Fig. 4.1). A standard synthesis protocol was developed based off of a facile modification to the method for producing SiO_2AuNR, introduced in Chapter 3.

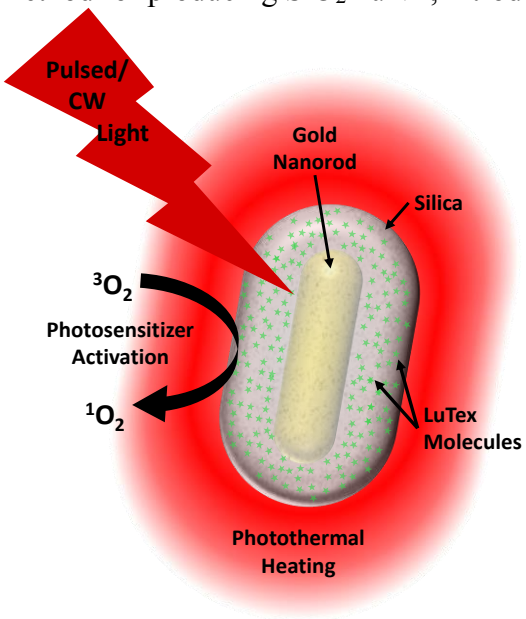

Figure 4.1: Schematic of LuTex/SiO_2AuNR for combined plasmonic photothermal therapy (PPTT) and photodynamic therapy (PDT).

4.2.1. Multifunctional Nanoparticle Synthesis

Cetyltrimethylammonium bromide (CTAB) stabilized gold nanorods were synthesized using an established seed mediated growth method which is described in Chapters 2 and 3 [40]. The as prepared CTAB-AuNR were then twice washed via

centrifugation at 18,000 rcf for 40 minutes and re-suspended in ultra-filtered deionized water at a final peak optical density (OD) of 15, as measured by UV-Vis spectroscopy (Synergy HT, BioTek). Poly ethylene glycol (PEG, 2kD) was then attached to the AuNR surface by adding 1 mL of mPEG-thiol (0.5 mM) per 5 mL of OD 15 CTAB-AUNR. The mixture was sonicated for 30 minutes and allowed to react overnight on a shaker under modest agitation to facilitate the replacement of CTAB with PEG. The resulting PEG-AuNR were washed via centrifuge filtration (Amicon ultra-15, Millipore) for 10 min at 3000 rcf and re-suspended in water at an OD of 15.

Silica coating of the PEG-AuNR in the presence of LuTex was achieved by a modification to the Stöber-based approach reported in Chapter 3, Section 3.2.1 [25]. Under vigorous stirring, 2.0 mL of the OD 15 PEG-AuNR were added to 3.0 mL of isopropanol, followed by the addition of 1.2 mL of tetraethyl orthosilicate (TEOS) in isopropanol (3% v/v). A 3.8% ammonia solution in isopropanol was added to adjust the solution to a pH of 11, and the solution was reacted under moderate stirring (400 rpm) for 20 minutes prior to the addition of the photosensitizer to initiate silica deposition on the AuNR surface.

LuTex, an expanded porphyrin, was synthesized as described in the literature [41,42]. LuTex was dissolved in dimethyl sulfoxide (DMSO) at a concentration 1 mg/mL and 1mL was added to the SiO_2AuNR reaction, followed by addition of the ammonia solution to maintain the reaction solution at a pH of 11. The solution was allowed to react in the dark under stirring at 400 rpm for an additional 2 hours, with the silica coating thickness monitored by a red shift in the longitudinal peak absorbance up to approximately 25 nm as measured by UV-Vis spectroscopy throughout the reaction. Additionally, some batches of the LuTex/SiO_2AuNR were encapsulated in a PEG surface layer through the addition of 900 μL of 3.3 mg/mL mPEG-silane and further reacting for

30 minutes. The resulting LuTex/SiO_2AuNR, or mPEG-LuTex/SiO_2AuNR, were diluted 2x in ultra-filtered deionized water and twice washed via centrifuge filtration (100 kD cut-off) for 10 min at 1000 rcf and re-suspended in water at the desired final OD. Free LuTex does not readily pass through the cellulose membrane of centrifuge filters. Therefore, residual unbound LuTex molecules were removed through a series of 3-4 centrifugation washing steps using a bench top microcentrifuge at 8000 rcf for 10 min. The UV-Vis spectrum of the supernatant from each washing step was measured to validate the successful removal of free LuTex from the LuTex/SiO_2AuNR.

Figure 4.2A provides representative UV-Vis spectra of LuTex/SiO_2AuNR synthesis, including the core PEG-AuNR (red), the reaction solution containing LuTex, silica, and AuNR prior to washing (blue) and the final washed product (green). A red shift in the longitudinal peak absorbance of approximately 20 nm is observed following the reaction, consistent with silica coting of the AuNR. Additionally, peaks at approximately 470 nm and 732 nm which correspond to LuTex absorbance peaks are clearly evident in the reaction mixture and, to a lesser extent, in the final washed product, indicative of successful LuTex encapsulation. Comparison of the LuTex/SiO_2AuNR supernatant obtained following centrifugation from the final wash during the nanoparticle synthesis and following one week in suspension at room temperature revealed no indications of AuNR aggregation or LuTex leakage from the silica layer, suggesting that the multifunctional nanoparticles exhibit adequate shelf-life stability for further evaluation (Fig. 4.2B).

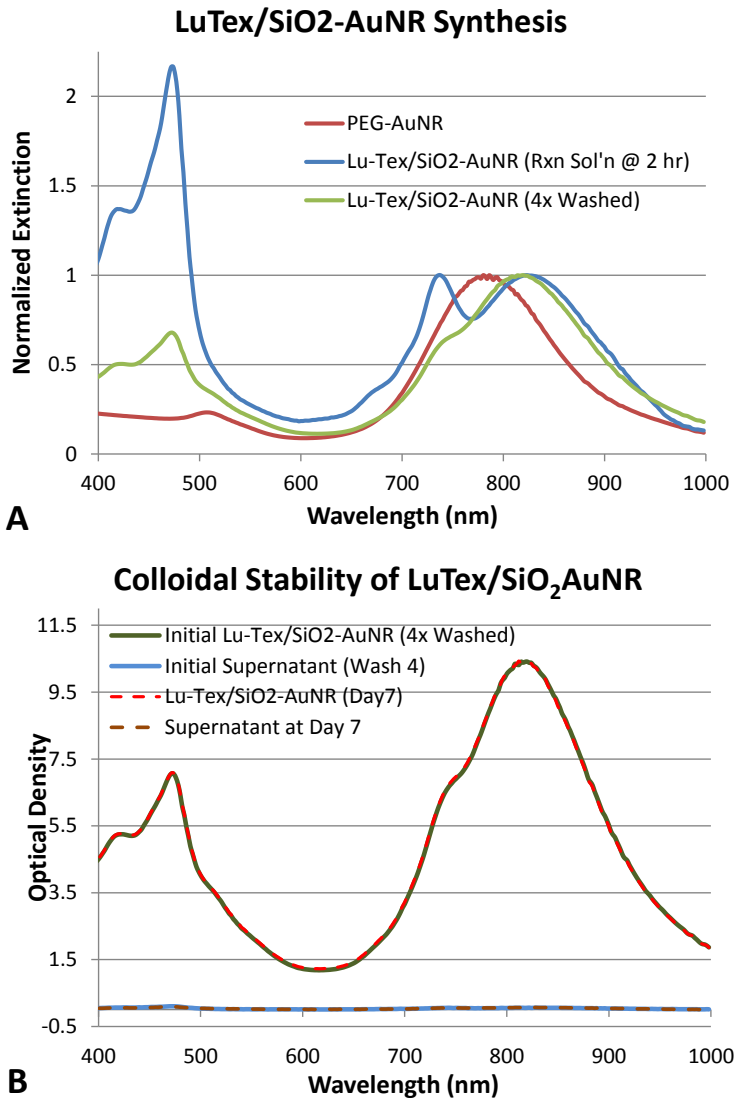

Figure 4.2: UV-Vis Spectra from a representative batch of LuTex/SiO_2AuNR. (A) Spectra of core PEG-AuNR, reaction solution containing LuTex prior to washing, and resulting washed product. (B) Validation of LuTex/SiO_2AuNR stability and low LuTex leakage in water.

4.2.2. Qualitative Assessment of LuTex Loading Efficiency under Variable Reaction Conditions

A qualitative assessment of reaction conditions on LuTex loading efficiency was performed to further refine the LuTex/SiO_2AuNR synthesis protocol. It has been shown

that the thickness of the silica layer deposited on the AuNR surface can be controlled by adjusting both the volume of TEOS and the overall reaction time [43]. Additionally, the impact of reaction pH and LuTex molecular structure were evaluated. Specifically, four parallel reactions using the same PEG-AuNR core particles and reagent solutions were initiated, with the only variation being the volume percent concentration of the ammonia solution used during the reaction. The resulting sensitivity of LuTex loading as over a reaction pH range from approximately 10.5 to 11.5 is clearly indicated by the resulting washed LuTex/SiO_2AuNR shown in Figure 4.3. The molar extinction coefficients for comparable AuNR dimensions and LuTex alone have been reported to be 4.4 x 10^9 and 4.2x10^4 M^{-1} cm^{-1} at the AuNR peak wavelength and the 732 nm absorbance peak of LuTex, respectively [44,45]. The extinction coefficient of LuTex at 732 nm was used to measure the corresponding extinction coefficient at the stronger 470 nm peak, found to be 1.2 x 10^5 M^{-1} cm^{-1}. Using the ratio of extinction coefficients between the AuNR peak and the 470 nm peak of LuTex and evaluating the relative contribution of the optical extinction spectra for each component, the LuTex loading is estimated to range from 7 x 10^2 to 7 x 10^3 LuTex molecules per AuNR for the pH= 10.5 and pH= 11.1 reactions.

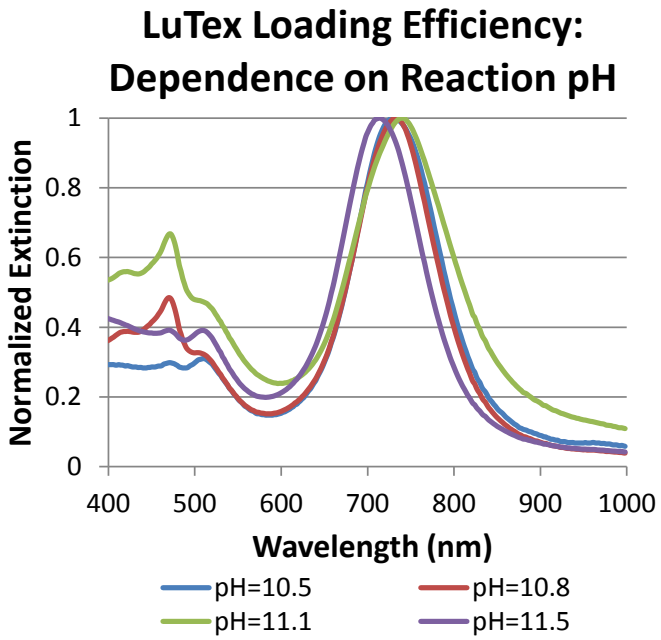

Figure 4.3: Effect of reaction pH on silica coating and LuTex loading efficiency.

The impact of the LuTex molecular structure itself was also evaluated using three different molecular structures, shown in Figure 4.4. The structures associated with the side branches R1, R2 and R3 notably vary in terms of the increasing presence from 0 to 2 carboxylic acid groups, which are expected to be negatively charged during the high pH synthesis reaction.

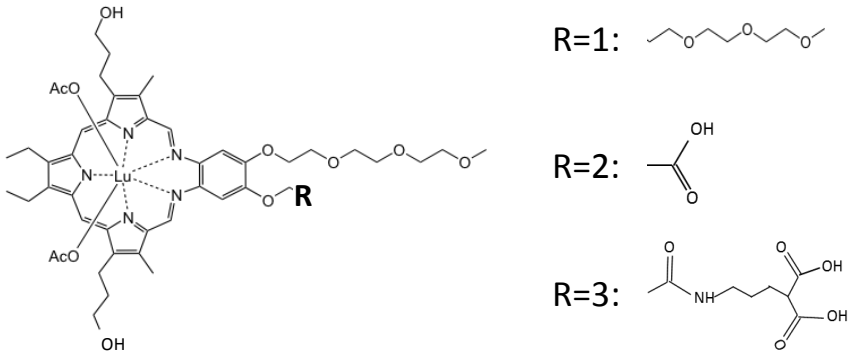

Figure 4.4: Molecular structures of LuTex utilized for assessment of the impact of functional groups on the loading efficiency during LuTex/SiO_2AuNR synthesis.

Figure 4.5 shows representative products obtained using each of the three LuTex structures. Assessment of the UV-Vis spectra of washed LuTex/SiO_2AuNR reveals an inverse relationship between carboxylic acid functional groups and the LuTex loading efficiency, with estimated LuTex molecules per AuNR ranging from 1.5 x 10^3 for R3 to 3.8 x 10^4 for R1 (Fig. 4.5A). However, assessment of transmission electron microscopy (TEM) images for each molecular structure indicates a relationship between increasing carboxylic acid functional groups LuTex structure and increasing uniformity of silica coating AuNR, with a decreased tendency of LuTex/SiO_2AuNR to aggregate, shown from top to bottom in Figure 4.5B. In fact, synthesis using the structure R1 demonstrated partial aggregation during initial filter centrifugation washing steps, whereas the other two structures were much more stable under comparable conditions. Note that different batches of PEG-AuNR core particles were used during synthesis with each of the LuTex molecular structures compared. As a result of the desired silica uniformity and particle stability, all subsequent results utilizing LuTex/SiO_2AuNR were obtained using the LuTex structure R3, despite the resulting sacrifice in LuTex loading efficiency.

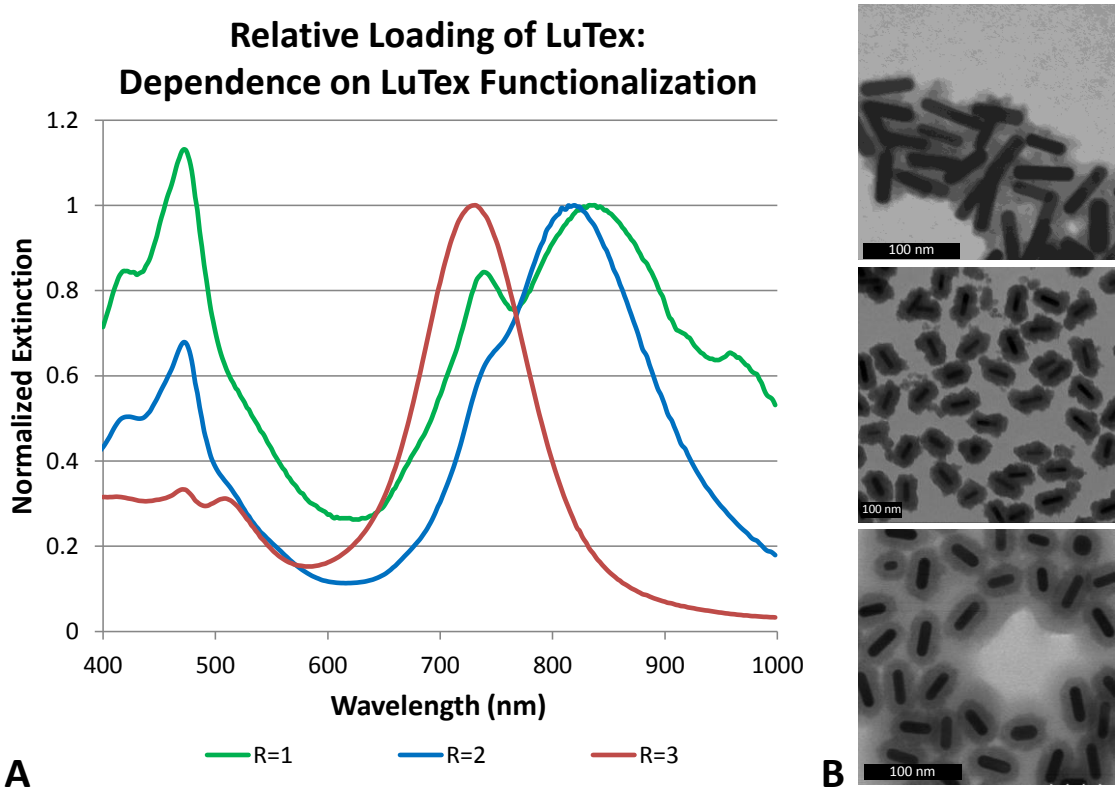

Figure 4.5: Relative loading efficiency of LuTex with different functional groups. (A) UV-Vis spectra normalized to the AuNR absorbance peak for functional groups R=1, 2 and 3. (B) Corresponding TEM images for LuTex/SiO_2AuNR synthesized with LuTex functional groups R=1 (top), R=2 (middle), and R=3 (bottom).

4. 3 SINGLET OXYGEN GENERATION

The ability of LuTex/SiO_2AuNR to generate singlet oxygen ($^1O_2$), a cytotoxic product of photosensitizer excitation during PDT, was further subsequently evaluated in comparison to free LuTex with and without AuNR. The photochemical oxidation of 9,10-anthracenediylbis(methylene) dimalonic acid (ABDA) by $^1O_2$ results in a decrease in the ABDA absorption peak located at approximately 400 nm and its corresponding fluorescence efficiency [46]. To compare the $^1O_2$ production efficiency between LuTex/SiO_2AuNR and free LuTex using the spectral changes induced in ABDA, the

optical density of SiO_2AuNR with either free and encapsulated LuTex, as well as free LuTex without AuNR were matched. Solutions containing 200 µL solutions of LuTex and/or AuNR at matched concentrations and 100 µL of freshly prepared 60 µM ABDA stock were prepared (Fig. 4.6A). Each of the four experimental solutions, water, free LuTex, free LuTex in the presence of PEG-SiO_2AuNR and PEG-LuTex/SiO_2AuNR were subsequently illuminated with a 735 nm LED (Thorlabs M735L3, Newtown, New Jersey) at a 40 mW/cm^2 for a total of 8 min. The fluorescence of ABDA (ex/em: 380/420) was recorded for each group in 30 second intervals during illumination (Fig. 4.6B) and the initial and final optical absorption spectrum were measured to confirm matching decrease in the ABDA absorbance spectrum (Fig. 4.6C). Subsequently, a rate constant for the exponential decay in ABDA fluorescence as a function of illumination time was calculated for each group using a previously reported approach as an approximation of $^1O_2$ production [47]. Following first order kinetics, the rate constant of ABDA decay can be determined by:

$$[ABDA]_t = [ABDA]_{t_o} e^{-kt} \quad \text{Eq. 4.1}$$

$$\ln\left(\frac{[ABDA]_t}{[ABDA]_{t_o}}\right) = -kt \quad \text{Eq. 4.2}$$

Figure 4.6D shows the linear best fit of the natural logarithm of measured ABDA fluorescence decay versus time. Therefore, the slope of each line is equivalent to the rate constant for each group, ranging from -2 x 10^{-4} $s^{-1}$for PEG-LuTex/SiO_2AuNR to -3.7 x 10^{-3} s^{-1} for free LuTex in the presence of PEG-SiO_2AuNR, indicating a significant reduction in the rate of $^1O_2$ production from LuTex entrapped within silica which,

depending on loading efficiencies within atherosclerotic plaques, may limit the efficacy of PDT using the multifunctional nanoparticles.

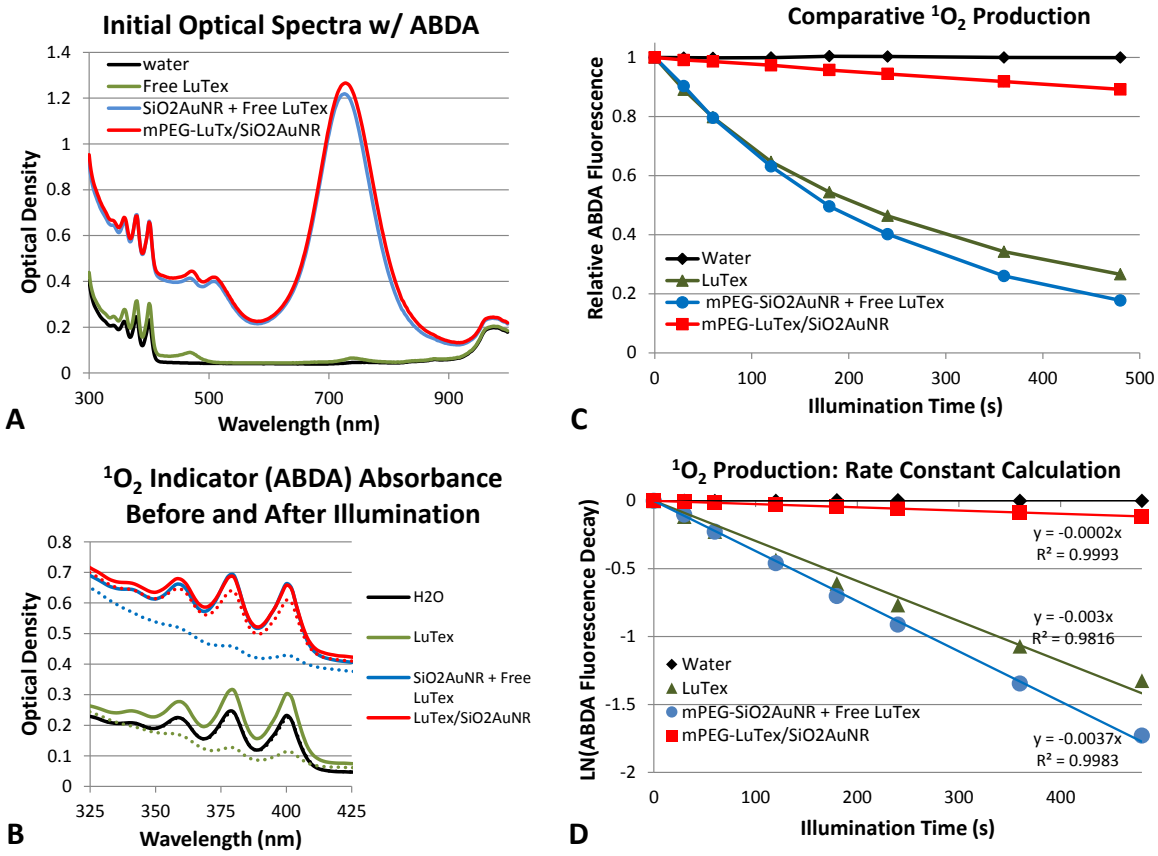

Figure 4.6: Singlet oxygen generation for LuTex and SiO_2AuNR combinations. (A) Optical extinction spectra of experimental groups with ABDA indicator, validating equal concentrations of LuTex and SiO_2AuNR. (B) Comparative decay of ABDA indicator before (solid) and after (dash) illumination for 8 min., indicating the varying degrees of oxidative decay of ABDA. (C) Relative ABDA fluorescence decay versus illumination. (D) Natural logarithm of ABDA fluorescence decay versus illumination time including best linear fits as indicators of $^1O_2$ production rate constant.

4. 4 MULTIFUNCTIONAL NANOPARTICLE STABILITY IN PHYSIOLOGICAL CONDITIONS

Stability of PEG-LuTex/SiO_2AuNR in variable physiologically relevant solutions was evaluated to further characterize the multifunctional nanoparticles. Figure 4.7 shows

representative TEM images obtained following incubation of PEG-SiO_2AuNR in water, PBS at low (endosomal) pH, PBS at neutral pH, and DMEM cell culture media with 5 % fetal bovine serum (FBS) at 37 °C for 24 hours. Particles incubated in both neutral PBS (Fig. 4.7C) and cell culture media (Fig. 4.7D) exhibit clear signs of reduced silica density or complete stripping of the silica layer from AuNR surfaces, while the particles incubated in low pH PBS remained stable over the same period of time.

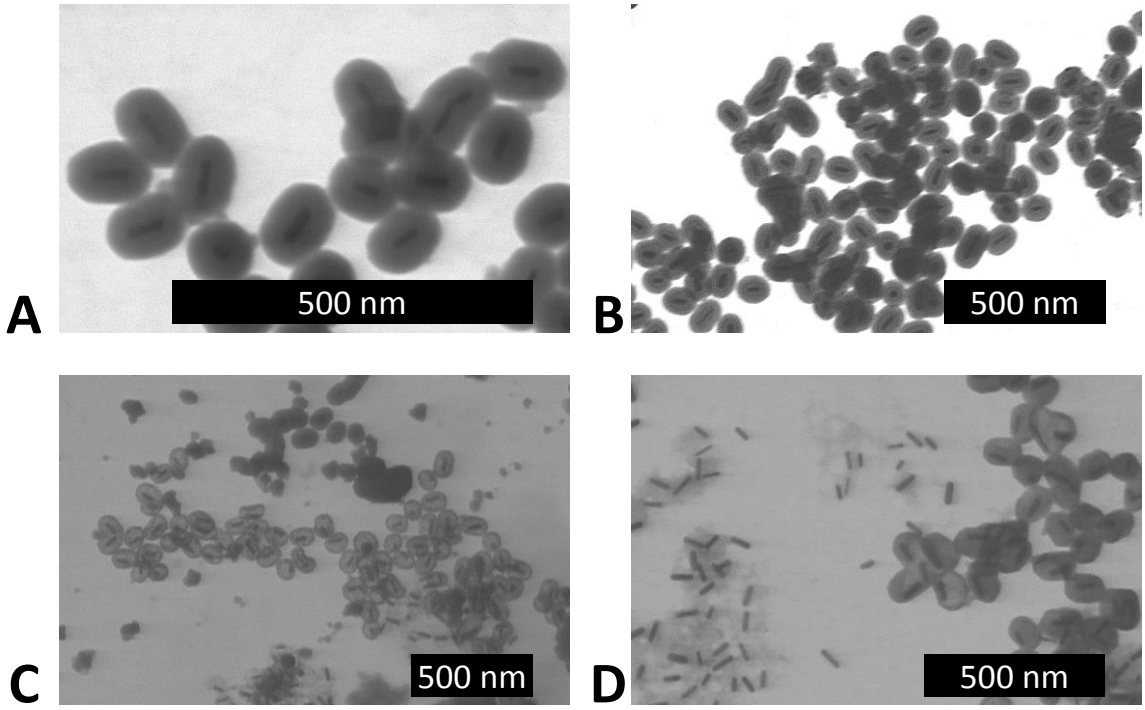

Figure 4.7: TEM revealing stability of PEG-SiO_2AuNR following 24 hours exposure to 37°C: (A) H_2O, (B) PBS at pH= 5.0, (C) PBS at pH=7.4, and (D) DMEM cell culture media with 5% FBS.

LuTex/SiO_2AuNR were then evaluated to verify similar silica degradation in cell culture media. TEM analysis reveals the same stripping effect of silica following 24 hour incubation of LuTex/SiO_2AuNR in the same cell culture media (Fig. 4.8).

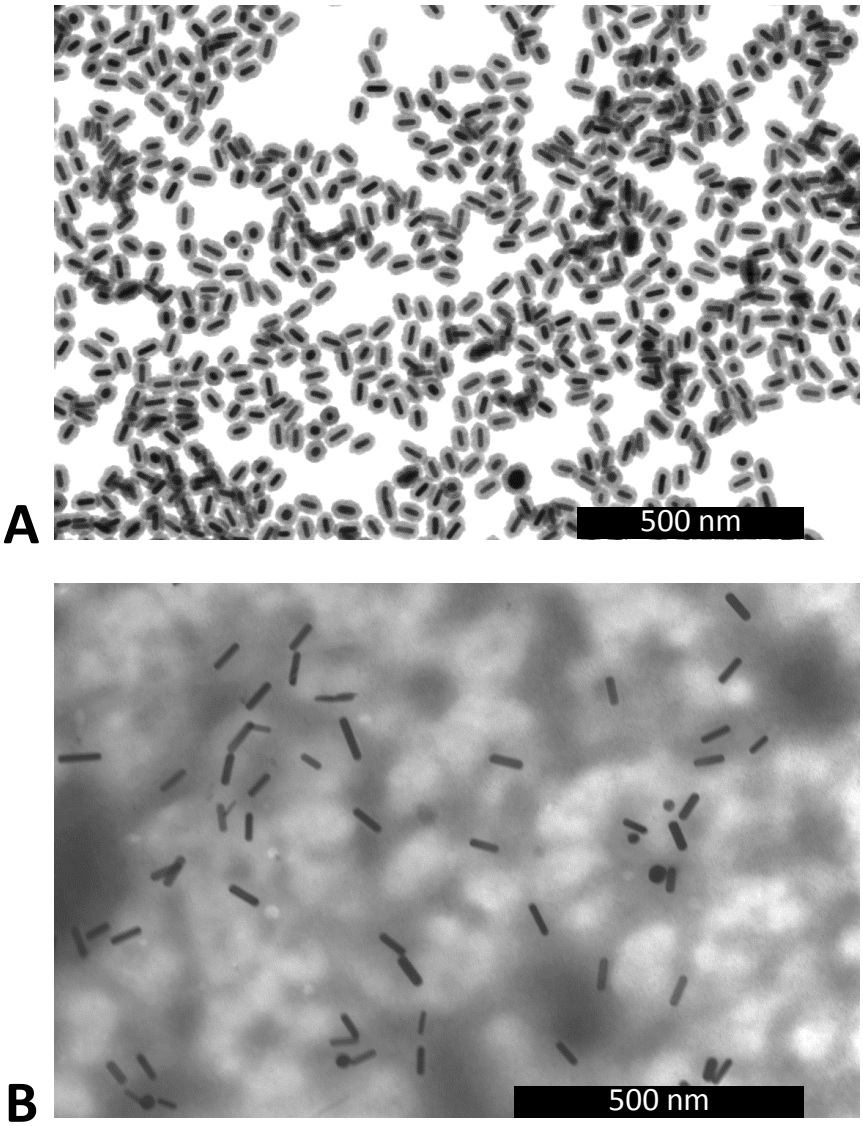

Figure 4.8: TEM images of LuTex/SiO_2AuNR following 24 hour incubation in (A) H_2O and (B) DMEM cell culture media with 5% FBS revealing the loss of SiO_2 coating.

4. 5 SILICA DEGRADATION KINETICS AND PASSIVE DYE RELEASE

The kinetics of silica degradation were evaluated through the synthesis of fluorescein isothiocyanate (FITC)-doped SiO_2AuNR. The PEG-FITC/SiO_2AuNR were synthesized using a one-to-one exchange of the dye for the synthesis protocol of PEG-LuTex/SiO_2AuNR described in Section 4.2.1. The prepared PEG-FITC/SiO_2AuNR were then incubated in DMEM cell culture media with 5% FBS for 12 hours. Comparison of the initial and final spectra of the nanoparticles presented in Figure 4.9A, a clear blue shift in the AuNR peak absorbance attributable to the stripping of silica is observed. Additionally, the fluorescence intensity of FITC from the PEG-FITC/SiO_2AuNR particles as well as from free FITC and PEG-SiO_2AuNR without the fluorescent dye in DMEM was tracked over the 12 hour period. In contrast to the gradual decay in fluorescence intensity for the free FTIC and PEG-SiO_2AuNR, the fluorescence intensity from PEG-FITC/SiO_2AuNR revealed a stable signal over the first two hours of incubation in in DMEM culture media, followed by a 8-fold increase between 2 and 6 hours for PEG-FITC/SiO_2AuNR (Fig. 4.9B), indicative of delayed initiation of silica decay.

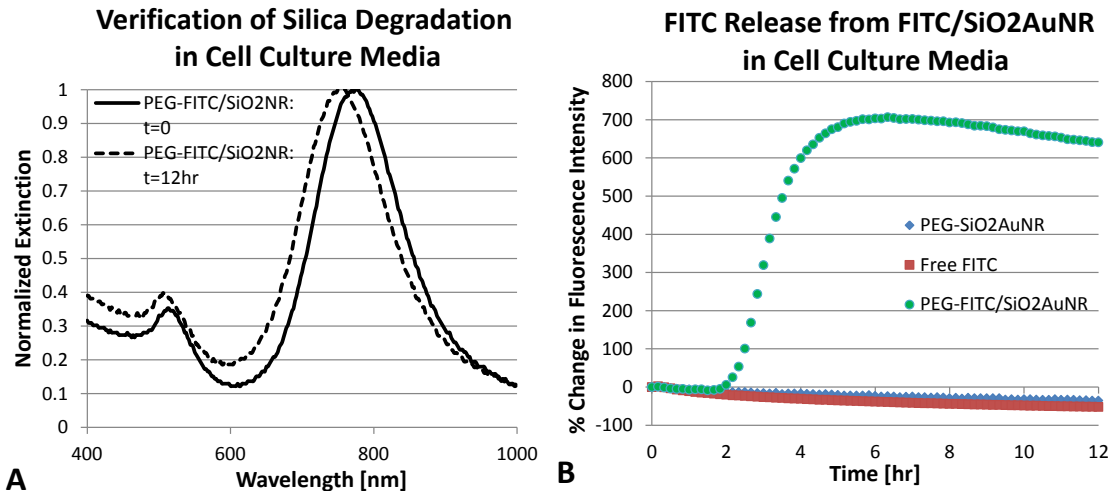

Figure 4.9: Validation of silica degradation and cargo release using PEG-FITC/SiO2AuNR. (A) UV-Vis spectrum taken before and after 12 hours of incubation in DMEM, 10% FBS culture media, revealing blue shift associated with loss of silica coating. (B) Kinetic study of fluorescence from controls and PEG-FITC/SiO_2AuNR in culture media over 12 hours.

Evaluation of LuTex/SiO_2AuNR revealed similar trends to that of FITC/SiO_2AuNR, including the blue shift in the AuNR peak absorbance following incubation in culture media (Fig. 4.10A). Confirmation of LuTex release following incubation in culture media was enabled through assessment of the supernatant by UV-Vis spectroscopy. Specifically, LuTex/SiO_2AuNR were incubated in culture media for 24 hours after which time the entire solution was centrifuged at 8000 rcf for 10 minutes to spin down the colloidal AuNR. Evaluation of the supernatant reveals a significantly increased peak at 470 nm relative to that of the AuNR peak absorbance at approximately 780 nm due to the increased presence of free LuTex (Fig. 4.10B). No detectable peak at 470 nm is observed from SiO_2AuNR without LuTex exposed to the same conditions.

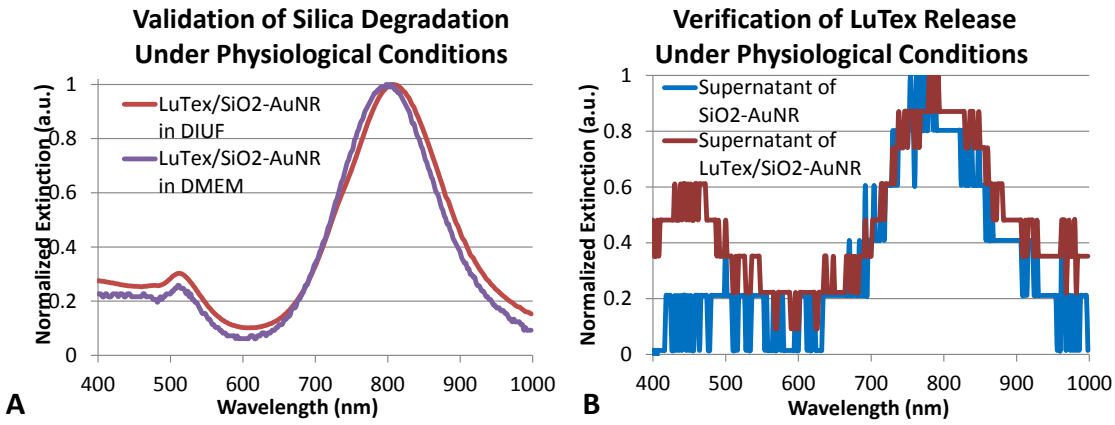

Figure 4.10: Validation of LuTex release as a result of silica stripping under physiological conditions. (A) LuTex/SiO_2AuNR in water and DMEM cell culture media with 5% FBS. (B) Supernatant of SiO_2AuNR with and without LuTex following incubation in culture media.

In light of the silica degradation which occurs under physiological conditions but not in water, further evaluation of $^1O_2$ production was conducted to assess the impact of LuTex/SiO_2AuNR pre-incubated in cell culture media for increasing amounts of time. Equal concentrations of LuTex/SiO_2AuNR were added to DMEM media with 5% FBS in triplicate at intervals from 24 hours, 4 hours, 2 hours and immediately prior to initiation of a study again assessing ABDA fluorescence decay versus illumination time. All wells were subsequently illuminated (735 nm, 40 mW/cm^2) for a total of 3 minutes with the fluorescence intensity of ABDA recorded at 30 second intervals. Figure 4.11 provides the resulting rate constant for $^1O_2$ production (inverse of ABDA decay rate constant), indicating a gradual increase in the efficiency for increasing pre-incubation time in cell culture media. A total increase in the $^1O_2$ production efficiency of approximately 68% was observed between the groups with 0 and 24 hours of pre-incubation time. Notably, the rate constant for the group which received no pre-incubation is agreement with the calculated rate constant for LuTex/SiO_2AuNR in water.

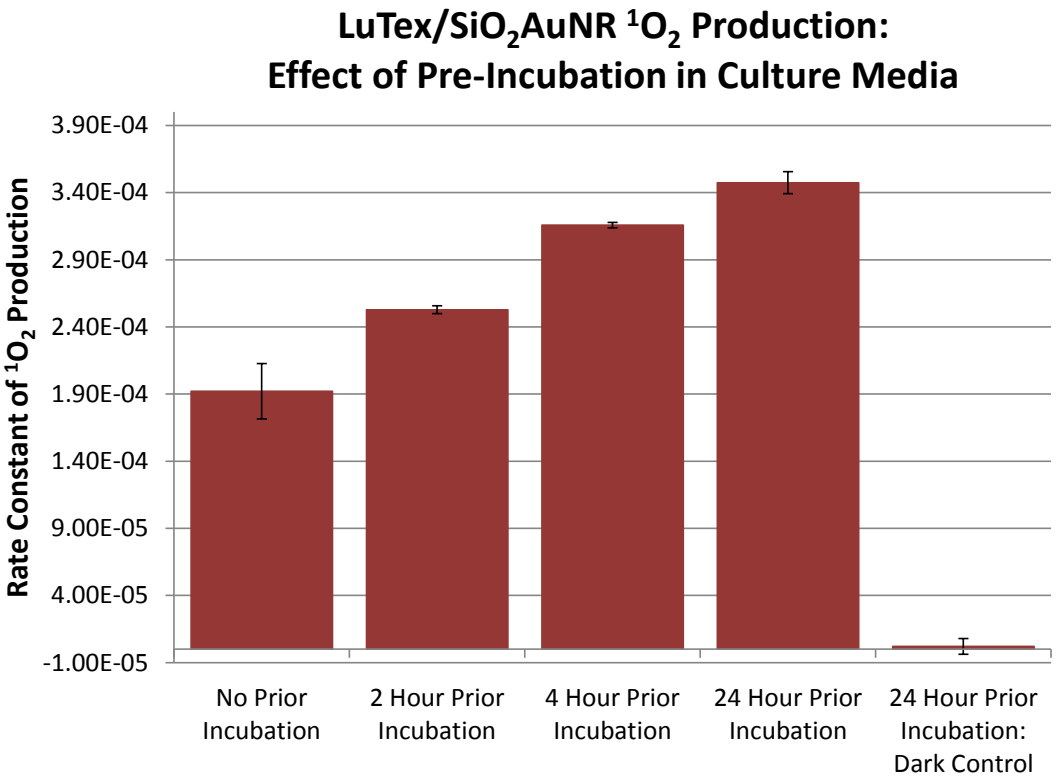

Figure 4.11: Effect of pre-incubation time in DMEM cell culture media with 5% FBS on $^1O_2$ production by LuTex/SiO_2AuNR during CW illumination.

4. 6 *IN VITRO* PHOTOTHERAPY OF MULTIFUNCTIONAL NANOPARTICLE-LOADED MACROPHAGES

Validation of the therapeutic efficacy of LuTex/SiO_2AuNR was performed by a series of *in vitro* studies designed to compare the induced cell toxicity of both nanoparticle and/or photosensitizer labeled macrophages and the effect of differing illumination parameters. For *in vitro* studies, J774A.1 murine monocyte-macrophages were plated at a density of $1x10^4$ cells per well of a 96-well plate in 100 µL of DMEM phenol-red free cell culture media with 5% FBS. Cells were allowed to incubate for 24 hours at 37°C under 5% CO_2. Desired experimental groups, comprising free LuTex, SiO_2AuNR, and LuTex/SiO_2AuNR were sterilized using 0.22 µm syringe filters and left

suspended in water until just prior to addition with cells, at which time 10% volume of sterile 10x PBS was added.

The cells were then washed and 5 μL of the photosensitizer of nanoparticle solutions were added. The final optical density of wells containing AuNR, either with or without LuTex, was 0.5, or approximately 113 pM ($6.84x10^9$ AuNR/well), and the nanorods utilized exhibited a peak absorbance near 808 nm. Wells containing LuTex in the absence of AuNR had a final concentration of 100 nM ($6.02x10^{12}$ LuTex/well). Nanoparticles were incubated with the macrophages at 37°C in 5% CO_2 for an additional 18 hours, after which the cell were gently washed three times with PBS and resuspended in fresh culture media. The cells were then exposed to the desired illumination for 3 minutes, either dark controls which received no illumination, PPTT illumination conditions using a continuous wave (CW) 808 nm diode laser (NIR DL 808-2000, Laser Lab Components, Inc.) emitting at 1 W/cm^2, PDT illumination conditions using the 735 nm LED emitting at 40 mW/cm^2, or the simultaneous combination of both optical sources.

After illumination of the experimental groups, cells were allowed to incubate for an additional 5 hours before exposure to live/dead cell staining assays. Calcein AM is a green fluorescent indicator for live cell staining, capitalizing on its conversion from an initially non-fluorescent state to the highly fluorescent calcein upon internalization and hydrolysis by intracellular esterases. Propidium iodide (PI) is a red fluorescent indicator which is cell-impermeant for healthy cells, but readily enters damaged cell membranes to bind nucleic acids. Therefore, these two indictors can be used together for live/dead cell staining using established protocols. Briefly, the cell media was replaced with a buffer solution for 5 minutes before being aspirated and replaced with buffer containing 1 μM PI and Calcein AM solutions and incubated for 20 minutes. The cells were gently washed

twice with buffer before measuring the fluorescence using a UV-VIS plate reader to generate quantitative plots and examining the wells using fluorescence microscopy for qualitative comparison.

Figure 4.12 shows the dependence of results of live/dead staining of control cells without any photosensitizers or nanoparticles, SiO_2AuNR-labeled macrophages, and LuTex/SiO_2AuNR-labeled macrophages after differing illumination conditions. While control cells and those labeled with SiO_2AuNR revealed no significant changes, a marked reduction in the Calcein AM fluorescence intensity (Fig. 4.12A) and increase in propidium iodide fluorescence intensity (Fig. 4.12B) was measured using the plate reader for the LuTex/SiO_2AuNR-labeled macrophages which were treated with PDT and combined PPTT/PDT illumination conditions. Figure 4.12C further confirms the trend through representative microscopy images including overlays of both PI and Calcein AM fluorescence for cells treated with LuTex/SiO_2AuNR but not illuminated (left) and those receiving both illumination sources (right).

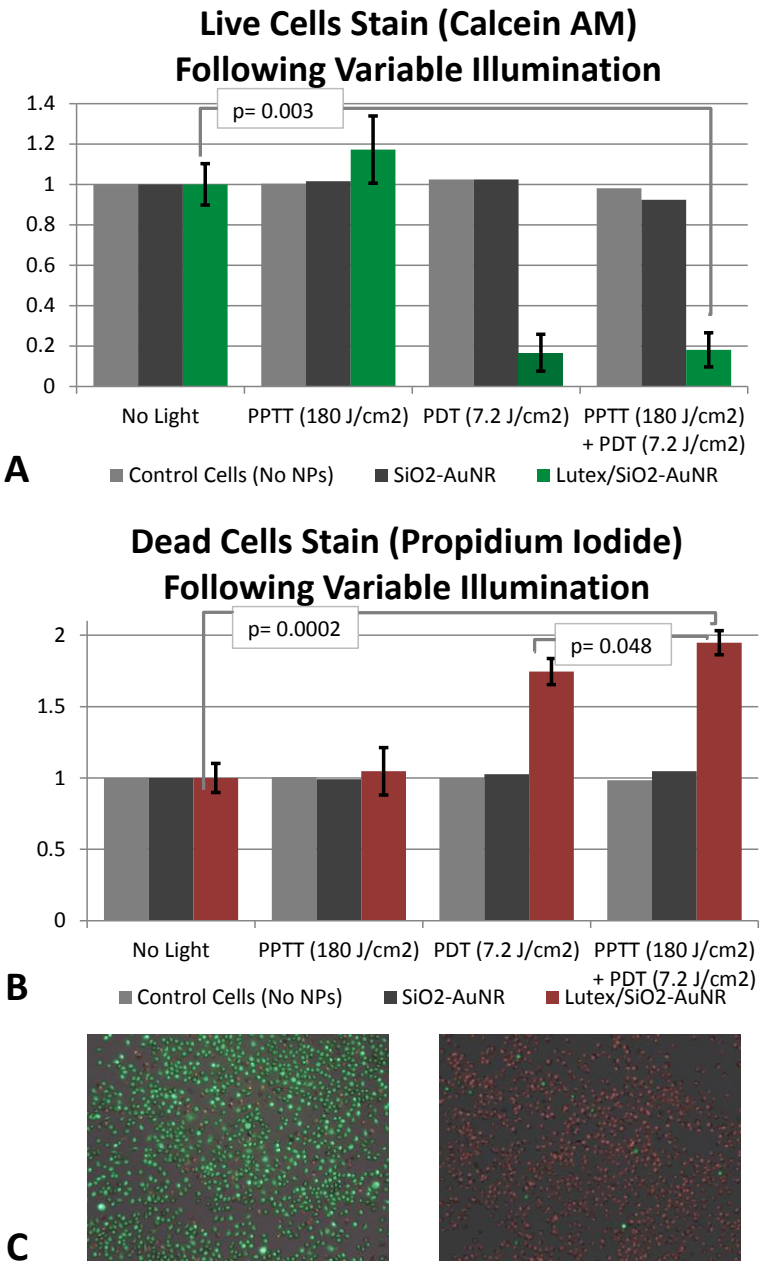

Figure 4.12: Live/Dead staining of macrophages containing control cells, SiO_2AuNR, or LuTex/SiO_2AuNR following exposure to illumination to induce PPTT, PDT or both. (A) Relative number of live cells, Calcein AM stain. (B) Relative number of dead cells, propidium iodide stain. (C) Representative fluorescence overlay images of LuTex/SiO_2AuNR after exposure to no light (left) or both PPTT and PDT conditions (right), showing live (green) and dead (red) cells; 10x objective.

A separate, complimentary, *in vitro* study comparing live dead staining results following PPTT and PDT illumination of macrophages labeled with LuTex/SiO_2AuNR, 100 nM free LuTex, SiO_2AuNR, or no nanoparticles (Figure 4.13). Again a reduction in number of live cells with a corresponding increase in dead cell staining intensity was measured for the LuTex/SiO_2AuNR-labeled macrophages which received PPTT/PDT illumination. In contrast, less difference in viability between illuminated and non-illuminated cells of the other experimental groups (free LuTex, SiO_2AuNR without LuTex, and control cells without LuTex or AuNR). This trend is supported by the inset fluorescence microscopy overlay images (Fig. 4.13C).

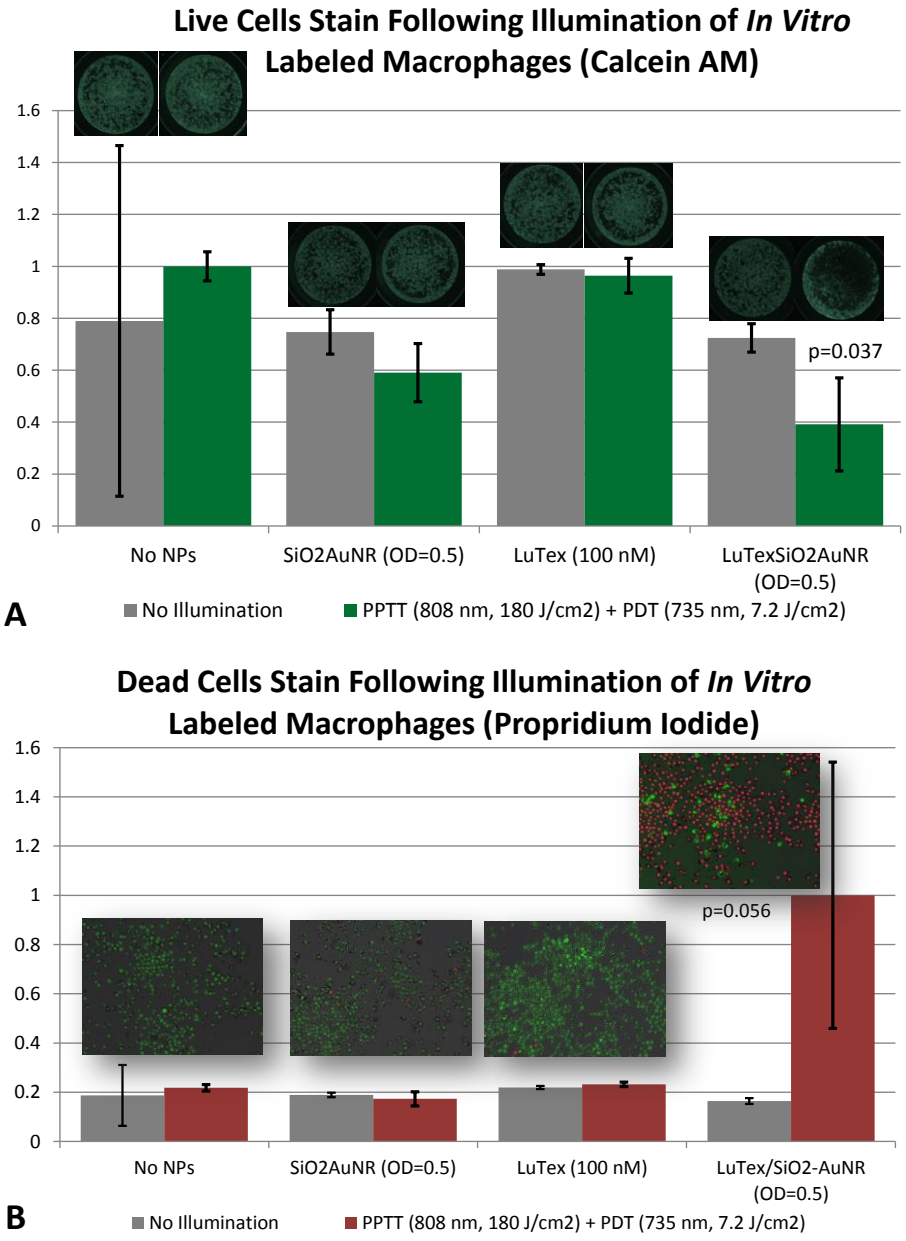

Figure 4.13: Labeled macrophage response to PPTT and PDT illumination relative to dark controls. (A) Relative intensity of Calcein AM live cell stain with representative fluorescence images insets for each group, 1.25x objective. (B) Relative intensity of Propidium Iodide dead cell stain with overlay fluorescence images inset for the illuminated cells of each group showing live (green) and dead (red) cells, 20x objective. Provided p values are based on the dark control and illuminated LuTex/SiO_2AuNR group.

4. 7 DISCUSSION AND CONCLUSIONS

Multifunctional nanoparticles comprising photosensitizer-doped, silica-coated gold nanorods were synthesized and characterized *in vitro*. Gold nanorods are known to provide excellent photoacoustic imaging contrast due to their high and tunable optical absorption resulting from localized surface plasmon resonance, which can be tuned to the near-infrared tissue optical window by tuning the AuNR aspect ratio. Chapters 2 and 3 focused on the use of AuNR as contrast agents and thermal beacons for intravascular photoacoustic (IVPA) imaging of atherosclerotic plaques and monitored photothermal heating. Herein, the incorporation of LuTex photosensitizer molecules into the nanoparticles platform allows for a second therapeutic modality (PPTT and PDT) in addition to the image contrast provided by the core particles. Several unique properties of the synthesized LuTex/SiO_2AuNR were observed and merit further discussion and/or continued investigation.

The ability to detect the presence of LuTex by its characteristic absorbance peaks at 470 nm and 732 nm in the presence of AuNR is in itself an indicator of high LuTex loading. AuNR exhibit a longitudinal peak absorbance extinction coefficient on the order of 10^9 M^{-1} cm^{-1}, whereas the extinction coefficient of a single LuTex molecule is four orders of magnitude less ($1.2x10^5$ M^{-1} cm^{-1} at the 470 nm peak). As synthesized LuTex/SiO_2AuNR were found to be stable in water at room temperature for several weeks, or several months at 4°C, no LuTex leakage detected by the UV-Vis spectrum of supernatants (Fig. 4.2B). However, several factors were found to influence the efficiency of LuTex encapsulation within silica during its growth on the AuNR surface. For example, the maximum loading efficiency for LuTex was found to occur at a reaction pH

of approximately 11, with significant deviations either above or below that value resulting in decreased loading (Fig. 4.3). This effect is not surprising given the expected effect of pH on the kinetics of silica deposition on the AuNR surface and, as a result, the porosity of the silica coating. However, it is interesting to note that the lowest pH reaction (pH=10.5) exhibited low LuTex loading while still achieving an AuNR peak absorbance wavelength similar to that of the other experimental groups (pH= 10.8, 11.1, 11.5), indicating that silica was deposited on the AuNR surface.

Additionally, the functional groups on the LuTex molecules themselves were found to significantly impact the relative LuTex loading efficiency and particle stability. In particular, under similar reaction conditions, an inverse relationship was observed between LuTex loading and the presence of carboxylic acid groups on the LuTex molecules, likely due to repulsion of the negative charges between the carboxylic acid functional groups and the silica-coated AuNR (Fig. 4.5A). However, the uniformity of the silica coating for LuTex/SiO_2AuNR and stability during washing steps was also found to be dependent on the molecular structure of LuTex, with the more highly loaded R=1 function group which contains no carboxylic acid groups exhibiting the most amorphous silica coating upon evaluation by TEM (Fig. 4.5B). Together, these trends indicate a molecular and environmental dependence of LuTex loading during LuTex/SiO_2AuNR and the resulting particle structure and stability.

Photosensitizers encapsulated within silica demonstrated a sizable reduction in singlet oxygen production relative to similar concentrations of free LuTex, as measured by the decay in ABDA fluorescence in water (Fig. 4.6). The calculated rate constant for ABDA decay for LuTex/SiO_2AuNR was 15-fold lower than that of an equivalent concentration of free LuTex in the absence of SiO_2AuNR and 18.5-fold lower than that of OD matched SiO_2AuNR co-incubated with free LuTex. This reduction is in agreement

with other studies investigating the effect of singlet oxygen production induced by photosensitizers encapsulated in silica nanoparticles which reported approximately 10-fold and 17-fold decreases for methylene blue silica nanoparticles relative to the free photosensitizers [47,48]. The reduction is likely due to a combination of factors introduced by the silica shell, including the limited lifetime and restricted diffusion of singlet oxygen from within the silica layer as well as increased optical scattering within the silica which reduces the potential for photosensitizer excitation.

Potential reduced efficiency of singlet oxygen production from LuTex entrapped within silica is likely avoided through the demonstrated biodegradation of the silica layer surrounding the AuNR within physiological conditions. PEG-SiO_2AuNR were found to be stable in acidic salt solutions, while the silica was stripped in PBS at pH=7.4 and in cell culture media with 10% FBS (Fig. 4.7). Assessment of the TEM imaging for degraded silica particles in PBS and DMEM reveal a heterogeneous distribution of particles in which some PEG-SiO_2AuNR appear to remain intact while others are completely stripped after 24 hours of incubation. Many of the particles also appear to have a lower silica density on the interior of the silica than at its periphery, indicating that the degradation may occur from the inside out rather than etching away at the outer surface of the silica layer. Each of these observations is likely due, at least in part, to incomplete and heterogenous PEG coating of the surface of the silica. Previous reports including an *in vitro* assessment of silica nanoparticles found differences in the kinetics of degradation based on the particles shape, surface properties and porosity [49]. These dependencies were similarly investigated as a means of creating silica xerogel materials with controlled release properties [50].

In order to better understand the kinetics silica degradation under physiological conditions, PEG-FITC/SiO_2AuNR were synthesized as a proxy for LuTex/SiO_2AuNR.

FITC is a highly fluorescent dye with similar charge to that of LuTex. The observed sigmoidal curve of FITC fluorescence intensity capitalizes on the fact that FITC entrapped within silica is quenched, but will fluoresce upon its release from the AuNR surface (Fig. 4.8B). By comparison, a separate report which utilized FITC-loaded silica nanoparticles prepared using the Stöber method in the absence of a metal nanoparticle core were shown to exhibit a drastic increase in particle degradation and FITC release between 4 and 17 hours in the same culture media [51].

Given the tendency for nanoparticles to exhibit long circulation times, the question remains whether or not the LuTex/SiO_2AuNR can be adequately delivered to intended treatment sites, such as atherosclerotic plaques, prior to degradation of the silica and LuTex release. It was recently shown that perfluorocarbon core nanoparticles with a diameter of approximately 250 nm showed a similar extent of extravasation within atherosclerotic lesions within 2 hours to what was measured after 6 hours of circulation, indicating that the majority of passive plaque labeling may occur within the first few hours following injection [52]. This reported timescale of *in vivo* labeling kinetics in atherosclerotic rabbit models suggests that the release kinetics observed for the FITC/SiO_2AuNR (Fig. 4.8B) may allow for sufficient time to label plaques before significant silica degradation occurs. Future work is needed to confirm if such *in vivo* kinetics and silica degradation kinetics hold true for LuTex/SiO_2AuNR or if further development of stabilizing surface conjugations will be required for appropriate *in vivo* delivery. Interestingly, free LuTex has been shown to localize primarily within lysosomes following cellular uptake [53]. This is also the expected fate of AuNR internalized by macrophages, indicating that LuTex/SiO_2AuNR are not expected to significantly alter the ultimate intracellular distribution of photosensitizers.

Together, the results from *in vitro* studies provided in Figures 4.12 and 4.13 indicate the therapeutic potential for dual PPTT/PDT using the synthesized multifunctional nanoparticles. Increased numbers of dead cells and reduced live cell fractions for experimental groups illuminated with both 732 nm PDT and 808 nm PPTT conditions relative to changes observed from other experimental groups was observed, including an enhanced therapeutic efficacy for combined PPTT/PDT over PPTT and PDT alone (Figs. 4.12B and 4.13B). This enhanced effect for combined photothermal and photodynamic therapy is in agreement with several recent reports investigating such combined approaches for cancer therapy applications [26-28,32,33].

As the multifunctional nanoparticle platform transitions from *in vitro* characterization to *in vivo* validation, several inter-related factors must be considered to help further refine the optimal nanoparticle design. For example, Adili et. al. demonstrated a wide range of biological responses which can be achieved through variations in the drug-light dosage in treatment intended for the treatment of intimal hyperplasia in the carotid artery of rats [54]. As the administered drug concentration and optical fluence were increased, therapeutic effects ranging from incomplete cell eradication following the treatment, to the desirable complete cell eradication with inhibited hyperplasia at two weeks following treatment, to rapid thrombus formation with vascular occlusion were all observed. This wide range of physiological effects suggests the importance of monitoring both drug delivery and light dosage prior to and during treatment. Once a desirable drug-light dosage has been established, the incorporation of intravascular photoacoustic (IVPA) imaging to verify and assess multifunctional nanoparticle delivery and to monitor the temperature rise induced by combined PPTT/PDT.

In conclusion, this chapter has focused on the introduction of novel multifunctional nanoparticles comprised of photosensitizer-doped, silica-coated gold nanorods. Encapsulation of LuTex photosensitizers onto gold nanorods was specifically chosen based on the prior research investigating each component individually for intravascular diagnostic and/or therapeutic applications. The synthesized LuTex/SiO_2AuNR have been characterized and shown to release the LuTex cargo within physiological media and increased *in vitro* therapeutic efficacy of combined PPTT/PDT of LuTex/SiO_2AuNR-labeled macrophages relative to either SiO_2AuNR or LuTex alone was demonstrated, supporting their continued investigation. In the context of prior research within this dissertation, the multifunctional nanoparticles provide a potential for improved control of therapy delivery under the guidance of combined IVUS/IVPA imaging.

4. 8 REFERENCES

1. A. S. Go, D. Mozaffarian, V. L. Roger, E. J. Benjamin, J. D. Berry, M. J. Blaha, S. Dai, E. S. Ford, C. S. Fox, S. Franco, H. J. Fullerton, C. Gillespie, S. M. Hailpern, J. A. Heit, V. J. Howard, M. D. Huffman, S. E. Judd, B. M. Kissela, S. J. Kittner, D. T. Lackland, J. H. Lichtman, L. D. Lisabeth, R. H. Mackey, D. J. Magid, G. M. Marcus, A. Marelli, D. B. Matchar, D. K. McGuire, E. R. Mohler, C. S. Moy, M. E. Mussolino, R. W. Neumar, G. Nichol, D. K. Pandey, N. P. Paynter, M. J. Reeves, P. D. Sorlie, J. Stein, A. Towfighi, T. N. Turan, S. S. Virani, N. D. Wong, D. Woo and M. B. Turner, "Heart Disease and Stroke Statistics—2014 Update: A Report From the American Heart Association," *Circulation*, 129(3):e28-e292, (2014).

2. R. Ross, "Cell Biology of Atherosclerosis," *Annual Review of Physiology*, 57(1):791-804, (1995).

3. P. S. Mullenix, C. A. Andersen and B. W. Starnes, "Atherosclerosis as Inflammation," *Annals of vascular surgery*, 19(1):130-138, (2005).

4. R. R. S. Packard and P. Libby, "Inflammation in Atherosclerosis: From Vascular Biology to Biomarker Discovery and Risk Prediction," *Clinical Chemistry*, 54(1):24-38, (2008).

5. R. P. Choudhury, V. Fuster and Z. A. Fayad, "Molecular, cellular and functional imaging of atherothrombosis," *Nat Rev Drug Discov*, 3(11):913-925, (2004).

6. S. Waxman, F. Ishibashi and J. E. Muller, "Detection and Treatment of Vulnerable Plaques and Vulnerable Patients: Novel Approaches to Prevention of Coronary Events," *Circulation*, 114(22):2390-2411, (2006).

7. S. Glagov, E. Weisenberg, C. K. Zarins, R. Stankunavicius and G. J. Kolettis, "Compensatory Enlargement of Human Atherosclerotic Coronary Arteries," *New England Journal of Medicine*, 316(22):1371-1375, (1987).

8. D. HACKETT, G. DAVIES and A. MASERI, "Pre-existing coronary stenoses in patients with first myocardial infarction are not necessarily severe," *European Heart Journal*, 9(12):1317-1323, (1988).

9. M. Summers and M. Patel, "Appropriateness of Percutaneous Coronary Intervention: A Review," *Current Cardiology Reports*, 15(7):1-8, (2013).

10. S. C. Smith, J. T. Dove, A. K. Jacobs, J. W. Kennedy, D. Kereiakes, M. J. Kern, R. E. Kuntz, J. J. Popma, H. V. Schaff, D. O. Williams, R. J. Gibbons, J. P. Alpert, K. A. Eagle, D. P. Faxon, V. Fuster, T. J. Gardner, G. Gregoratos, R. O. Russell and S. C. Smith, "ACC/AHA Guidelines for Percutaneous Coronary Intervention (Revision of the 1993 PTCA Guidelines)â€"Executive Summary: A Report of the American College of Cardiology/American Heart Association Task Force on Practice Guidelines (Committee to Revise the 1993 Guidelines for Percutaneous Transluminal Coronary Angioplasty) Endorsed by the Society for Cardiac Angiography and Interventions," *Circulation*, 103(24):3019-3041, (2001).

11. J. A. Goldstein, C. Grines, T. Fischell, R. Virmani, D. Rizik, J. Muller and S. R. Dixon, "Coronary embolization following balloon dilation of lipid-core plaques," *JACC Cardiovasc Imaging*, 2(12):1420-4, (2009).

12. J. A. Goldstein, B. Maini, S. R. Dixon, E. S. Brilakis, C. L. Grines, D. G. Rizik, E. R. Powers, D. H. Steinberg, K. A. Shunk, G. Weisz, P. R. Moreno, A. Kini, S. K. Sharma, M. J. Hendricks, S. T. Sum, S. P. Madden, J. E. Muller, G. W. Stone and M. J. Kern, "Detection of Lipid-Core Plaques by Intracoronary Near-Infrared Spectroscopy Identifies High Risk of Periprocedural Myocardial Infarction," *Circulation: Cardiovascular Interventions*, 4(5):429-437, (2011).

13. S. R. A. S. Sethuraman, J. H. Amirian, R. W. Smalling, and S. Y. Emelianov, "Intravascular photoacoustic imaging using an IVUS imaging catheter," *IEEE Trans. Ultrason. Ferroelectr. Freq. Control*, 54:978-986, (2007).

14. S. Sethuraman, J. H. Amirian, S. H. Litovsky, R. W. Smalling and S. Y. Emelianov, "Ex vivo Characterization of Atherosclerosis using Intravascular Photoacoustic Imaging," *Opt. Express*, 15(25):16657-16666, (2007).

15. S. Sethuraman, J. H. Amirian, S. H. Litovsky, R. W. Smalling and S. Y. Emelianov, "Spectroscopic intravascular photoacoustic imaging to differentiate atherosclerotic plaques," *Optics Express*, 16(5):3362-3367, (2008).

16. B. Wang, J. L. Su, J. Amirian, S. H. Litovsky, R. Smalling and S. Emelianov, "Detection of lipid in atherosclerotic vessels using ultrasound-guided spectroscopic intravascular photoacoustic imaging," *Opt. Express*, 18(5):4889-4897, (2010).

17. K. Jansen, A. F. W. van der Steen, H. M. M. van Beusekom, J. W. Oosterhuis and G. van Soest, "Intravascular photoacoustic imaging of human coronary atherosclerosis," *Opt. Lett.*, 36(5):597-599, (2011).

18. B. Wang, A. Karpiouk, D. Yeager, J. Amirian, S. Litovsky, R. Smalling and S. Emelianov, "Intravascular photoacoustic imaging of lipid in atherosclerotic plaques in the presence of luminal blood," *Opt Lett*, 37(7):1244-6, (2012).

19. B. Wang, A. Karpiouk, D. Yeager, J. Amirian, S. Litovsky, R. Smalling and S. Emelianov, "In vivo Intravascular Ultrasound-guided Photoacoustic Imaging of Lipid in Plaques Using an Animal Model of Atherosclerosis," *Ultrasound in medicine & biology*, 38(12):2098-2103, (2012).

20. K. Jansen, M. Wu, A. F. van der Steen and G. van Soest, "Lipid detection in atherosclerotic human coronaries by spectroscopic intravascular photoacoustic imaging," *Opt Express*, 21(18):21472-84, (2013).

21. D. Yeager, Y. S. Chen, S. Litovsky and S. Emelianov, "Intravascular photoacoustics for image-guidance and temperature monitoring during plasmonic photothermal therapy of atherosclerotic plaques: a feasibility study," *Theranostics*, 4(1):36-46, (2013).

22. J. Oh, H. Yoon and J.-H. Park, "Nanoparticle platforms for combined photothermal and photodynamic therapy," *Biomedical Engineering Letters*, 3(2):67-73, (2013).

23. J. Wang, G. Zhu, M. You, E. Song, M. I. Shukoor, K. Zhang, M. B. Altman, Y. Chen, Z. Zhu, C. Z. Huang and W. Tan, "Assembly of Aptamer Switch Probes and Photosensitizer on Gold Nanorods for Targeted Photothermal and Photodynamic Cancer Therapy," *ACS Nano*, 6(6):5070-5077, (2012).

24. D. Yoo, H. Jeong, C. Preihs, J.-s. Choi, T.-H. Shin, J. L. Sessler and J. Cheon, "Double-Effector Nanoparticles: A Synergistic Approach to Apoptotic Hyperthermia," *Angewandte Chemie International Edition*, 51(50):12482-12485, (2012).

25. W.-S. Kuo, C.-N. Chang, Y.-T. Chang, M.-H. Yang, Y.-H. Chien, S.-J. Chen and C.-S. Yeh, "Gold Nanorods in Photodynamic Therapy, as Hyperthermia Agents, and in Near-Infrared Optical Imaging," *Angewandte Chemie International Edition*, 49(15):2711-2715, (2010).

26. W.-S. Kuo, Y.-T. Chang, K.-C. Cho, K.-C. Chiu, C.-H. Lien, C.-S. Yeh and S.-J. Chen, "Gold nanomaterials conjugated with indocyanine green for dual-modality photodynamic and photothermal therapy," *Biomaterials*, 33(11):3270-3278, (2012).

27. B. Jang, J.-Y. Park, C.-H. Tung, I.-H. Kim and Y. Choi, "Gold Nanorod−Photosensitizer Complex for Near-Infrared Fluorescence Imaging and Photodynamic/Photothermal Therapy In Vivo," *ACS Nano*, 5(2):1086-1094, (2011).

28. M. K. Khaing Oo, Y. Yang, Y. Hu, M. Gomez, H. Du and H. Wang, "Gold Nanoparticle-Enhanced and Size-Dependent Generation of Reactive Oxygen Species from Protoporphyrin IX," *ACS Nano*, 6(3):1939-1947, (2012).

29. Y. Zhang, J. Qian, D. Wang, Y. Wang and S. He, "Multifunctional Gold Nanorods with Ultrahigh Stability and Tunability for In Vivo Fluorescence Imaging, SERS Detection, and Photodynamic Therapy," *Angewandte Chemie International Edition*, 52(4):1148-1151, (2013).

30. B. Jain, A. Uppal, P. K. Gupta and K. Das, "Photophysical properties of Chlorin-p6 bound to coated gold nanorods," *Journal of Molecular Structure*, 1032(0):23-28, (2013).

31. J. Wang, M. You, G. Zhu, M. I. Shukoor, Z. Chen, Z. Zhao, M. B. Altman, Q. Yuan, Z. Zhu, Y. Chen, C. Z. Huang and W. Tan, "Photosensitizer–Gold Nanorod Composite for Targeted Multimodal Therapy," *Small*:n/a-n/a, (2013).

32. J. Lin, S. Wang, P. Huang, Z. Wang, S. Chen, G. Niu, W. Li, J. He, D. Cui, G. Lu, X. Chen and Z. Nie, "Photosensitizer-Loaded Gold Vesicles with Strong Plasmonic Coupling Effect for Imaging-Guided Photothermal/Photodynamic Therapy," *ACS Nano*, 7(6):5320-5329, (2013).

33. J.-Y. Kim, W. I. Choi, M. Kim and G. Tae, "Tumor-targeting nanogel that can function independently for both photodynamic and photothermal therapy and its

synergy from the procedure of PDT followed by PTT," *Journal of Controlled Release*, (0), (2013).

34. A. N. Kharlamov and J. L. Gabinsky, "Plasmonic photothermic and stem cell therapy of atherosclerotic plaque as a novel nanotool for angioplasty and artery remodeling," *Rejuvenation Res*, 15(2):222-230, (2012).

35. A. N. Kharlamov, A. E. Tyurnina, V. S. Veselova, O. S. Novoselova, A. S. Filatova, O. P. Kovtun, V. Y. Shur and J. L. Gabinsky, "Plasmonics for Treatment of Atherosclerosis: Results of NANOM-FIM Trial," *Nanomedicine & Nanotechnology*, 4(160):doi: 10.4172/2157-7439.1000160, (2013).

36. M. Hayase, K. W. Woodburn, J. Perlroth, R. A. Miller, W. Baumgardner, P. G. Yock and A. Yeung, "Photoangioplasty with local motexafin lutetium delivery reduces macrophages in a rabbit post-balloon injury model," *Cardiovasc Res*, 49(2):449-55, (2001).

37. R. Waksman, P. E. McEwan, T. I. Moore, R. Pakala, F. D. Kolodgie, D. G. Hellinga, R. C. Seabron, S. J. Rychnovsky, J. Vasek, R. W. Scott and R. Virmani, "PhotoPoint photodynamic therapy promotes stabilization of atherosclerotic plaques and inhibits plaque progression," *J Am Coll Cardiol*, 52(12):1024-32, (2008).

38. S. G. Rockson, P. Kramer, M. Razavi, A. Szuba, S. Filardo, P. Fitzgerald, J. P. Cooke, S. Yousuf, A. R. DeVault, M. F. Renschler and D. C. Adelman, "Photoangioplasty for Human Peripheral Atherosclerosis: Results of a Phase I Trial of Photodynamic Therapy With Motexafin Lutetium (Antrin)," *Circulation*, 102(19):2322-2324, (2000).

39. D. J. Kereiakes, A. M. Szyniszewski, D. Wahr, H. C. Herrmann, D. I. Simon, C. Rogers, P. Kramer, W. Shear, A. C. Yeung, K. A. Shunk, T. M. Chou, J. Popma, P. Fitzgerald, T. E. Carroll, D. Forer and D. C. Adelman, "Phase I drug and light dose-escalation trial of motexafin lutetium and far red light activation (phototherapy) in subjects with coronary artery disease undergoing percutaneous coronary intervention and stent deployment: procedural and long-term results," *Circulation*, 108(11):1310-5, (2003).

40. N. R. Jana, L. Gearheart and C. J. Murphy, "Seed-Mediated Growth Approach for Shape-Controlled Synthesis of Spheroidal and Rod-like Gold Nanoparticles Using a Surfactant Template," *Advanced Materials*, 13(18):1389-1393, (2001).

41. J. L. Sessler, G. Hemmi, T. D. Mody, T. Murai, A. Burrell and S. W. Young, "Texaphyrins: Synthesis and Applications," *Accounts of Chemical Research*, 27(2):43-50, (1994).

42. C. Preihs, J. F. Arambula, D. Magda, H. Jeong, D. Yoo, J. Cheon, Z. H. Siddik and J. L. Sessler, "Recent Developments in Texaphyrin Chemistry and Drug Discovery," *Inorganic Chemistry*, 52(21):12184-12192, (2013).

43. Y.-S. Chen, W. Frey, S. Kim, P. Kruizinga, K. Homan and S. Emelianov, "Silica-Coated Gold Nanorods as Photoacoustic Signal Nanoamplifiers," *Nano Letters*, 11(2):348-354, (2011).

44. H. Liao and J. H. Hafner, "Gold Nanorod Bioconjugates," *Chemistry of Materials*, 17(18):4636-4641, (2005).

45. K. W. Woodburn, Q. Fan, D. Kessel, Y. Luo and S. W. Young, "Photodynamic Therapy of B16F10 Murine Melanoma with Lutetium Texaphyrin," 110(5):746-751, (1998).

46. B. A. Lindig, M. A. J. Rodgers and A. P. Schaap, "Determination of the lifetime of singlet oxygen in water-d2 using 9,10-anthracenedipropionic acid, a water-soluble probe," *Journal of the American Chemical Society*, 102(17):5590-5593, (1980).

47. W. Tang, H. Xu, R. Kopelman and M. A. Philbert, "Photodynamic Characterization and In Vitro Application of Methylene Blue-containing Nanoparticle Platforms¶," *Photochemistry and Photobiology*, 81(2):242-249, (2005).

48. D. B. Tada, L. L. R. Vono, E. L. Duarte, R. Itri, P. K. Kiyohara, M. S. Baptista and L. M. Rossi, "Methylene Blue-Containing Silica-Coated Magnetic Particles: A Potential Magnetic Carrier for Photodynamic Therapy," *Langmuir*, 23(15):8194-8199, (2007).

49. N. Hao, H. Liu, L. Li, D. Chen, L. Li and F. Tang, "In vitro degradation behavior of silica nanoparticles under physiological conditions," *J Nanosci Nanotechnol*, 12(8):6346-54, (2012).

50. S. Radin, S. Falaize, M. H. Lee and P. Ducheyne, "In vitro bioactivity and degradation behavior of silica xerogels intended as controlled release materials," *Biomaterials*, 23(15):3113-3122, (2002).

51. E. Mahon, D. R. Hristov and K. A. Dawson, "Stabilising fluorescent silica nanoparticles against dissolution effects for biological studies," *Chemical Communications*, 48(64):7970-7972, (2012).

52. H. Zhang, L. Zhang, J. Myerson, K. Bibee, M. Scott, J. Allen, G. Sicard, G. Lanza and S. Wickline, "Quantifying the evolution of vascular barrier disruption in

advanced atherosclerosis with semipermeant nanoparticle contrast agents," *PLoS One*, 6(10):e26385, (2011).

53. K. W. Woodburn, Q. Fan, D. R. Miles, D. Kessel, Y. Luo and S. W. Young, "Localization and Efficacy Analysis of the Phototherapeutic Lutetium Texaphyrin (PCI-0123) in the Murine EMT6 Sarcoma Model," *Photochemistry and Photobiology*, 65(3):410-415, (1997).

54. F. Adili, R. G. Statius van Eps and G. M. LaMuraglia, "Significance of dosimetry in photodynamic therapy of injured arteries: classification of biological responses," *Photochem Photobiol*, 70(4):663-8, (1999).

Chapter 5: Conclusions and Future Directions

5.1. Summary of Completed Research

The pathophysiology associated with progression and destabilization of atherosclerotic plaques is a multifaceted process which leads to characteristic changes in arterial morphology and composition. Combined intravascular ultrasound and photoacoustic (IVUS/IVPA) imaging is a novel modality currently in preclinical development which seeks to expand upon the ability of clinically utilized intravascular ultrasound (IVUS) imaging to assess vessel anatomy by adding improved sensitivity to image the underlying cellular and molecular composition through intravascular photoacoustic (IVPA) imaging. The motivation for IVUS/IVPA imaging lies in this ability to provide complimentary vessel information, capitalizing on the unique capability of IVPA imaging to yield optical contrast at significantly deeper penetration depths than other optical techniques. Such contrast can be obtained from endogenous chromophores within atherosclerotic plaques, such as lipid, or through the delivery of exogenous contrast agents designed to localize within atherosclerotic plaques and provide high IVPA signal contrast relevant to molecular and cellular composition of plaques.

The present work has focused on methods of expanding the applications of IVPA imaging using exogenous contrast agents, plasmonic gold nanorods, to enable the detection and subsequent optically-triggered therapy of atherosclerotic plaques. The passive extravasation and aggregation of systemically injected plasmonic gold nanorods absorbing within the near infrared tissue optical window within plaques of atherosclerotic rabbit models was demonstrated, along with the ability to localize the contrast agents using *ex vivo* IVUS/IVPA imaging. The motivation for nanoparticle labeling of atherosclerosis was then expanded from that of purely image contrast agents to vehicles for image-guided, dual-modality phototherapy.

In Chapter 2, the potential for using polyethylene glycol conjugated gold nanorods (PEG-AuNR) as contrast agents for IVUS/IVPA imaging of atherosclerosis was evaluated. Biocompatibility of the nanoparticle contrast agents was evaluated *in vitro*, showing no signs of reduced viability of macrophages following their incubation and labeling with PEG-AuNR, including after application of nanosecond pulsed laser illumination of intensity comparable to that required for IVPA signal generation. IVUS/IVPA imaging of atherosclerotic rabbit aortas following systemic injection of PEG-AuNR with peak absorbance within the tissue optical window was performed. *Ex vivo* imaging revealed a high photoacoustic signal from localized AuNRs in regions with atherosclerotic plaques, with corresponding histological staining further confirming the preferential extravasation of AuNR in atherosclerotic regions with compromised luminal endothelium and acute macrophage accumulation. The ability to detect AuNRs using combined IVUS and photoacoustic imaging in the presence of luminal saline and luminal blood was evaluated using spectroscopic IVPA imaging.

Chapter 3 further introduced IVUS/IVPA imaging as a tool for localized temperature monitoring during plasmonic photothermal therapy. The temperature dependent change in IVPA signal intensity of silica coated gold nanorod (SiO_2AuNR) contrast agents absorbing within the near infrared wavelength range is evaluated and shown to have a linear relationship, with a slope greater than that of endogenous tissue. A continuous wave laser was subsequently incorporated into the IVUS/IVPA integrated catheter and utilized to selectively heat the nanoparticles with simultaneous IVPA temperature monitoring. As a result, IVUS/IVPA provides a platform for detection and therapy monitoring of atherosclerotic plaques through the selective heating of plasmonic gold nanoparticle contrast agents.

The theranostic potential of coupling the optical delivery enabled by the IVUS/IVPA imaging system with selectively delivered nanoparticles was further expanded in Chapter 4 through the synthesis and characterization of multifunctional nanoparticles designed to enable combined plasmonic photothermal therapy (PPTT) using illumination at 808 nm and photodynamic therapy (PDT) using lower intensity illumination at 735 nm. SiO_2AuNR doped with the photosensitizer lutetium texaphyrin (LuTex/SiO_2AuNR) were shown to passively release the photosensitizer after a delay of several hours, resulting in an improved efficiency of cytotoxic singlet oxygen production during PDT. *In vitro* studies further confirmed an increased therapeutic efficacy of combined PPTT/PDT for macrophages labeled with LuTex/SiO_2AuNR than was observed using either PPTT or PDT alone.

Together, the results presented within this dissertation provide a framework for ongoing research into the expansion of IVUS/IVPA imaging as a platform for complimentary diagnosis and local treatment of atherosclerotic plaques using multifunctional theranostic nanoparticle contrast/therapeutic agents.

5.2. FUTURE DIRECTIONS

5.2.1. Outlook for Clinical Translation of Intravascular Ultrasound and Photoacoustic Imaging: Characterizing Lipid-Rich Plaques

Translation of combined IVUS/IVPA imaging into the catheterization laboratory is dependent on several factors, including existing technical hurdles, safety concerns, and the extent of demonstrated advantages of IVUS/IVPA imaging over existing diagnostic modalities. The established correlation of lipid distribution within atherosclerotic plaques and the risk of acute coronary events, as well as the ability of IVPA imaging to detect lipid without introducing exogenous contrast agents, make lipid imaging a likely first

clinical application of IVUS/IVPA imaging [1-3]. This section, therefore, focuses on factors effecting the clinical translation of IVUS/IVPA imaging for that initial application, while additional considerations brought about by the introduction of exogenous contrast and/or therapeutic agents are discussed in Section 5.2.2.

5.2.1.1. Technical Hurdles

The primary technical hurdles restricting clinical translation of IVUS/IVPA imaging relate to the required laser sources for development of a real-time system and miniaturization of the integrated catheter. To date, the majority of applications of IVPA imaging have utilized commercially available US transducers and illumination from Q-switched Nd:YAG lasers coupled with optical parametric oscillators (OPO). Such optical systems are attractive in preclinical settings because they offer high pulse energies, on the order of tens of millijoules (mJ), over a broad range of wavelengths, allowing optical tuning for IVPA detection of a wide range of absorbers of interest. The versatility of these laser sources, however, is available at the expense of pulse repetition frequency (PRF), which is on the order of 10 Hz.

Whereas OPO lasers may be adequate for some US/PA applications which utilize array transducers to capture full two dimensional images with a single laser pulse, intravascular imaging using mechanically scanned single element ultrasound transducer provides an extreme case for optical source requirements if real-time imaging is to be achieved. Using an integrated IVUS/IVPA catheter which is mechanically rotated and pulled back to enable three dimensional imaging, an optical source operating at several kilohertz (kHz) and providing approximately 1 mJ/pulse would be required to maintain real-time IVPA imaging capabilities. For imaging lipid within plaques the requirements for the optical source are further restricted based on the need for an output wavelength

which matches an optical absorption peak of lipid, approximately 1210 nm or 1720 nm. Such sources are becoming commercially available. However, real-time IVUS/IVPA imaging has not yet been demonstrated. Further progression of IVPA towards the initiation of clinical trials hinges on the development of such systems; their completion will enable validation of *in vivo* IVUS/IVP lipid detection in large sample sizes of animal models of atherosclerosis and excised human coronary arteries. While *in vivo* IVUS/IVPA imaging has been demonstrated on rabbit models of atherosclerosis (see Figure 1.7), characterization of the received IVPA signal was restricted to qualitative comparison with histology sections and the small sample sizes have not allowed quantification of the sensitivity and specificity of IVPA-based lipid imaging.

In addition to the need for real-time IVUS/IVPA imaging systems, continued improvements to the overall integrated imaging catheter design are still needed before clinical translation can occur. Results presented within this dissertation have all utilized a catheter design with an outer diameter of approximately 2 mm and an inflexible region at the distal tip of approximately 5 mm. Future designs should exhibit comparable physical dimensions and flexibility to existing clinical catheters. To date, the smallest diameter IVPA catheter which has been reported is comprised of a rigid distal tip and an outer diameter of approximately 1.25 mm [4]. Additionally, our lab is currently working on developing and characterizing catheter prototypes which are assembled within a drive cable with an outer diameter of 1 mm. However, clinically used, mechanically rotated IVUS catheters rotate within a sheath that has an outer diameter of approximately 700 μm and with a rigid segment surrounding the transducer of less than 1 mm. Combined IVUS/IVPA catheters must meet similar criteria prior to its clinical adoption. While such a miniaturization is conceptually feasible, it is yet to be demonstrated, and the

effectiveness of light delivery for PA signal generation from the small optical fibers that would be required remains a potential obstacle.

5.2.1.2. Safety of IVPA Imaging

Beyond remaining technical challenges, the clinical acceptance of IVPA imaging will also require a more thorough investigation into its safety. In particular, the desire for achieving enhanced signal-to-noise (SNR) from the imaging target (e.g. lipid) should be balanced with the potential for unintentional laser-tissue interactions which may lead to tissue damage during IVPA imaging. The American National Standards Institute (ANSI) has established wavelength dependent laser fluence exposure limits, ranging from 20 mJ/cm^2 in the visible range to 100 mJ/cm^2 in the near infrared range, which can be used as a benchmark for predicting laser safety during IVPA signal generation [5,6]. While these limits were primarily set in place for considerations of safety to ocular exposure as well as that of skin, which is significantly more absorbing than other tissues due to the pigment/melanin content, they are treated as a conservative benchmark in predicting safety for all tissue exposure. For IVPA imaging, continued miniaturization of the integrated IVUS/IVPA catheter to a size acceptable for clinical use in human coronary arteries, $\leq$ 1 mm, will necessitate the use of an optical fiber with a diameter on the order of 300 μm, resulting in a high optical fluence at the distal end of the integrated catheter. Pulse energy of 0.5-1.0 mJ equate to fluences of several hundred mJ/cm^2, potentially resulting in local heating during imaging and well over the ANSI standard at any wavelength [7,8]. While optical diffusion will rapidly reduce fluences further away from the catheter and natural blood flow will help to mitigate any potential for heat buildup during imaging, ongoing studies are needed to evaluate the potential negative effects

which can result from IVPA imaging through luminal blood, particularly the presence and extent of optically-induced hemolysis.

5.2.1.3. Motivation for Clinical Adoption

If existing technical challenges are met and IVUS/IVPA imaging is shown to be well tolerated, the extent and rate of its adoption will be highly dependent on the effect which it has on clinical practice. In the short term, the question is how additional information provided by the coupling of IVPA imaging will impact existing interventional practices. Currently, intravascular imaging is reserved primarily for providing guidance of revascularization during percutaneous coronary intervention (PCI) and aiding in the diagnosis of lesions of unclear severity upon angiographic assessment [9,10]. Therefore, the immediate impact of combined IVUS/IVPA imaging will be largely determined by the ability to demonstrate improved therapeutic outcomes achieved through changes in clinical standards of care that are enabled by the new information provided by the imaging modality. While this remains to be demonstrated specifically by IVUS/IVPA imaging as it is translated into the clinic, several recent and ongoing clinical trials provide evidence of the potential impact that it may have on existing treatment strategies and outcomes.

First, the Providing Regional Observations to Study Predictors of Events in the Coronary Tree (PROSPECT) study has confirmed two critical points which support the expanded use of intravascular imaging modalities which are capable of accurately assessing atherosclerotic plaque composition in addition to its morphology- the demonstrations that angiography alone is not a good predictor of future coronary events and that plaque composition plays a significant role in determining the underlying risk profile for a given lesion [11,12]. Using virtual histology IVUS, the accuracy of which

has recently been questioned, to assess lesion composition, the PROSPECT trial found significantly higher incidence rates among patients with thin-cap fibroatheroma (TCFA) than in those with no identified TCFA plaques (Fig. 5.1) [11].

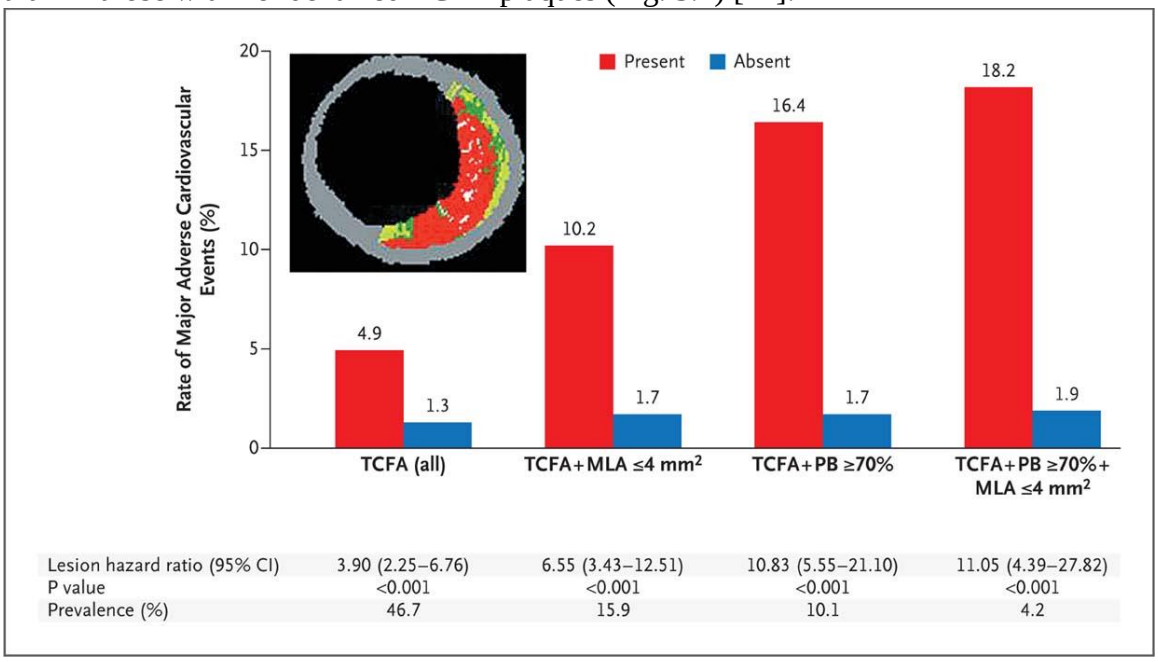

Lesion hazard ratio (95% CI)	3.90 (2.25–6.76)	6.55 (3.43–12.51)	10.83 (5.55–21.10)	11.05 (4.39–27.82)
P value	<0.001	<0.001	<0.001	<0.001
Prevalence (%)	46.7	15.9	10.1	4.2

Figure 5.1: Event Rates for Lesions That Were and Those That Were Not Thin-Cap Fibroatheromas, at a Median Follow-up of 3.4 Years. Event rates associated with 595 nonculprit lesions that were characterized as thin-cap fibroatheromas (TCFA) and 2114 that were not by means of radiofrequency intravascular ultrasonographic imaging are shown according to minimal luminal area (MLA) and plaque burden (PB) as detected on gray-scale intravascular ultrasonography. The inset shows an example of a thin-cap fibroatheroma imaged by radiofrequency ultrasonography. Data on prevalence are for one or more such lesions per patient. Lesions in patients with indeterminate events were excluded. Reproduced with permission from [11].

In addition, Infraredx Inc. (Burlington, MA), the company which has commercialized near-infrared spectroscopy for the detection (albeit not depth-resolved) of lipid-rich plaques has led additional clinical trials investigating the role of lipid detection in guiding coronary intervention. For example, the Coronary Assessment by

Near-infrared of Atherosclerotic Rupture-prone Yellow (CANARY) trial is actively investigating criteria for defining lipid core plaques which are at increased risk of rupturing and inducing intra-procedural complications during PCI [13,14]. From a more long term perspective, Infraredx has also initiated the Chemometric Observations of Lipid Core Plaque of Interest in Native Coronary Arteries (COLOR) registry to be used for assessment of the varieties of lipid-rich plaques and their long-term clinical significance and responses to available therapies as well as the large scale Lipid-Rich Plaque Study trial which is intended to assess whether their imaging modality can be utilized as a predictor of future coronary events [15]. Combined IVUS/IVPA imaging is well positioned to capitalize on the results from each of these clinical trials. Experimental results shown to date support the hypothesis that image guidance by IVUS/IVPA will provide the only imaging technique capable of localizing the distribution of lipid during PCI guidance and will, therefore, lead to a more complete understanding of the relationship between lipid-rich plaques and periprocedural complications as well as an improved ability to identify such lesions during therapy guidance.

This dissertation has focused on applications of IVUS/IVPA imaging for novel diagnostic and therapy guidance applications through the delivery of exogenous agents, the clinical translation of which are, in all likelihood, more long term and admittedly higher risk techniques to be translated into clinical practice. The introduction of exogenous agents will require an additional layer of safety concerns to be addressed in preclinical trials, while the therapeutic approaches which served as the motivation for Chapters 3 and 4 of the dissertation are at early stages of development and represent significant deviations from current PCI standards of care. Each of these factors will

necessitate substantial preclinical and clinical testing to validate safety and efficacy in comparison with existing alternatives.

5.2.2. Outlook for the Clinical Use of Noble Metal Nanoparticles as Imaging Contrast Agents and Therapeutic Vehicles

Plasmonic nanoparticle contrast agents provide great promise as tools for expanding the cellular/molecular sensitivity of IVPA imaging, as demonstrated through the labeling of phagocytically active macrophages throughout this dissertation. However, the long-term safety of such contrast agents is not yet fully understood. It has been shown in systemically-injected animal models, for example, that metallic nanoparticles larger than 6 nm do not ever fully clear the body and that high percentages of the initial injection are retained within the liver and spleen. However, particles smaller than 6 nm are quickly cleared from circulation and therefore may not allow enough time for sufficient accumulation within the desired targets [16]. In an effort to address these conflicting restrictions, biodegradable clusters of nanoparticles with suitable PA properties have been developed which are comprised of cross-linked 4 nm primary particles that form larger initial sizes until exposed to reduced pH values within intracellular lysosomes [17-19]. While such an approach which increases the likelihood of contrast agent clearance is ideal in the clinical setting, the overall safety of metallic nanoparticle contrast agents, including gold and gold/silica nanoparticles, which are greater than 6 nm are also being studied in ongoing FDA clinical trials for applications within and beyond cardiovascular medicine (Table 5.1) [20]. While the majority of inorganic nanoparticles already approved and currently in clinical trials in Europe and the United States are focused on cancer imaging and therapy, it is noteworthy that three of the nanoparticle platforms utilize gold nanoparticles. These studies are paving the way for clinical adoption of nano-gold. It is also notable that each of the gold nanoparticles in

clinical trials is being investigated for therapeutic applications rather than merely as imaging contrast agents. Most importantly, one of the nanoparticles under development involved the use of gold nanoparticles for plasmonic photothermal therapy (PPTT) of atherosclerotic plaques in first-in-man clinical trials, the NANOM FIM trial [21]. While there is limited preclinical research into the use of gold nanoparticles for PPTT of coronary atherosclerosis, the preliminary results seem to support its continued investigation and have, in part, motivated the coupling of such a strategy with the use of gold nanoparticles for contrast during IVPA imaging [22]. Together, these studies will help guide future research utilizing metallic nanoparticle contrast agents by demonstrating their biological interactions and potential toxicity. Such relationships will likely need to be further investigated to assess potential additional effects, such as local heating, which can result from the interaction between the nanoparticles and nanosecond-pulsed optical illumination during IVPA imaging.

Table 5.1: Inorganic nanoparticles on the market and in clinical trials, Adapted with permission from [20].

Commercial name	Compound	Function	Target disease	Development stage
Feridex I.V.®	Dextran-coated SPIO	MRI contrast agent	Liver tumors	FDA approval in 1996
GastroMARK™	Silicone-coated SPIO	MRI contrast agent	Gastrointestinal forms of cancer	FDA approval in 1996
Resovist®	Carboxydextrane-coated SPIO	MRI contrast agent	Liver tumors	EU approval in 2001
Acticoat	Silver nanoparticles	Antimicrobial barrier dressing	Wound healing	FDA approval in 2005
NanoTherm	Aminosilane-coated SPIO	Magnetic thermotherapy	Brain tumors Prostate and pancreatic carcinoma	EU approval in 2010 Phase I
NBTXR3	Hafnium oxide nanoparticle	Radiation therapy	Soft-tissue sarcoma	Phase 1
-	Silica-gold nanoparticles	Photothermal ablation of atherosclerotic plaques	Atherosclerosis	Phase 1/phase 2
AuroShell®	Gold@silica nanoshells	Photothermal therapy	Refractory head and neck cancers Primary and metastatic tumors in the lung	Phase 1 Approved by FDA for clinical trials in 2012
Aurimmune	TNF-α-bound PEGylated colloidal gold particles	Targeted delivery of TNF-α	Solid tumors	Completed phase 1
Cornell dots	Silica nanoparticles embedded with fluorophores or radioactive iodine	Fluorescence/PET contrast agents	Cancer	Approved by FDA for clinical trials in 2011

Beyond demonstrations of nanoparticle safety and regulatory approval, the use of plasmonic nanoparticles for intravascular contrast and therapy also presents unique constraints beyond that of many other applications, most notably the need for delivery of the nanoparticles within a suitable timeframe for intravascular imaging. Given that intravascular imaging is, at present, utilized during PCI for clarification of uncertainties arising from the use of other diagnostic approaches, it may be difficult to plan which

patients will benefit from an injection of contrast agents far in advance of the time at which imaging is performed. Therefore, the use of long circulating nanoparticles, such as nanoparticles with the circulation times of > 24 hours utilized for systemic injection in animal models of atherosclerosis, may limit their future clinical impact. Achieving similar plaque- and macrophage- specific labeling of the nanoparticles within a time span of a few hours following injection should, therefore, be a goal moving forward. Ideally, agents would be modified to enable rapid labeling following delivery directly into the coronary tree though a flushing port during the intervention, similar to the injection of contrast for angiography. This would limit both effective lead time for contrast enhanced IVPA imaging and reduce concerns of system toxicity by significantly limiting the injected dose.

5.2.3. *In Vivo* Response to Macrophage-Specific Therapy

Chapters 3 and 4 of this dissertation have focused on introducing therapeutic approaches which are complemented by combined IVUS/IVPA imaging using exogenous theranostic agents. The feasibility of IVPA temperature monitoring during PPTT using gold nanorods (AuNR) and *in vitro* characterization of multifunctional nanoparticles for combined IVPA contrast, PPTT and photodynamic therapy (PDT) have been introduced and serve as a foundation for continued research into the utilization of an IVUS/IVPA imaging system for combined diagnostics and optically-triggered, local therapy under image guidance. Moving forward, a key topic to investigate are the immediate and long term effects following *in vivo* application of the proposed therapeutic approach.

Within advanced atherosclerotic lesions, it has been well established that endothelial cells and smooth muscle cells provide plaque stability while macrophages contribute to plaque destabilization [23,24]. Therefore, macrophage-specific therapy and

elimination within atherosclerotic plaques has been proposed using numerous techniques such as delivery of the mammalian target of rapamycin (mTOR) inhibitor everolimus or cytotoxic clodronate-containing liposomes [24-27]. Due to adverse effects of systemic drug delivery, however, these approaches are restricted to local delivery, such as through their incorporation within drug eluting stents [28]. It has also been shown that phagocytic clearance of apoptotic macrophages is compromised in advanced atherosclerotic lesions, leading to questions of the *in vivo* response which will result from therapeutic approaches designed to selectively deplete plaque macrophages in vulnerable lesions [29]. This concern is difficult to test using experimental models of atherosclerosis because such models tend to more closely resemble early atherosclerotic lesions in which the clearance of apoptotic cells is still effective.

With regard to the phototherapy approaches investigated within this dissertation, experimental investigations utilizing either PPTT or PDT for the treatment of atherosclerotic plaques have demonstrated encouraging results, including reduction in atheroma burden following PPTT and a reduction in inflammatory macrophages coupled with reduced plaque volume following PDT [21,22,30,31]. However, the mechanisms involved in creating such an effect are yet to be fully defined.

Studies evaluating the mechanisms of PDT host tissue response have primarily focused on the treatment and response of cancerous tumors [32]. In this case, it has been shown that the tissue injury induced during PDT treatment invokes an innate immune response characterized by an immediate inflammatory response with accompanying neutrophil infiltration followed by efferocytosis, or removal of dead cells from the treated site. If a similar process is maintained in the treatment of atherosclerotic tissue, the magnitude and effect of the short term inflammatory response is important for therapeutic outcome, particularly for the case of treating unstable atherosclerotic plaques. The

efficiency of efferocytosis in advanced lesions is also critical for achieving favorable therapeutic outcome. It has been well established that inefficient clearance of apoptotic and necrotic macrophages plays a role in destabilizing advanced atherosclerotic lesions [33]. Uncertainty regarding how atherosclerotic plaques, and particularly advanced lesions, will respond to the inflammatory response and subsequent need for efficient clearance is supported by a report demonstrating a variable range of therapeutic responses achieved for the PDT treatment of rat carotid arteries at different drug and light dosages [34].

In the case of PPTT, investigations into the underlying nanoparticle-cellular interaction have demonstrated that cell apoptosis is initiated by disruption of the plasma membrane [35,36]. The same study also showed that a 10 fold reduction in laser energy is required for similar cell death if the nanoparticles are attached to the cell membrane versus internalized within the cytoplasm, as well as a 10 fold reduction in energy required when using a femtosecond pulsed laser rather than a continuous wave laser source [35]. These findings offer insights into important considerations related to both the instrumentation utilized for PPTT and nanoparticle targeting strategies. Combination of PPTT and PDT for the treatment of atherosclerotic plaques will require several areas of ongoing research to evaluate whether each of these mechanisms holds true for atherosclerotic tissue.

5.2.4. Modifications and Alternatives for Exogenous Contrast or Therapeutic Agents

Continued development of IVUS/IVPA imaging for diagnosis and image-guided treatment of atherosclerosis offers several avenues for ongoing research, particularly regarding the design and delivery of contrast and/or theranostic agents. The expansive field of nanobiotechnology offers a huge array of potential designs which may offer

advantages for future integration of nanomaterials with diagnosing and treating atherosclerosis; this section focuses on a few specific applications which are of particular interest given the scope of this dissertation.

5.2.4.1. Modifications to Silica-Coated Plasmonic Multifunctional Nanoparticles

Tailoring Degradation and Photosensitizer Release Kinetics

One area of further development and modification to the doped-silica coated nanoparticle design rests in the refinement of the release kinetics of photosensitizing agents, or other therapeutics, from within the silica. A few initial potential avenues for tailoring the release have been investigated, but additional techniques merit further development. For example, the PEG-FITC/SiO_2AuNR utilized within Chapter 4 required the quenching of SiO_2 through the addition of 0.1 mg of 5 kD mPEG-silane per OD·mL of core AuNR. To investigate the effect of PEG on the release kinetics of FITC in cell culture media, a second PEGylation step was performed, whereby the PEG-FITC/SiO_2AuNR were reacted at a pH of 11 in isopropyl alcohol for four hours with 1 mg per OD·mL PEG-silane. Surprisingly, the FITC release from the higher density PEG layer was found to occur on a faster time scale than that of the initial PEGylation protocol, indicating that they may exhibit more rapid silica degradation under physiological conditions (Fig. 5.2).

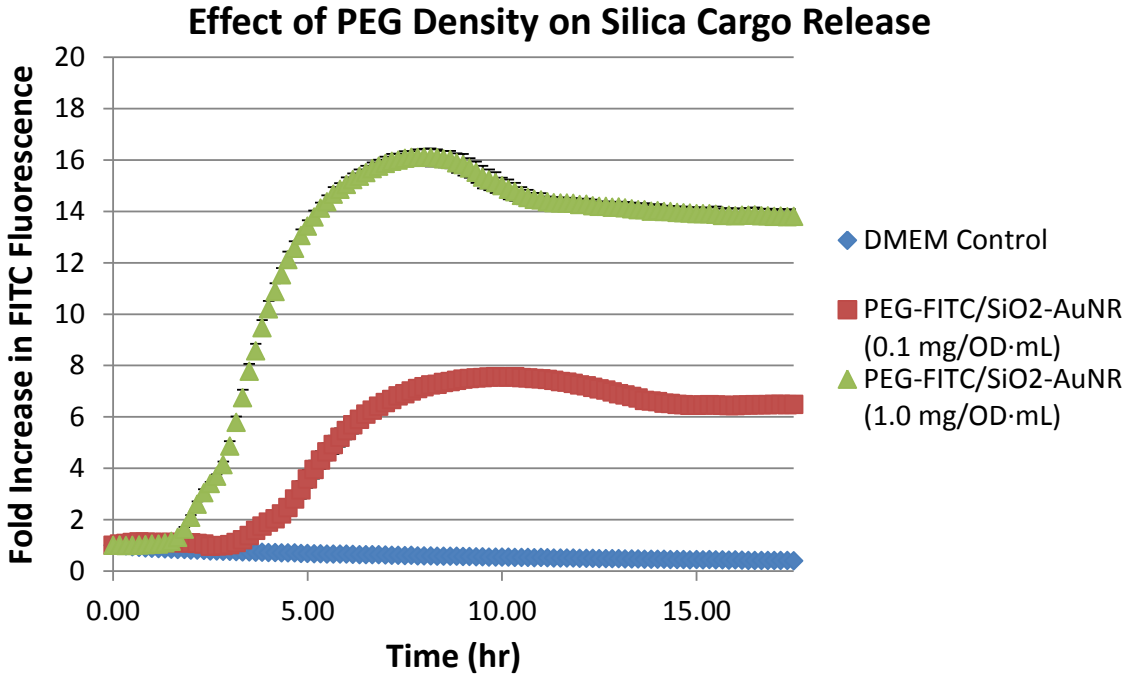

Figure 5.2: Effect of PEG Density on cargo release for PEG-FITC/SiO_2AuNR.

The effect of optical pre-treatment using either the continuous wave (CW) or nanosecond pulsed laser on the release kinetics of PEG-FITC/SiO_2AuNR was also investigated. Exposure of PEG-FITC/SiO_2AuNR in cell culture media to 3 min of 10 mJ/cm^2 nanosecond pulsed irradiation at the AuNR peak absorbance wavelength was ineffective in directly inducing silica disruption and FITC release into the supernatant (Fig. 5.3A). A separate study evaluated the potential for CW or nanosecond pulsed laser irradiation to result in annealing of the silica layer as a means of elongating the release kinetics. Figure 5.3B demonstrated that no significant change was observed in the FITC release temporal profile from a dark control (green), and PEG-FITC/SiO_2AuNR exposed to either 1 W/cm^2 CW illumination (orange) or 2 mJ/cm^2 nanosecond pulsed illumination (red) for 3 min. prior to incubation in culture media. A slight decay in the FITC fluorescence measurement over time was observed for the control group with only cell

culture media (blue) as well as all three experimental groups following the silica degradation and FITC release (after approximately 8 hours) due to photobleaching of fluorophores from the culture medium itself as well as FITC.

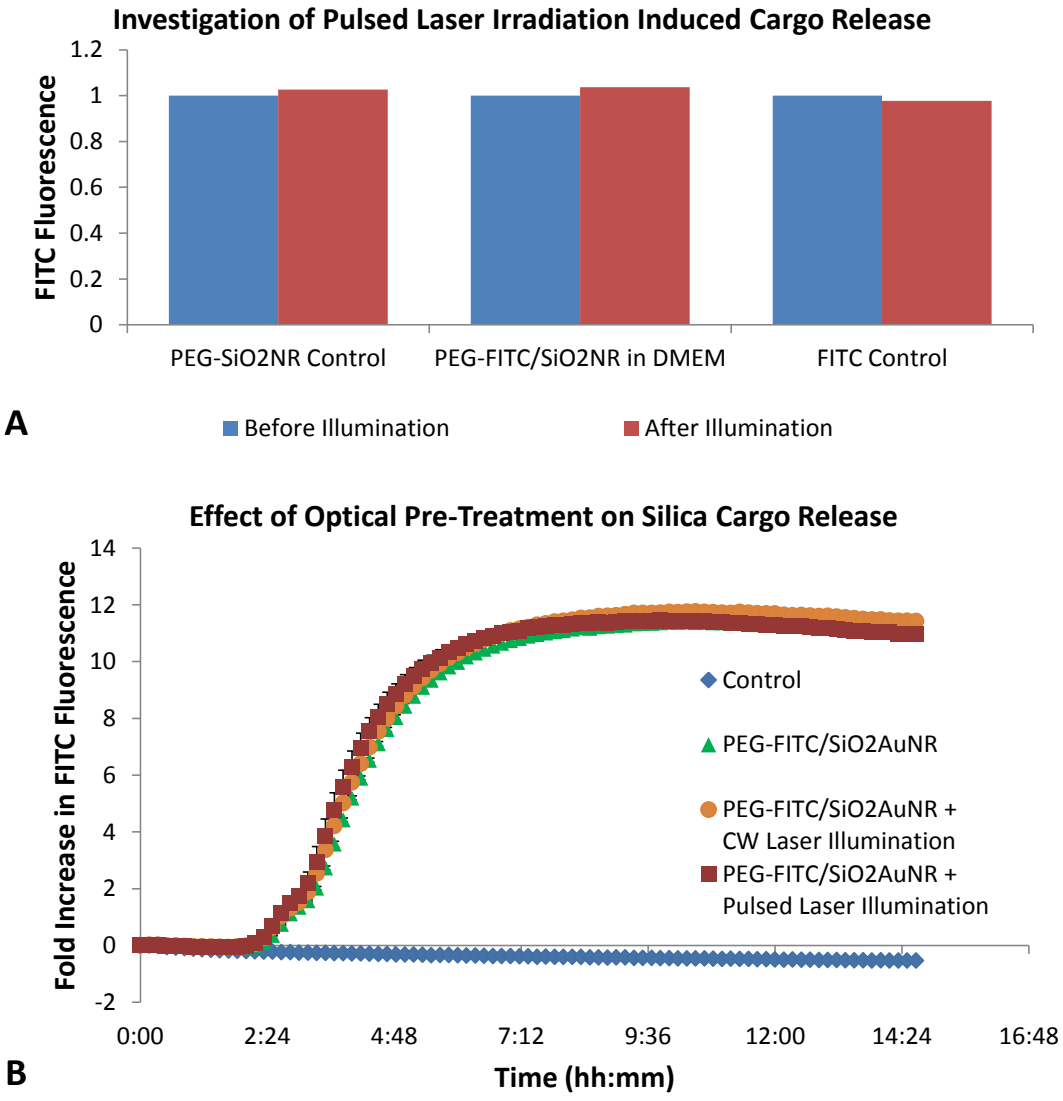

Figure 5.3: Evaluation of laser induced modification of silica cargo release. (A) Fluorescence of supernatant before and after exposure of PEG-FITC/SiO_2AuNR to 10 mJ/cm^2 nanosecond pulsed illumination for 3 min at 800 nm. (B) Release kinetics of PEG-FITC/SiO_2AuNR pre-treated with no illumination (green), 1 W/cm^2 808 nm continuous wave illumination (orange), or 2 mJ/cm^2 nanosecond pulsed illumination (red) for 3 min.

Mesoporous Silica

Utilizing the same fundamental structure as the multifunctional nanoparticles discussed in Chapter 4, comprising a noble metal nanoparticle core with a therapeutic agent doped in a silica shell, several notable modifications merit further investigation. For example, mesoporous silica particles have been widely investigated as high-payload drug carriers which can be modified to enable pH-triggered or thermally-trigger cargo release [37]. The direct doping of photosensitizing agents into an amorphous silica layer may be modified through the introduction of a templated mesoporous silica layer. In an initial attempt to create a mesoporous silica shell covering existing silica-coated gold nanorods, 5 mL of SiO_2AuNR were mixed with 250 µL of ammonia, 25 µL of tetraethylorthosilicate (TEOS) and 10 µL of octadecyltrimethoxysilane (ODTMS) and stirred for 3 hours before being triple washed. In order to ensure that the organic templating molecules, in this case ODTMS, are efficiently removed, the resulting particles were then resuspended in ethanol and vacuum dried overnight prior to being heated to 250 °C for one hour. Figure 5.4, however, shows a resulting TEM revealing that the core AuNR particles were broken apart during heating, further evidenced by a color change from red-orange to purple to teal blue. While classic mesoporous silica nanoparticle synthesis protocol utilize similar approaches for template removal, two recently reported applications utilizing mesoporous silica coated AuNR utilize only washing via centrifugation [38,39]. These approaches merit further investigation, as they may open the door for more easily controlled loading of photosensitizers and additional therapeutic agents.

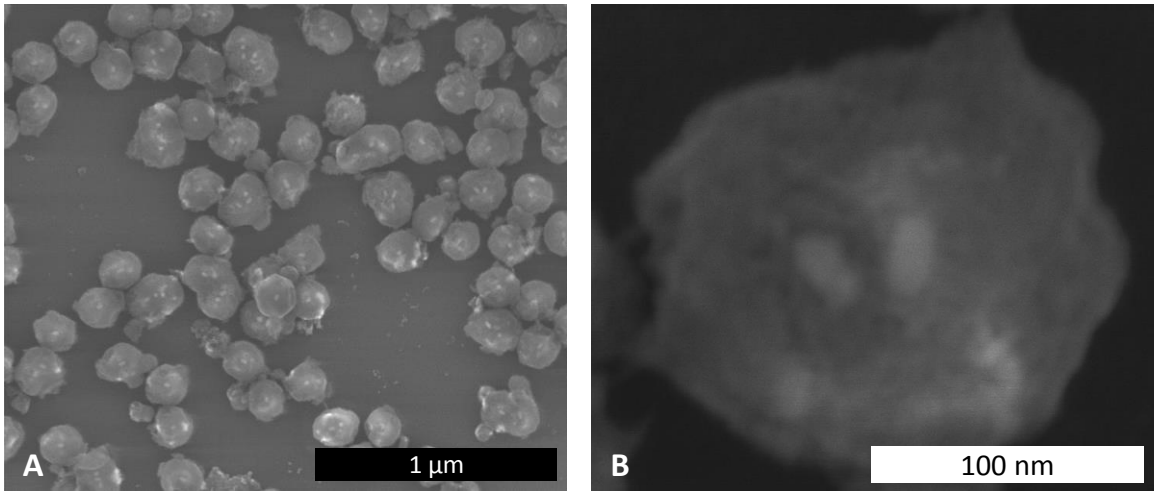

Figure 5.4: Mesoporous silica coated SiO_2AuNR at (A) low and (B) high resolution, revealing the breaking apart of core AuNR particles during organic template removal.

Silver Nanoplate Core Particles

Additionally, the AuNR core particles can be replaced with silver nanoplates (AgNP) which can also be tuned to absorb in the near infrared wavelength range for high-contrast photoacoustic imaging [40]. AgNP were synthesized and tuned to a peak absorbance near 800 nm utilizing an established protocol and then coated with LuTex-doped silica using the same procedure detailed in Chapter 4 (Fig. 5.5). The prepared silver-based multifunctional nanoparticles had an edge length of approximately 160 nm with a silica thickness of approximately 12 nm which degraded following incubation in cell culture media, suggesting that similar characteristics to the multifunctional AuNR discussed in Chapter 4 can be achieved using AgNP. The use of silver nanoparticles is of interest due to their known antibacterial and anti-inflammatory characteristics [41]. However, at this stage, the effect that such particles would have for intravascular applications seems to remain controversial, with conflicting reports regarding their interactions within the vasculature [42]. On one hand, silver nanoparticles have been

linked to endothelial cell dysfunction via oxidative stress as well as platelet aggregation and enhanced thrombus formation [43,44]. Contrarily, silver nanoparticles were also demonstrated to exhibit antiplatelet and anti-clot formation properties [45,46]. Clearly further investigation as to the true nature of their vascular interactions is needed. However, if the antiplatelet properties are verified, silver nanoparticles may provide an advantage over gold-core nanoparticles whereby the core particles themselves provide a localized vaso-protective effect following silica shell degradation and cargo release. The use of silver may have an additional long term advantage in that the gradual release of silver ions from the core particles may enable the entire multifunctional nanoparticle platform to exhibit biodegradability, although the kinetics of the core particle biodegradation should be carefully evaluated [47].

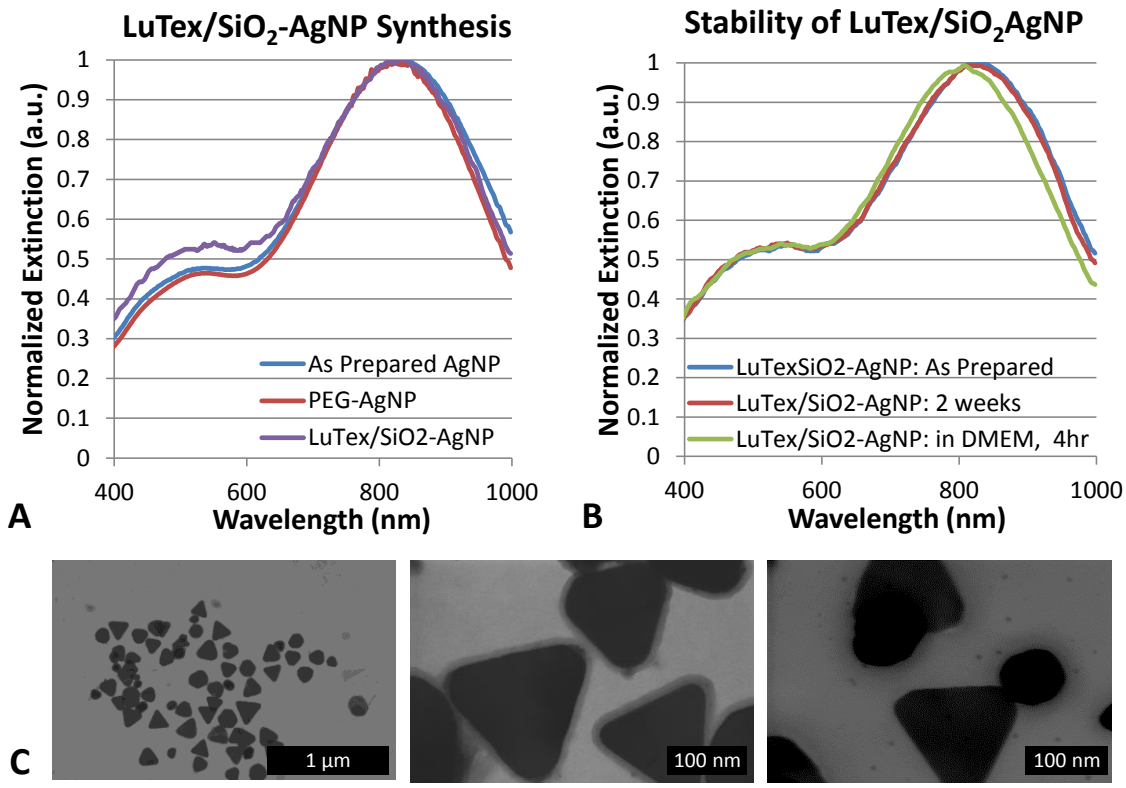

Figure 5.5: Multifunctional silver nanoplates. (A) Optical extinction spectra at different stages of synthesis. (B) Validation of temporal stability of LuTex/SiO_2AgNP in water and SiO2 degradation in cell culture media. (C) Representative TEM images of LuTex/SiO_2AgNP as prepared (left, center) and following silica degradation in culture media for 72 hours (right).

5.2.4.2. Alternative Nanoparticle Surface Functionalization Schemes

Another consideration of nanoparticle design which should be investigated in greater detail is the surface functionalization. This dissertation has focused exclusively on the use of polyethylene glycol (PEG) stabilized nanoparticles, utilizing nonspecific phagocytosis of macrophages for selective, or at least preferential, cell labeling. In Chapter 3 the preferential phagocytosis of silica coated nanoparticles by macrophages relative to endothelial cells was demonstrated *in vitro*. However, the incorporation of macrophage-specific ligands may help further improve cellular specificity and

nanoparticle phagocytosis kinetics. One potential alternative is the polysaccharide dextran, which enables nanoparticles to be efficiently endocytosed by interaction with scavenger receptors [48,49]. To demonstrate this potential, AuNR were coated with a 10 kD dextran using a modification of the protocol utilized for AuNR PEGylation. Two milliliters of 10 mg/mL Dextran containing 10% Rhodamine-B Isothiocyanate conjugated dextran was mixed with 10 mL of AuNR at an optical density of 10, sonicated for 30 minutes and left on a shaker under modest agitation for four hours. The particles were then triple washed with water, resuspended in phosphate buffered saline, and passed through a 200 nm syringe filter for sterilization. The dextran-conjugated AuNR were then incubated with macrophages at variable nanoparticle concentrations under similar experimental conditions to those reported in Chapter 2 using PEG-AuNR. Figure 5.6 reveals the resulting J774A.1 murine macrophage uptake following 18 hours of incubation as well as the maintained cell viability the day following nanoparticle incubation. In comparison to macrophage uptake of comparable concentrations of PEG-AuNR, previously shown in Figures 2.2 and 2.4, higher labeling is achieved using dextran-AuNR.

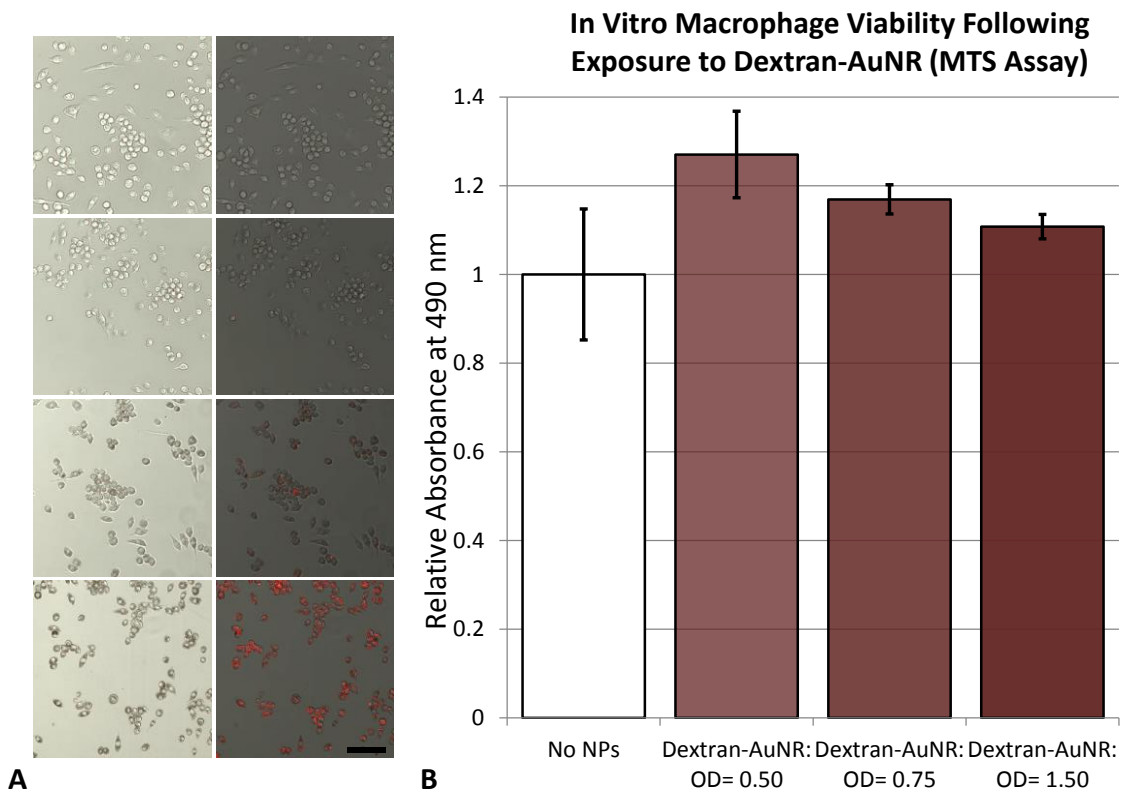

Figure 5.6: J774A.1 murine macrophage uptake of dextran-stabilized gold nanorods and subsequent viability. (A) Brightfield (left) and fluorescence overlay (right) revealing extent of dextran-AuNR uptake for cells incubated with optical density 0, 0.5, 0.75, and 1.5 nanoparticles (top to bottom). Scale bar = 50 μm. (B) Resulting cell viability as assessed by MTS assay the day following nanoparticle incubation with cells.

In addition to the use of PEG or dextran to enable selectivity towards macrophage labeling, more sophisticated nanoparticle functionalization strategies may also be evaluated to enable expanded molecular-specific IVPA imaging. There are numerous biomarkers within atherosclerotic plaques which could be targeted at various stages of atherosclerotic plaque destabilization, ranging from vascular adhesion molecules to

matrix metalloproteinases to thrombin. For example, a cyclic peptide containing an arginine-glycine-aspartic acid (RGD) sequence was conjugated to AuNR using an established protocol involving the attachment of carboxylic acid functionalized PEG to the AuNR surface followed by the use of carbodiimide (EDC) chemistry to conjugate the peptide via an exposed amine group [50]. Figure 5.7 shows the AuNR optical spectra at various stages of synthesis and bioconjugation as well as the significantly enhanced uptake of the nanoparticles with RGD (right) as compared to PEGylated nanoparticles (left) in cells expressing a receptor for RGD peptide sequences. One such receptor is the integrin $\alpha_v\beta_3$, which is highly expressed in neovasculature of the vasa vasorum in advanced atherosclerotic lesions. Therefore, continued investigation into this and other targeting moieties may serve to expand the cellular and molecular specificity for IVPA imaging as well as targeted therapy.

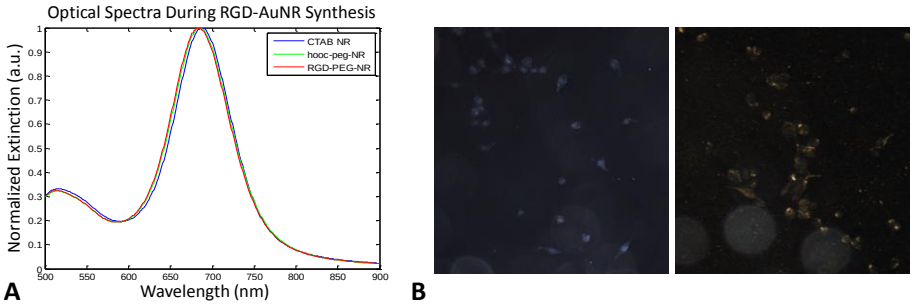

Figure 5.7: RGD peptide-conjugated AuNR. (A) Optical spectra of AuNR as prepared, PEGylated, and conjugated with RGD peptides. (B) 20X darkfield microscopy images of $\alpha_v\beta_3$ expressing MDA-MB-435 cells following incubation with PEG-AuNR (left) and RGD-PEG-AuNR (right).

Another approach for improve cellular specificity utilizes a significant deviation in the nanoparticle design. Biomimetic nanoparticles which resemble high density lipoprotein (HDL) in size, shape and surface chemistry have recently been evaluated as contrast agents for magnetic resonance imaging and computer tomography [51-54]. Due

to the limited size of natural HDL, this particle design necessitates the use of smaller, spherical gold nanoparticles, approximately 5 nm, encompassed in a phospholipid shell with apolipoprotein A1 (Apo-A1), the protein natural found on the surface of HDL particles, embedded. HDL-mimicking gold nanospheres (AuNS) were prepared according to an established protocol, with the nanoparticle schematic and resulting negative stain TEM revealing gold core and phospholipid coating provided in Figures 5.8A and 5.8B, respectively [52]. Figure 5.8C demonstrates that incubation of phospholipid coated AuNS lacking Apo-A1 protein (left) and HDL-mimicking AuNS (right) with J774A.1 murine macrophages for 12 hours resulted in significantly higher HDL-mimicking nanoparticle uptake, as seen in the bright field images (top) and fluorescence images revealing the distribution of Rhodamine-labeled phospholipid which was incorporated into the particles. This result is expected based on the direct recognition of Apo-A1 by macrophage scavenger receptor A.

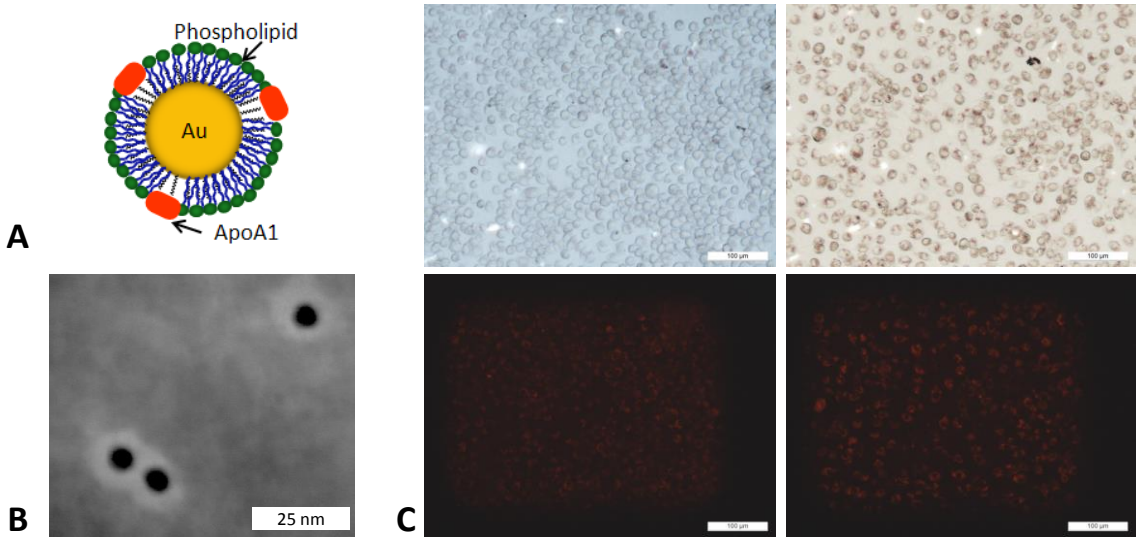

Figure 5.8: HDL-mimicking AuNS design and labeling efficiency. (A) Schematic design of biomimetic nanoparticles. (B) Negative stain TEM revealing AuNS core (dark) and phospholipid core (light). (C) Brightfield and fluorescence imaging of J774A.1 incubated with phospholipid-AuNS (left) and HDL-mimicking-AuNS (right). Scale bar = 100 μm.

The HDL-mimicking AuNS design offers a tradeoff between the inherent optical properties and the nanoparticle biodistribution. On the one hand, the small size of the core AuNR may enable their eventual clearance, as it has been demonstrated that 5 nm nanoparticles can be cleared through renal filtration [16]. This advantage may become significant if larger nanoparticles are shown to induce adverse long term effects following delivery into the vasculature. However, the potential for clearance has not been demonstrated specifically for the HDL-mimicking AuNS. The potential advantage is also offset by the less desirable optical characteristics of AuNS relative to AuNR. The optical absorption peak of AuNS falls at approximately 520 nm, which overlaps with strong hemoglobin absorption. While plasmon resonance coupling of AuNS within intracellular endosomes is known to cause a red shift and significant broadening of the absorbance peak, the extent of such coupling for macrophage labeled with HDL-mimicking AuNS

does not appear to provide contrast within the tissue optical window of the near infrared wavelength region, as assessed by hyperspectral microscopy (Fig. 5.9). Therefore, the use of AuNS-based nanoparticles is expected to provide low contrast than AuNR for IVPA imaging applications, and imaging through luminal blood is likely not an option.

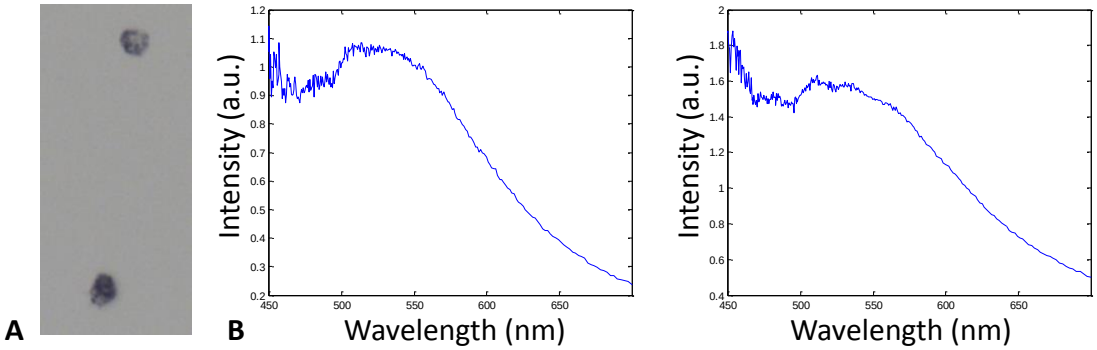

Figure 5.9: Plasmon resonance coupling of intracellular HDL-mimicking AuNS. (A) 40X brightfiled microscopy image of two HDL-mimicking AuNS labeled J774A.1 macrophage cells. (B) Brightfield hyperspectral analysis of the two cells shown in A, revealing little optical absorption beyond 650 nm.

5.2.4.3. Indocyanine Green as a Contrast Agent for Intravascular Photoacoustic Imaging

The use of metallic nanoparticles can be altogether eliminated through the use of organic chromophores such as indocyanine green (ICG). ICG is widely investigated as a biomedical optical contrast agents because it has already been approved for clinical use for limited indications [55]. Among these investigation applications is a recent report demonstrating that systemically injected ICG preferentially co-localizes with atherosclerotic plaques in animal models of atherosclerosis, similar to the labeling pattern shown in Chapter 2 for AuNR [56]. The organic fluorophore also is known to yield a concentration depended optical absorption spectrum, presenting both a challenge and potential means of quantification of contrast delivery using IVPA imaging. Figure 5.10

demonstrates an initial investigation into the sensitivity of IVPA to detect ICG at carious concentrations, revealing a minimum detectable concentration of approximately 500 µM.

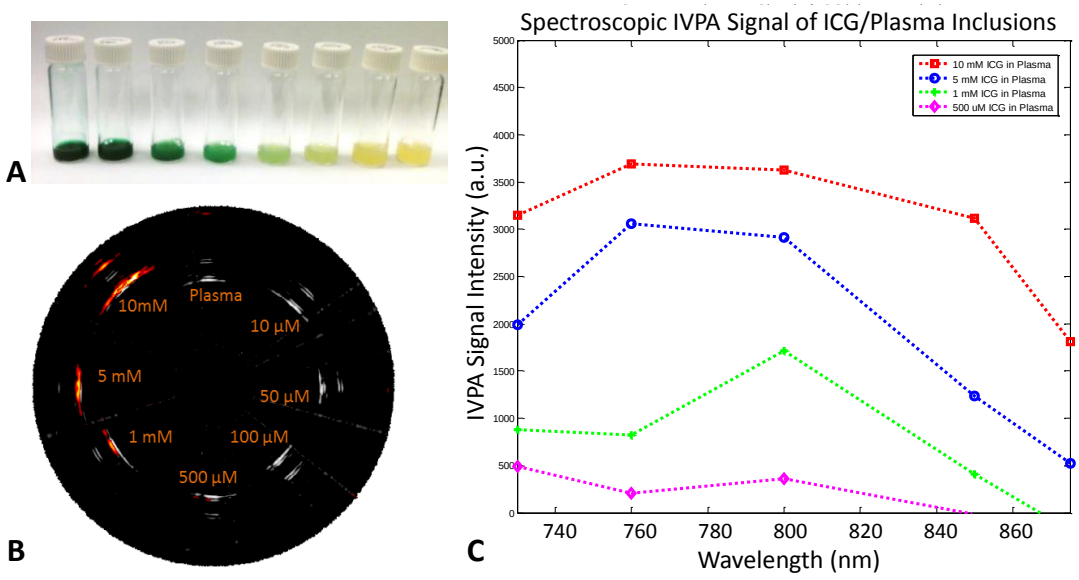

Figure 5.10: IVPA imaging of an ICG phantom. (A) Photograph of ICG in plasma at 10 mM, 5 mM, 1 mM, 500 µM, 100 µM, 50 µM, 10 µM and 0 µM. (B) IVUS/IVPA image of cylindrically oriented inclusions containing the ICG concentrations shown in A. (C) Spectroscopic IVPA signal for inclusions in which ICG was detected, ≥ 500 µM.

Continued development of IVPA imaging of ICG represents an attractive alternative to the use of metallic nanoparticles, primarily because of the rapid clearance of ICG. However, elimination of the metallic core particles will greatly reduce specificity for photothermal heating over background tissue due to the lower extinction coefficient of organic fluorophores in comparison to metallic nanoparticles. Therefore, alternative therapeutic strategies should also be investigated in parallel with studies evaluating the use of ICG for IVPA imaging contrast.

5.3. CONCLUSIONS

Combined intravascular ultrasound and photoacoustic (IVUS/IVPA) imaging is actively being developed as a tool for improved characterization of high-risk atherosclerotic plaques. The use of exogenous contrast agents offers the potential for expanding the cellular and molecular specificity of IVPA imaging as well as the introduction of optically-triggered, local therapy of identified lesions. This dissertation has focused on introducing methods for expanding the IVUS/IVPA imaging platform to enable theranostics of atherosclerotic lesions using image-guided excitation of exogenous contrast agents delivered to macrophages within atherosclerotic lesions. While the overall approach needs continued refinement as it is translated to *in vivo* imaging and therapeutic applications, the potential for providing a new standard of interventional therapy that is cell-specific and locally-delivered merit its continued investigation.

5.4. REFERENCES

1. R. Virmani, A. P. Burke, A. Farb and F. D. Kolodgie, "Pathology of the Vulnerable Plaque," *Journal of the American College of Cardiology*, 47(8, Supplement):C13-C18, (2006).

2. B. Wang, J. L. Su, J. Amirian, S. H. Litovsky, R. Smalling and S. Emelianov, "Detection of lipid in atherosclerotic vessels using ultrasound-guided spectroscopic intravascular photoacoustic imaging," *Opt. Express*, 18(5):4889-4897, (2010).

3. R. D. Madder, J. L. Smith, S. R. Dixon and J. A. Goldstein, "Composition of Target Lesions by Near-Infrared Spectroscopy in Patients With Acute Coronary Syndrome Versus Stable Angina," *Circulation: Cardiovascular Interventions*, 5(1):55-61, (2012).

4. K. Jansen, A. F. van der Steen, H. M. van Beusekom, J. W. Oosterhuis and G. van Soest, "Intravascular photoacoustic imaging of human coronary atherosclerosis," *Opt Lett*, 36(5):597-9, (2011).

5. Institute, A.N.S., *ANSI Z136.1-2007 American national standard for safe use of lasers*. 2007.

6. Institute, A.N.S., *ANSI Z136.3- Safe Use of Lasers in Health Care*. 2011.

7. S. Sethuraman, A. Rakalin, S. Aglyamov, J. Amirian, R. Smalling and S. Emelianov, "6G-3 Temperature Monitoring in Intravascular Photoacoustic Imaging," *Ultrasonics Symposium, 2006. IEEE*, (714-717), (2006).

8. S. Sethuraman, S. R. Aglyamov, R. W. Smalling and S. Y. Emelianov, "Remote temperature estimation in intravascular photoacoustic imaging," *Ultrasound Med Biol*, 34(2):299-308, (2008).

9. P. J. Fitzgerald and P. G. Yock, "Mechanisms and outcomes of angioplasty and atherectomy assessed by intravascular ultrasound imaging," *J Clin Ultrasound*, 21(9):579-88, (1993).

10. S. Waxman, F. Ishibashi and J. E. Muller, "Detection and Treatment of Vulnerable Plaques and Vulnerable Patients: Novel Approaches to Prevention of Coronary Events," *Circulation*, 114(22):2390-2411, (2006).

11. G. W. Stone, A. Maehara, A. J. Lansky, B. de Bruyne, E. Cristea, G. S. Mintz, R. Mehran, J. McPherson, N. Farhat, S. P. Marso, H. Parise, B. Templin, R. White, Z. Zhang and P. W. Serruys, "A Prospective Natural-History Study of Coronary Atherosclerosis," *New England Journal of Medicine*, 364(3):226-235, (2011).

12. J. L. Fleg, G. W. Stone, Z. A. Fayad, J. F. Granada, T. S. Hatsukami, F. D. Kolodgie, J. Ohayon, R. Pettigrew, M. S. Sabatine, G. J. Tearney, S. Waxman, M. J. Domanski, P. R. Srinivas and J. Narula, "Detection of high-risk atherosclerotic plaque: report of the NHLBI Working Group on current status and future directions," *JACC Cardiovasc Imaging*, 5(9):941-55, (2012).

13. J. A. Goldstein, C. Grines, T. Fischell, R. Virmani, D. Rizik, J. Muller and S. R. Dixon, "Coronary embolization following balloon dilation of lipid-core plaques," *JACC Cardiovasc Imaging*, 2(12):1420-4, (2009).

14. J. A. Goldstein, B. Maini, S. R. Dixon, E. S. Brilakis, C. L. Grines, D. G. Rizik, E. R. Powers, D. H. Steinberg, K. A. Shunk, G. Weisz, P. R. Moreno, A. Kini, S. K. Sharma, M. J. Hendricks, S. T. Sum, S. P. Madden, J. E. Muller, G. W. Stone and M. J. Kern, "Detection of Lipid-Core Plaques by Intracoronary Near-Infrared Spectroscopy Identifies High Risk of Periprocedural Myocardial Infarction," *Circulation: Cardiovascular Interventions*, 4(5):429-437, (2011).

15. M. J. Suter, S. K. Nadkarni, G. Weisz, A. Tanaka, F. A. Jaffer, B. E. Bouma and G. J. Tearney, "Intravascular optical imaging technology for investigating the coronary artery," *JACC Cardiovasc Imaging*, 4(9):1022-39, (2011).

16. M. Longmire, P. L. Choyke and H. Kobayashi, "Clearance properties of nano-sized particles and molecules as imaging agents: considerations and caveats," *Nanomedicine (Lond)*, 3(5):703-17, (2008).

17. J. M. Tam, A. K. Murthy, D. R. Ingram, R. Nguyen, K. V. Sokolov and K. P. Johnston, "Kinetic assembly of near-IR-active gold nanoclusters using weakly adsorbing polymers to control the size," *Langmuir*, 26(11):8988-99, (2010).

18. J. M. Tam, J. O. Tam, A. Murthy, D. R. Ingram, L. L. Ma, K. Travis, K. P. Johnston and K. V. Sokolov, "Controlled assembly of biodegradable plasmonic nanoclusters for near-infrared imaging and therapeutic applications," *ACS Nano*, 4(4):2178-84, (2010).

19. S. J. Yoon, S. Mallidi, J. M. Tam, J. O. Tam, A. Murthy, K. P. Johnston, K. V. Sokolov and S. Y. Emelianov, "Utility of biodegradable plasmonic nanoclusters in photoacoustic imaging," *Opt Lett*, 35(22):3751-3, (2010).

20. G. Bao, S. Mitragotri and S. Tong, "Multifunctional nanoparticles for drug delivery and molecular imaging," *Annu Rev Biomed Eng*, 15:253-82, (2013).

21. A. N. Kharlamov, A. E. Tyurnina, V. S. Veselova, O. S. Novoselova, A. S. Filatova, O. P. Kovtun, V. Y. Shur and J. L. Gabinsky, "Plasmonics for Treatment of Atherosclerosis: Results of NANOM-FIM Trial," *Nanomedicine & Nanotechnology*, 4(160):doi: 10.4172/2157-7439.1000160, (2013).

22. A. N. Kharlamov and J. L. Gabinsky, "Plasmonic photothermic and stem cell therapy of atherosclerotic plaque as a novel nanotool for angioplasty and artery remodeling," *Rejuvenation Res*, 15(2):222-230, (2012).

23. A. Lafont, "Basic aspects of plaque vulnerability," *Heart*, 89(10):1262-7, (2003).

24. S. Verheye, W. Martinet, M. M. Kockx, M. W. Knaapen, K. Salu, J. P. Timmermans, J. T. Ellis, D. L. Kilpatrick and G. R. De Meyer, "Selective clearance of macrophages in atherosclerotic plaques by autophagy," *J Am Coll Cardiol*, 49(6):706-15, (2007).

25. I. De Meyer, W. Martinet and G. R. De Meyer, "Therapeutic strategies to deplete macrophages in atherosclerotic plaques," *Br J Clin Pharmacol*, 74(2):246-63, (2012).

26. N. van Rooijen, A. Sanders and T. K. van den Berg, "Apoptosis of macrophages induced by liposome-mediated intracellular delivery of clodronate and propamidine," *J Immunol Methods*, 193(1):93-9, (1996).

27. W. Martinet, S. Verheye and G. R. De Meyer, "Selective depletion of macrophages in atherosclerotic plaques via macrophage-specific initiation of cell death," *Trends Cardiovasc Med*, 17(2):69-75, (2007).

28. W. Martinet and G. R. Y. De Meyer, "Selective Depletion of Macrophages in Atherosclerotic Plaques: Myth, Hype, or Reality?," *Circulation Research*, 100(6):751-753, (2007).

29. D. M. Schrijvers, G. R. De Meyer, M. M. Kockx, A. G. Herman and W. Martinet, "Phagocytosis of apoptotic cells by macrophages is impaired in atherosclerosis," *Arterioscler Thromb Vasc Biol*, 25(6):1256-61, (2005).

30. M. Hayase, K. W. Woodbum, J. Perlroth, R. A. Miller, W. Baumgardner, P. G. Yock and A. Yeung, "Photoangioplasty with local motexafin lutetium delivery reduces macrophages in a rabbit post-balloon injury model," *Cardiovasc Res*, 49(2):449-55, (2001).

31. R. Waksman, P. E. McEwan, T. I. Moore, R. Pakala, F. D. Kolodgie, D. G. Hellinga, R. C. Seabron, S. J. Rychnovsky, J. Vasek, R. W. Scott and R. Virmani, "PhotoPoint Photodynamic Therapy Promotes Stabilization of Atherosclerotic Plaques and Inhibits Plaque Progression," *Journal of the American College of Cardiology*, 52(12):1024-1032, (2008).

32. M. Korbelik, "PDT-associated host response and its role in the therapy outcome," *Lasers Surg Med*, 38(5):500-8, (2006).

33. I. Tabas, "Consequences and therapeutic implications of macrophage apoptosis in atherosclerosis: the importance of lesion stage and phagocytic efficiency," *Arterioscler Thromb Vasc Biol*, 25(11):2255-64, (2005).

34. F. Adili, R. G. Statius van Eps and G. M. LaMuraglia, "Significance of dosimetry in photodynamic therapy of injured arteries: classification of biological responses," *Photochem Photobiol*, 70(4):663-8, (1999).

35. L. Tong, Y. Zhao, T. B. Huff, M. N. Hansen, A. Wei and J. X. Cheng, "Gold Nanorods Mediate Tumor Cell Death by Compromising Membrane Integrity," *Adv Mater*, 19:3136-3141, (2007).

36. X. Huang and M. A. El-Sayed, "Plasmonic photo-thermal therapy (PPTT)," *Alexandria Journal of Medicine*, 47(1):1-9, (2011).

37. W. Fang, J. Yang, J. Gong and N. Zheng, "Photo- and pH-Triggered Release of Anticancer Drugs from Mesoporous Silica-Coated Pd@Ag Nanoparticles," *Advanced Functional Materials*, 22(4):842-848, (2012).

38. Z. Zhang, L. Wang, J. Wang, X. Jiang, X. Li, Z. Hu, Y. Ji, X. Wu and C. Chen, "Mesoporous Silica-Coated Gold Nanorods as a Light-Mediated Multifunctional Theranostic Platform for Cancer Treatment," *Advanced Materials*, 24(11):1418-1423, (2012).

39. G. Terentyuk, E. Panfilova, V. Khanadeev, D. Chumakov, E. Genina, A. Bashkatov, V. Tuchin, A. Bucharskaya, G. Maslyakova, N. Khlebtsov and B. Khlebtsov, "Gold nanorods with a hematoporphyrin-loaded silica shell for dual-modality photodynamic and photothermal treatment of tumors in vivo," *Nano Research*, 7(3):325-337, (2014).

40. K. A. Homan, M. Souza, R. Truby, G. P. Luke, C. Green, E. Vreeland and S. Emelianov, "Silver nanoplate contrast agents for in vivo molecular photoacoustic imaging," *ACS Nano*, 6(1):641-50, (2012).

41. L. Ge, Q. Li, M. Wang, J. Ouyang, X. Li and M. M. Xing, "Nanosilver particles in medical applications: synthesis, performance, and toxicity," *Int J Nanomedicine*, 9:2399-407, (2014).

42. A. N. Ilinskaya and M. A. Dobrovolskaia, "Nanoparticles and the blood coagulation system. Part II: safety concerns," *Nanomedicine (Lond)*, 8(6):969-81, (2013).

43. J. Shi, X. Sun, Y. Lin, X. Zou, Z. Li, Y. Liao, M. Du and H. Zhang, "Endothelial cell injury and dysfunction induced by silver nanoparticles through oxidative stress via IKK/NF-kappaB pathways," *Biomaterials*, 35(24):6657-66, (2014).

44. E. A. Jun, K. M. Lim, K. Kim, O. N. Bae, J. Y. Noh, K. H. Chung and J. H. Chung, "Silver nanoparticles enhance thrombus formation through increased platelet aggregation and procoagulant activity," *Nanotoxicology*, 5(2):157-67, (2011).

45. S. Shrivastava, S. K. Singh, A. Mukhopadhyay, A. S. Sinha, R. K. Mandal and D. Dash, "Negative regulation of fibrin polymerization and clot formation by nanoparticles of silver," *Colloids Surf B Biointerfaces*, 82(1):241-6, (2011).

46. S. Shrivastava, T. Bera, S. K. Singh, G. Singh, P. Ramachandrarao and D. Dash, "Characterization of antiplatelet properties of silver nanoparticles," *ACS Nano*, 3(6):1357-64, (2009).

47. J. Kim, J. Lee, S. Kwon and S. Jeong, "Preparation of biodegradable polymer/silver nanoparticles composite and its antibacterial efficacy," *J Nanosci Nanotechnol*, 9(2):1098-102, (2009).

48. Y. Chao, P. P. Karmali and D. Simberg, "Role of carbohydrate receptors in the macrophage uptake of dextran-coated iron oxide nanoparticles," *Adv Exp Med Biol*, 733:115-23, (2012).

49. A. K. Silva, D. Letourneur and C. Chauvierre, "Polysaccharide nanosystems for future progress in cardiovascular pathologies," *Theranostics*, 4(6):579-91, (2014).

50. X. Huang, X. Peng, Y. Wang, Y. Wang, D. M. Shin, M. A. El-Sayed and S. Nie, "A reexamination of active and passive tumor targeting by using rod-shaped gold nanocrystals and covalently conjugated peptide ligands," *ACS Nano*, 4(10):5887-96, (2010).

51. T. Skajaa, D. P. Cormode, E. Falk, W. J. Mulder, E. A. Fisher and Z. A. Fayad, "High-density lipoprotein-based contrast agents for multimodal imaging of atherosclerosis," *Arterioscler Thromb Vasc Biol*, 30(2):169-76, (2010).

52. D. P. Cormode, T. Skajaa, M. M. van Schooneveld, R. Koole, P. Jarzyna, M. E. Lobatto, C. Calcagno, A. Barazza, R. E. Gordon, P. Zanzonico, E. A. Fisher, Z. A. Fayad and W. J. Mulder, "Nanocrystal core high-density lipoproteins: a multimodality contrast agent platform," *Nano Lett*, 8(11):3715-23, (2008).

53. T. Skajaa, D. P. Cormode, P. A. Jarzyna, A. Delshad, C. Blachford, A. Barazza, E. A. Fisher, R. E. Gordon, Z. A. Fayad and W. J. Mulder, "The biological properties of iron oxide core high-density lipoprotein in experimental atherosclerosis," *Biomaterials*, 32(1):206-13, (2011).

54. C. S. Thaxton, W. L. Daniel, D. A. Giljohann, A. D. Thomas and C. A. Mirkin, "Templated spherical high density lipoprotein nanoparticles," *J Am Chem Soc*, 131(4):1384-5, (2009).

55. S. Zonghai, H. Dehong, X. Miaomiao, H. Meng, G. Ping and C. Lintao, "Indocyanine Green Nanoparticles for Theranostic Applications," *Nano-Micro Letters*, 5(3):145-150, (2013).

56. C. Vinegoni, I. Botnaru, E. Aikawa, M. A. Calfon, Y. Iwamoto, E. J. Folco, V. Ntziachristos, R. Weissleder, P. Libby and F. A. Jaffer, "Indocyanine green enables near-infrared fluorescence imaging of lipid-rich, inflamed atherosclerotic plaques," *Sci Transl Med*, 3(84):84ra45, (2011).

References

Adili, F., R.G. Statius van Eps, and G.M. LaMuraglia, *Significance of dosimetry in photodynamic therapy of injured arteries: classification of biological responses.* Photochem Photobiol, 1999. **70**(4): p. 663-8.

Alkilany, A.M., et al., *Toxicity and cellular uptake of gold nanorods in vascular endothelium and smooth muscles of isolated rat blood vessel: importance of surface modification.* Small, 2012. **8**(8): p. 1270-8.

Alkilany, A.M., et al., *Gold nanorods: Their potential for photothermal therapeutics and drug delivery, tempered by the complexity of their biological interactions.* Advanced Drug Delivery Reviews, 2012. **64**(2): p. 190-199.

Allen, T.J., et al., *Spectroscopic photoacoustic imaging of lipid-rich plaques in the human aorta in the 740 to 1400 nm wavelength range.* J Biomed Opt, 2012. **17**(6): p. 061209.

Andrei, B.K., W. Bo, and Y.E. Stanislav, *Development of a catheter for combined intravascular ultrasound and photoacoustic imaging.* Review of Scientific Instruments, 2010. **81**(1): p. 014901.

Bao, G., S. Mitragotri, and S. Tong, *Multifunctional nanoparticles for drug delivery and molecular imaging.* Annu Rev Biomed Eng, 2013. **15**: p. 253-82.

Baraga, J.J., M.S. Feld, and R.P. Rava, *In situ optical histochemistry of human artery using near infrared Fourier transform Raman spectroscopy.* Proc Natl Acad Sci U S A, 1992. **89**(8): p. 3473-7.

Baraga, J.J., et al., *Laser induced fluorescence spectroscopy of normal and atherosclerotic human aorta using 306-310 nm excitation.* Lasers Surg Med, 1990. **10**(3): p. 245-61.

Baumbach, A., et al., *Acute complications of excimer laser coronary angioplasty: A detailed analysis of multicenter results.* Journal of the American College of Cardiology, 1994. **23**(6): p. 1305-1313.

Bayer, C.L., et al., *Multiplex photoacoustic molecular imaging using targeted silica-coated gold nanorods.* Biomed Opt Express, 2011. **2**(7): p. 1828-35.

Beard, P., *Biomedical photoacoustic imaging.* Interface Focus, 2011. **1**(4): p. 602-31.

Bell, A.G., *Upon the production and reproduction of sound by light.* Telegraph Engineers, Journal of the Society of, 1880. **9**(34): p. 404-426.

Bhattacharyya, S., et al., *Synthesis and evaluation of near-infrared (NIR) dye-herceptin conjugates as photoacoustic computed tomography (PCT) probes for HER2 expression in breast cancer.* Bioconjug Chem, 2008. **19**(6): p. 1186-93.

Bowen, T. *Radiation-Induced Thermoacoustic Soft Tissue Imaging*. in *1981 Ultrasonics Symposium*. 1981.

Brennan Iii, J.F., et al., *The vPredict™ Optical Catheter System: Intravascular Raman Spectroscopy.* EuroIntervention, 2008. **3**(5): p. 635-638.

Brennan, J.F., et al., *Determination of Human Coronary Artery Composition by Raman Spectroscopy.* Circulation, 1997. **96**(1): p. 99-105.

Brugaletta, S., et al., *NIRS and IVUS for Characterization of Atherosclerosis in Patients Undergoing Coronary Angiography.* JACC: Cardiovascular Imaging, 2011. **4**(6): p. 647-655.

Brunetaud, J.M., et al., *Non-PDT Uses of lasers in oncology.* Lasers in Medical Science, 1995. **10**(1): p. 3-8.

Buschman, H.P., et al., *In Vivo Determination of the Molecular Composition of Artery Wall by Intravascular Raman Spectroscopy.* Analytical Chemistry, 2000. **72**(16): p. 3771-3775.

Caplan, J.D., et al., *Near-infrared spectroscopy for the detection of vulnerable coronary artery plaques.* J Am Coll Cardiol, 2006. **47**(8 Suppl): p. C92-6.

Cassis, L.A. and R.A. Lodder, *Near-IR imaging of atheromas in living arterial tissue.* Anal Chem, 1993. **65**(9): p. 1247-56.

Chao, Y., P.P. Karmali, and D. Simberg, *Role of carbohydrate receptors in the macrophage uptake of dextran-coated iron oxide nanoparticles.* Adv Exp Med Biol, 2012. **733**: p. 115-23.

Chapman, I., *Relationships of recent coronary artery occlusion and acute myocardial infarction.* J Mt Sinai Hosp N Y, 1968. **35**(2): p. 149-54.

Chau, A.H., et al., *Fingerprint and high-wavenumber Raman spectroscopy in a human-swine coronary xenograft in vivo.* J Biomed Opt, 2008. **13**(4): p. 040501.

Chen, Y.-S., et al., *Environment-Dependent Generation of Photoacoustic Waves from Plasmonic Nanoparticles.* Small, 2012. **8**(1): p. 47-52.

Chen, Y.-S., et al., *Enhanced thermal stability of silica-coated gold nanorods for photoacoustic imaging and image-guided therapy.* Opt. Express, 2010. **18**(9): p. 8867-8878.

Chen, Y.-S., et al., *Silica-Coated Gold Nanorods as Photoacoustic Signal Nanoamplifiers.* Nano Letters, 2011. **11**(2): p. 348-354.

Chen, Y.-S., et al., *Sensitivity enhanced nanothermal sensors for photoacoustic temperature mapping.* Journal of Biophotonics, 2013. **6**(6-7): p. 534-542.

Cheruvu, P.K., et al., *Frequency and Distribution of Thin-Cap Fibroatheroma and Ruptured Plaques in Human Coronary Arteries: A Pathologic Study.* Journal of the American College of Cardiology, 2007. **50**(10): p. 940-949.

Choudhury, R.P., V. Fuster, and Z.A. Fayad, *Molecular, cellular and functional imaging of atherothrombosis.* Nat Rev Drug Discov, 2004. **3**(11): p. 913-925.

Clarke, R.H., et al., *Gas chromatographic-light microscopic correlative analysis of excimer laser photoablation of cardiovascular tissues: evidence for a thermal mechanism.* Circ Res, 1987. **60**(3): p. 429-37.

Constantinides, P., *Pathogenesis of cerebral artery thrombosis in man.* Arch Pathol, 1967. **83**(5): p. 422-8.

Cormode, D.P., et al., *Nanocrystal core high-density lipoproteins: a multimodality contrast agent platform.* Nano Lett, 2008. **8**(11): p. 3715-23.

Davies, M.J. and A.C. Thomas, *Plaque fissuring--the cause of acute myocardial infarction, sudden ischaemic death, and crescendo angina.* Br Heart J, 1985. **53**(4): p. 363-73.

Davignon, J. and P. Ganz, *Role of Endothelial Dysfunction in Atherosclerosis.* Circulation, 2004. **109**(23 suppl 1): p. III-27-III-32.

De la Zerda, A., et al., *Ultrahigh sensitivity carbon nanotube agents for photoacoustic molecular imaging in living mice.* Nano Lett, 2010. **10**(6): p. 2168-72.

De la Zerda, A., et al., *Carbon nanotubes as photoacoustic molecular imaging agents in living mice.* Nat Nanotechnol, 2008. **3**(9): p. 557-62.

De Meyer, I., W. Martinet, and G.R. De Meyer, *Therapeutic strategies to deplete macrophages in atherosclerotic plaques.* Br J Clin Pharmacol, 2012. **74**(2): p. 246-63.

Deckelbaum, L.I., et al., *Discrimination of normal and atherosclerotic aorta by laser-induced fluorescence.* Lasers Surg Med, 1987. **7**(4): p. 330-5.

Diebold, G.J. and T. Sun, *Properties of Photoacoustic Waves in One, Two, and Three Dimensions.* Acta Acustica united with Acustica, 1994. **80**(4): p. 339-351.

Duck, F.A., *Chapter 2 - Thermal Properties of Tissue*, in *Physical Properties of Tissues*, F.A. Duck, Editor. 1990, Academic Press: London. p. 9-42.

Eghtedari, M., et al., *High Sensitivity of In Vivo Detection of Gold Nanorods Using a Laser Optoacoustic Imaging System.* Nano Letters, 2007. **7**(7): p. 1914-1918.

Elson, D.S., J.A. Jo, and L. Marcu, *Miniaturized side-viewing imaging probe for fluorescence lifetime imaging (FLIM): validation with fluorescence dyes, tissue structural proteins and tissue specimens.* New J Phys, 2007. **9**: p. 127.

Evans, J.W., et al., *Optical coherence tomography and Raman spectroscopy of the ex-vivo retina.* J Biophotonics, 2009. **2**(6-7): p. 398-406.

Falk, E., *Plaque rupture with severe pre-existing stenosis precipitating coronary thrombosis. Characteristics of coronary atherosclerotic plaques underlying fatal occlusive thrombi.* Br Heart J, 1983. **50**(2): p. 127-34.

Fang, W., et al., *Photo- and pH-Triggered Release of Anticancer Drugs from Mesoporous Silica-Coated Pd@Ag Nanoparticles.* Advanced Functional Materials, 2012. **22**(4): p. 842-848.

Finn, A.V., et al., *Concept of Vulnerable/Unstable Plaque.* Arteriosclerosis, Thrombosis, and Vascular Biology, 2010. **30**(7): p. 1282-1292.

Fitzgerald, P.J. and P.G. Yock, *Mechanisms and outcomes of angioplasty and atherectomy assessed by intravascular ultrasound imaging.* J Clin Ultrasound, 1993. **21**(9): p. 579-88.

Fleg, J.L., et al., *Detection of high-risk atherosclerotic plaque: report of the NHLBI Working Group on current status and future directions.* JACC Cardiovasc Imaging, 2012. **5**(9): p. 941-55.

Franzen, D., U. Sechtem, and H.W. Hopp, *Comparison of angioscopic, intravascular ultrasonic, and angiographic detection of thrombus in coronary stenosis.* Am J Cardiol, 1998. **82**(10): p. 1273-5, a9.

Friedman, M. and G.J. Van den Bovenkamp, *Role of thrombus in plaque formation in the human diseased coronary artery.* Br J Exp Pathol, 1966. **47**(6): p. 550-7.

Gaglia, M., Jr., D. Steinberg, and N. Weissman, *Intravascular ultrasound: Virtual histology IVUS, integrated backscatter IVUS, and palpography.* Current Cardiovascular Imaging Reports, 2009. **2**(4): p. 268-274.

Gardner, C.M., et al., *Detection of Lipid Core Coronary Plaques in Autopsy Specimens With a Novel Catheter-Based Near-Infrared Spectroscopy System.* JACC: Cardiovascular Imaging, 2008. **1**(5): p. 638-648.

Gautier, E.L., et al., *Macrophage Apoptosis Exerts Divergent Effects on Atherogenesis as a Function of Lesion Stage.* Circulation, 2009. **119**(13): p. 1795-1804.

Ge, L., et al., *Nanosilver particles in medical applications: synthesis, performance, and toxicity.* Int J Nanomedicine, 2014. **9**: p. 2399-407.

Glagov, S., et al., *Compensatory Enlargement of Human Atherosclerotic Coronary Arteries.* New England Journal of Medicine, 1987. **316**(22): p. 1371-1375.

Go, A.S., et al., *Heart Disease and Stroke Statistics—2014 Update: A Report From the American Heart Association.* Circulation, 2014. **129**(3): p. e28-e292.

Goldstein, J.A., et al., *Coronary embolization following balloon dilation of lipid-core plaques.* JACC Cardiovasc Imaging, 2009. **2**(12): p. 1420-4.

Goldstein, J.A., et al., *Detection of Lipid-Core Plaques by Intracoronary Near-Infrared Spectroscopy Identifies High Risk of Periprocedural Myocardial Infarction.* Circulation: Cardiovascular Interventions, 2011. **4**(5): p. 429-437.

Grabinski, C., et al., *Effect of Gold Nanorod Surface Chemistry on Cellular Response.* ACS Nano, 2011. **5**(4): p. 2870-2879.

Graf, I.M., et al., *Noninvasive detection of intimal xanthoma using combined ultrasound, strain rate and photoacoustic imaging.* Ultrasonics, 2012. **52**(3): p. 435-41.

Grzelczak, M., et al., *Shape control in gold nanoparticle synthesis.* Chemical Society Reviews, 2008. **37**(9): p. 1783-1791.

Gusev, V.E. and A.A. Karabutov, *Laser optoacoustics*. Lazernai͡a optoakustika.English. 1993, New York: American Institute of Physics. xvii, 271 p.

Hackett, D., G. Davies, and A. Maseri, *Pre-existing coronary stenoses in patients with first myocardial infarction are not necessarily severe.* European Heart Journal, 1988. **9**(12): p. 1317-1323.

Hao, N., et al., *In vitro degradation behavior of silica nanoparticles under physiological conditions.* J Nanosci Nanotechnol, 2012. **12**(8): p. 6346-54.

Hayase, M., et al., *Photoangioplasty with local motexafin lutetium delivery reduces macrophages in a rabbit post-balloon injury model.* Cardiovasc Res, 2001. **49**(2): p. 449-55.

Hillenbrand, C.M., et al., *Active device tracking and high-resolution intravascular MRI using a novel catheter-based, opposed-solenoid phased array coil.* Magn Reson Med, 2004. **51**(4): p. 668-75.

Hoang, K.C., et al., *Use of an oxygen-carrying blood substitute to improve intravascular optical coherence tomography imaging.* J Biomed Opt, 2009. **14**(3): p. 034028.

Holmes, D.R., Jr., et al., *Coronary perforation after excimer laser coronary angioplasty: the Excimer Laser Coronary Angioplasty Registry experience.* J Am Coll Cardiol, 1994. **23**(2): p. 330-5.

Homagk, A.-K., et al., *An expandable catheter loop coil for intravascular MRI in larger blood vessels.* Magnetic Resonance in Medicine, 2010. **63**(2): p. 517-523.

Homan, K.A., et al., *Silver nanoplate contrast agents for in vivo molecular photoacoustic imaging.* ACS Nano, 2012. **6**(1): p. 641-50.

Hosokawa, R., et al., *A Catheter-Based Intravascular Radiation Detector of Vulnerable Plaques.* Journal of Nuclear Medicine, 2006. **47**(5): p. 863-867.

Hsieh, B.Y., et al., *All-optical scanhead for ultrasound and photoacoustic dual-modality imaging.* Opt Express, 2012. **20**(2): p. 1588-96.

Huang, X. and M.A. El-Sayed, *Plasmonic photo-thermal therapy (PPTT).* Alexandria Journal of Medicine, 2011. **47**(1): p. 1-9.

Huang, X., S. Neretina, and M.A. El-Sayed, *Gold Nanorods: From Synthesis and Properties to Biological and Biomedical Applications.* Advanced Materials, 2009. **21**(48): p. 4880-4910.

Huang, X., et al., *A reexamination of active and passive tumor targeting by using rod-shaped gold nanocrystals and covalently conjugated peptide ligands.* ACS Nano, 2010. **4**(10): p. 5887-96.

Hurst, G.C., et al., *Intravascular (catheter) NMR receiver probe: preliminary design analysis and application to canine iliofemoral imaging.* Magn Reson Med, 1992. **24**(2): p. 343-57.

Ilinskaya, A.N. and M.A. Dobrovolskaia, *Nanoparticles and the blood coagulation system. Part II: safety concerns.* Nanomedicine (Lond), 2013. **8**(6): p. 969-81.

Institute, A.N.S., *ANSI Z136.1-2007 American national standard for safe use of lasers*. 2007.

Institute, A.N.S., *ANSI Z136.3- Safe Use of Lasers in Health Care*. 2011.

Ishibashi, F., et al., *Update on coronary angioscopy: review of a 20-year experience and potential application for detection of vulnerable plaque.* J Interv Cardiol, 2006. **19**(1): p. 17-25.

Jain, B., et al., *Photophysical properties of Chlorin-p6 bound to coated gold nanorods.* Journal of Molecular Structure, 2013. **1032**(0): p. 23-28.

Jain, P.K., et al., *Calculated absorption and scattering properties of gold nanoparticles of different size, shape, and composition: applications in biological imaging and biomedicine.* J Phys Chem B, 2006. **110**(14): p. 7238-48.

Jana, N.R., L. Gearheart, and C.J. Murphy, *Seed-Mediated Growth Approach for Shape-Controlled Synthesis of Spheroidal and Rod-like Gold Nanoparticles Using a Surfactant Template.* Advanced Materials, 2001. **13**(18): p. 1389-1393.

Janecek, M., et al., *Intravascular probe for detection of vulnerable plaque.* Mol Imaging Biol, 2004. **6**(3): p. 131-8.

Jang, B., et al., *Gold Nanorod−Photosensitizer Complex for Near-Infrared Fluorescence Imaging and Photodynamic/Photothermal Therapy In Vivo.* ACS Nano, 2011. **5**(2): p. 1086-1094.

Jang, I.-K., et al., *Visualization of coronary atherosclerotic plaques in patients using optical coherence tomography: comparison with intravascular ultrasound.* Journal of the American College of Cardiology, 2002. **39**(4): p. 604-609.

Jansen, K., et al., *Intravascular photoacoustic imaging of human coronary atherosclerosis.* Opt. Lett., 2011. **36**(5): p. 597-599.

Jansen, K., G. van Soest, and A.F. van der Steen, *Intravascular Photoacoustic Imaging: A New Tool for Vulnerable Plaque Identification.* Ultrasound Med Biol, 2014. **40**(6): p. 1037-1048.

Jansen, K., et al., *Lipid detection in atherosclerotic human coronaries by spectroscopic intravascular photoacoustic imaging.* Opt Express, 2013. **21**(18): p. 21472-84.

Jun, E.A., et al., *Silver nanoparticles enhance thrombus formation through increased platelet aggregation and procoagulant activity.* Nanotoxicology, 2011. **5**(2): p. 157-67.

Karpiouk, A.B., et al., *Feasibility of in vivo intravascular photoacoustic imaging using integrated ultrasound and photoacoustic imaging catheter.* J Biomed Opt, 2012. **17**(9): p. 96008-1.

Karpiouk, A.B., B. Wang, and S.Y. Emelianov, *Development of a catheter for combined intravascular ultrasound and photoacoustic imaging.* Rev Sci Instrum, 2010. **81**(1): p. 014901.

Kereiakes, D.J., et al., *Phase I drug and light dose-escalation trial of motexafin lutetium and far red light activation (phototherapy) in subjects with coronary artery disease undergoing percutaneous coronary intervention and stent deployment: procedural and long-term results.* Circulation, 2003. **108**(11): p. 1310-5.

Khaing Oo, M.K., et al., *Gold Nanoparticle-Enhanced and Size-Dependent Generation of Reactive Oxygen Species from Protoporphyrin IX.* ACS Nano, 2012. **6**(3): p. 1939-1947.

Khan, K.M., et al., *Depth-sensitive Raman spectroscopy combined with optical coherence tomography for layered tissue analysis.* Journal of Biophotonics, 2014. **7**(1-2): p. 77-85.

Kharlamov, A.N. and J.L. Gabinsky, *Plasmonic photothermic and stem cell therapy of atherosclerotic plaque as a novel nanotool for angioplasty and artery remodeling.* Rejuvenation Res, 2012. **15**(2): p. 222-230.

Kharlamov, A.N., et al., *Plasmonics for Treatment of Atherosclerosis: Results of NANOM-FIM Trial.* Nanomedicine & Nanotechnology, 2013. **4**(160): p. doi: 10.4172/2157-7439.1000160.

Kim, G., et al., *Indocyanine-green-embedded PEBBLEs as a contrast agent for photoacoustic imaging.* J Biomed Opt, 2007. **12**(4): p. 044020.

Kim, J., et al., *Preparation of biodegradable polymer/silver nanoparticles composite and its antibacterial efficacy.* J Nanosci Nanotechnol, 2009. **9**(2): p. 1098-102.

Kim, J.-Y., et al., *Tumor-targeting nanogel that can function independently for both photodynamic and photothermal therapy and its synergy from the procedure of PDT followed by PTT.* Journal of Controlled Release, (0).

Kim, J.-Y., et al., *Tumor-targeting nanogel that can function independently for both photodynamic and photothermal therapy and its synergy from the procedure of PDT followed by PTT.* Journal of Controlled Release, 2013(0).

Kim, S.W., et al., *The virtual histology intravascular ultrasound appearance of newly placed drug-eluting stents.* Am J Cardiol, 2008. **102**(9): p. 1182-6.

Kinney, J.B. and R.H. Staley, *Applications of Photoacoustic Spectroscopy.* Annual Review of Materials Science, 1982. **12**(1): p. 295-321.

Koie, S., et al., *[Intravascular ultrasound and angioscopy].* Nihon Rinsho, 2003. **61**(10): p. 1744-50.

Kolodgie, F.D., et al., *Pathologic assessment of the vulnerable human coronary plaque.* Heart, 2004. **90**(12): p. 1385-1391.

Korbelik, M., *PDT-associated host response and its role in the therapy outcome.* Lasers Surg Med, 2006. **38**(5): p. 500-8.

Kruger, R.A., et al., *Photoacoustic ultrasound (PAUS)--reconstruction tomography.* Med Phys, 1995. **22**(10): p. 1605-9.

Kubo, T., et al., *Implication of plaque color classification for assessing plaque vulnerability: a coronary angioscopy and optical coherence tomography investigation.* JACC Cardiovasc Interv, 2008. **1**(1): p. 74-80.

Kubo, T., et al., *Assessment of culprit lesion morphology in acute myocardial infarction: ability of optical coherence tomography compared with intravascular ultrasound and coronary angioscopy.* J Am Coll Cardiol, 2007. **50**(10): p. 933-9.

Kumar, S., J. Aaron, and K. Sokolov, *Directional conjugation of antibodies to nanoparticles for synthesis of multiplexed optical contrast agents with both delivery and targeting moieties.* Nat. Protocols, 2008. **3**(2): p. 314-320.

Kuo, W.-S., et al., *Gold Nanorods in Photodynamic Therapy, as Hyperthermia Agents, and in Near-Infrared Optical Imaging.* Angewandte Chemie International Edition, 2010. **49**(15): p. 2711-2715.

Kuo, W.-S., et al., *Gold nanomaterials conjugated with indocyanine green for dual-modality photodynamic and photothermal therapy.* Biomaterials, 2012. **33**(11): p. 3270-3278.

Lafont, A., *Basic aspects of plaque vulnerability.* Heart, 2003. **89**(10): p. 1262-7.

Lederman, R.J., et al., *Detection of atherosclerosis using a novel positron-sensitive probe and 18-fluorodeoxyglucose (FDG).* Nucl Med Commun, 2001. **22**(7): p. 747-53.

Li, C. and L.V. Wang, *Photoacoustic tomography and sensing in biomedicine.* Phys Med Biol, 2009. **54**(19): p. R59-97.

Li, P.C., et al., *In vivo photoacoustic molecular imaging with simultaneous multiple selective targeting using antibody-conjugated gold nanorods.* Opt Express, 2008. **16**(23): p. 18605-15.

Liangzhong, X., et al. *Gold nanoshell-based photoacoustic imaging application in biomedicine*. in *Biophotonics, Nanophotonics and Metamaterials, 2006. Metamaterials 2006. International Symposium on*. 2006.

Liao, H. and J.H. Hafner, *Gold Nanorod Bioconjugates.* Chemistry of Materials, 2005. **17**(18): p. 4636-4641.

Lin, J., et al., *Photosensitizer-Loaded Gold Vesicles with Strong Plasmonic Coupling Effect for Imaging-Guided Photothermal/Photodynamic Therapy.* ACS Nano, 2013. **7**(6): p. 5320-5329.

Lindig, B.A., M.A.J. Rodgers, and A.P. Schaap, *Determination of the lifetime of singlet oxygen in water-d2 using 9,10-anthracenedipropionic acid, a water-soluble probe.* Journal of the American Chemical Society, 1980. **102**(17): p. 5590-5593.

Longmire, M., P.L. Choyke, and H. Kobayashi, *Clearance properties of nano-sized particles and molecules as imaging agents: considerations and caveats.* Nanomedicine (Lond), 2008. **3**(5): p. 703-17.

Luke, G., D. Yeager, and S. Emelianov, *Biomedical Applications of Photoacoustic Imaging with Exogenous Contrast Agents.* Annals of Biomedical Engineering, 2012. **40**(2): p. 422-437.

Mackey, M.A., et al., *The Most Effective Gold Nanorod Size for Plasmonic Photothermal Therapy: Theory and In Vitro Experiments.* The Journal of Physical Chemistry B, 2014. **118**(5): p. 1319-1326.

MacNeill, B.D., et al., *Intravascular Modalities for Detection of Vulnerable Plaque: Current Status.* Arteriosclerosis, Thrombosis, and Vascular Biology, 2003. **23**(8): p. 1333-1342.

Madder, R.D., et al., *Composition of Target Lesions by Near-Infrared Spectroscopy in Patients With Acute Coronary Syndrome Versus Stable Angina.* Circulation: Cardiovascular Interventions, 2012. **5**(1): p. 55-61.

Mahon, E., D.R. Hristov, and K.A. Dawson, *Stabilising fluorescent silica nanoparticles against dissolution effects for biological studies.* Chemical Communications, 2012. **48**(64): p. 7970-7972.

Mallidi, S., et al., *Multiwavelength photoacoustic imaging and plasmon resonance coupling of gold nanoparticles for selective detection of cancer.* Nano Lett, 2009. **9**(8): p. 2825-31.

Manoharan, R., et al., *Quantitative histochemical analysis of human artery using Raman spectroscopy.* J Photochem Photobiol B, 1992. **16**(2): p. 211-33.

Marcu, L., et al., *In vivo detection of macrophages in a rabbit atherosclerotic model by time-resolved laser-induced fluorescence spectroscopy.* Atherosclerosis, 2005. **181**(2): p. 295-303.

Marcu, L., et al., *Detection of rupture-prone atherosclerotic plaques by time-resolved laser-induced fluorescence spectroscopy.* Atherosclerosis, 2009. **204**(1): p. 156-64.

Martin, A.J., D.B. Plewes, and R.M. Henkelman, *MR imaging of blood vessels with an intravascular coil.* J Magn Reson Imaging, 1992. **2**(4): p. 421-9.

Martinet, W. and G.R.Y. De Meyer, *Selective Depletion of Macrophages in Atherosclerotic Plaques: Myth, Hype, or Reality?* Circulation Research, 2007. **100**(6): p. 751-753.

Martinet, W., S. Verheye, and G.R. De Meyer, *Selective depletion of macrophages in atherosclerotic plaques via macrophage-specific initiation of cell death.* Trends Cardiovasc Med, 2007. **17**(2): p. 69-75.

Mendis S, P.P., Norrving B, *Global Atlas on Cardiovascular Disease Prevention and Control*, ed. W.H.O.W.h.F.W.S. Organization. 2011, Geneva. 164.

Meng-Lin, L., et al., *Simultaneous Molecular and Hypoxia Imaging of Brain Tumors <emphasis emphasistype="italic">In Vivo</emphasis> Using Spectroscopic Photoacoustic Tomography.* Proceedings of the IEEE, 2008. **96**(3): p. 481-489.

Millstone, J.E., et al., *Colloidal gold and silver triangular nanoprisms.* Small, 2009. **5**(6): p. 646-64.

Mintz, G.S., *Quantitative and Qualitative Analyses*. Intrascoronary Ultrasound. 2005, Oxon, UK: Taylor & Francis.

Moreno, P.R., et al., *Detection of lipid pool, thin fibrous cap, and inflammatory cells in human aortic atherosclerotic plaques by near-infrared spectroscopy.* Circulation, 2002. **105**(8): p. 923-7.

Motz, J.T., et al., *In vivo Raman spectral pathology of human atherosclerosis and vulnerable plaque.* J Biomed Opt, 2006. **11**(2): p. 021003.

Mullenix, P.S., C.A. Andersen, and B.W. Starnes, *Atherosclerosis as Inflammation.* Annals of vascular surgery, 2005. **19**(1): p. 130-138.

Muller, J.E., et al., *Triggers, acute risk factors and vulnerable plaques: The lexicon of a new frontier.* Journal of the American College of Cardiology, 1994. **23**(3): p. 809-813.

Muller, J.E., G.H. Tofler, and P.H. Stone, *Circadian variation and triggers of onset of acute cardiovascular disease.* Circulation, 1989. **79**(4): p. 733-43.

Naghavi, M., et al., *From Vulnerable Plaque to Vulnerable Patient Part III: Executive Summary of the Screening for Heart Attack Prevention and Education (SHAPE) Task Force Report.* The American Journal of Cardiology, 2006. **98**(2, Supplement 1): p. 2-15.

Naghavi, M., et al., *From Vulnerable Plaque to Vulnerable Patient: A Call for New Definitions and Risk Assessment Strategies: Part I.* Circulation, 2003. **108**(14): p. 1664-1672.

Niidome, T., et al., *PEG-modified gold nanorods with a stealth character for in vivo applications.* J Control Release, 2006. **114**(3): p. 343-7.

Nikoobakht, B. and M.A. El-Sayed, *Preparation and Growth Mechanism of Gold Nanorods (NRs) Using Seed-Mediated Growth Method.* Chemistry of Materials, 2003. **15**(10): p. 1957-1962.

Nissen, S.E. and P. Yock, *Intravascular ultrasound: novel pathophysiological insights and current clinical applications.* Circulation, 2001. **103**(4): p. 604-16.

Obaid, D.R., et al., *Identification of Coronary Plaque Sub-Types Using Virtual Histology Intravascular Ultrasound Is Affected by Inter-Observer Variability and Differences in Plaque Definitions.* Circulation: Cardiovascular Imaging, 2011. **5**(1): p. 86-93.

Oh, J., H. Yoon, and J.-H. Park, *Nanoparticle platforms for combined photothermal and photodynamic therapy.* Biomedical Engineering Letters, 2013. **3**(2): p. 67-73.

Oraevsky A. A., J.S.L., Esenaliev R. O., and Tittel F. K., *Laser based optoacoustic imaging in biological tissues.* Proc. SPIE, 1994. **0277-786X**(2134A): p. 122-128.

Packard, R.R.S. and P. Libby, *Inflammation in Atherosclerosis: From Vascular Biology to Biomarker Discovery and Risk Prediction.* Clinical Chemistry, 2008. **54**(1): p. 24-38.

Pasterkamp, G., et al., *Inflammation of the atherosclerotic cap and shoulder of the plaque is a common and locally observed feature in unruptured plaques of femoral and coronary arteries.* Arterioscler Thromb Vasc Biol, 1999. **19**(1): p. 54-8.

Phipps, J., et al., *Fluorescence lifetime imaging for the characterization of the biochemical composition of atherosclerotic plaques.* J Biomed Opt, 2011. **16**(9): p. 096018.

Phipps, J., et al., *Fluorescence lifetime imaging microscopy for the characterization of atherosclerotic plaques.* Proc Soc Photo Opt Instrum Eng, 2009. **7161**: p. 71612g.

Piao, D., et al., *Hybrid positron detection and optical coherence tomography system: design, calibration, and experimental validation with rabbit atherosclerotic models.* J Biomed Opt, 2005. **10**(4): p. 44010.

Pramanik, M. and L.V. Wang, *Thermoacoustic and photoacoustic sensing of temperature.* J Biomed Opt, 2009. **14**(5): p. 054024.

Preihs, C., et al., *Recent Developments in Texaphyrin Chemistry and Drug Discovery.* Inorganic Chemistry, 2013. **52**(21): p. 12184-12192.

Raber, L., et al., *Offline fusion of co-registered intravascular ultrasound and frequency domain optical coherence tomography images for the analysis of human atherosclerotic plaques.* EuroIntervention, 2012. **8**(1): p. 98-108.

Radin, S., et al., *In vitro bioactivity and degradation behavior of silica xerogels intended as controlled release materials.* Biomaterials, 2002. **23**(15): p. 3113-3122.

Razansky, D., et al., *Multispectral optoacoustic tomography of matrix metalloproteinase activity in vulnerable human carotid plaques.* Mol Imaging Biol, 2012. **14**(3): p. 277-85.

Regar, E., et al., *First-In-Man application of a miniature self-contained intracoronary magnetic resonance probe. A multi-centre safety and feasibility trial.* EuroIntervention, 2006. **2**(1): p. 77-83.

Reifart, N., et al., *Randomized comparison of angioplasty of complex coronary lesions at a single center. Excimer Laser, Rotational Atherectomy, and Balloon Angioplasty Comparison (ERBAC) Study.* Circulation, 1997. **96**(1): p. 91-8.

Richard Spears, J., *Percutaneous laser treatment of atherosclerosis: An overview of emerging techniques.* CardioVascular and Interventional Radiology, 1986. **9**(5-6): p. 303-312.

Richards-Kortum, R., et al., *A one-layer model of laser-induced fluorescence for diagnosis of disease in human tissue: applications to atherosclerosis.* Biomedical Engineering, IEEE Transactions on, 1989. **36**(12): p. 1222-1232.

Rockson, S.G., et al., *Photoangioplasty for Human Peripheral Atherosclerosis: Results of a Phase I Trial of Photodynamic Therapy With Motexafin Lutetium (Antrin).* Circulation, 2000. **102**(19): p. 2322-2324.

Roger, V.r.L., et al., *Heart Disease and Stroke Statistics-2012 Update: A Report From the American Heart Association.* Circulation, 2012. **125**(1): p. e2-e220.

Romer, T.J., et al., *Histopathology of human coronary atherosclerosis by quantifying its chemical composition with Raman spectroscopy.* Circulation, 1998. **97**(9): p. 878-85.

Romer, T.J., et al., *Intravascular ultrasound combined with Raman spectroscopy to localize and quantify cholesterol and calcium salts in atherosclerotic coronary arteries.* Arterioscler Thromb Vasc Biol, 2000. **20**(2): p. 478-83.

Rosencwaig, A., *Photoacoustic Spectroscopy*, in *Advances in Electronics and Electron Physics*, L. Marton, Editor. 1978, Academic Press. p. 207-311.

Ross, R., *Cell Biology of Atherosclerosis.* Annual Review of Physiology, 1995. **57**(1): p. 791-804.

S. Sethuraman, S.R.A., J. H. Amirian, R. W. Smalling, and S. Y. Emelianov, *Intravascular photoacoustic imaging using an IVUS imaging catheter.* IEEE Trans. Ultrason. Ferroelectr. Freq. Control, 2007. **54**: p. 978-986.

Sanz, J. and Z.A. Fayad, *Imaging of atherosclerotic cardiovascular disease.* Nature, 2008. **451**(7181): p. 953-957.

Scepanovic, O.R., et al., *Multimodal spectroscopy detects features of vulnerable atherosclerotic plaque.* J Biomed Opt, 2011. **16**(1): p. 011009.

Šćepanović, O.R., et al., *A multimodal spectroscopy system for real-time disease diagnosis.* Review of Scientific Instruments, 2009. **80**(4): p. -.

Schneiderman, J., et al., *Diagnosis of Thin-Cap Fibroatheromas by a Self-Contained Intravascular Magnetic Resonance Imaging Probe in Ex Vivo Human Aortas and In Situ Coronary Arteries.* Journal of the American College of Cardiology, 2005. **45**(12): p. 1961-1969.

Schrijvers, D.M., et al., *Phagocytosis of apoptotic cells by macrophages is impaired in atherosclerosis.* Arterioscler Thromb Vasc Biol, 2005. **25**(6): p. 1256-61.

Schwartz, B.G., et al., *Therapeutic hypothermia for acute myocardial infarction and cardiac arrest.* Am J Cardiol, 2012. **110**(3): p. 461-6.

Sessler, J.L., et al., *Texaphyrins: Synthesis and Applications.* Accounts of Chemical Research, 1994. **27**(2): p. 43-50.

Sethuraman, S., et al., *Intravascular photoacoustic imaging using an IVUS imaging catheter.* IEEE Trans. Ultrason. Ferroelectr. Freq. Control, 2007. **54**: p. 978-986.

Sethuraman, S., et al., *Remote temperature estimation in intravascular photoacoustic imaging.* Ultrasound Med Biol, 2008. **34**(2): p. 299-308.

Sethuraman, S., et al., *Ex vivo Characterization of Atherosclerosis using Intravascular Photoacoustic Imaging.* Opt. Express, 2007. **15**(25): p. 16657-16666.

Sethuraman, S., et al., *Spectroscopic intravascular photoacoustic imaging to differentiate atherosclerotic plaques.* Optics Express, 2008. **16**(5): p. 3362-3367.

Sethuraman, S., et al. *6G-3 Temperature Monitoring in Intravascular Photoacoustic Imaging*. in *Ultrasonics Symposium, 2006. IEEE*. 2006.

Seungsoo, K., et al. *Ultrasound and photoacoustic image-guided photothermal therapy using silica-coated gold nanorods: In-vivo study*. in *Ultrasonics Symposium (IUS), 2010 IEEE*. 2010.

Shah, J., et al., *Photoacoustic imaging and temperature measurement for photothermal cancer therapy.* J Biomed Opt, 2008. **13**(3): p. 034024.

Sherman, C.T., et al., *Coronary angioscopy in patients with unstable angina pectoris.* N Engl J Med, 1986. **315**(15): p. 913-9.

Shi, J., et al., *Endothelial cell injury and dysfunction induced by silver nanoparticles through oxidative stress via IKK/NF-kappaB pathways.* Biomaterials, 2014. **35**(24): p. 6657-66.

Shikhaliev, P.M., et al., *Positron autoradiography for intravascular imaging: feasibility evaluation.* Phys Med Biol, 2006. **51**(4): p. 963-79.

Shiomi, M. and T. Ito, *The Watanabe heritable hyperlipidemic (WHHL) rabbit, its characteristics and history of development: a tribute to the late Dr. Yoshio Watanabe.* Atherosclerosis, 2009. **207**(1): p. 1-7.

Shrivastava, S., et al., *Characterization of antiplatelet properties of silver nanoparticles.* ACS Nano, 2009. **3**(6): p. 1357-64.

Shrivastava, S., et al., *Negative regulation of fibrin polymerization and clot formation by nanoparticles of silver.* Colloids Surf B Biointerfaces, 2011. **82**(1): p. 241-6.

Sigrist, M.W., *Laser generation of acoustic waves in liquids and gases.* Journal of Applied Physics, 1986. **60**(7): p. R83-R122.

Silva, A.K., D. Letourneur, and C. Chauvierre, *Polysaccharide nanosystems for future progress in cardiovascular pathologies.* Theranostics, 2014. **4**(6): p. 579-91.

Simsek, C., et al., *The ability of high dose rosuvastatin to improve plaque composition in non-intervened coronary arteries: rationale and design of the Integrated Biomarker and Imaging Study-3 (IBIS-3).* EuroIntervention, 2012. **8**(2): p. 235-41.

Skajaa, T., et al., *High-density lipoprotein-based contrast agents for multimodal imaging of atherosclerosis.* Arterioscler Thromb Vasc Biol, 2010. **30**(2): p. 169-76.

Skajaa, T., et al., *The biological properties of iron oxide core high-density lipoprotein in experimental atherosclerosis.* Biomaterials, 2011. **32**(1): p. 206-13.

Skrabalak, S.E., et al., *Gold nanocages: synthesis, properties, and applications.* Acc Chem Res, 2008. **41**(12): p. 1587-95.

Smith, S.C., et al., *ACC/AHA Guidelines for Percutaneous Coronary Intervention (Revision of the 1993 PTCA Guidelines)â€"Executive Summary: A Report of the American College of Cardiology/American Heart Association Task Force on Practice Guidelines (Committee to Revise the 1993 Guidelines for Percutaneous Transluminal Coronary Angioplasty) Endorsed by the Society for Cardiac Angiography and Interventions.* Circulation, 2001. **103**(24): p. 3019-3041.

Song, K.H., et al., *Noninvasive in vivo spectroscopic nanorod-contrast photoacoustic mapping of sentinel lymph nodes.* Eur J Radiol, 2009. **70**(2): p. 227-31.

Song, K.H., et al., *Noninvasive photoacoustic identification of sentinel lymph nodes containing methylene blue in vivo in a rat model.* J Biomed Opt, 2008. **13**(5): p. 054033.

Spears, J.R., A.M. Spokojny, and H.J. Marais, *Coronary angioscopy during cardiac catheterization.* J Am Coll Cardiol, 1985. **6**(1): p. 93-7.

Stantz, K.M., et al. *Molecular imaging of neutropilin-1 receptor using photoacoustic spectroscopy in breast tumors*. 2010.

Stone, G.W., et al., *A Prospective Natural-History Study of Coronary Atherosclerosis.* New England Journal of Medicine, 2011. **364**(3): p. 226-235.

Strauss, H.W., et al., *Intravascular Radiation Detectors for the Detection of Vulnerable Atheroma.* Journal of the American College of Cardiology, 2006. **47**(8, Supplement): p. C97-C100.

Su, J.L.-S., B. Wang, and S.Y. Emelianov, *Photoacoustic imaging of coronary artery stents.* Optics Express, 2009. **17**(22): p. 19894-19901.

Suh, W.M., et al., *Intravascular Detection of the Vulnerable Plaque.* Circulation: Cardiovascular Imaging, 2011. **4**(2): p. 169-178.

Summers, M. and M. Patel, *Appropriateness of Percutaneous Coronary Intervention: A Review.* Current Cardiology Reports, 2013. **15**(7): p. 1-8.

Suter, M.J., et al., *Intravascular optical imaging technology for investigating the coronary artery.* JACC Cardiovasc Imaging, 2011. **4**(9): p. 1022-39.

Tabas, I., *Consequences and therapeutic implications of macrophage apoptosis in atherosclerosis: the importance of lesion stage and phagocytic efficiency.* Arterioscler Thromb Vasc Biol, 2005. **25**(11): p. 2255-64.

Tada, D.B., et al., *Methylene Blue-Containing Silica-Coated Magnetic Particles: A Potential Magnetic Carrier for Photodynamic Therapy.* Langmuir, 2007. **23**(15): p. 8194-8199.

Takano, M., et al., *Changes in coronary plaque color and morphology by lipid-lowering therapy with atorvastatin: serial evaluation by coronary angioscopy.* J Am Coll Cardiol, 2003. **42**(4): p. 680-6.

Tam, A.C., *Applications of photoacoustic sensing techniques.* Reviews of Modern Physics, 1986. **58**(2): p. 381-431.

Tam, J.M., et al., *Kinetic assembly of near-IR-active gold nanoclusters using weakly adsorbing polymers to control the size.* Langmuir, 2010. **26**(11): p. 8988-99.

Tam, J.M., et al., *Controlled assembly of biodegradable plasmonic nanoclusters for near-infrared imaging and therapeutic applications.* ACS Nano, 2010. **4**(4): p. 2178-84.

Tang, W., et al., *Photodynamic Characterization and In Vitro Application of Methylene Blue-containing Nanoparticle Platforms*¶. Photochemistry and Photobiology, 2005. **81**(2): p. 242-249.

Taruttis, A., et al., *Real-time imaging of cardiovascular dynamics and circulating gold nanorods with multispectral optoacoustic tomography.* Opt Express, 2010. **18**(19): p. 19592-602.

Tawakol, A. and J. Muller, *Through the looking glass: an angioscopic view of the effect of statin therapy on coronary artery plaques.* J Am Coll Cardiol, 2003. **42**(4): p. 687-9.

Tearney, G.J., et al., *Consensus Standards for Acquisition, Measurement, and Reporting of Intravascular Optical Coherence Tomography Studies: A Report From the International Working Group for Intravascular Optical Coherence Tomography Standardization and Validation.* Journal of the American College of Cardiology, 2012. **59**(12): p. 1058-1072.

Terentyuk, G., et al., *Gold nanorods with a hematoporphyrin-loaded silica shell for dual-modality photodynamic and photothermal treatment of tumors in vivo.* Nano Research, 2014. **7**(3): p. 325-337.

Thaxton, C.S., et al., *Templated spherical high density lipoprotein nanoparticles.* J Am Chem Soc, 2009. **131**(4): p. 1384-5.

Thim, T., et al., *Unreliable Assessment of Necrotic Core by Virtual Histology Intravascular Ultrasound in Porcine Coronary Artery Disease.* Circulation: Cardiovascular Imaging, 2010. **3**(4): p. 384-391.

Thorp, E. and I. Tabas, *Mechanisms and consequences of efferocytosis in advanced atherosclerosis.* J Leukoc Biol, 2009. **86**(5): p. 1089-95.

Tokuhiro, K., et al., *Evaluation of Annuloaortic Ectasia by Angioscopy and IVUS "Report of 2 cases".* Diagn Ther Endosc, 2000. **7**(1): p. 35-45.

Tong, L., et al., *Gold Nanorods Mediate Tumor Cell Death by Compromising Membrane Integrity.* Adv Mater, 2007. **19**: p. 3136-3141.

Ueda, Y., et al., *Assessment of plaque vulnerability by angioscopic classification of plaque color.* Am Heart J, 2004. **148**(2): p. 333-5.

van de Poll, S.W., et al., *On-line detection of cholesterol and calcification by catheter based Raman spectroscopy in human atherosclerotic plaque ex vivo.* Heart, 2003. **89**(9): p. 1078-82.

van de Poll, S.W.E., et al. *Coronary atherosclerotic plaque characterization using IVUS elastography and Raman spectroscopy*. in *Ultrasonics Symposium, 2000 IEEE*. 2000.

van Leeuwen, T.G., et al., *Origin of arterial wall dissections induced by pulsed excimer and mid-infrared laser ablation in the pig.* J Am Coll Cardiol, 1992. **19**(7): p. 1610-8.

van Rooijen, N., A. Sanders, and T.K. van den Berg, *Apoptosis of macrophages induced by liposome-mediated intracellular delivery of clodronate and propamidine.* J Immunol Methods, 1996. **193**(1): p. 93-9.

van Velzen, J.E., et al., *Comparison of the Relation Between the Calcium Score and Plaque Characteristics in Patients With Acute Coronary Syndrome Versus Patients With Stable Coronary Artery Disease, Assessed by Computed Tomography Angiography and Virtual Histology Intravascular Ultrasound.* The American Journal of Cardiology, 2011. **108**(5): p. 658-664.

Van Vré, E.A., et al., *Apoptotic Cell Death and Efferocytosis in Atherosclerosis.* Arteriosclerosis, Thrombosis, and Vascular Biology, 2012. **32**(4): p. 887-893.

Verheye, S., et al., *Selective clearance of macrophages in atherosclerotic plaques by autophagy.* J Am Coll Cardiol, 2007. **49**(6): p. 706-15.

Vinegoni, C., et al., *Indocyanine green enables near-infrared fluorescence imaging of lipid-rich, inflamed atherosclerotic plaques.* Sci Transl Med, 2011. **3**(84): p. 84ra45.

Virmani, R., et al., *Pathology of the Vulnerable Plaque.* Journal of the American College of Cardiology, 2006. **47**(8, Supplement): p. C13-C18.

Virmani, R., et al., *Atherosclerotic plaque progression and vulnerability to rupture: angiogenesis as a source of intraplaque hemorrhage.* Arterioscler Thromb Vasc Biol, 2005. **25**(10): p. 2054-61.

Waksman, R., et al., *PhotoPoint photodynamic therapy promotes stabilization of atherosclerotic plaques and inhibits plaque progression.* J Am Coll Cardiol, 2008. **52**(12): p. 1024-32.

Walsh, J., *Basic Interactions of Light with Tissue*, in *Optical-Thermal Response of Laser-Irradiated Tissue*, A.J. Welch and M.J.C. Gemert, Editors. 2011, Springer Netherlands. p. 13-26.

Wang, B. and S. Emelianov, *Thermal intravascular photoacoustic imaging.* Biomed Opt Express, 2011. **2**(11): p. 3072-8.

Wang, B., et al. *Intravascular photoacoustic imaging of macrophages using molecularly targeted gold nanoparticles*. 2010.

Wang, B., et al., *In vivo intravascular ultrasound-guided photoacoustic imaging of lipid in plaques using an animal model of atherosclerosis.* Ultrasound Med Biol, 2012. **38**(12): p. 2098-103.

Wang, B., et al., *Intravascular photoacoustic imaging of lipid in atherosclerotic plaques in the presence of luminal blood.* Opt Lett, 2012. **37**(7): p. 1244-6.

Wang, B., et al., *Detection of lipid in atherosclerotic vessels using ultrasound-guided spectroscopic intravascular photoacoustic imaging.* Opt. Express, 2010. **18**(5): p. 4889-4897.

Wang, B., et al., *Intravascular Photoacoustic Imaging.* IEEE J Quantum Electron, 2010. **16**(3): p. 588-599.

Wang, B., et al., *Plasmonic Intravascular Photoacoustic Imaging for Detection of Macrophages in Atherosclerotic Plaques.* Nano Letters, 2008. **9**(6): p. 2212-2217.

Wang, H.-W., et al., *Label-Free Bond-Selective Imaging by Listening to Vibrationally Excited Molecules.* Physical Review Letters, 2011. **106**(23): p. 238106.

Wang, J., et al., *Photosensitizer–Gold Nanorod Composite for Targeted Multimodal Therapy.* Small, 2013: p. n/a-n/a.

Wang, J., et al., *Assembly of Aptamer Switch Probes and Photosensitizer on Gold Nanorods for Targeted Photothermal and Photodynamic Cancer Therapy.* ACS Nano, 2012. **6**(6): p. 5070-5077.

Waxman, S., et al., *In vivo validation of a catheter-based near-infrared spectroscopy system for detection of lipid core coronary plaques: initial results of the SPECTACL study.* JACC Cardiovasc Imaging, 2009. **2**(7): p. 858-68.

Waxman, S., F. Ishibashi, and J.E. Muller, *Detection and Treatment of Vulnerable Plaques and Vulnerable Patients: Novel Approaches to Prevention of Coronary Events.* Circulation, 2006. **114**(22): p. 2390-2411.

Wei, W., et al., *Integrated ultrasound and photoacoustic probe for co-registered intravascular imaging.* J Biomed Opt, 2011. **16**(10): p. 106001.

Willerson, J.T., et al., *Conversion from chronic to acute coronary artery disease: speculation regarding mechanisms.* Am J Cardiol, 1984. **54**(10): p. 1349-54.

Woodburn, K.W., et al., *Photodynamic Therapy of B16F10 Murine Melanoma with Lutetium Texaphyrin.* 1998. **110**(5): p. 746-751.

Woodburn, K.W., et al., *Localization and Efficacy Analysis of the Phototherapeutic Lutetium Texaphyrin (PCI-0123) in the Murine EMT6 Sarcoma Model.* Photochemistry and Photobiology, 1997. **65**(3): p. 410-415.

Xia, Y., et al., *Shape-Controlled Synthesis of Metal Nanocrystals: Simple Chemistry Meets Complex Physics?* Angewandte Chemie International Edition, 2009. **48**(1): p. 60-103.

Yamamoto, M., et al., *Relationship between neointimal coverage of sirolimus-eluting stents and lesion characteristics: a study with serial coronary angioscopy.* Am Heart J, 2009. **158**(1): p. 99-104.

Yang, X., et al., *Photoacoustic tomography of a rat cerebral cortex in vivo with au nanocages as an optical contrast agent.* Nano Lett, 2007. **7**(12): p. 3798-802.

Yeager, D., et al., *Intravascular photoacoustics for image-guidance and temperature monitoring during plasmonic photothermal therapy of atherosclerotic plaques: a feasibility study.* Theranostics, 2013. **4**(1): p. 36-46.

Yeager, D., et al., *Intravascular photoacoustic imaging of exogenously labeled atherosclerotic plaque through luminal blood.* Journal of Biomedical Optics, 2012. **17**(10): p. 106016-106016.

Yin, J., et al., *Novel combined miniature optical coherence tomography ultrasound probe for in vivo intravascular imaging.* J Biomed Opt, 2011. **16**(6): p. 060505.

Yokoyama, S., et al., *Extended follow-up by serial angioscopic observation for bare-metal stents in native coronary arteries: from healing response to atherosclerotic transformation of neointima.* Circ Cardiovasc Interv, 2009. **2**(3): p. 205-12.

Yoo, D., et al., *Double-Effector Nanoparticles: A Synergistic Approach to Apoptotic Hyperthermia.* Angewandte Chemie International Edition, 2012. **51**(50): p. 12482-12485.

Yoon, S.J., et al., *Utility of biodegradable plasmonic nanoclusters in photoacoustic imaging.* Opt Lett, 2010. **35**(22): p. 3751-3.

Zhang, H., et al., *Quantifying the evolution of vascular barrier disruption in advanced atherosclerosis with semipermeant nanoparticle contrast agents.* PLoS One, 2011. **6**(10): p. e26385.

Zhang, Y., et al., *Multifunctional Gold Nanorods with Ultrahigh Stability and Tunability for In Vivo Fluorescence Imaging, SERS Detection, and Photodynamic Therapy.* Angewandte Chemie International Edition, 2013. **52**(4): p. 1148-1151.

Zhang, Z., et al., *Mesoporous Silica-Coated Gold Nanorods as a Light-Mediated Multifunctional Theranostic Platform for Cancer Treatment.* Advanced Materials, 2012. **24**(11): p. 1418-1423.

Zhang Z, W.J., Chen C, *Gold Nanorods Based Platforms for Light-Mediated Theranostics.* Theranostics, 2013. **3**(3): p. 223-238.

Zhao, X.-Q., et al., *Effects of Prolonged Intensive Lipid-Lowering Therapy on the Characteristics of Carotid Atherosclerotic Plaques In Vivo by MRI: A Case-Control Study.* Arteriosclerosis, Thrombosis, and Vascular Biology, 2001. **21**(10): p. 1623-1629.

Zonghai, S., et al., *Indocyanine Green Nanoparticles for Theranostic Applications.* Nano-Micro Letters, 2013. **5**(3): p. 145-150.